POLITECNICO
MILANO 1863

SCUOLA DI INGEGNERIA INDUSTRIALE
E DELL'INFORMAZIONE

Preliminary Design and Optimization of a Subsonic Turbine for Rotating Detonation Engine Applications

TESI DI LAUREA MAGISTRALE IN
MECHANICAL ENGINEERING-INGEGNERIA MECCANICA

Author: **Matteo Bertelli**

Student ID:	944979
Advisor:	Prof. Paolo Gaetani
Co-advisor:	Dott. Noraiz Mushtaq
Academic Year:	2021-2022

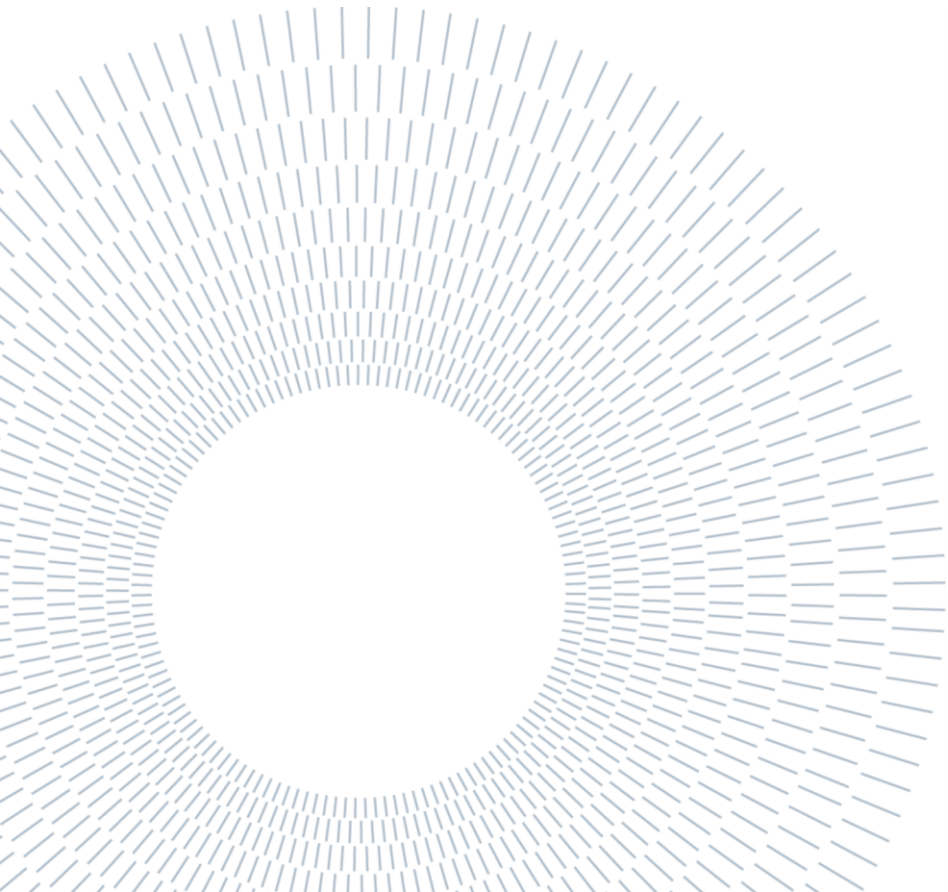

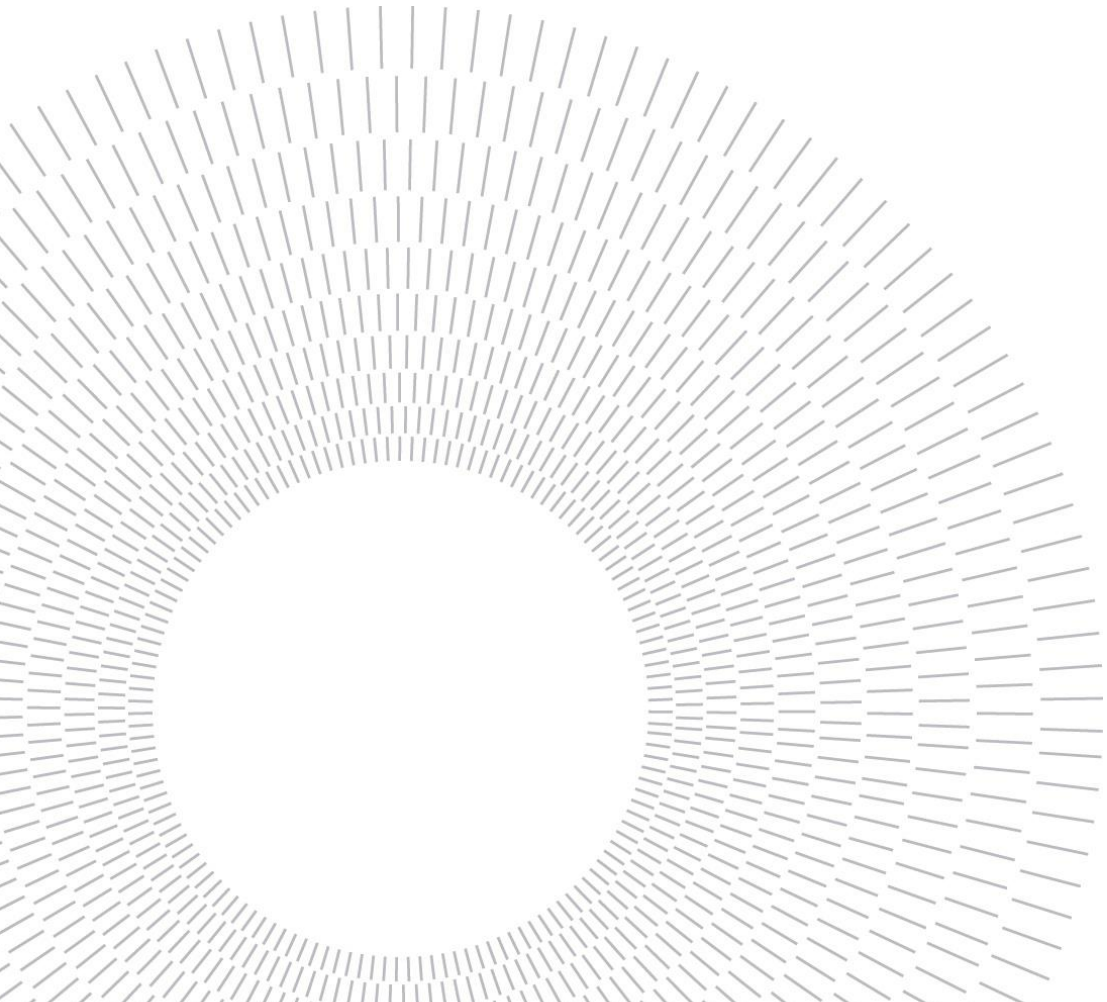

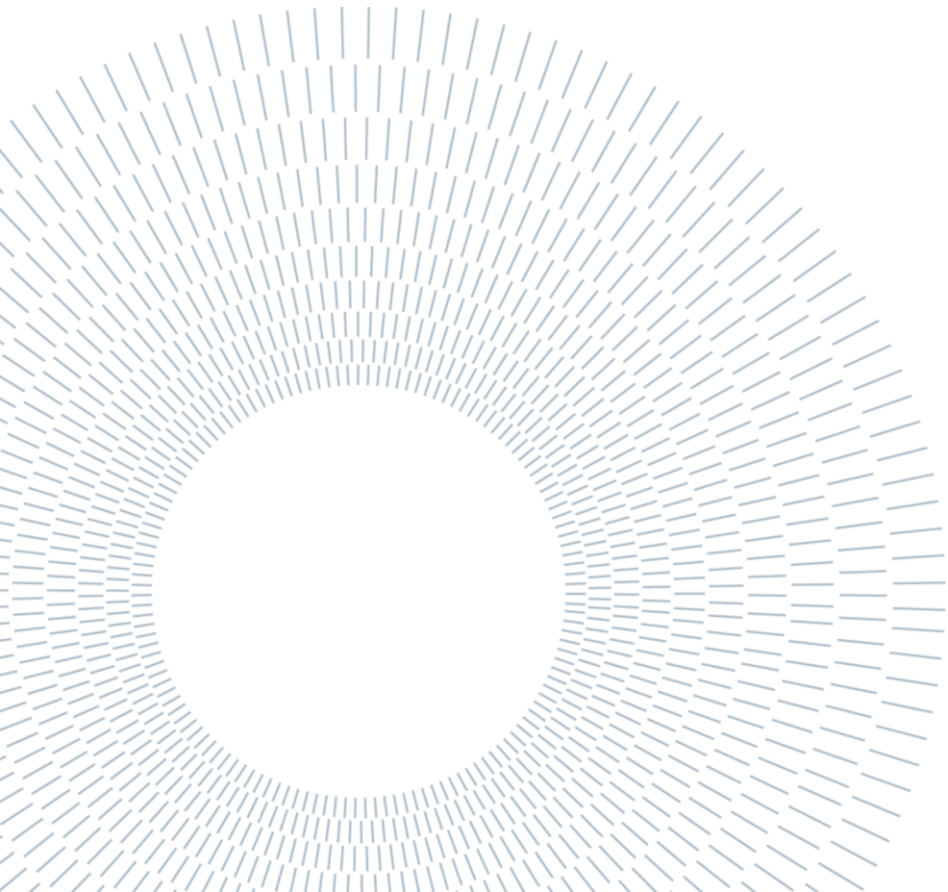

Abstract

The aim of this thesis is the design of a subsonic turbine with high inlet Mach number. To improve the efficiency of gas turbines, recently it was investigated the possibility to replace a classic combustor with a Rotating Detonation Combustor (RDC). This is a novel technology based on the detonation combustion mode and thermodynamic cycle studies have shown optimistic results in terms of performance, efficiency and emission of pollutants. The flow coming out from the detonative combustor is supersonic, non-uniform and unsteady. Efficient design of supersonic turbines is possible to deal with the outlet supersonic flow, but losses associated to shocks will always be present. For this reason, we investigated an alternative approach to couple an RDC with a gas turbine, adopting a transition duct that decelerate the flow to a subsonic condition. Due to the high non uniformities and unsteadiness of the flow, the deceleration to conventional turbine inlet Mach number of 0.2÷0.3 will produce a high amount of losses, cancelling the advantage of detonative combustion. The design of the turbine was approached starting from a mean-line parametric analysis, to find the point of maximum efficiency. The mean-line software zTurbo was used and a tailored algorithm was created to run the analysis. Due to the particular inlet flow, we were out of validity range of losses correlations implemented in zTurbo, so an extrapolation strategy for Traupel correlations was adopted. It works well for profile losses, but it is inadequate for secondary ones. The following step was the design of the blade profile and meridional channel geometry through 2D CFD simulations. For both stator and rotor we varied the solidity, chord length, blade thickness, camber line and meridional channel shapes to find the combination that produces the lowest amount of losses. Then, a shape optimization procedure using software FORMA was performed to improve turbine performances. The optimized shapes were developed in 3D to assess the 3D flow behavior, finding optimistic results. Finally, mechanical assessment and off-design working conditions analysis were performed, showing that the blades can withstand the static loadings and that performance reduction in off-design conditions are limited.

Key-words: High inlet Mach number; Non-conventional turbine design; Rotating detonation engines; Shape optimization; RDE-turbine coupling.

Sommario

Lo scopo di questo lavoro è la progettazione di una turbina subsonica con un flusso ad alto Mach in ingresso. Per migliorare l'efficienza delle turbine a gas, recenti ricerche hanno studiato la possibilità di adottare un Combustore a Detonazione Rotante (RDC), al posto del classico combustore. Si tratta di una tecnologia basata sulla combustione a detonazione e studi sul ciclo termodinamico hanno mostrato risultati ottimistici in termini di prestazioni, efficienza e riduzione delle emissioni inquinanti. Il flusso che esce dal combustore detonante è supersonico, non uniforme e instabile. Design efficienti di turbine supersoniche sono possibili, ma le perdite dovute agli shock sono sempre presenti. Per questo motivo abbiamo investigato un approccio alternativo per accoppiare RDC e turbina: creare un condotto di transizione che decelera il flusso rendendolo subsonico. A causa delle disuniformità e instabilità, la decelerazione fino a Mach convenzionali di 0.2÷ 0.3 produrrebbe tante perdite da vanificare i vantaggi della combustione a detonazione. La progettazione della turbina è partita da un'analisi parametrica alla linea media, per trovare il punto di massima efficienza. È stato utilizzato il software zTurbo per i calcoli alla linea media ed è stato creato un algoritmo specifico per l'analisi parametrica. A causa del flusso particolare, il caso analizzato è al di fuori del range di validità delle correlaioni delle perdite implementate in zTurbo, per cui abbiamo creato una strategia di estrapolazione per le perdite di Traupel. Questa funziona bene per le perdite di profilo, ma non funziona per quelle secondarie. Il passo successivo è stato la progettazione del profilo della pala e del canale meridionale tramite simulazioni CFD 2D. Per statore e rotore sono stati analizzati il numero di pale, la lunghezza della corda, lo spessore della pala e la forma della linea media e del canale meridionale per trovare la combinazione che produce meno perdite. Poi è stata eseguita un'ottimizzazione dei profili tramite il codice FORMA, per migliorare le prestazioni. I profili ottimizzati sono stati sviluppati in 3D per verificarne il comportamento, ottenendo risultati ottimisitici. Infine sono state eseguite due verifiche: meccanica e lavoro in condizioni off-design. Entrambe hanno restituito buoni risultati.

Parole chiave: Mach elevato in ingresso; Progettazione della turbina non convenzionale; Motore a detonazione rotante; Ottimizzazione dei profili; Accopiamento RDE-turbina.

Contents

1. Rotating Detonation Engines

World energy consumption has increased in the past decades, and it is still increasing as shown in Figure 1.1.

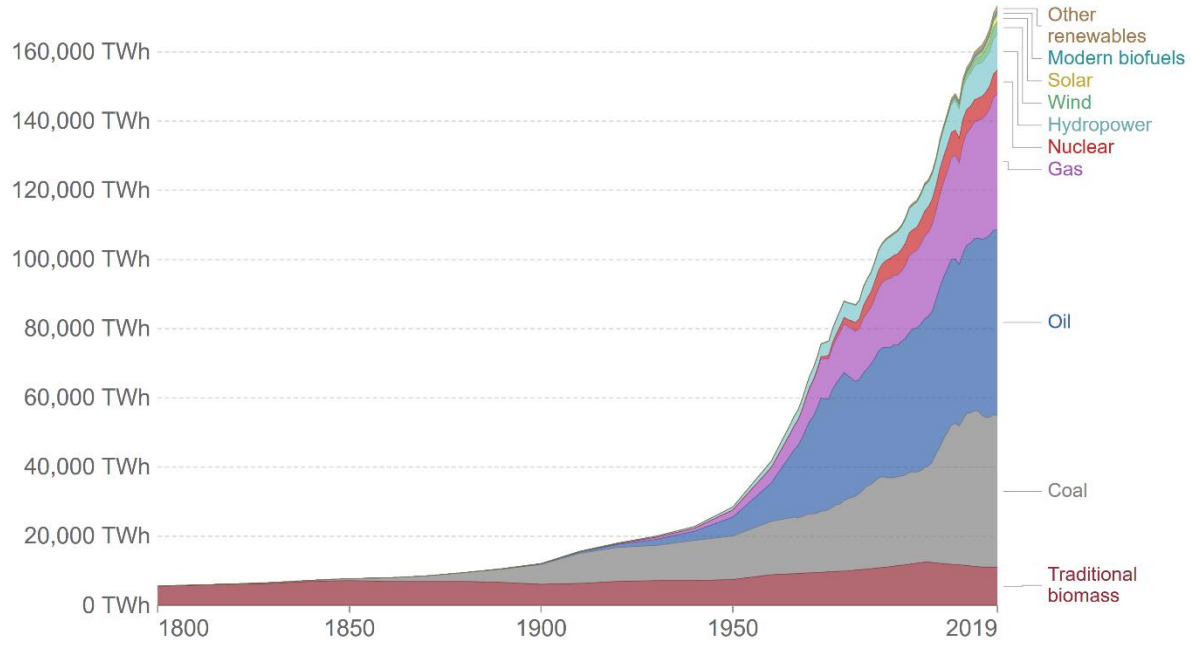

Figure 1.1: Global energy consumption trend in past years divided by energy source [9]

From 1950 the trend shows an important acceleration in energy consumption. Main sources are coal, oil and gas, while the use of renewable energy is marginal, even if it is increasing.

Gas Cycles (GCs) play a key role in energy extraction and, their applications range from aeronautical to stationary power production and naval propulsion. Since GCs

are mainly fueled with fossil fuels (i.e. oil and gas), they have a great impact on environmental problems like pollution and climate change. Therefore, recent research in energy field is focused on finding different and more efficient ways to extract energy, namely green power generation processes. There are three main paths that are followed to reduce environmental impact of energy production:

- Use of renewable energy, like solar, wind and hydropower.
- Use of alternative fuels, like hydrogen.
- Efficiency improvement of energy extraction processes, like gas turbine combined cycles.

Rotating Detonation Engines (RDE) working principle is the mixture burning through a continuously rotating detonation wave, which generate pressure gain. This is why they are part of pressure gain combustion devices. This combustion process allows to apply two of the three paths: efficiency improvement and use of alternative fuels.

1.1 Pressure gain combustion

The idea is to exploit detonation combustion to extract power from fuels [1,3]. The application of this combustion process is of particular interest since it allows to increase the efficiency of the conventional Brayton cycle of more than 15% [1]. To explain this increase of efficiency it is convenient to compare the deflagrative combustion mode, that is the one used by the Bryton cycle, with the detonative one. In deflagrative mode, the combustion wave propagates with subsonic speed causing a reduction of pressure and density, while detonation combustion produces a strong shock wave followed by the reaction front, which propagates with sonic velocity as related to the leading front, causing an increase of pressure and density [2,3]. Moreover, for the same mixture composition, the maximum temperatures of the combustion products reached by the detonation mode are higher than the maximum temperatures reached with deflagration mode [2]. In Figure 1.1.1 and Figure 1.1.2 are represented the Bryton cycle, where the combustion is isobaric, the Humphrey cycle, where the combustion is isochoric, and the Fickett-Jacobs cycle, where detonative combustion is applied.

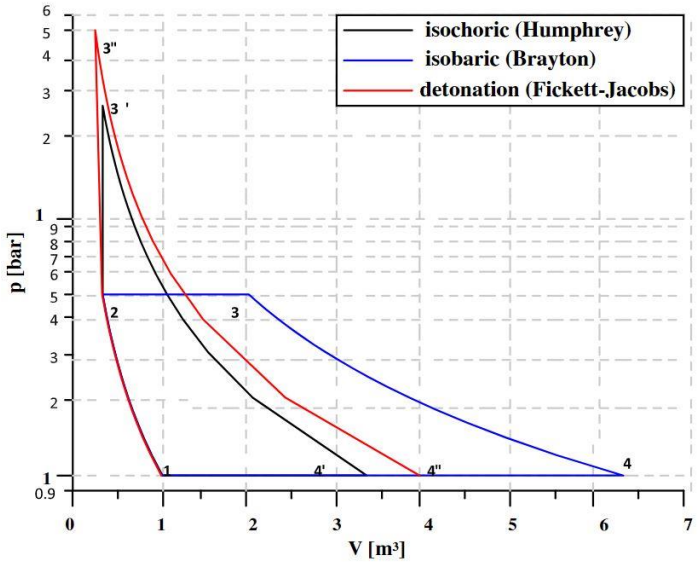

Figure 1.1.1: P-V diagram of Brayton-Joule, Humphrey and Fickett-Jacobs cycles [1,2]

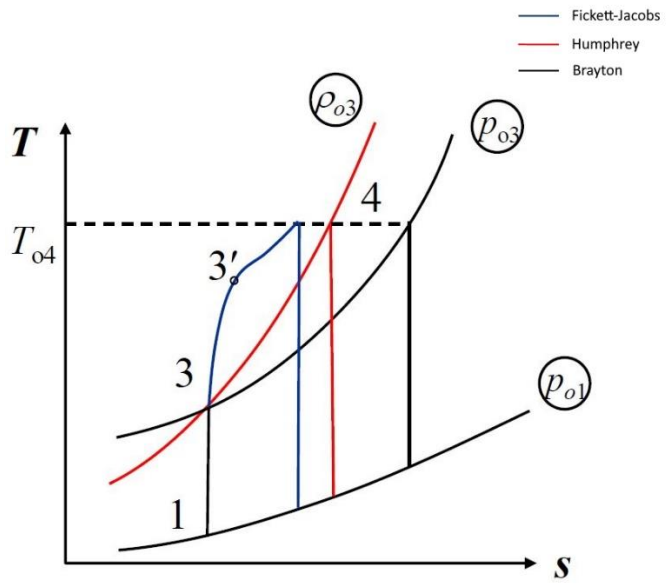

Figure 1.1.2: T-S diagram of Brayton-Joule, Humphrey and Fickett-Jacobs cycles [3]

In the T-S diagram it is evident that the maximum level of entropy reached by the detonative combustion is the lowest, justifying the higher efficiency of the cycle, even if it cannot be modelled as reversible since it involves a shock wave [3].

In Table 1.1.1 are reported the efficiencies of the different cycles for different fuels, considering a compression ratio of 5 for all the cycles, in order to have the same compression process [2].

Table 1.1.1: Comparison of calculated efficiencies for different cycles with different fuels at compression ratio of 5 [2].

Fuel	*Brayton [%]*	*Humphrey [%]*	*Fickett-Jacobs [%]*
Hydrogen-H_2	36.9	54.3	59.3
Methane–CH_4	31.4	50.5	53.2
Acetylene–C_2H_2	36.9	54.1	61.4

The highest efficiency is reached with the Fickett-Jacobs cycle. This is the main reason that makes detonative combustion interesting to be studied, but there are also other motivations that make it interesting, compared to deflagrative combustion [2,3]:

1. Combustion velocities for deflagrative mode is of the order of m/s, while for detonative mode it is of km/s, so the combustion zone is shorter and the combustion chamber can be more compact.
2. Deflagrative combustion uses stoichiometric mixtures, causing high temperatures, high NOx emission and so the need of introducing extra air before turbine, while in detonation mode lean mixtures could be used also allowing NOx reduction.
3. Detonation combustion causes pressure increase, so the number of stages of the compressor can be reduced. This, combined with the compact combustion chamber, allows a reduction of engine weight.
4. Previous points allow a simpler design of the detonation combustion cycle compared to the deflagrative one.

An important observation must be done also on fuels: detonative combustion needs fuels with high detonative power, allowing the use of hydrogen, that would be dangerous in deflagrative combustors; the components for deflagrative combustion applications are not designed to withstand the high pressure waves and high temperatures generated by the detonation, which can easily happen if hydrogen is used. The advantages of using hydrogen are the absence of carbon, so there will not

be carbon oxides (COx) productions, and the high specific energy of about 140 MJ/kg, about 2.8 times natural gas specific energy, allowing to use less fuel to extract the same amount of energy. The disadvantage of using hydrogen is mainly related to the stockage: in gas phase its density is very low, so the tank to contain it will be very big and heavy, instead, in liquid phase where the density is higher, the problem is related to the cryogenic stockage temperatures.

Another advantage of pressure gain combustion is the reduction of fuel consumption, which for small aircrafts can be of the 8%, while for larger aircrafts can be of 5% [5].

There are mainly three ways to implement detonation combustion: standing wave detonation engines, pulsed detonation engines (PDE) and rotating detonation engines (RDE) [1].

1.2 Standing Wave Detonation Engines

The working principle of standing wave detonation engine is relatively simple: fuel is injected in a supersonic flow, the combustion wave is stabilized trough wedge or other means and the combustion products are expanded inside a nozzle [1]. Figure 1.2.1 represents a typical scheme of such an engine.

The biggest disadvantage is the limited range of operating conditions. The velocity at which it can operate must be higher than the Chapman-Jouguet detonation velocity, but the Mach number should be lower than 7, otherwise the pressure losses on the outer contour of the engine will be higher than the thrust produced in the core [1].

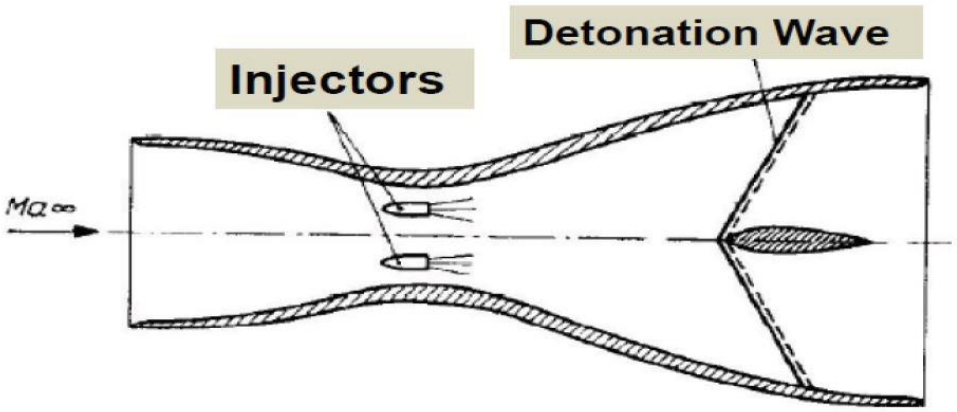

Figure 1.2.1: Schematic diagram of Standing Wave Detonation Engine [1]

1.3 Pulsed Detonation Engines

A simple pulse detonation engine consists of a sufficiently long tube filled with fuel-oxidizer mixture that is ignited through an energy source [1]. A schematic representation is given in Figure 1.3.1.

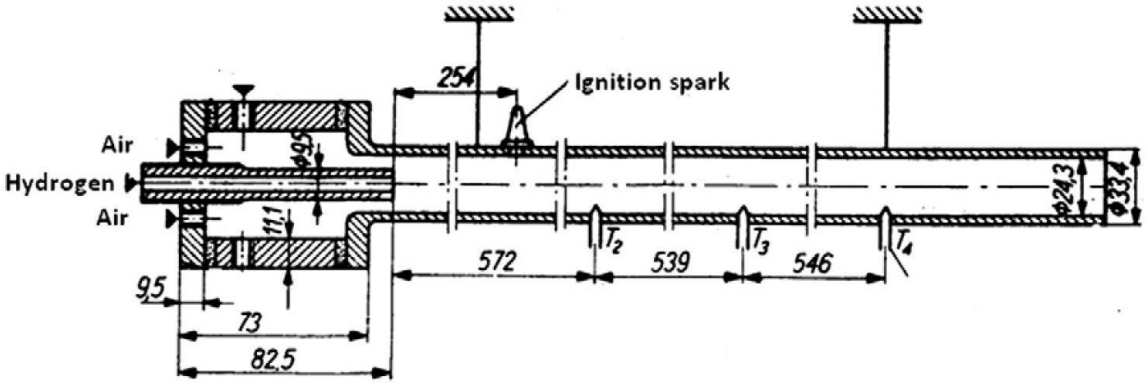

Figure 1.3.1: First PDE designed by J.A. Nicholls at the University of Michigan [1]

The initiated flame must evolve in a detonative way in a relatively short time to produce the increase of pressure, which is transformed into trust. Then the exhaust gases are evacuated, and new fresh mixture is injected for the next cycle [1]. So PDE works in pulsating mode in a frequency range of 10-100 Hz [2].

To make PDEs work successfully, the initiation of detonation must be reliable and fast. Detonation can be initiated into two different modes: direct initiation, that requires a high amount of energy, or by accelerating a deflagrative combustion front, that requires lower energy to ignite the flame, but a longer tube to accelerate the flow [2]. The latter method is more practical since it requires a low energy system to ignite the fresh mixture and, to accelerate efficiently the flow and reduce the transition distance to detonation, some obstacles can be placed in the tube [2].

Ideal cycle of PDE is relatively simple. Graphical representation is given in Figure 1.3.2. It consists of six phases: first of all, the tube is filled with fresh mixture (t1), then, after a sufficient amount of mixture is entered, the opening at the tube entry is closed (t2). Then detonation is initiated, causing the formation of rarefaction waves that propagate inside the tube, generating pressure that is converted to thrust at the closed end of the tube (t3). Finally, the detonation front reaches the open end of the tube (t4) and the evacuation of combustion products begin (t5) and continue until the

most of them are expelled and the pressure drops below the surrounding pressure (t6). So the cycle is completed and a new one can start [2]. In real cycle the process differs from the ideal one, so it is more complicate. First, the combustion products will not be completely exhausted out, a part of them will remain in the tube diluting the fresh mixture. Then, the tube will be only partially filled with fresh mixture and the initialisation of the detonation front is not instantaneous, it needs some time to accelerate the deflagrative front to the detonative one. All these elements result in a lower pressure and therefore a lower thrust developed by the real cycle compared with the ideal one [2].

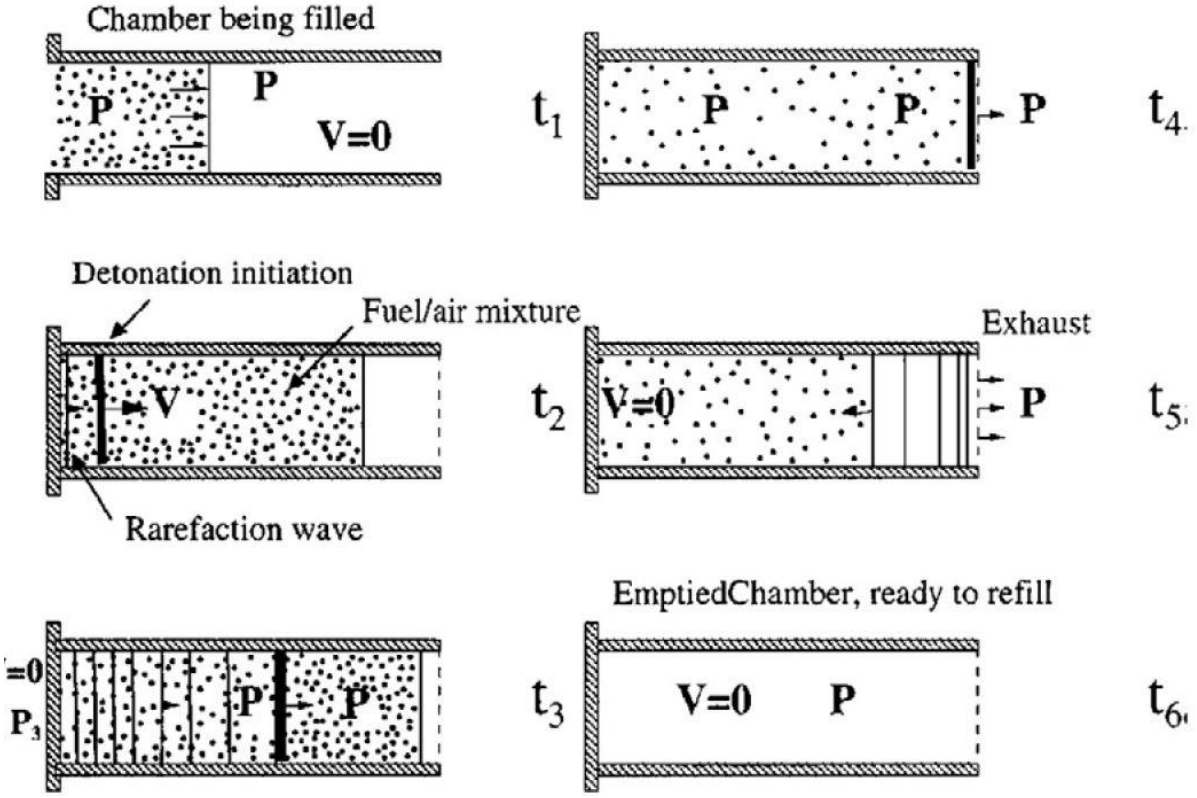

Figure 1.3.2: Ideal PDE cycle [2]

PDEs have several applications since their size can range from micrometres to meters. Moreover, their combustor can be used in different ways: it can be used to produce thrust in PDE configuration or it can be implemented with gas turbine

cycles [2]. To produce thrust, PDEs can have different configurations: they can be made by a single tube or more tubes can be placed circumferentially on a rotating drum in order to increase the frequency of the thrust [3]. In Figure 1.3.3 there is a representation of such a kind of PDE.

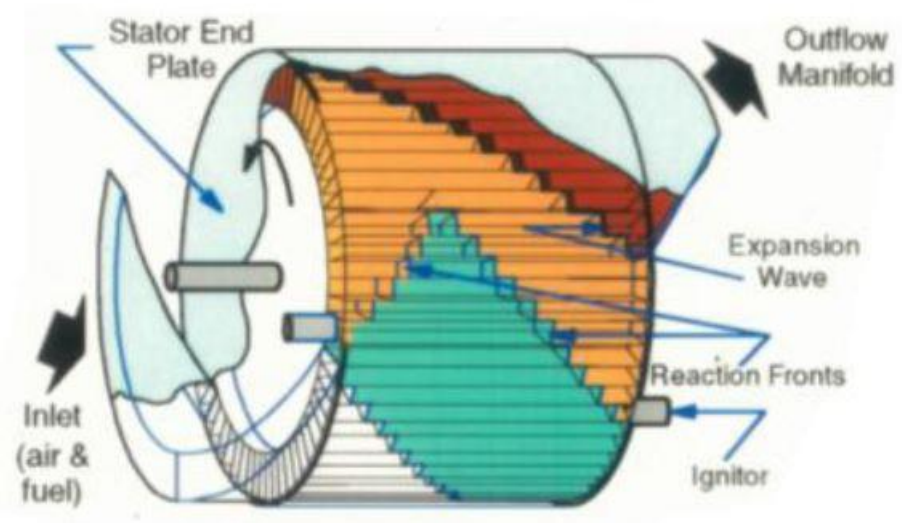

Figure 1.3.3: Schematic of PDE made by a set of tubes [3]

The implementation of pulsed detonation combustor with gas turbines can be done with conventional gas turbines engines, turbojet engines and gas turbines for stationary power production. In all the cases the idea is to increase the efficiency using the improved thermodynamic cycle exploiting detonation combustion [2]. Such a kind of hybrid system was built and successfully tested at a GE facility [4].

PDEs have different advantages, like their simplicity, size range and high efficiency thermodynamic cycle. But they have also some problems related to the pulsating mode in which they work. It will produce unsteady trust and strong vibrations that can be harmful for the engine and the system constrained to it [3].

1.4 Rotating Detonation Engines

The basic geometry of RDE combustion chamber is an annular tube where one or more detonation waves travel circumferentially burning the fresh mixture injected from one end of the tube [6]. This approach allows the detonation to be self-sustained, so it must be initiated only once at the beginning of the operation. In Figure 1.4.1 a schematic of the combustion chamber is shown.

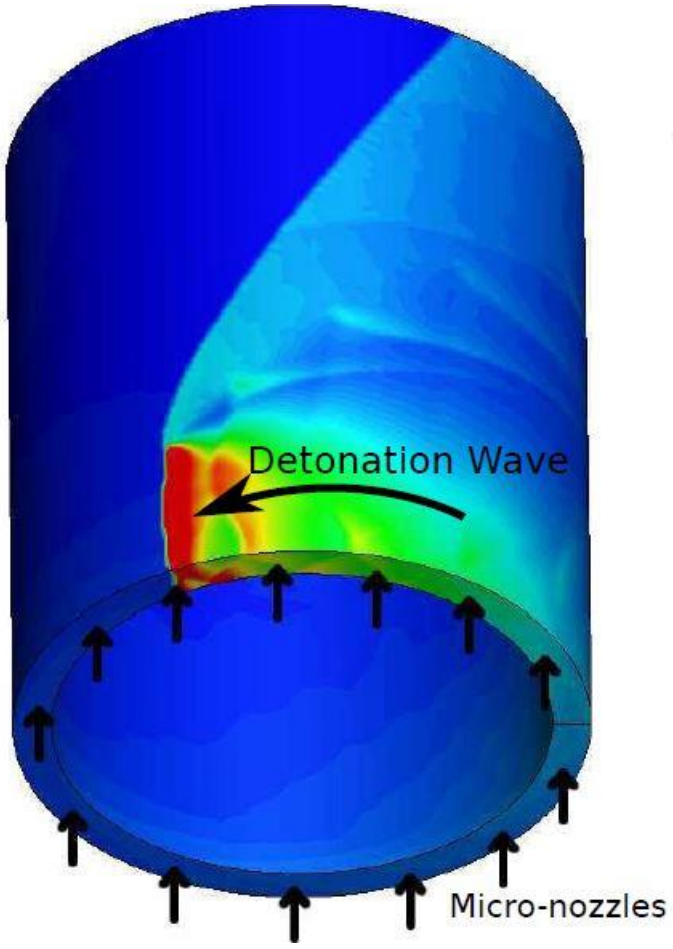

Figure 1.4.1: Basic schematic of RDE with detonation wave [7]

The fresh mixture can be injected from a premixing plenum or fuel and oxidizer can be injected separately. In any case, reactants are injected from the micro-nozzles at the extremity of the chamber.

Usually, the gap between the duct walls is very small respect to the radius of the chamber, so the radial effect can be neglected analysing the flow in 2 dimensions instead of 3, reducing the computational time for simulations [6,7].

The feasibility of the RDE has been experimentally shown at the Lavrentyev Institute of Hydrodynamics [13].

1.4.1 Flow Field

Figure 1.4.2 represents the unwrapped chamber and shows the main features of a rotating detonation engine [7].

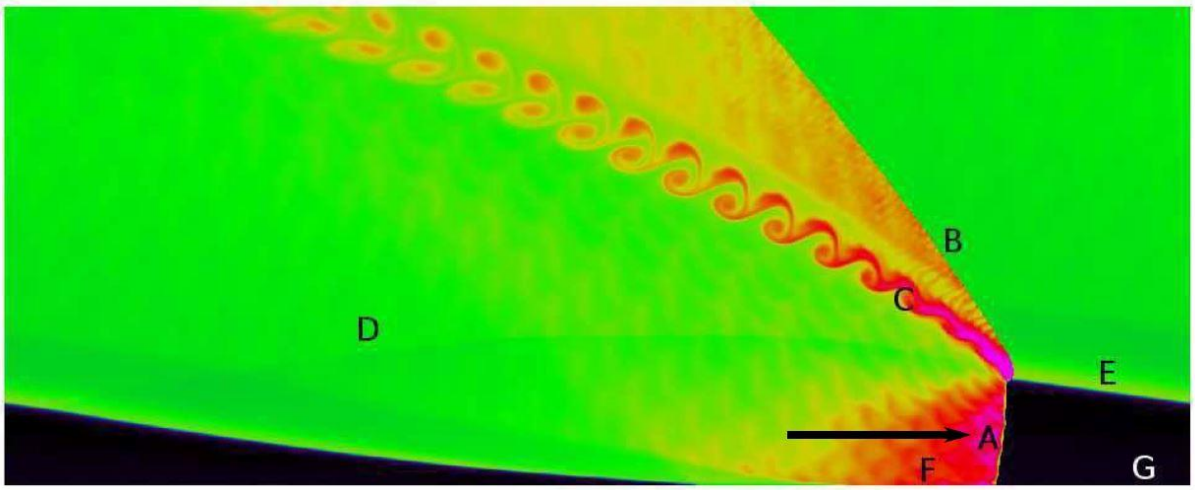

Figure 1.4.2: RDE flow main feature [7]

Fuel is being injected from the bottom and is represented by the black region. The detonation wave (A) is propagating in the circumferential direction as shown by the black arrow. Its propagation speed is in the order of km/s and it can rotate in clockwise or counter-clockwise direction, depending on the conditions of detonation initiation. The detonated products expand circumferentially and axially to the exit plane, so, at the exit of the chamber, a supersonic flow can be achieved even without a geometric throat. The secondary shock wave (D) varies considerably depending on the inlet stagnation pressure and the outlet pressure. The pressure just behind the detonation wave is high enough that the micro-nozzles are completely blocked (F).

Experimentally this can be a problem because of the potential for back flow into the premixture plenum. Further behind the detonation front, the premixture begins to penetrate into the chamber (G). For most of this region, the flow through the micro-nozzles is choked, which is why the premixture region expands almost linearly. Also of interest is the region where the premixture and the reacted gases meet (E), because here the premixture experiences deflagrative combustion, which reduces the performance of the RDE since it consumes part of the available combustion heat release reducing the wave propagation velocity [6,8]. Region (C) represents the slip line between freshly detonated products and older product while in (B) there is the oblique shock wave that develops from the detonation front [7].

In Figure 1.4.3 is represented the Mach number with superimposed streamlines from the frame of reference of the detonation wave [6].

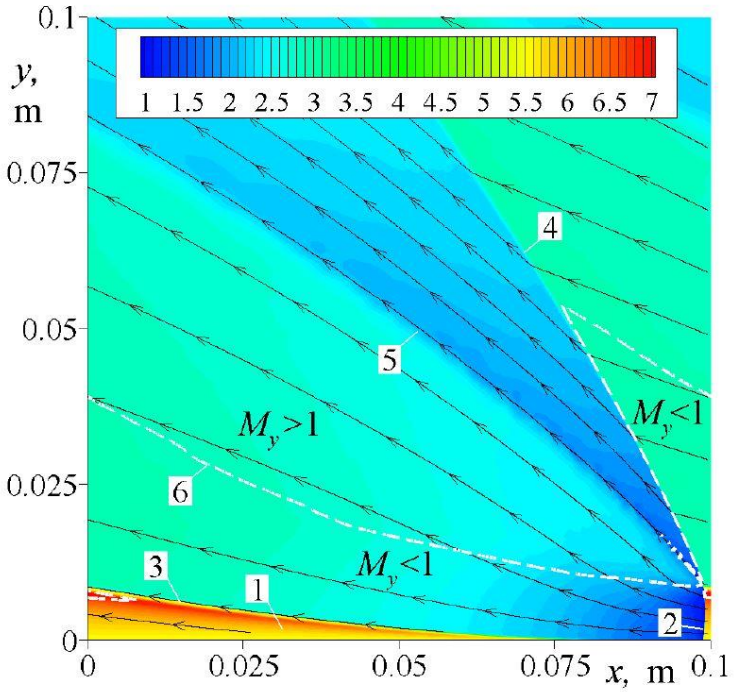

Figure 1.4.3: flow field structure in the combustion chamber. The colored band shows the Mach number in the detonation wave frame of reference [6]

In the region just behind the detonation front, delimited by the white dashed lines, the flow is subsonic due to the increase of pressure caused by detonation. Then, due

to the rapid expansion of gases that is visible from the divergence of the streamlines, the flow becomes supersonic [6].

The oblique shock recompresses the gases, so the flow at the exit can be fully supersonic or it can be mixed, so partly supersonic and partly subsonic, depending on the outlet pressure [6,7,12].

Depending on the geometry of the chamber it can happen that a part of reactants does not undergo detonation process, so it will be a source of loss. In Figure 1.4.4 this is clearly visible form streamline 5 [7].

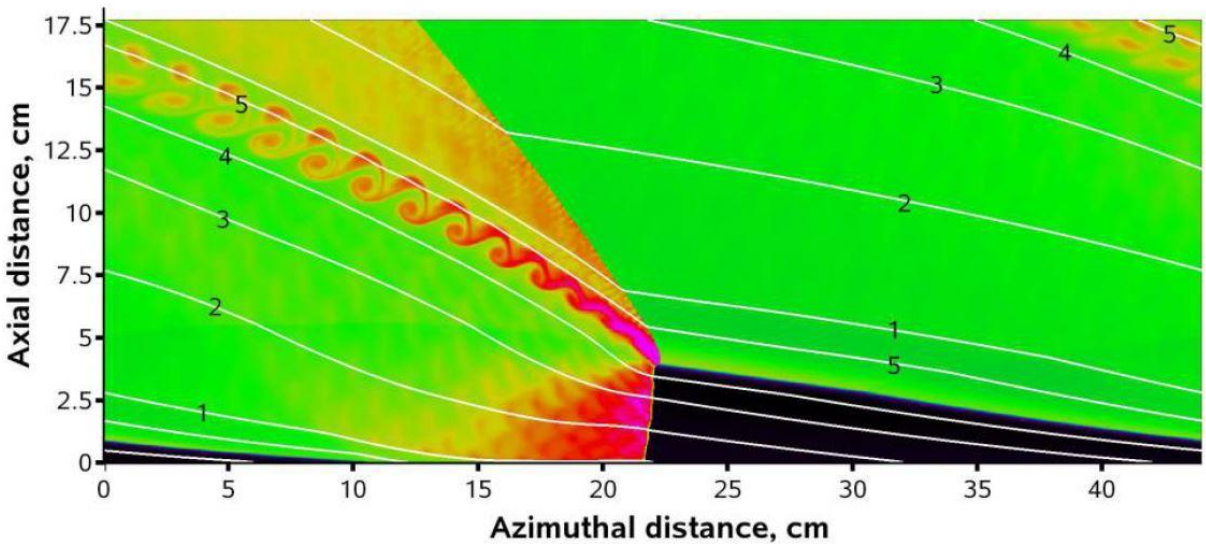

Figure 1.4.4: fluid particles path in RDE combustion chamber from detonation wave reference frame [7]

Due to the presence of the oblique shock, the flow at the outlet of the combustion chamber is non-uniform: pressure, temperature, flow velocity magnitude and direction will depend on time and on the circumferential position.

In Figure 1.4.5 are reported the diagrams for pressure, temperature, axial and azimuthal velocities in function of azimuthal location for both inlet and outlet sections [7]. Values are taken from the detonation wave frame of reference, therefore it is possible to notice the strong azimuthal component of the velocity at inlet. Dashed lines show the non-uniformity of the flow at the combustion chamber exit,

underlying important variations of all thermo-fluid dynamic quantities. Moreover, in the pressure diagram, lines at 10 atm and 5.45 atm are represented, which are respectively the stagnation pressure of the inlet micro-nozzles and the critical pressure for the chocked flow. The comparison of the inlet pressure with these two lines underlines the presence of a small portion of blocked flow behind the detonation front (13% of the inlet plane) and a wide portion of chocked flow at micro-nozzles (63% of the inlet plane) [7]. This agrees with the qualitative observations made previously.

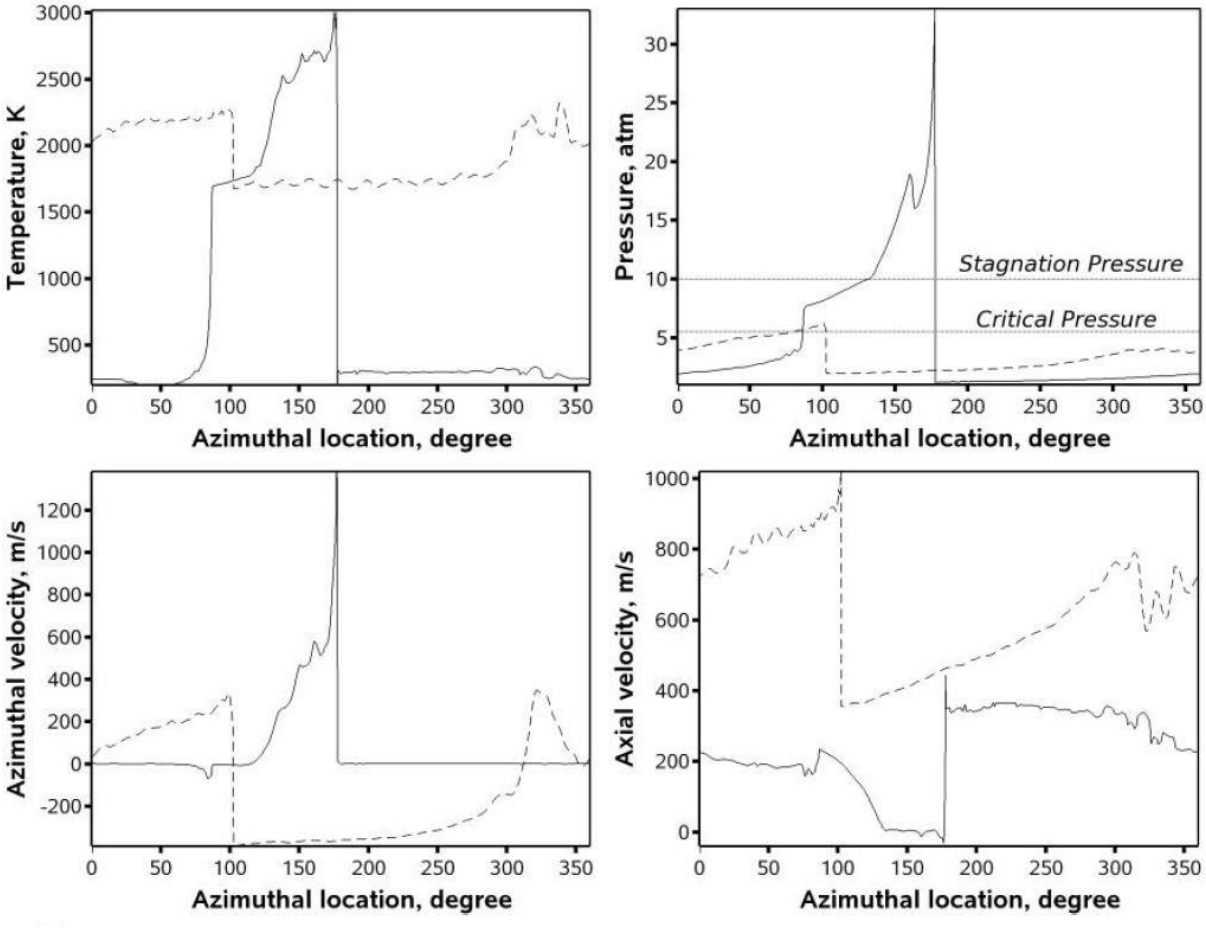

Figure 1.4.5: Inlet (solid) and outlet (dashed) plane flow variables as function of azimuthal location [7]

Even if the flow in the rotating frame has important azimuthal component, in the stationary frame of reference it can be considered axial in absence of pre-swirl. This is because, without any external applied torque, the overall angular momentum must be constant, and, in absence of pre-swirl and considering an inviscid flow, it must be zero even in the face of the spinning detonation wave [8]. This concept is better explained in the following rows, referring to Figure 1.4.6.

For zero pre-swirl the flux of the angular momentum integrated over any cross-sectional area is zero [10]. This results from circumferential periodicity and holds even in unsteady flows as long as the rotational speed of the wave Ω is constant and the flow is steady in the wave frame spinning with Ω. The physical reasons why this zero-average of angular momentum relates to the circumferential periodicity are illustrated in Figure 1.4.6. Let's focus on the segments of gas between two detonation waves, where sliced planar sheets of gas just ahead and behind the waves are also shown. Locally the blast wind just behind the shock swirls in the same direction as the detonation wave, as shown in Figure 1.4.6 (a), but it is counterbalanced by the counter swirl, spinning in the opposite direction, Figure 1.4.6 (b). The counter-swirl results from circumferential periodicity between the detonation waves, Figure 1.4.6 (a) and (c). The higher pressure just behind the detonation wave 1, which generates the blast wave driving the gas towards the lower pressure ahead of the detonation wave 1, also acts, by action and reaction, to drive the flow backwards, towards the lower pressure region ahead of the detonation wave 2. Note that when viewed in the detonation wave frame of reference, the flow relative to the shock would appear to spin in the direction opposite to that of the detonation wave, and this would be so even in the absence of any pre- swirl. This flow-spin in the detonation frame should not be confused, and would not conflict, with the net zero angular momentum in the stationary frame [8].

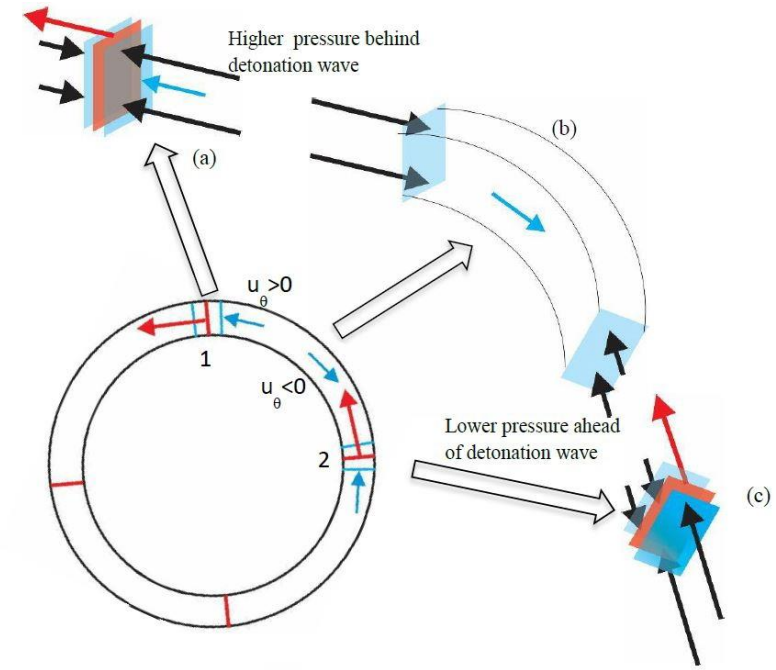

Figure 1.4.6: Coexistence of swirl blast wind and counter swirl [8]. a) Gas surfaces just ahead and behind detonation wave 1 (red), pressures (black arrows), and blast wind (blue arrow). b) Region of gas between detonation wave 1 and 2, pressures acting on it, and counter swirl (blue arrow). c) Gas surfaces just ahead and behind detonation wave 2 (red), and pressures (black) acting on them.

For a narrow annulus, the radial velocity is also small. Hence, without pre-swirl injection, the flow in stationary frame of reference is essentially axial, which simplifies the model that can be adopted [8].

1.4.2 Detonation Waves number

It was found that different detonation front can be present in the combustion chamber. In Figure 1.4.7, using high speed photography, the presence of eight detonation wave fronts was detected [11].

Figure 1.4.7: Image of luminescent spots corresponding with eight detonation wave fronts in an RDE combustor by Canteins [11].

The number of detonation waves depends mainly on mass flow rate of fresh mixture and on combustor geometry. About geometry dependence, increasing the injector slot width with respect to the channel width appears to reduce the number of detonation waves because the pressure ratio between the manifold and combustor is altered [11]. Moreover, at the increasing of the combustion chamber diameter, also the number of detonation waves increases because the height of detonation front increases [11]. The reason for this will be explained in mass flow rate effects.

About mass flow rate dependence, it was found that the height h of the detonation front, shown in Figure 1.4.8, must be included in the range $h^* \leq h \leq 2h^*$, where h^* is the critical height for which the rotating wave can be sustained [11].

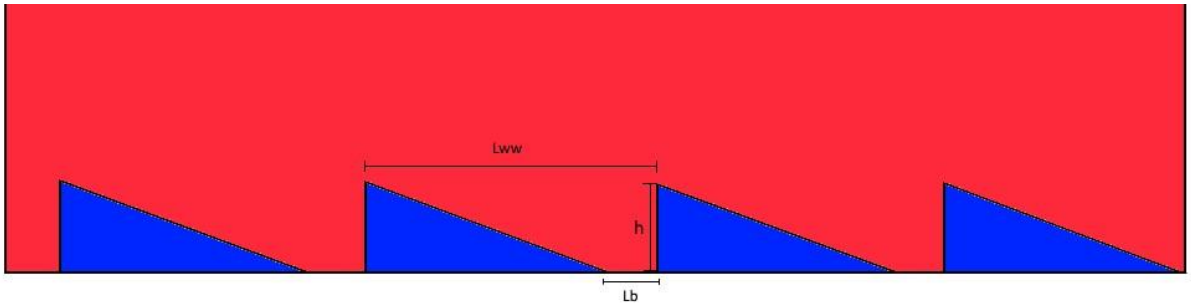

Figure 1.4.8: Dimensions of Detonation waves

The reason for which h must be included in that range is related to the distances Lb and Lww, respectively the distance that nozzles need to be recovered from the blockage and the distance needed by another front to be successfully sustained [11]. At the increasing of mass flow rate also the ratio $\frac{Lb}{Lww}$ increases, showing that a lower distance between two consecutive fronts is needed to successfully sustain more detonation waves.

Another reason for which multiple detonation fronts can form is the insufficient mixing of the reactants before the incoming detonation wave: after the passage of the wave, the unburnt gases continue to combust with fresh propellants injected and form a second wave [11].

There are two causes as for why the number of detonation waves changes: first, the height of the waves remains around h^* for stable engines with good mixing, and the number of waves increases in a predictable manner related to $\frac{Lb}{Lww}$ and the circumference of the combustor; second, an engine with poorly mixed propellants may weaken the developed wave fronts, whereas subsequent fronts form and transition into detonation waves. The latter case is undesirable and should be avoided by designing a suitable injection system [11].

Since critical height is linked to the detonation cell width, also initial pressure, temperature and reactivity of the mixture can influence the number of waves.

1.4.3 Injection System

It was already mentioned that the high pressure behind detonation front causes blockage of the injector micro-nozzles. This because detonation waves run near the inlet section of the combustion chamber, causing severe mechanical and thermal stress cycles to the injector system [12].

Injection system plays a key role in the functioning of a RDE, because it must guarantee the presence of a sufficient premixture that allows the detonation wave to be stable. If fuel and oxidizer are injected separately, then the role of injection system is even more critical since it must allow a good mixing of reactants before the arrival of the wave, which happens in a very short time. So, the presence of backflow in the injection micro-nozzles can be problematic for the operation of RDEs and the good functioning of injection system is challenging.

For different micro-nozzles geometries, the results are different flow behaviours in mixing zone of combustion chamber and in the injection system. The first injection system considered has premixing chamber and slot micro injectors. The two-

dimensional geometry of injectors is represented in Figure 1.4.9 and it runs the entire radial depth of the injection plate [12].

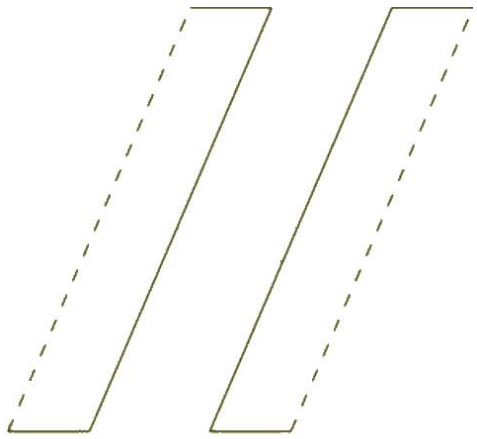

Figure 1.4.9: Slot Micro Injector geometry [12]

Figure 1.4.10 represents pressure, density, temperature and reactants mass-fraction fields that are obtained through an axial slot micro injector with an injection total pressure of 4 atm [12]. Some features of these fields that are different from an ideal injection system were analysed: the presence of injectors creates a much more complex fill region than with ideal injectors. In particular, over-expanded jets from the injectors (best shown in the density plot) dominate the fill region, and dead areas between the injectors with hot reacted flow persistent throughout the fill region. These jets strongly interact with the detonation wave and weaken the detonation wave right by the injection plane (shown in the pressure), while creating strong pressure oscillations behind the detonation wave that propagate through the combustion chamber. This enhances the non-uniformity of the flow at the chamber outlet. Above the jets in the fill zone, there is a turbulent region of mixing and there is also a broad transition region between unreacted and reacted flow from the detonation wave. At low pressure ratios (outlet pressure over injectors total pressure) for these injectors, there is also incomplete combustion extending from this transition region into the expansion region, although it is only a small percentage of the overall reactant injection. Examining the reactant mass-fraction, it can be noticed that there is almost no back flow into the micro-injectors, which is a positive fact, even though there is a strong pressure wave that propagates through the micro-injectors into the mixture plenum (which can also be seen clearly in the density plots) [12]. This cause

mechanical fatigue in the injection system, so this must be considered during the design phase. The presence of this pressure wave is visible also form Figure 1.4.11 that represents the pressure into two different locations of the premixing chamber in function of time [12].

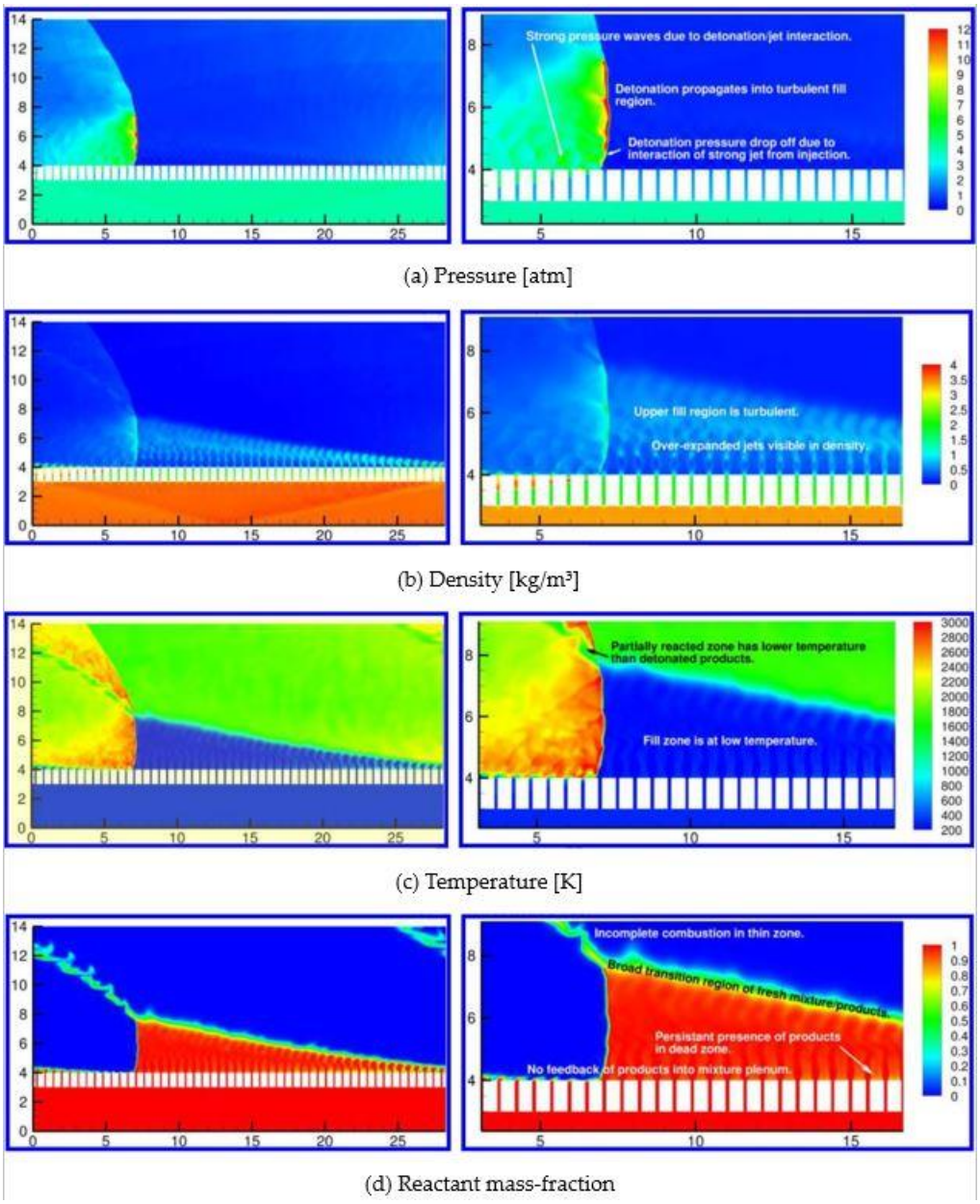

Figure 1.4.10: Flow field for the slot micro-injector of pressure, density, temperature, and reactant mass fraction. Left side plots include the entire combustion chamber, injector plate, and mixture plenum, while right side plots are close-ups of the detonation and fill region [12]

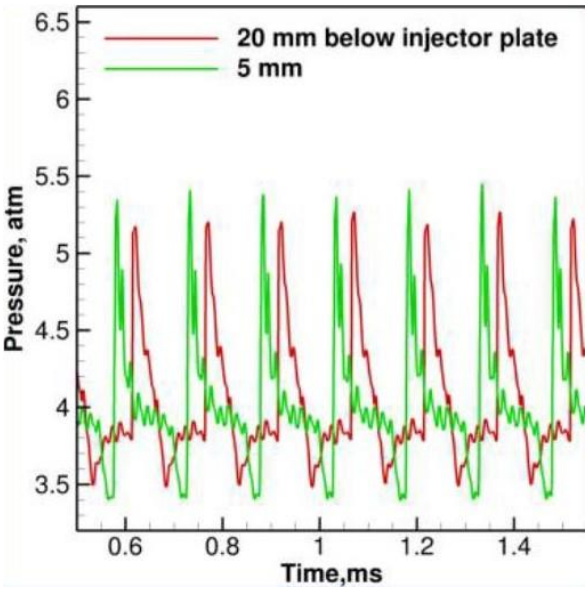

Figure 1.4.11: Pressure vs time in premixing chamber [12]

Changing the inclination of the slot micro injectors or changing the geometry of the injectors it is possible to change the flow field just analysed, in order to improve some features like reducing dead and partially reacted zones or limiting the pressure oscillations in plenum. For example, it is possible to incline the slot micro injectors against or in the same direction of the detonation wave, like in figure Figure 1.4.12. The results are that some improvements were achieved: the detonation front is more stable for all the inclinations, for higher inclinations (in modulus) partially reacted zone disappears, while for smaller inclinations it persists. Dead zones between injector nozzles are still present, but for the inclinations against the wave front (negative once) they are much smaller than the other cases. About pressure oscillations in plenum, for injectors inclined toward the detonation wave the amplitude of oscillations increases, while for the other inclinations it decreases [12].

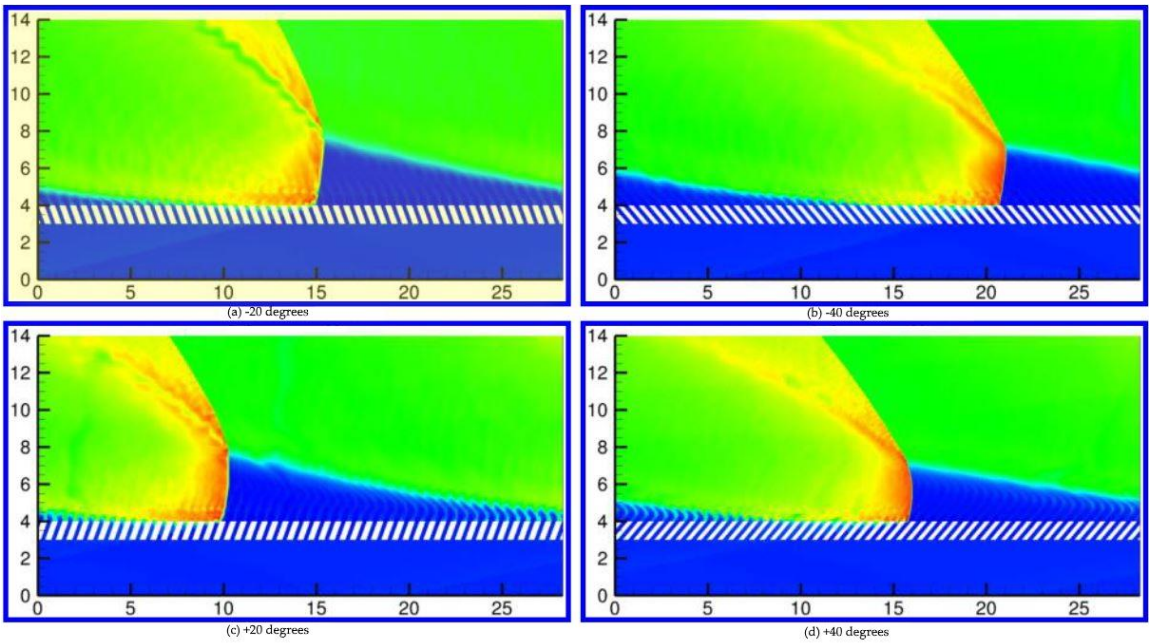

Figure 1.4.12: Inclined slot micro injectors. Detail of temperature field. Same scale as for Figure 1.4.10[12].

Applying different geometries to improve the flow field leads to similar conclusions. In particular, considering the geometries of Figure 1.4.13, the following results can be obtained [12]:

a) The flow is strongly turbulent, the dead zones are still presents, but the unreacted mixture in the transition region is much less than for axial slot micro injectors.
b) The flow is more uniform than the other injector types, there are no dead and partially reacted zones, but at the nozzle exit there is a normal shock. The transition region between fresh mixture and reacted flow is still wide.
c) Detonation front is more stable than for the other geometries, there is no partially reacted zone, but the dead zones are still present.

For all the three cases there is no reduction of pressure oscillations amplitude in the plenum [12].

These results show that improvements can be achieved by acting on geometry and inclinations, and that there is the need to focus on reducing pressure oscillations in plenum.

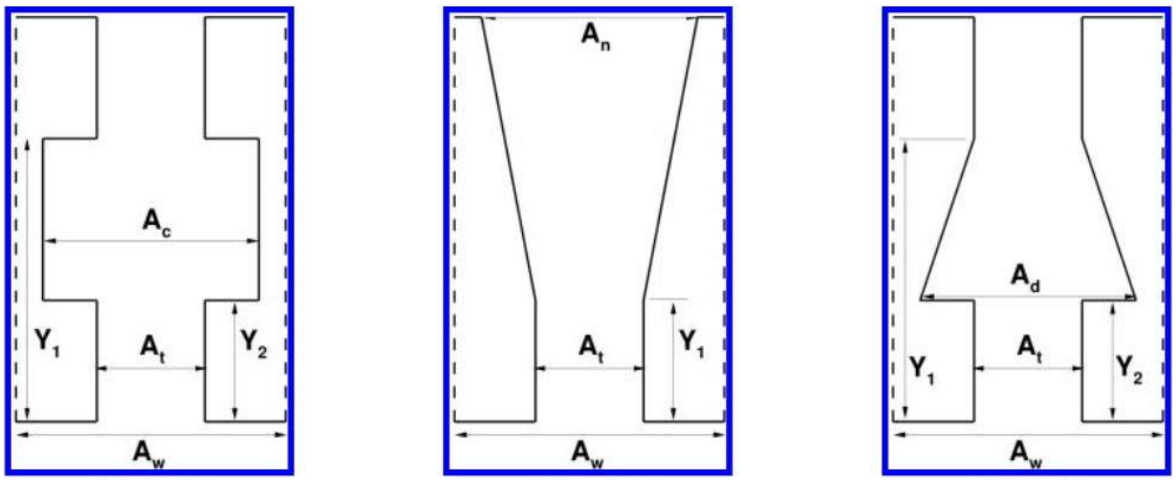

Figure 1.4.13: Injectors geometry [12]

1.4.4 Detonation Initiation System

Another crucial mechanism for the good and safe operation of RDEs is the detonation initiation system. Mainly two different methods are used: spark plug and pre-detonator. They have been tested successfully [14], even if spark plug is weaker than pre-detonator, since it is more sensitive to detonation power of reactants [8,11].

In both cases the detonation is not directly initiated since it requires a big amount of energy, so firstly a deflagration front is initiated and then it transforms into a detonation front.

1.4.4.1 Spark plug

Usually, several spark plugs are used to initiate detonation, because each spark generates a hemispherical shock wave that travels in the combustion chamber (Figure 1.4.14) and generates free radicals which act as seeds to set off chain reaction that generate deflagration. The use of more spark plugs allows to sum up the hemispherical waves, which, interacting with free radicals, trigger the deflagration to detonation transition [8].

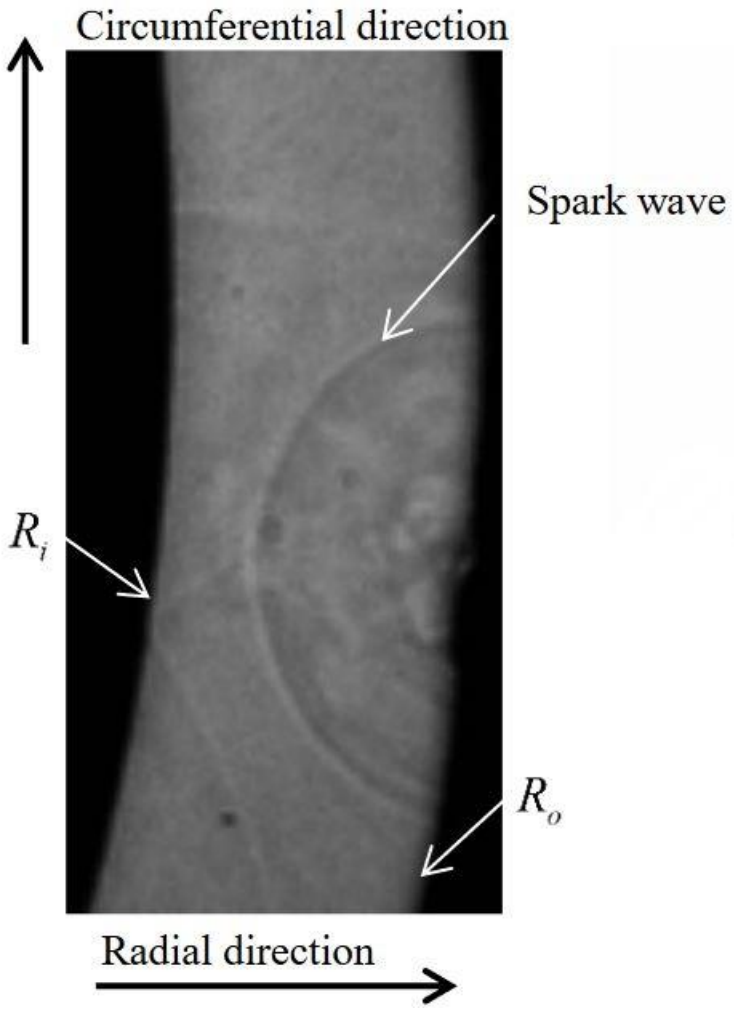

Figure 1.4.14: Spark hemispherical wave. Ri and Ro are the inner and outer walls of combustion chamber [8].

Detonation, after being initated, is self sustained since it generates the free radicals that are involved in the combustion reaction.

1.4.4.2 Pre-detonator

The schematic of a pre detonator is presented in Figure 1.4.15. It works like a PDE: at the extremity of a tube a deflagration is initiated through a spark, then it evolves in a detonation front and enters tangentially in the combustion chamber. The advantage is that here the detonation must be initiated only once since it is self sustained in the combustion chamber. This allows the igniter to have a longer life than a PDE [11].

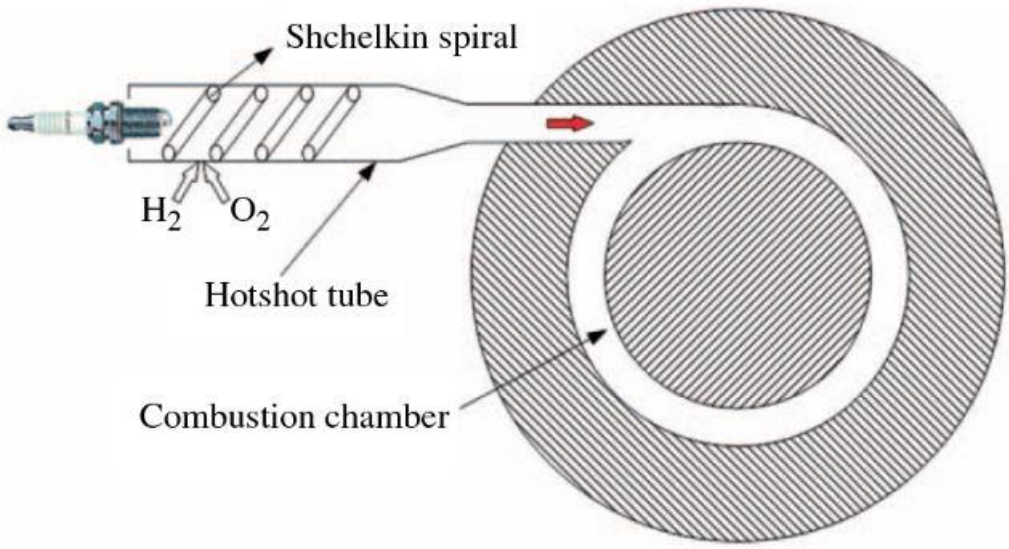

Figure 1.4.15: Scheme of a pre-detonator [11]

Like for PDE, also here some obstacles (like Shchelkin spiral) can be placed to reduce the deflagrative to detonative transition distance.

1.4.5 Parametric study of RDEs

Now let's have a look at how the RDE behaves changing five main parameters:

- Pressure ratio between inlet total pressure and outlet static pressure (back pressure) $\frac{P_o}{P_b}$
- Area ratio between the injection nozzles area and inlet wall area $\frac{A_t}{A_w}$
- Annular diameter size
- Chamber length
- Chamber radial extention (width).

1.4.5.1 Pressure ratio effects

The first parametric study looked at the effect of pressure ratio on the pressure ahead of detonation wave, detonation wave height, mass flow and Mach number for a constant geometry. The results are shown in Figure 1.4.16 [7]. In this study, the pressure ratio was obtained in two ways. First, the back pressure was held constant at 1 atm, and the inlet pressure was varied. Another set of simulations was done by

varying the back pressure and holding the inlet pressure constant at 10 atm. The pressure in front of the detonation wave is primarily dependent on the inlet pressure upstream of the combustion chamber, with only a small dependence on the back pressure, while the detonation heigth depends on both pressures. It must be said that also the mass flow depends on inlet pressure and increases with it [7].

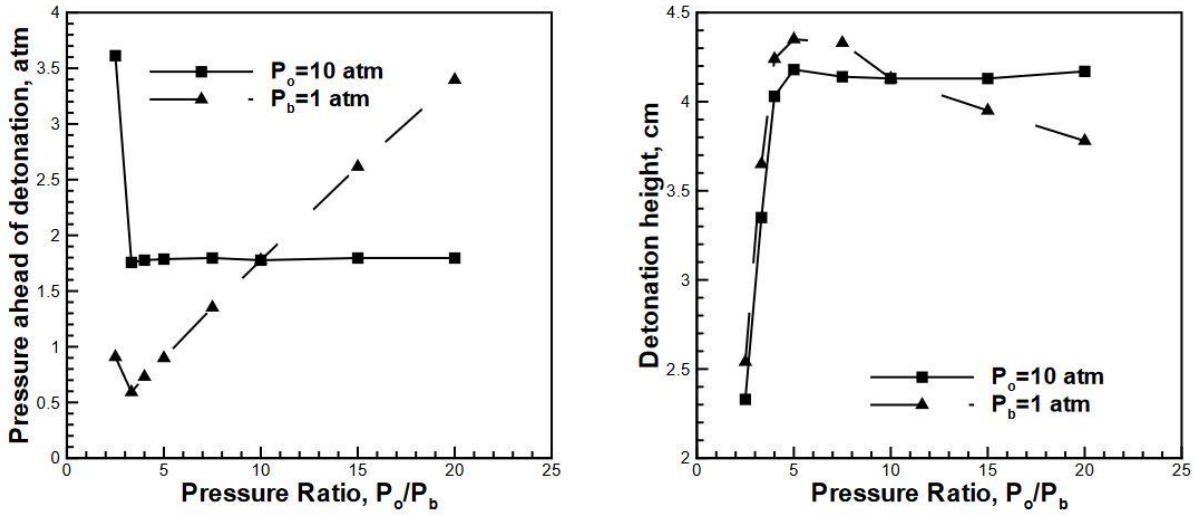

Figure 1.4.16: Pressure ahead of detonation and detonation height against pressure ratio [7]

Another intersting aspect is the mass flow that passes through the oblique shock, since it is associated to entropy increase, so loss of efficiency and total pressure in the combustor. Figure 1.4.17 shows two cases, $\frac{P_o}{P_b}$= 3.3 and $\frac{P_o}{P_b}$= 5, where the flow is divided into different thermal regions. We see that more of the flow is processed through the oblique shock as the pressure ratio decreases [7].

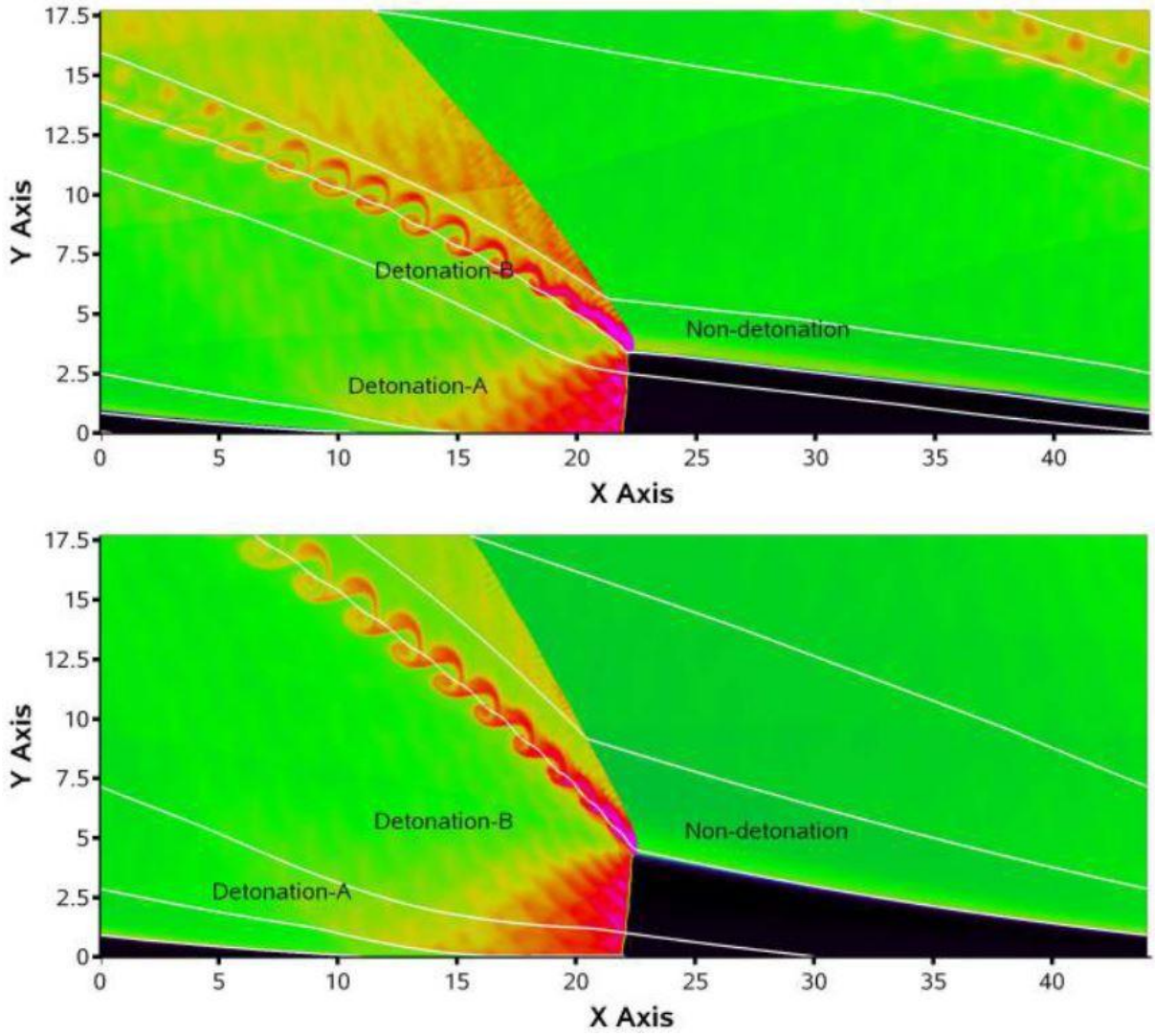

Figure 1.4.17: Streamlines through the detonation wave for a pressure ratio of 3.3 (top) and pressure ratio of 5 (bottom). Inlet pressure is held at 10 atm for both cases [7]

Moreover, as shown in Figure 1.4.18, also the Mach number depends on the pressure ratio. For low pressure ratio values, secondary and tertiary shocks arises to match the flow pressure with the outlet one. This causes mixed subsoic and supersonic flow conditions introducing losses associated to shocks. Instead, at high pressure ratios, the flow is fully supersonic, the secondary shock wave is very weak and the tertiary shock wave is non-existent. The white regions represent the regions of supersonic flow, to show how they changes with pressure ratio variation [7].

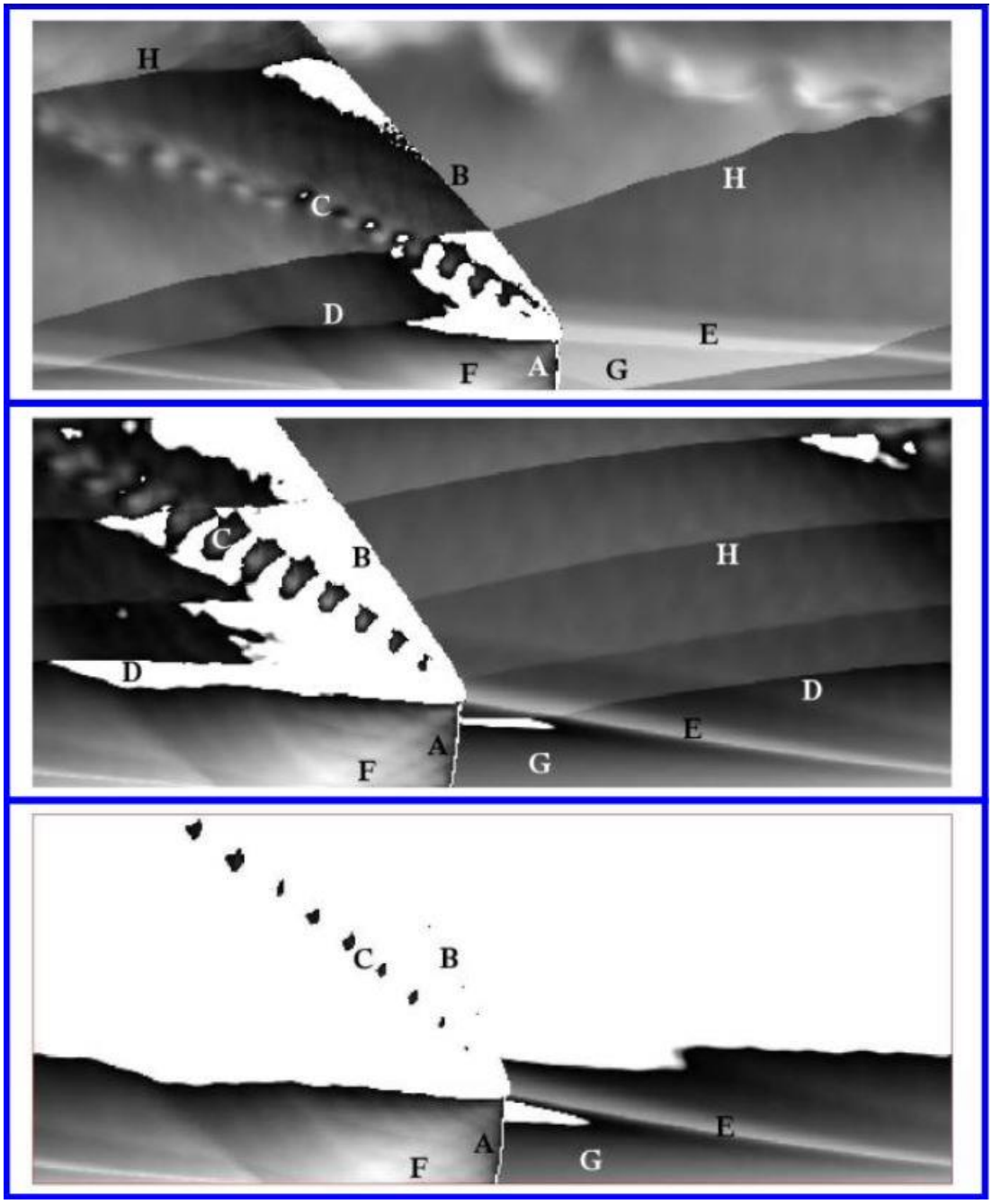

Figure 1.4.18: Mach number and supersonic region (in white) for $\frac{P_o}{P_b}$ = 2.5 (top), $\frac{P_o}{P_b}$= 4 (mid), and $\frac{P_o}{P_b}$= 5 (bottom). Same labeling as Figure 1.4.2, with the addition of H) tertiary shock waves that form near the exit boundary and propagate towards the detonation wave. Inlet pressure is held at 10 atm for all cases [7].

1.4.5.2 Area ratio effects

Let's look at the effect of inlet area ratio on the detonation height and performance characteristics. Although not strictly a sizing parameter (the overall size of the RDE is not dependent on this size ratio), mass flow and performance are tightly connected to this area ratio, thus it is an interesting parameter to vary [15]. For an RDE, the injection area is an incredibly important area. It must deliver enough fuel and oxidizer to the fill region in a very short time frame (based on the detonation wave speed). In addition, it must also prevent mass and heat from back flowing from the combustion chamber back into the plenum. The following results are taken from a simplified simulation where plenum backflow is neglected, however, it is instructive to see how changings in this area ratio changes the flow field and performance in the ideal situation. For this parametric study, the area ratio At/Aw was varied from 0.1 to 0.5 and held the plenum pressure and temperature at 10 atm and 300 K [15].

The temperature solution at the end of the run is shown in Figure 1.4.19 for At/Aw = 0.1 and At/Aw = 0.5. They are remarkably similar, although there is some difference in the structure behind the detonation wave and in the expansion portion of the domain. There is little apparent change in the detonation height and basic characteristics of the flow field, although it was expected the larger area ratio to have significantly more mass flow [15].

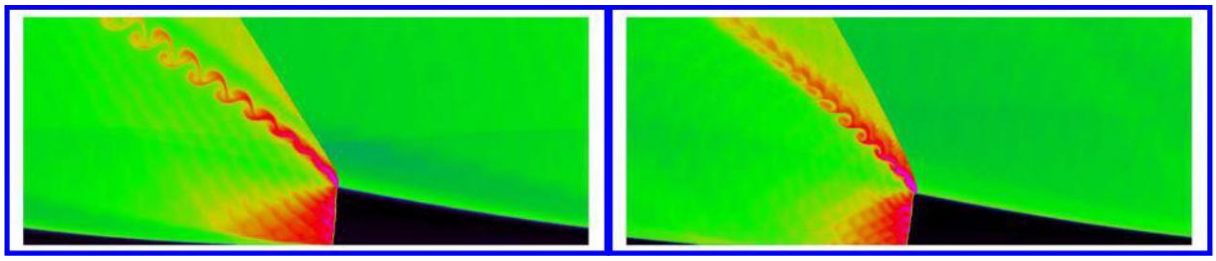

Figure 1.4.19: Instantaneous temperature solution as the area ratio At/Aw is increased from 0.1 (left) to 0.5 (right) [15]

Figure 1.4.20 takes a closer look at the detonation height and pressure in the fill region ahead of the detonation wave for a range of area ratios [15]. The detonation height shows a slight reduction in its height as the area ratio increases, while the pressure in front of the detonation wave increases dramatically. The increase in pressure, thanks to lower pressure losses across the nozzle [16], should result in a higher mass flow through the RDE and in an improved thermal efficiency [15].

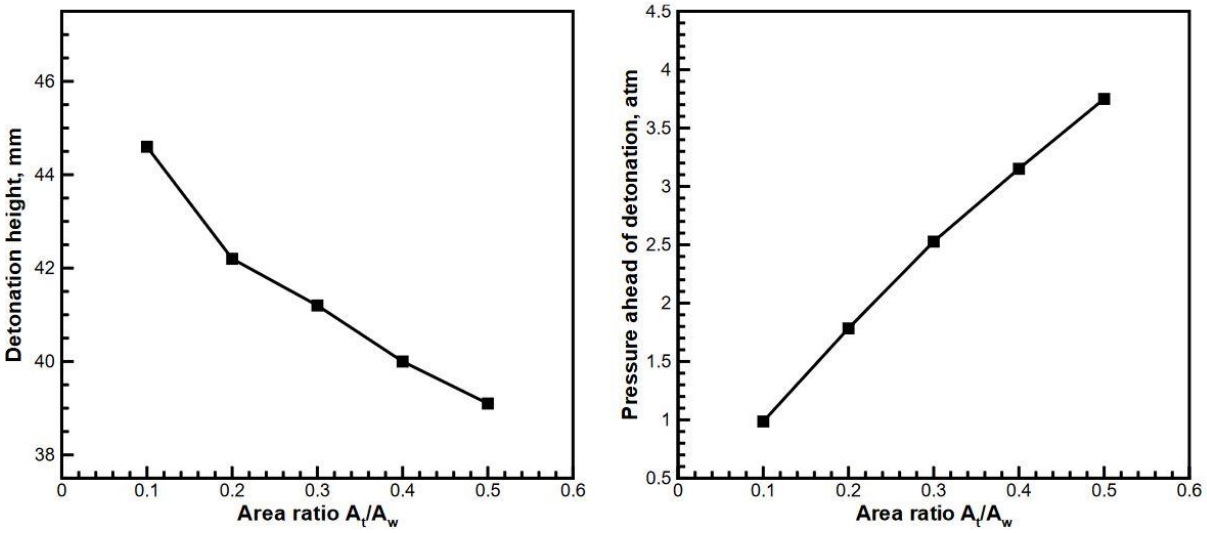

Figure 1.4.20: Height of detonation wave (left) and pressure ahead of the detonation wave (right) as the area ratio At/ Aw is varied from 0.1 to 0.5 [15]

1.4.5.3 Annular diameter size effects

The next parameter of interest is the diameter of the RDE combustion chamber. The inner and outer diameter dictate how important curvature and three-dimensionality are, however, it was also of interest the diameter variation while keeping small a chamber height, thus allowing the two-dimensional approximation. For these cases, it was intresting seeing if, under high plenum pressures, the detonation height and performance scale as the diameter is increased. For this case the diameter was varied from 70 mm to 350 mm. The temperature snapshot at the end of the simulation is shown in Figure 1.4.21. In this plot, a clear difference in the height of the detonation wave is seen. The height was plotted in Figure 1.4.22 and compared with a 1:1 scaling with diameter, showing that the detonation wave height does in fact scale vary closely with the diameter. Interesting, examining pressures in front of the detonation wave near the inlet face and near the top of the detonation wave, the results are values that are independent of the diameter and stay near 1.6 atm (near head-end wall) and 1.1 atm (near the top of the detonation wave). The mass flow increases linearly with the diameter [15].

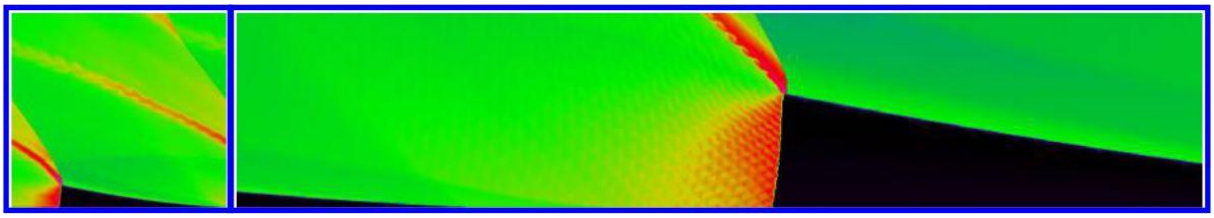

Figure 1.4.21: Temperature solution as mean diameter is increased from 70 mm (left) to 350 mm (right) [15]

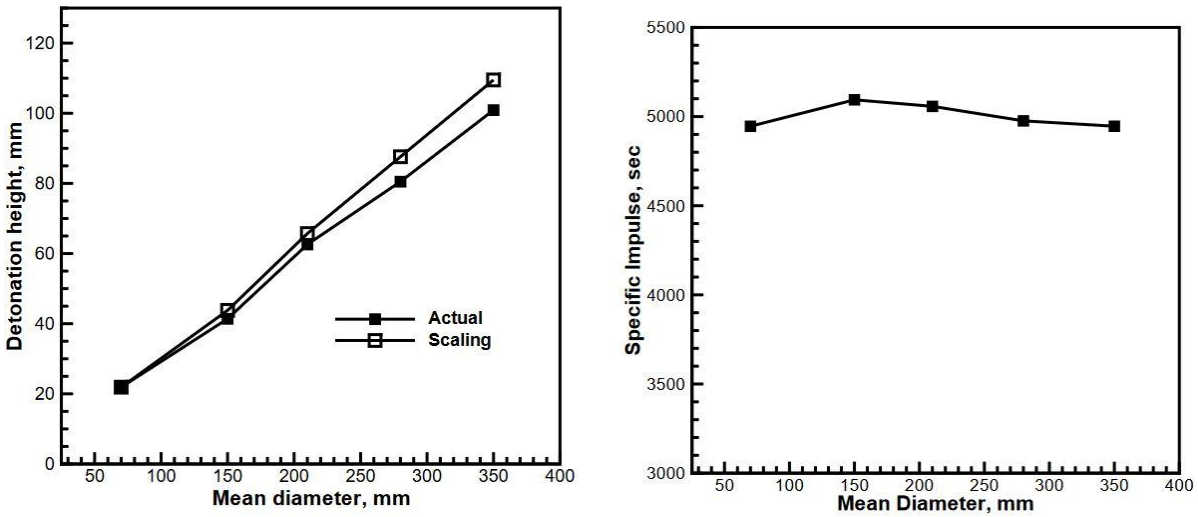

Figure 1.4.22: Detonation height (left) and specific impulse (right) as mean diameter is increased from 70 mm to 350 mm [15]

1.4.5.4 Chamber length effects

The next geometric parameter to consider is the effect of chamber length. For these computations two plenum pressures were considered: 4 atm and 10 atm. The reason for this is that pressure ratio changes significantly the flow development and exit conditions of the combustor, as show in paragraph 1.4.5.1, and changing chamber length means to cut thet flow in different points. So two different flows were considered [15].

For the high pressure ratios (such as $\frac{P_o}{P_b}$ = 10), the flow in the expansion region of the RDE becomes completely supersonic. Thus, for a constant area diameter, the length would not be expected to have a significant impact on the solution. For realistic RDE's, as the length is increased the wetted area of the RDE is also increased, creating viscous and heat transfer losses; however, these simulations do not consider these effects. Increasing the length, also the amount of mass that passes through the oblique shock increases, introducing more losses as shown in Figure 1.4.23 [16] . For lower pressure ratios ($\frac{P_o}{P_b} \leq 4$), the exit is partially subsonic, and so the length was expected to have a significant effect on the performance and flow field. For these cases, the axial length was varied from 44.25 mm to 236 mm. The lower number was chosen to be just above the detonation height found from previous studies [15].

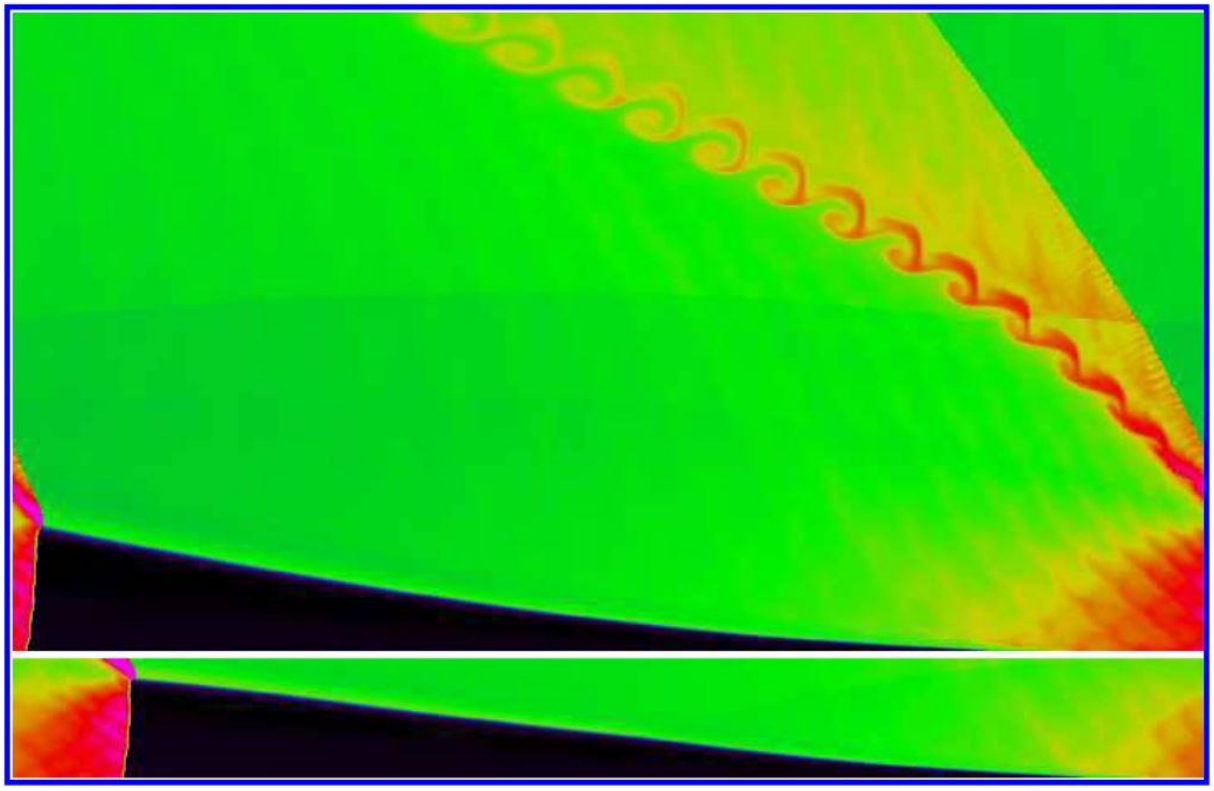

Figure 1.4.23: Temperature solution as chamber length is increased from 44.25 mm (bottom) to 263 mm (top). Po = 10 atm, Pb = 1 atm [15]

Figure 1.4.24 shows the average detonation wave height and average pressure in front of the detonation wave. Here there is a distinct trend, especially for the low pressure cases. As the length is increased, so does the wave height, and this in turn lowers the pressure. For high pressure ratios, the expansion quickly becomes supersonic and isolates the fill region from the exit, so only a small effect of chamber length on performance can be seen [15].

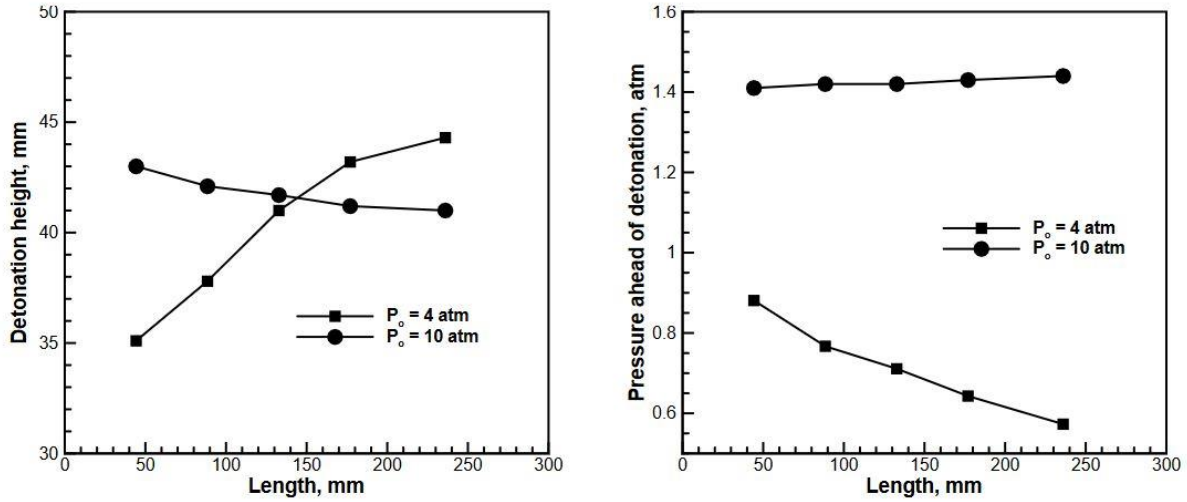

Figure 1.4.24: Detonation height (left) and Pressure ahead of detonation (right) as chamber length L is increased from 44.25 mm to 263 mm.

1.4.5.5 Chamber radial extention

The final parametric study looks at the effect of chamber depth (the difference between outer and inner diameters for the combustion chamber) on the flow field for the RDE. This study is very important, since increasing the chamber thickness is the ideal way of increasing mass flow without increasing the wetted area for the RDE or the overall size of the engine. For this case inner-outer diameters of 60-80 mm, 60-90 mm, and 60-100 mm were used, corresponding to a thickness of δ = 10 mm, 15 mm, 20 mm. The reason for this was that the curvature effects on the detonation wave were also of interest and it was felt that the smaller diameter would have a stronger effect [15].

The pressure on the outer combustion chamber is shown in Figure 1.4.25. Clearly, as the diameter of the chamber increases, it is possible to see considerable radial differences in the detonation wave. In fact, the entire detonation process becomes very much more variable as the depth of the combustion chamber goes from 10 to 20 mm [15]. This because, reducing inner radius, the detonation at the smaller radius becomes unstable and may fail creating a dead region where reactants are not available for detonation [8,11].

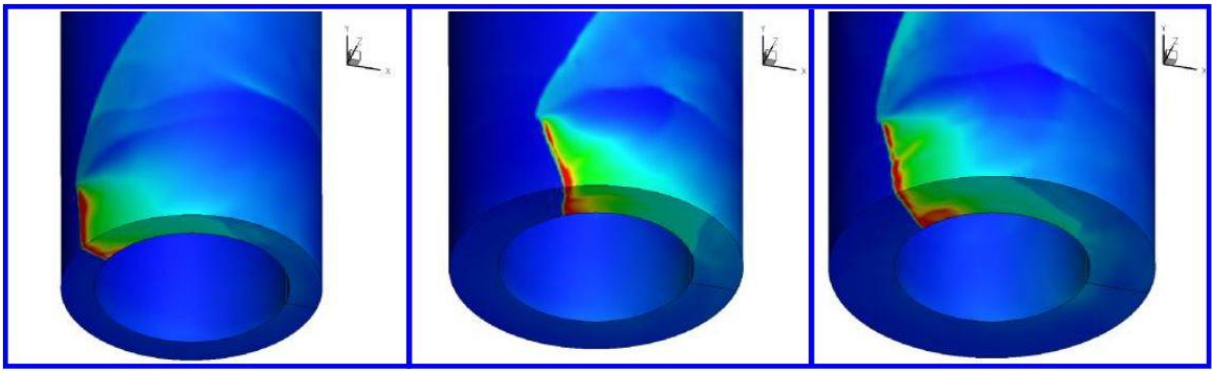

Figure 1.4.25: Pressure solution for diameters of 60-80 mm (left), 60-90 mm (center), and 60-100 mm (right) [15]

To sum up the results of this parametric analysis, it can be said that the results demonstrated that using the maximum area ratio possible resulted in the best performance, that flow field characteristics scaled very nicely with diameter with little change in performance and that axial length had only a small effect on performance for large pressure ratios, but a large effect for smaller pressure ratios. As the depth to diameter ratio is increased for the RDE, the detonation becomes much more unsteady. Further research may help to define secondary effects on the performance parameters (such as viscous or chemical effects), however, these results suggest an important conclusion: RDEs can be run for a wide range of engine sizes and still have acceptable performance and stability characteristics [15].

1.4.6 Applications

Rotating detonation combustors can be used in aerospace filed because they are able to generate thrust, so can be used as propulsion systems [17,18,19]. They can be used also in aeronautical and power production fields because they can be coupled with gas turbines to exploit the pressure gain combustion cycles advantages [14,20].

1.4.6.1 Propulsion system

In paragraph 1.4.1 it was already seen that across the detonation wave there is a pressure increase and that the product gases follow an expansion downstream of detonation. This causes an imbalance of pressure between inlet and outlet of the combustor that generate a thrust force on the inlet wall of the combustor. In Figure 1.4.26 it is possible to see this pressure difference [19].

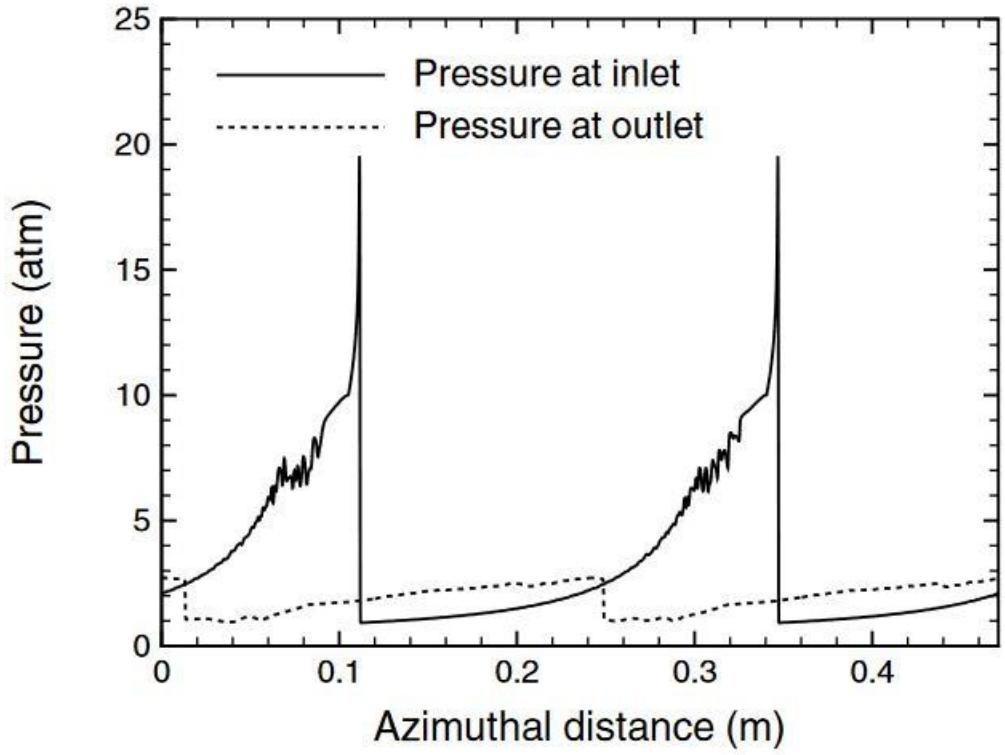

Figure 1.4.26: Pressure distribution at inlet and outlet sections of RDE combustor [19].

To increase the thrust produced by the engine, a nozzle can be attached downstream of the combustor [17]. Since the flow at combustor outlet is supersonic, the nozzle will be only divergent to accelerate the flow [18]. Such a kind of configuration is schematized in Figure 1.4.27.

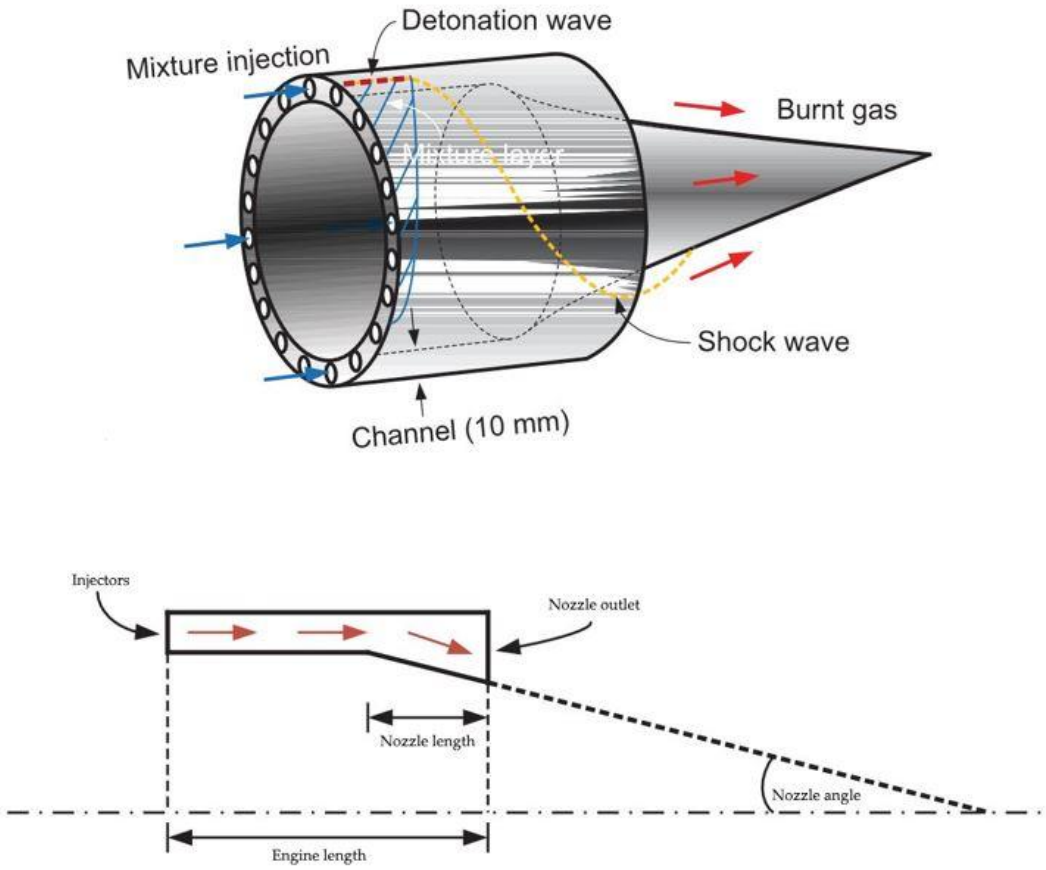

Figure 1.4.27: Annular chamber with an aerospike nozzle [17].

Studying shows that the best performance in thrust is obtained for a nozzle angle of 10° and a nozzle length of 0.04 m: for lower or higher inclinations the propulsive performance decreases [17]. Moreover, propulsive performance is dependent on injection total pressure, area ratio between injectors and inlet wall and increases at their increase [19]. Another interesting result is that the specific impulse of the engine is not dependent on the number of detonation waves [11] and that the thrust is constant, and not pulsed like PDEs, for given operating conditions [19].

1.4.6.2 Gas Turbine Cycles coupling

Due to the non-uniformity of the flow exiting from the rotating detonation combustor and to the backpressure in the mixing plenum caused by the detonation wave, the coupling of a rotating detonation combustor in a gas cycle presents different issues related to the coupling with both compressor and turbine. In paragraph 1.4.3 it was already seen that some trial to reduce the back pressure were done, but with little improvements, so an isolator can be added between compressor and combustion chamber to reduce the effect of backpressure on compressor and improve its operability [20]. For the turbine, if a conventional one is used, in order to reduce the effect of non-uniformity, a mixer can be added after the combustion chamber in order to mix part of the cool flow coming from compressor with the hot gasses. This will obviously reduce the engine performances but allows a conventional turbine to work [20]. Otherwise, a robust design of the turbine can be considered, which reduces efficiency loss while working in off-design conditions.

Zifei et al. [20] carried out some numerical simulations on the integration of a rotating detonation combustor in an aero-turbine engine. The compressor pressure ratio π_c and turbine inlet temperature T_4 play a crucial role in the overall performance of the engine based on the thermodynamic cycle. The variations in the specific thrust Fs, thermal efficiency η_{th} and specific fuel consumption s_{fc} with respect to π_c and T_4 under different flight conditions are respectively illustrated in Figure 1.4.28 [20].

For a constant turbine inlet temperature T_4, Fs and η_{th} first increase but then decrease, while s_{fc} decreases monotonically with an increase in the compressor pressure ratio π_c. As π_c increases, the turbine outlet temperature decreases, owing to the increase of turbine and nozzle pressure ratio. This is beneficial for the increase in η_{th}. Meanwhile, a higher value of π_c implies a lower heat release and temperature rise of the rotating detonation combustor (RDC) at a constant T_4, which is detrimental to the increase in η_{th}. At low values of π_c , the decrease of turbine outlet temperature is the main factor influencing the η_{th}, and η_{th} increases rapidly with the increase of π_c . When the value of π_c is relatively high, the decrease of heat release versus π_c becomes the dominant factor decreasing η_{th}, and η_{th} decreases monotonically as π_c increases, owing to the higher proportion of heat loss to heat release. The specific thrust Fs is uniquely defined by the cycle specific work, which is the product of the RDC heat release and thermal efficiency. When the value of π_c is low, the increase in η_{th} is the main factor influencing the specific thrust Fs; as π_c increases, the decrease in the heat release eventually becomes the dominant factor influencing Fs. Therefore, Fs first increases and then decreases as π_c increases. For a constant compressor pressure ratio π_c, the specific thrust Fs and specific fuel consumption s_{fc} exhibit a

positive correlation with the turbine inlet temperature T_4, while the thermal efficiency η_{th} first increases but then decreases as T_4 increases. Furthermore, η_{th} is sensitive to changes in the turbine inlet temperature compared to Fs and s_{fc} [20].

According to the variations in the performance metrics of the engine versus the compressor pressure ratio π_c, there exists an optimum compressor pressure ratio π_{opt} that maximizes the specific thrust and an optimum pressure ratio π'_{opt} that maximizes the thermal efficiency. Furthermore, π'_{opt} is nominally larger than π_{opt} [20].

With the performance metrics compared under various flight conditions, it can be observed that the higher flight Mach number results in greater thermal efficiency. The effects of the flight Mach number Ma_0 on the thermal efficiency η_{th} indicate two important aspects [20]:

1. the total pressure ratio increases as Ma_0 increases owing to the ram compression, which improves the thermal efficiency;
2. the combustor heat release decreases as the total temperature of the inflow increases and therefore, the proportion of heat loss owing to the exhaust gas to the heat release increases, which decreases the thermal efficiency.

At low values of Ma_0, the total pressure ratio is the main factor influencing the variation in η_{th} and therefore, the thermal efficiency η_{th} increases with an increase in the flight Mach number [20].

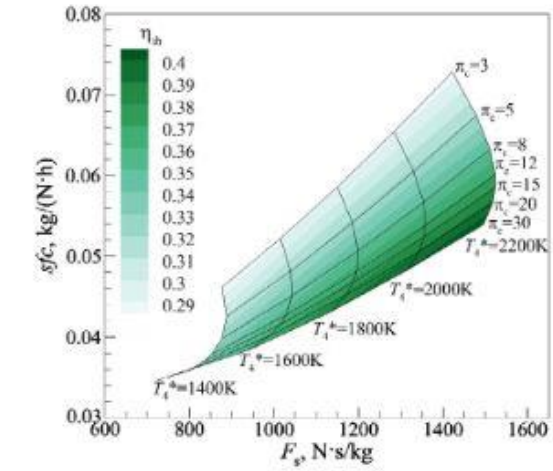

(a) Standard sea-level condition at takeoff (Ma_0=0, H=0)

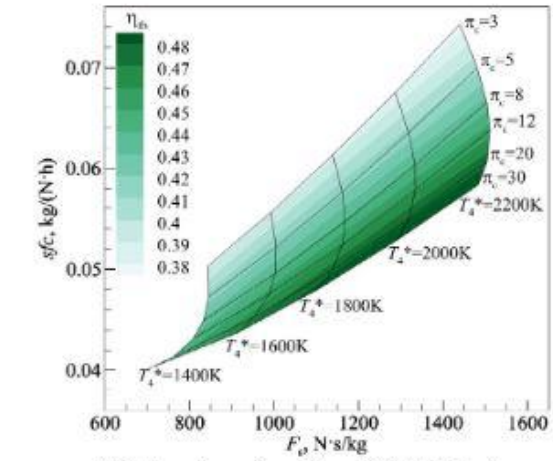

(b) Subsonic cruise (Ma_0=0.8, H=11km)

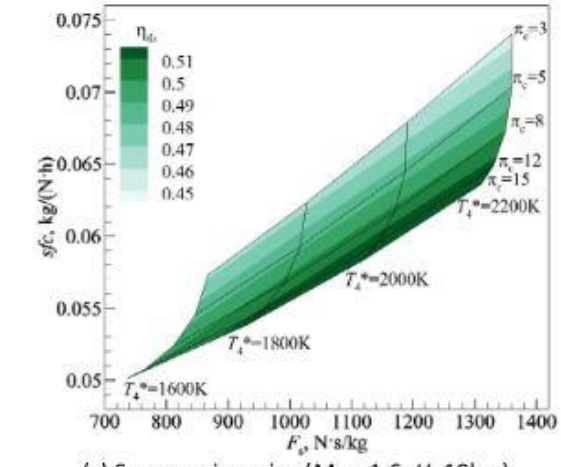

(c) Supersonic cruise (Ma_0=1.6, H=18km)

Figure 1.4.28: Variations of specific thrust Fs, thermal efficiency η_{th} and specific fuel consumption s_{fc} with π_c and T_4 [20].

Now that the main parameters that affects the RDE aero engine are known, a brief comparison with a conventional turbine engine can be done. The variations in the overall performances of the RDE and conventional turbojet engine versus the compressor pressure ratio under standard sea-level conditions are compared in Figure 1.4.29 [20]. The working medium and models utilized in the analysis of the conventional turbojet are the same as those in the RDE model. Figure 1.4.29 a) reveals the specific thrust improvement of the RDE over a wide range of compressor pressure ratios, with the turbine inlet temperature remaining constant at 1600 K. Furthermore, the improvement decreases continuously with an increase in π_c. It can also be observed that the optimum pressure ratio corresponding to the maximum specific thrust of the RDE is significantly lower than that of the turbojet. At low values of π_c, the RDE exhibits competitive improvements in thermal efficiency and specific fuel consumption compared to the conventional turbojet. However, the improvements decrease as π_c increases, and tend to disappear for high compressor pressure ratios, as interpreted intuitively in Figure 1.4.29 b). Moreover, Figure 1.4.29 also reveals that the overall performance of the RDE is not sensitive to changes in π_c compared to the conventional turbojet. In summary, it is evident that the overall performance of the RDE is enhanced at lower compressor pressure ratios. This because π_c appeared to have an unfavourable effect on the total pressure gain across the rotating detonation combustor as shown in Table 1.4.1 [20].

So, these results show that the implementation of an RDC in a gas turbine cycle can give improvements in terms of efficiency, specific fuel consumption and thrust (in case of propulsive engines) compared to conventional gas cycles. Of course, efforts must be done in order to understand how to couple the RDC with turbomachinery and how to design turbomachinery that can be efficiently coupled with RDC, but these results show that improvements are possible.

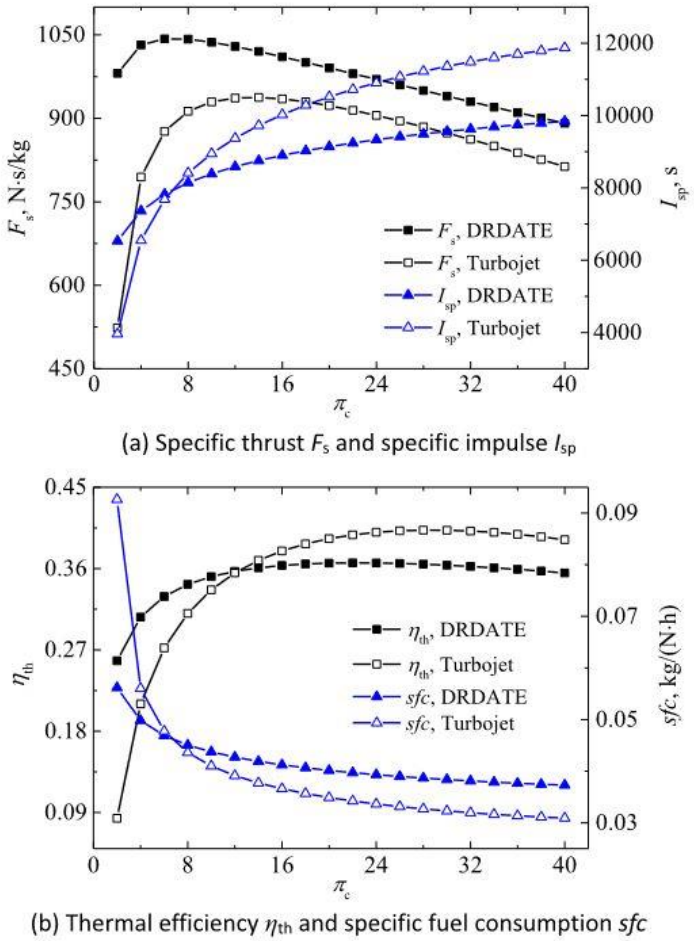

Figure 1.4.29: Overall performance comparison of RDE and conventional turbojet for different compressor pressure ratios [20].

Table 1.4.1: Pressure gain across RDC versus compressor pressure ratio [20]

π_c	Pressure gain across RDC
5	1.806
10	1.467
15	1.306
20	1.205
25	1.134

1.4.7 Comparison with PDE

Since PDEs and RDEs are the most common type of detonation-based propulsion systems, it's worth to make a brief comparison between them. Some comparison points, updated with most recent information, are reported in Table 1.4.2 .

The first difference is the propagation direction of the detonation wave: in PDEs it travels axially along the tube, while in RDEs it travels circumferentially in an annular chamber. The second important difference is the operating frequency, because for PDEs, during the combustion the injection valves are closed and, at every cycle, before injecting the fresh reactants, exhaust gases must be expulsed. This requires a lot of time, so the PDEs running frequency is low. Instead, for RDEs, the injection of reactants and expulsion of burnt gases is continuous and simultaneous in different locations of the combustion chamber, so the running frequency is high, so the thrust and in general the flow is more uniform than in PDEs. These working conditions leads to the third important difference, which is the initiation of the detonation. For PDEs, in each cycle detonation must be initiated, while for RDEs detonation needs to be initiated only once, giving to RDEs' initiation system a longer life.

Table 1.4.2: Qualitative similarities and differences between pulsed and rotating detonation engines [11].

Feature	**PDE**	**RDE**
Deflagrative to detonative transition device	Likely needed	Likely unnecessary
Purge	Likely needed	Unknown
Frequency	1-50 Hz	1-10 kHz
Ignition	One per pulse	Once at start
Exhaust flow unsteadiness	Yes	Reduced
Vibration	Yes	Reduced
Acoustics	Noisy	Unknown
Scalability	Yes	Yes
Fuel type	Gaseous and liquid	Gaseous and liquid
Oxidizer	Air and oxygen	Air and oxygen
Heating	High	High
Integration with turbomachinery	Yes	Yes
Different vehicle platforms	Yes	Yes

1.4.8 Advantage of NOx Reduction

The main parameters that affect NOx production in an RDE are pressure ratio across combustor, equivalence ratio, combustion chamber dimensions and number of detonation front [21].

As the pressure ratio decreases, NOx production also decreases, reducing also RDE performances. Equivalence ratio has a great impact on NOx: reducing it also NOx production is reduced drastically. For an equivalence ratio of 1 the NOx flux concentration is of 500 ppm, while for an equivalence ratio of 0.6 the NOx flux concentration is of 20 ppm, giving a reduction of about 16 times from the stoichiometric mixture [21].

NOx production is also fairly independent of the length of the RDE, slightly increasing for the longer RDEs, because most of the NOx production occurs just behind the detonation wave, with only a small amount of NOx production occurring further downstream in the expansion flow and slip line. Instead, combustion chamber diameter influences NOx production because at larger diameters, the residence time of gases under high temperature increases, leading to an increase of NOx emission. But this increase can be limited because for large diameters the number of detonation waves increases, as seen in paragraph 1.4.2, and this brings to a reduction of residence time of gases at high temperatures, reducing NOx formation [21].

So these results are encouraging and show that RDEs can be run with reasonable level of NOx production and that efforts have to be done in order to deepen and improve this aspect [21].

2. Analysis Methodologies

2.1 Mean Line Analysis

We have seen that RDE can have different advantages compared to conventional gas turbine cycles and that the RDC can be coupled with a downstream turbine. But we have also seen that the flow at the exit of the RDC is non uniform and presents features that are very different from the flow in a conventional gas turbine. For example, the temperature at combustor exit is in the order of 2100 °C for RDC, while for a conventional gas turbine, it is 1350 °C. The flow speed is also very different: for RDC the exiting flow can be fully supersonic or mixed subsonic-supersonic, while in a conventional gas turbine combustors exit the flow is subsonic with a Mach between 0.2 and 0.3 (Figure 1.4.5). These differences lead to different designs of a gas turbine that is coupled with the RDC. The high temperature and speed of the flow suggest a first turbine stage that extracts a lot of work to reduce the flow temperature; then it should also reduce the flow speed, otherwise the losses due to shock and friction will be extremely high in the following stages.

Due to the characteristics of the flow, the transition duct that links the RDC with the turbine can be designed to have two different flow evolution inside it:

1. The flow is accelerated in order to have a fully supersonic flow at turbine inlet and exploit the high speed to extract a high amount of work.
2. The flow is decelerated to have a subsonic flow at turbine inlet to reduce shock losses.

They both have advantages and disadvantages that are summarised in Table 2.1.1.

Table 2.1.1: Comparison between fully supersonic flow and subsonic flow

Fully supersonic flow	Subsonic flow
Lower losses in transition duct	Higher losses in transition duct due to shocks
Higher losses in blades rows due to interaction between flow and blades (shocks)	Lower losses in blades rows due to weaker shocks (the flow is chocked)
Higher extraction of work due to higher velocities	Lower extraction of work due to lower velocities

The design of the turbine with the fully supersonic flow was carried out by my colleague Noraiz Mushtaq [22], so this work aims to design the turbine with subsonic flow at inlet.

Since the flow at the RDC outlet has a very high velocity, the transition duct cannot reduce the speed to Mach of 0.2-0.3 because the losses will be extremely high; so we considered a Mach between 0.6 and 0.8 at turbine inlet, to limit the transition duct losses. Since a Mach between 0.6 and 0.8 is still high and the first stage must reduce the flow speed to reduce losses in downstream stages, the turbine stage designed in this thesis can be also applied as a second stage after a supersonic stage in which the flow enters fully supersonic and exits subsonic due to the speed reduction. So this stage can be applied both as a first stage after a transition duct that behaves like a diffuser, or as second stage after a supersonic stage that reduces the flow speed to subsonic.

The scope of the thesis is to design the turbine stage with the highest efficiency possible, so we started with a parametric analysis, looking at how different parameters influence the stage performances (i.e. efficiency, losses, extracted work).

The parameters that were varied are:

- Inlet Mach number M_0
- Inlet hub radius R_0
- Blade flaring $fl = \frac{b_{out}}{b_{in}}$
- Rotational speed ω
- Absolute rotor outlet flow angle α_2

The schematic meridional view of the stage, with the representation of the different sections, is reported in Figure 2.1.1.

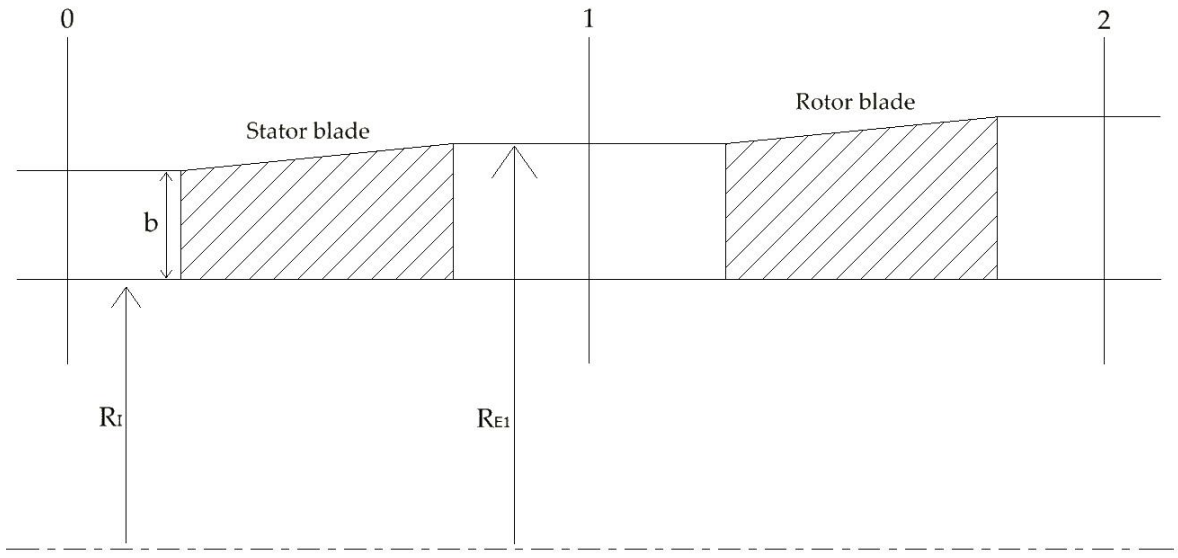

Figure 2.1.1: Schematic of stage meridional view with sections representation

This analysis was carried out using the mean line code zTurbo. We started with the mean line calculations because they are very fast compared to CFD, so they allow to perform a lot of simulations in a short time, which is fundamental for a parametric analysis aimed at investigating a large design space.

Through this analysis we extracted the behaviour of stage performances at the variation of the parameters, finding out the region where the efficiency is maximum.

Then, starting from the parameters values that give maximum efficiency, we generated the 2D geometry of stator and rotor to perform a CFD analysis of the turbine stage, to look at how geometry influences performances and flow field.

There will be shocks in the stage because we need high velocities to extract a lot of work; since the inlet Mach number is high, the highest speed we can reach without going supersonic is for Mach=1, so we decided to have the absolute Mach number at stator outlet (M_1) and the relative Mach number at rotor outlet (M_{2w}) equal to 1.

Always due to the high inlet Mach number, the deflection of the stator and consequently of rotor will be small. So, to increase it, we decided to use flaring, also allowing a higher extraction of work. We decided to use as maximum flaring 1.2 for both stator and rotor, since applying grater slopes could cause flow separation at hub or shroud making the advantages of flaring vanish.

About stage inlet conditions, considering pressures reached by terrestrial power production turbines, we put the total pressure at 15 bar. Then, about the total temperature, we considered 1773.15 K, because zTurbo can manage temperatures up to 1897 K and we did not want to risk of going out from temperature range. Finally, for the mass flow rate, we decided to use the same used in [22], so 100 $\frac{kg}{s}$. All the conditions applied to the stage are listed in Table 2.1.2.

Table 2.1.2: Stage data summary

Physical quantity	Value
$\boldsymbol{M_0}$	0.6 – 0.8
$\boldsymbol{P_{t0}}$	15 bar
$\boldsymbol{T_{t0}}$	1773.15 K
$\boldsymbol{M_1}$	1
$\boldsymbol{M_{2w}}$	1
$\boldsymbol{\dot{m}}$	100 $\frac{kg}{s}$
$\boldsymbol{fl_{max}}$	1.2

2.1.1 zTurbo software

zTurbo is a code for mean line calculations of turbomachinery in which are implemented different losses correlations, namely SimpleVavra, Soderberg, Craig-Cox and Traupel. It can also perform isentropic calculations. Craig-Cox and Traupel

are the once that take into account more losses sources and, between these two, we decided to use Traupel since it was already successfully tested in different non-conventional cases by Professor Persico.

Due to the peculiarity of the case analysed in this thesis, the code needed some adjustments to correctly work:

1. The code works with look up tables, which are tables containing the values of thermodynamic variables (i.e. entropy, enthalpy, pressure, temperature, density, sound speed, specific heat and dynamic viscosity) for a range of pressures and temperatures (up to 1897 K). In Appendix A it is reported an example of look up table. These tables are useful because, if you know two different thermodynamic variables, then the thermodynamic state of the fluid is fully defined, so, instead of applying thermodynamic calculations, you can enter the look up table and find the values of all the unknown variables through the interpolation of the table values. This allows to fasten up calculations.
   zTurbo code is written in order to call an external software to generate the table starting from the inlet conditions of the simulation, so the inlet thermodynamic state is directly calculated by this software. The problem is that it generates a table at every run of the code, loosing time. So, the first modification I applied to zTurbo was the addition of a script that reads the simulation inlet values and find the unknown variables through the interpolation of table values. This allows to use the same look up table for different simulations instead of generating a table at every run of zTurbo.
2. In the interpolating procedure, if pressure was used as inlet value for the look up table, the results were wrong. This because in the subsection of the code in which values were interpolated from pressure, there were some conditions in "while" loops that made table indexes take wrong values. So I modified these conditions to make them take the right values.
3. A numerical procedure to compute the zero of a function gave unphysical results, like negative density. So I modified it in order to bound the values in the physical region.
4. The Reynolds and Mach numbers passed to Traupel correlation were fixed respectively to $1 \cdot 10^5$ and 0.8. The problem is that losses changes with Reynolds and Mach numbers because they are characteristics of the flow. So I modified the code in order to pass the correct values calculated at the inlet of the row. For Reynolds number I considered as characteristic length the blade axial chord.
5. Since the inlet Mach number is high, blades deflection will be small to reach the sonic conditions, both for stator and rotor. These results are outside the

range of validity of all the implemented losses correlations [23, 24], so we decided to modify Traupel correlations in order to allow it to extrapolate values of losses and deviation with a physical sense.
The minimum deflection for which Traupel is valid is 45°, and since we reach deflections of 20°, the previous extrapolation procedure was giving negative losses coefficients, which are unphysical. So we decided to put the losses of a straight profile to 1% and to make a linear interpolation between Traupel losses at 45° and the 1% losses of the straight profile. Instead, the deviation for deflections smaller than 45° was put to zero. In Appendix B a deeper explanation of this modifications is reported.

2.1.2 zTurbo input code

zTurbo works with the inputs listed in Table 2.1.3, but we have only the values listed in Table 2.1.2, so there is the need of a code to generate the inputs required by zTurbo.

Table 2.1.3: zTurbo required input

Input required by zTurbo		
Mass flow rate [kg/s]	Rotational speed [rpm]	Inlet total temperature [°C]
Inlet total pressure [bar]	Outlet static pressure [bar]	Stator inlet angle [deg]
Stator inlet blade height [m]	Stator inlet blade height to mean diameter ratio	Expansion ratio
Reaction degree	Stator-rotor distance to stator chord ratio	Rotor-stator distance to rotor chord ratio
Stator outlet to stator inlet mean diameter ratio	Rotor outlet to rotor inlet mean diameter ratio	Stator axial chord [m]
Stator outlet angle [deg]	Stator trailing edge to stator throat ratio	Stator pitch to stator chord ratio
Rotor axial chord [m]	Rotor trailing edge to Rotor throat ratio	Rotor pitch to Rotor chord ratio
Rotor outlet angle [deg]		

zTurbo requires isentropic values for these inputs, so I created a code that evaluates these isentropic values in the three sections of the stage (look at Figure 2.1.1) starting from the stage data of Table 2.1.2.

2.1.2.1 Section 0

Total temperature, total pressure and Mach number in section zero are known (see Table 2.1.2). So, it is possible to find all the other quantities. Starting from the energy conservation I found the static temperature through Equation 2.1. Then, through adiabatic transformation from total state to static one, I calculated static pressure with Equation 2.2.

$$\frac{T_t}{T} = 1 + \frac{\gamma-1}{2} \cdot M^2 \qquad \text{Equation 2.1}$$

$$\frac{P_t}{P} = \left(1 + \frac{\gamma-1}{2} \cdot M^2\right)^{\frac{\gamma}{\gamma-1}} \qquad \text{Equation 2.2}$$

Then, through Mach number, I found inlet velocity with Equation 2.3.

$$V = \sqrt{\gamma \cdot R \cdot T} \cdot M \qquad \text{Equation 2.3}$$

At this point it was possible to find the enthalpy, both static and total, through Equation 2.1 and Equation 2.4.

$$h = C_p \cdot T \qquad \text{Equation 2.4}$$

Finally, also the blade height was found through mass balance in Equation 2.5, Equation 2.6 and Equation 2.7.

$$\dot{m} = S_0 \cdot V_0 \cdot \rho_0 \quad \rightarrow \quad S_0 = \frac{\dot{m}}{V_0 \cdot \rho_0} \qquad \text{Equation 2.5}$$

$$S_0 = \pi \cdot (R_{e0}^2 - R_i^2) \quad \rightarrow \quad R_{e0} = \sqrt{\frac{S_0}{\pi} + R_i^2} \qquad \text{Equation 2.6}$$

$$b_0 = R_{e0} - R_i \qquad \text{Equation 2.7}$$

2.1.2.2 Section 1

Now that section 0 values are defined, knowing that $M_1 = 1$, also the other thermodynamic quantities of section 1 can be defined through Equation 2.8.

$$\begin{cases} T_{t1} = T_{t0} \\ T_1 = T_{t1} - \frac{V_1^2}{2C_p} \\ V_1 = a_1 \cdot M_1 \\ a_1 = \sqrt{\gamma \cdot R \cdot T_1} \\ \frac{P_{t1}}{P_1} = \left(\frac{T_{t1}}{T_1}\right)^{\frac{\gamma}{\gamma-1}} \\ Y_s = \frac{P_{t0} - P_{t1}}{P_{t1} - P_1} \end{cases} \qquad \text{Equation 2.8}$$

Since zTurbo requires isentropic values, then stator losses Y_s will be considered zero. Mathematical procedure of Equation 2.8 solution is reported in Appendix C.

Successively, knowing stator flaring fl_s, the geometry of the stator was defined through Equation 2.9.

$$\begin{cases} b_1 = fl_s \cdot b_0 \\ R_{e1} = R_i + b_1 \\ S_1 = \pi \cdot (R_{e1}^2 - R_i^2) \end{cases} \qquad \text{Equation 2.9}$$

Considering that rotational speed is known since it is a parameter to be varied, the velocity triangles can be calculated thanks to Equation 2.10.

$$\begin{cases} \rho_1 = \frac{P_1}{R \cdot T_1} \\ \dot{m} = \rho_1 \cdot V_{1ax} \cdot S_1 \quad \rightarrow \quad V_{1ax} = \frac{\dot{m}}{\rho_1 \cdot S_1} \\ \alpha_1 = arcos\left(\frac{V_{1ax}}{V1}\right) \\ V_{1\tan} = V_1 \cdot \sin(\alpha_1) \\ U_1 = \omega \cdot \frac{R_{e1}+R_i}{2} \\ W_{1ax} = V_{1ax} \\ W_{1\tan} = V_{1\tan} - U_1 \\ W_1 = \sqrt{W_{1ax}^2 + W_{1\tan}^2} \\ \beta_1 = arctan\left(\frac{W_{1\tan}}{W_{1ax}}\right) \\ M_{1w} = \frac{W_1}{a_1} \\ T_{t1w} = T_1 + \frac{W_2^2}{2c_p} \\ P_{t1w} = \left(\frac{T_{t1w}}{T_1}\right)^{\frac{\gamma}{\gamma-1}} \cdot P_1 \end{cases} \qquad \text{Equation 2.10}$$

Finally, Zweifel loading criterion is used to find the inverse of the stator solidity sb_s. Then, supposing that axial chord is equal to the inlet blade height b_0, the stator pitch and number of blades were also determined. The hypothesis on the axial chord is needed to find the number of blades, but it is an initial guess that will be further analysed in the CFD analysis.

$$chord_s = b_0 \qquad \text{Equation 2.11}$$

$$pitch_s = sb_s \cdot chord_s \qquad \text{Equation 2.12}$$

$$bld_s = \left\lfloor \frac{\pi \cdot (R_{e0}+R_i)}{pitch_s} \right\rfloor \qquad \text{Equation 2.13}$$

$$pitch_s = \frac{\pi \cdot (R_{e0}+R_i)}{bld_s} \qquad \text{Equation 2.14}$$

Since the number of blades bld must be an integer number, the floor operation in Equation 2.13 is present. But this leads to a variation of the pitch value calculated in Equation 2.12, so Equation 2.14 is needed to find the updated pitch value, based on the integer number of blades.

At the end also static and total enthalpy can be found in Equation 2.15.

$$\begin{cases} h_1 = c_p \cdot T_1 \\ h_{t1} = c_p \cdot T_{t1} \end{cases}$$ Equation 2.15

2.1.2.3 Section 2

In Equation 2.16 are reported the equations that characterise section 2.

$$\begin{cases} Rot_1 = c_p T_1 + \frac{W_1^2}{2} - \frac{U_1^2}{2} = c_p T_2 + \frac{W_2^2}{2} - \frac{U_2^2}{2} \\ M_{2w} = \frac{W_2}{a_2} \\ a_2 = \sqrt{\gamma R T_2} \\ \frac{P_1}{P_2} = \left(\frac{T_1}{T_2}\right)^{\frac{\gamma}{\gamma-1}} \\ \dot{m} = \frac{P_2}{R \cdot T_2} \cdot V_2 \cdot \cos(\alpha_2) \cdot S_2 \\ T_{t2w} = T_2 + \frac{W_2^2}{2c_p} \\ V_{2tan} = V_2 \cdot \sin(\alpha_2) \\ V_{2ax} = V_2 \cdot \cos(\alpha_2) \\ W_{2tan} = V_{2tan} - U_2 \\ W_{2ax} = V_{2ax} \\ W_2^2 = W_{2ax}^2 + W_{2tan}^2 \\ U_2 = \omega \cdot \frac{R_{e2} + R_i}{2} \\ S_2 = \pi \cdot (R_{e2}^2 - R_i^2) \end{cases}$$ Equation 2.16

As already explained, we want $M_{2w} = 1$. But the system is still open, because we need another information to close it. This information can be the imposition of the rotor flaring or the imposition of the absolute outlet angle. We decided to impose the absolute outlet angle and to study how it influence performance parameters of the stage and also the rotor flaring, considering to not overcome the values of $fl_r = 1.2$ in order to avoid boundary layer separation at endwalls. In any case this limit value will be analysed in the CFD analysis.

We used $\alpha_1 = 0$ as first guess to reduce the outlet kinetic energy, but this is not a strict motivation since the stage is not the last one, so the outlet kinetic energy is not lost, but can be recovered by following stages.

In Appendix D the mathematical solution of Equation 2.16 is explained.

Similarly to section 1, also here the number of blades is found through Zweifel criterion. As initial guess, we considered to give to rotor the same axial chord of stator, but this choice will be further analysed during the CFD analysis.

$$chord_r = chord_s \qquad \text{Equation 2.17}$$

$$pitch_r = sb_r \cdot chord_r \qquad \text{Equation 2.18}$$

$$bld_r = \left\lfloor \frac{\pi \cdot (R_{e1} + R_i)}{pitch_r} \right\rfloor \qquad \text{Equation 2.19}$$

$$pitch_r = \frac{\pi \cdot (R_{e1} + R_i)}{bld_r} \qquad \text{Equation 2.20}$$

Finally, also here, it is possible to find static and total enthalpies in Equation 2.21.

$$\begin{cases} h_2 = c_p \cdot T_2 \\ h_{t2} = c_p \cdot (T_2 + \frac{V_1^2}{2c_p}) \end{cases} \qquad \text{Equation 2.21}$$

2.1.2.4 zTurbo input calculation

Now that geometric and thermodynamic quantities have been evaluated in the three different sections, it is possible to calculate the input for zTurbo. About geometric quantities, we consider having a trailing edge thickness of 1 mm ($TE = 1\,mm$), in order to have it the thinnest possible without creating problem for blade cooling and vibration issue during the machining of the blade. About the distance between stator and rotor of same stage and rotor and stator of two following stages, we considered to put them equal to the axial chord of the cascades.

Input calculations are performed in Table 2.1.4.

Table 2.1.4: zTurbo input calculations

zTurbo input	
Mass flow rate = 100 kg/s	Inlet total pressure = 15 bar
Inlet total temperature = 1500 °C	Outlet static pressure = P_2
Rotational speed = $\boldsymbol{\omega}$	Expansion ratio = $\frac{P_{t0}}{P_2}$
Reaction degree = $\frac{\boldsymbol{h_1 - h_2}}{\boldsymbol{h_{t0} - h_2}}$	Stator inlet blade height = b_0
Stator inlet blade height to mean diameter ratio = $\frac{\boldsymbol{b_0}}{\boldsymbol{R_{e0} + R_i}}$	Stator-rotor distance to stator chord ratio = 1
Rotor-stator distance to rotor chord ratio = 1	Stator outlet to stator inlet mean diameter ratio = $\frac{R_{e1} + R_i}{R_{e0} + R_i}$
Rotor outlet to rotor inlet mean diameter ratio = $\frac{\boldsymbol{R_{e2} + R_i}}{\boldsymbol{R_{e1} + R_i}}$	Stator axial chord = $chord_s$
Stator inlet angle = $\boldsymbol{\alpha_0}$	Stator outlet angle = α_1
Stator trailing edge to stator throat ratio = $\frac{\boldsymbol{TE}}{\boldsymbol{pitch_s \cdot \cos(\alpha_1)}}$	Stator pitch to stator chord ratio = $\frac{pitch_s}{chord_s}$
Rotor axial chord = $\boldsymbol{chord_r}$	Rotor trailing edge to Rotor throat ratio = $\frac{TE}{pitch_r \cdot \cos(\beta_1)}$
Rotor pitch to Rotor chord ratio = $\frac{\boldsymbol{pitch_r}}{\boldsymbol{chord_r}}$	Rotor outlet angle = $arctan\left(\frac{W_{2tan}}{W_{2ax}}\right)$

2.1.3 Iterative Algorithm

We know that we want specific values of Mach numbers, flaring and absolute flow angle, so I call them reference values and I indicate them as $M_{0_{ref}}, M_{1_{ref}}, M_{2w_{ref}}, fl_{ref}$ and $\alpha_{2_{ref}}$. About $M_{0_{ref}}, fl_{ref}$ and $\alpha_{2_{ref}}$, since they are parameters of the parametric analysis, their values depend on which point of the analysis I am considering, while $M_{1_{ref}} = 1$ and $M_{2w_{ref}} = 1$.

These reference values represent the point in which we want to make the turbine work, so they must consider losses. This means that, since zTurbo is the code that implements losses correlations, the values coming out from zTurbo must be equal to the corresponding reference values. Let's call zTurbo outlet quantities as $M_{0_z}, M_{1_z}, M_{2w_z}, fl_z$ and α_{2_z}. There are also other output quantities, but they are not constrained, since they are the quantities we want to find and analyse.

The problem is that $M_{0_{ref}}, M_{1_{ref}}, M_{2w_{ref}}, fl_{ref}$ and $\alpha_{2_{ref}}$ cannot be used as inputs for zTurbo as already seen in Table 2.1.3. This means that the corresponding quantities coming from zTurbo (i.e. $M_{0_z}, M_{1_z}, M_{2w_z}, fl_z$ and α_{2_z}) are zTurbo outputs. So to make $M_{0_z}, M_{1_z}, M_{2w_z}, fl_z$ and α_{2_z} equal to $M_{0_{ref}}, M_{1_{ref}}, M_{2w_{ref}}, fl_{ref}$ and $\alpha_{2_{ref}}$ we need to find the right inputs to zTurbo.

To find the inputs of zTurbo we need the *zTurbo input code* as explained in paragraph 2.1.2, and the code needs the values of M_0, M_1, M_{2w}, fl and α_2 to be able to close the mathematical systems and find the zTurbo input values. This means that M_0, M_1, M_{2w}, fl and α_2 are inputs of *zTurbo input code*. Here another problem arises: *zTurbo input code* performs isentropic calculations, while zTurbo calculates losses, so $M_1, M_{2w}, fl, \alpha_2$ will be different from $M_{1_z}, M_{2w_z}, fl_z, \alpha_{2_z}$. This means that, to make the outlet values of zTurbo equal to reference values, I cannot simply put $M_1, M_{2w}, fl, \alpha_2$ equal to $M_{1_{ref}}, M_{2w_{ref}}, fl_{ref}, \alpha_{2_{ref}}$, because then $M_{1_z}, M_{2w_z}, fl_z, \alpha_{2_z}$ will be different from $M_{1_{ref}}, M_{2w_{ref}}, fl_{ref}, \alpha_{2_{ref}}$.

So, to solve this problem, there is the need of an iterative algorithm that starts putting $M_1, M_{2w}, fl, \alpha_2$ equal to $M_{1_{ref}}, M_{2w_{ref}}, fl_{ref}, \alpha_{2_{ref}}$, and then modifies $M_1, M_{2w}, fl, \alpha_2$ until zTurbo outputs are equal to the reference values.

Instead M_0 does not create problems. It will be equal to M_{0_z} since the inlet conditions are not influenced by losses.

I tried also other logics for the algorithm, like to insert losses in the *zTurbo input code* through Y_s and Y_r instead of modifying $M_1, M_{2w}, fl, \alpha_2$, but none of them worked.

A schematic representation of the algorithm is reported in Algorithm 1 and Figure 2.1.2.

Since the algorithm is long, I divided it into blocks highlighted by the orange lines in Algorithm 1. The division is the following (extremes are included):

- Block 1: from row 1 to row 7
- Block 2: from row 8 to row 59
- Block 3: from row 60 to row 103
- Block 4: from row 104 to row 155
- Block 5: from row 156 to row 177

The algorithm is composed by an outer loop, i.e. the ***while*** condition at row 7, and by different inner loops. The aim of the outer loop is to find all the wanted values, while the aim of inner loops is to modify the quantities M_1, M_{2w}, fl and α_2 one by one, in order to reduce the error between the zTurbo output and the reference value of the specific quantity considered.

It must be said that this algorithm was found after many trials and is the one that gave the best results in terms of convergence.

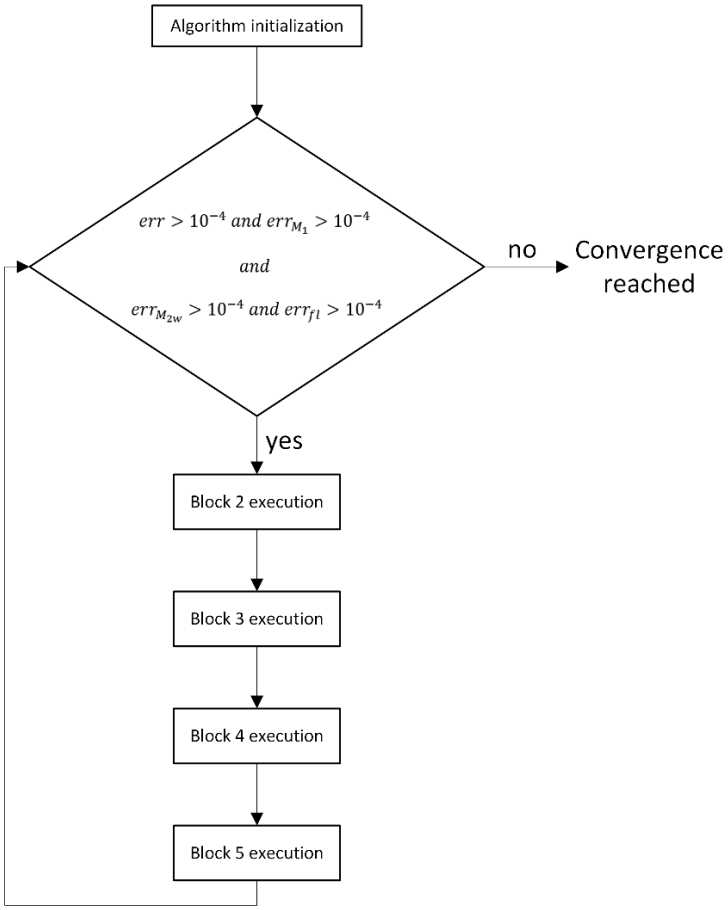

Figure 2.1.2: Iterative algorithm structure

2.1.3.1 Block 1

In block 1 there is the initialization of the quantities to enter the outer loop. Firstly, zTurbo inputs are calculated through *zTurbo input code*, using $M_{0_{ref}}, M_{1_{ref}}, M_{2w_{ref}}, fl_{ref}$ and $\alpha_{2_{ref}}$ (row 1). Then zTurbo is run (row 2) and the outputs are extracted to calculate the errors respect to the reference values (rows from 3 to 6).

Finally, it is possible to enter in the outer loop (row 7). The threshold values for the errors were put to 10^{-4}, since they are sufficiently small to consider the algorithm converged in a preliminary analysis with an acceptable calculation time.

2.1.3.2 Block 2

In block 2 there is the first inner loop. The flow chart is reported in Figure 2.1.8. It is used to reduce the error on M_{1_z} (i.e. err_{M_1}). The logic of the cycle is to modify M_1 in order to get M_{1_z} closer to $M_{1_{ref}}$. The modified M_1 is called M_1^+ (row 15) and it produces the need of a new error definition: $err_{M_1}^+$, which contains the difference between the M_{1_z} calculated with the zTurbo inputs generated through M_1^+, and $M_{1_{ref}}$ (rows from 15 to 22). When $err_{M_1}^+$ is lower than err_{M_1} it means that the M_1^+ produces zTurbo inputs that give a M_{1_z} closer to $M_{1_{ref}}$ than the older M_1. When the aim of reducing the error between M_{1_z} and $M_{1_{ref}}$ is reached (i.e. $err_{M_1}^+ < err_{M_1}$), the code saves the new values of M_1 and $err_{M_1}$and exits this inner loop going to block 3 (row from 25 to 27).

To enter in the cycle, the $err_{M_1}^+$ must be greater than err_{M_1}, so I initialise $err_{M_1}^+$ as shown in row 8.

The quantity of which M_1 is modified (i.e. ΔM_1) depends on the error in both modulus and sign (row 10). This because the closer is M_{1_z} to $M_{1_{ref}}$, the smaller will be the variation of M_1 to get the right M_{1_z}. For the sign, if M_{1_z} is lower than $M_{1_{ref}}$, to increase M_{1_z} also M_1 must increase. So, if the error err_{M_1} has a positive sign, then M_{1_z} is smaller than $M_{1_{ref}}$, so ΔM_1 is positive and M_1 will increase ($M_1^+ > M_1$, row 15). If $err_{M_1} < 0$ then $\Delta M_1 < 0$, so M_1 will decrease ($M_1^+ < M_1$, row 15).

I noticed that modifying M_1 two different things can happen. The first is that $err_{M_1}^+ < err_{M_1}$ and so the error is reduced, so the cycle has reached its aim as explained in previous rows. The second is that $err_{M_1}^+ > err_{M_1}$, so the value of M_1 variation (i.e ΔM_1) is not good. In this case the value of the modulus of $|\Delta M_1|$ must be changed to reduce $err_{M_1}^+$ until $err_{M_1}^+ < err_{M_1}$. Only the modulus of ΔM_1 must be changed because the

sign is given by error sign, so it is correct. The problem is that changing $|\Delta M_1|$ is not straightforward because four different things can happen:

1. Reducing $|\Delta M_1|$ reduces also $err_{M_1}^+$
2. Reducing $|\Delta M_1|$ increases $err_{M_1}^+$
3. Increasing $|\Delta M_1|$ reduces $err_{M_1}^+$
4. Increasing $|\Delta M_1|$ increases also $err_{M_1}^+$.

About points 1. and 3. the $|\Delta M_1|$ changing is good since $err_{M_1}^+$ is reducing. About 2. and 4., they can happen simply because $|\Delta M_1|$ is too small or big, or because M_{1_z} does not vary linearly with M_1: for a small increment of M_1, M_{1_z} can have a small decrease and vice versa. This can be due to different causes: the non-linear losses correlations from which M_{1_z} is calculated or to the implementation of zTurbo code. Figure 2.1.4 shows the qualitative trend that links M_1 to M_{1_z}.

The way in which the algorithm deals with these four situations is following explained through an example: let's imagine to be in the situation of Figure 2.1.3, where err_{M_1} is greater than zero, so M_1^+ will be bigger than M_1.

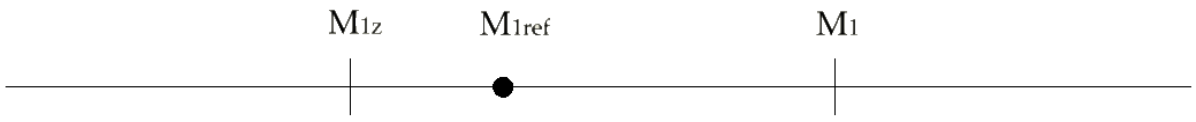

Figure 2.1.3: Algorithm, example of starting point

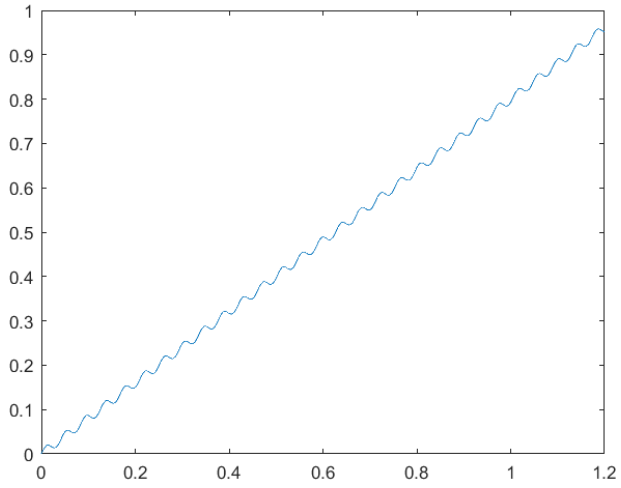

Figure 2.1.4: Qualitative representation of M_1 and M_{1_z} relation

Increasing a little bit M_1 ($\Delta M_1 > 0$) can bring $err^+_{M_1}$ to be bigger than err_{M_1}, as already explained. In Figure 2.1.5 are shown the two different ways for which we get $err^+_{M_1} > err_{M_1}$: due to non-linearity, the new M_{1_z}, which is called $M_{1_z}^+$ and comes from M_1^+, is lower than the old M_{1_z} (case a), or the $|\Delta M_1|$ is too big (case b).

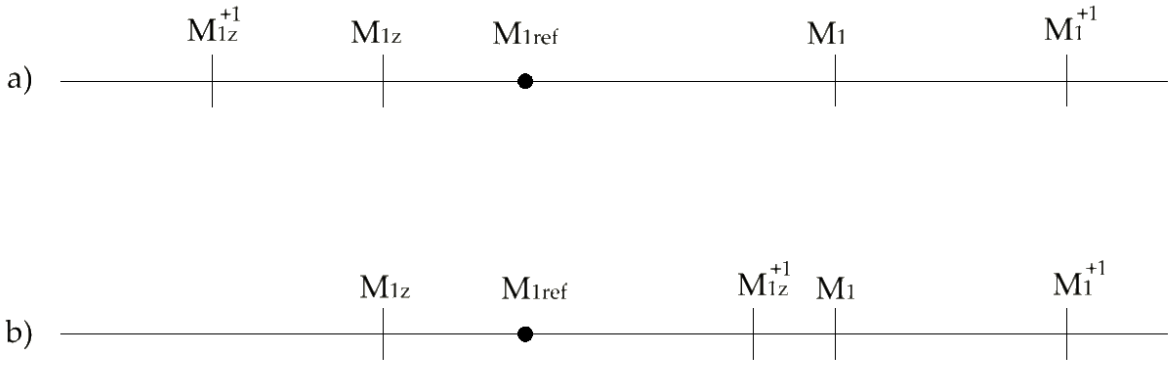

Figure 2.1.5: Possible evolutions of starting point at first iteration. Case a) is due to oscillations in M_1 and M_{1_z} relation. Apex '1' indicates the iteration number of the inner loop.

In both cases the algorithm tries some corrective actions and then look at the trend of $err_{M_1}^+$. Now, to look at this trend, the algorithm needs to know the last smallest value of $err_{M_1}^+$ to understand if, with the corrective actions, it is going towards the right direction, so $err_{M_1}^+$ reduction, or it is going towards the wrong one. So $err_{M_{1_{old}}}$ is defined as the last smallest value of $err_{M_1}^+$ and it will be compared with the $err_{M_1}^+$ coming from the corrective actions. Due to the initialization (row 9), $err_{M_{1_{old}}}$ will be much greater than $err_{M_1}^+$ coming from the first iteration of the algorithm. This because $|err_{M_1}^+|$ coming from the first iteration will be smaller than 1 since the variation of M_1 will be proportional to err_{M_1} and $|err_{M_1}|$ will be smaller than 1 since the algorithm starts from the reference conditions and not a random point.

The corrective actions that the algorithm can take are two: increase $|\Delta M_1|$ or decrease $|\Delta M_1|$. In order to check if the corrective action applied is reducing $err_{M_1}^+$ or not, the algorithm needs to remember which corrective action it applied, so the ΔM_1 value of the previous iteration is stored in $\Delta M_{1_{old}}$, to be able to see if $|\Delta M_1|$ is decreasing or increasing and see the effects on $err_{M_1}^+$.

From the way the algorithm is designed, the first corrective action that is taken is to reduce ΔM_1 (rows from 35 to 40). This because the initialization set $\left|err_{M_{1_{old}}}\right|$ to be greater than $|err_{M_1}^+|$, and set $\Delta M_{1_{old}}$ to be equal to ΔM_1 (row 11). At last, $|\Delta M_1|$ will be smaller than $|\Delta M_{1_{old}}|$, having so the same corrective action, if *zTurbo input code* returns non-physical values for some iterations. This happens because I placed a check to verify that, also with the variation of M_1, the code returns physical values. This check is needed because, for some cases, *zTurbo input code* returns values with no sense, like an axial velocity greater than the velocity itself. If the results of *zTurbo input code* are with no physical sense, then ΔM_1 is adjusted through n_{M_1} to find a variation of M_1 that can be physically possible (rows from 17 to 24).

Going back to the corrective action, it can give positive result reducing $err_{M_1}^+$, so the algorithm will continue with reducing $|\Delta M_1|$ (rows from 35 to 40) (Figure 2.1.6), or $err_{M_1}^+$ can increase, so this will lead the algorithm to try to increase $|\Delta M_1|$ (rows from 49 to 56). Then, if increasing $|\Delta M_1|$ results in $err_{M_1}^+$ reduction (Figure 2.1.7), it will continue to increase $|\Delta M_1|$ (rows from 29 to 34). But, if also increasing $|\Delta M_1|$ the algorithm does not find a reduction of $err_{M_1}^+$, it means that the variation of $|\Delta M_1|$ is too high, so $|\Delta M_1|$ variation is reduced through $n_{M_{1_{old}}}$ (rows from 43 to 46). Then, since increasing $|\Delta M_1|$ did not worked, $|\Delta M_1|$ is reduced considering the new value of the variation (row 47). This is why there is the control $contr_{M_1}$ (row 42 and row 50): if it is equal to 2 it means that both the increment and the reduction of $|\Delta M_1|$ were tried with no success, so there is the need to modify the variation of $|\Delta M_1|$. To be clear, the variation of $|\Delta M_1|$ was put to 0.05 because it gives the best results for convergence.

The instructions from row 43 to row 46, so $|\Delta M_1|$ variation reduction, are performed when firstly $|\Delta M_1|$ is reduced and then increased with no success, as explained in previous rows. But it can also happen that $|\Delta M_1|$ is firstly increased with no success, leading so to try its reduction (rows from 41 to 48). If also this reduction does not work, then $|\Delta M_1|$ variation must be reduced (rows from 51 to 54), since both increment and reduction were performed with no success. In this case, $|\Delta M_1|$ is then increased with the new value of variation (row 55), because the last action that did not worked was the reduction of $|\Delta M_1|$. This is why the part of the algorithm between rows 41 and 48 is similar to the part between rows 49 and 56: because they perform similar operations for cases that have opposite histories of decrement/increment of $|\Delta M_1|$ with no success.

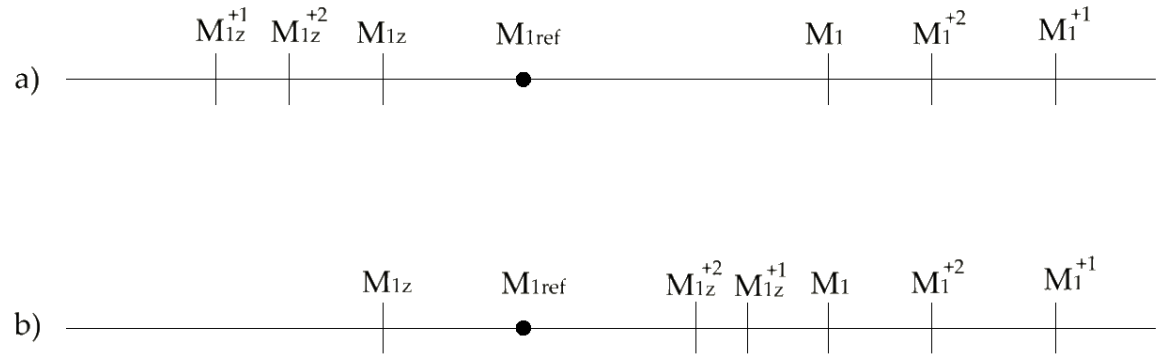

Figure 2.1.6: Possible evolution of the starting point at second iteration. Case a) is due to oscillations in M_1 and M_{1_z} relation.

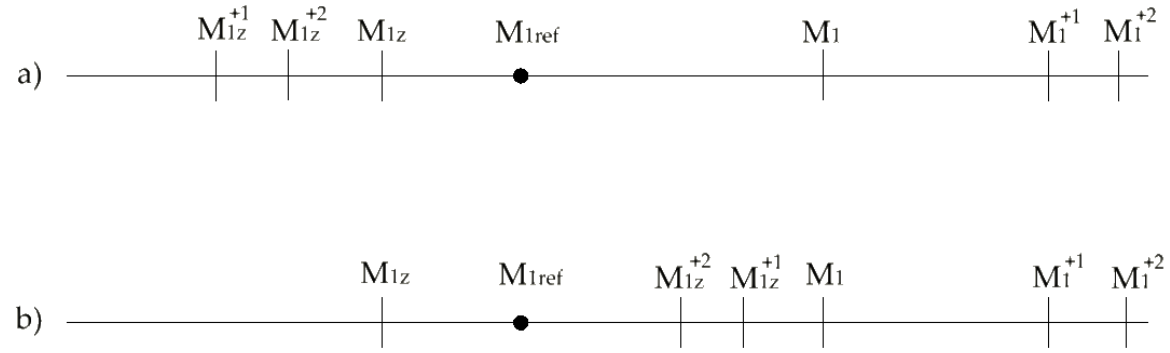

Figure 2.1.7: Another possible evolution of the starting point at second iteration. Case b) is due to oscillations in M_1 and M_{1_z} relation.

It must be noticed that in case b) of Figure 2.1.6 and Figure 2.1.7 the ΔM_1 is still positive even if $M_{1_z}^{+1}$ is greater than $M_{1_{ref}}$ because ΔM_1 is based on the difference between $M_{1_{ref}}$ and M_{1_z}, and not on $M_{1_z}^{+}$.

The example shows the logic of the algorithm starting from $M_{1_z} < M_{1_{ref}}$, but if the starting point is $M_{1_z} > M_{1_{ref}}$, the behaviour will be specular due to the presence of the modulus in the ***if*** conditions.

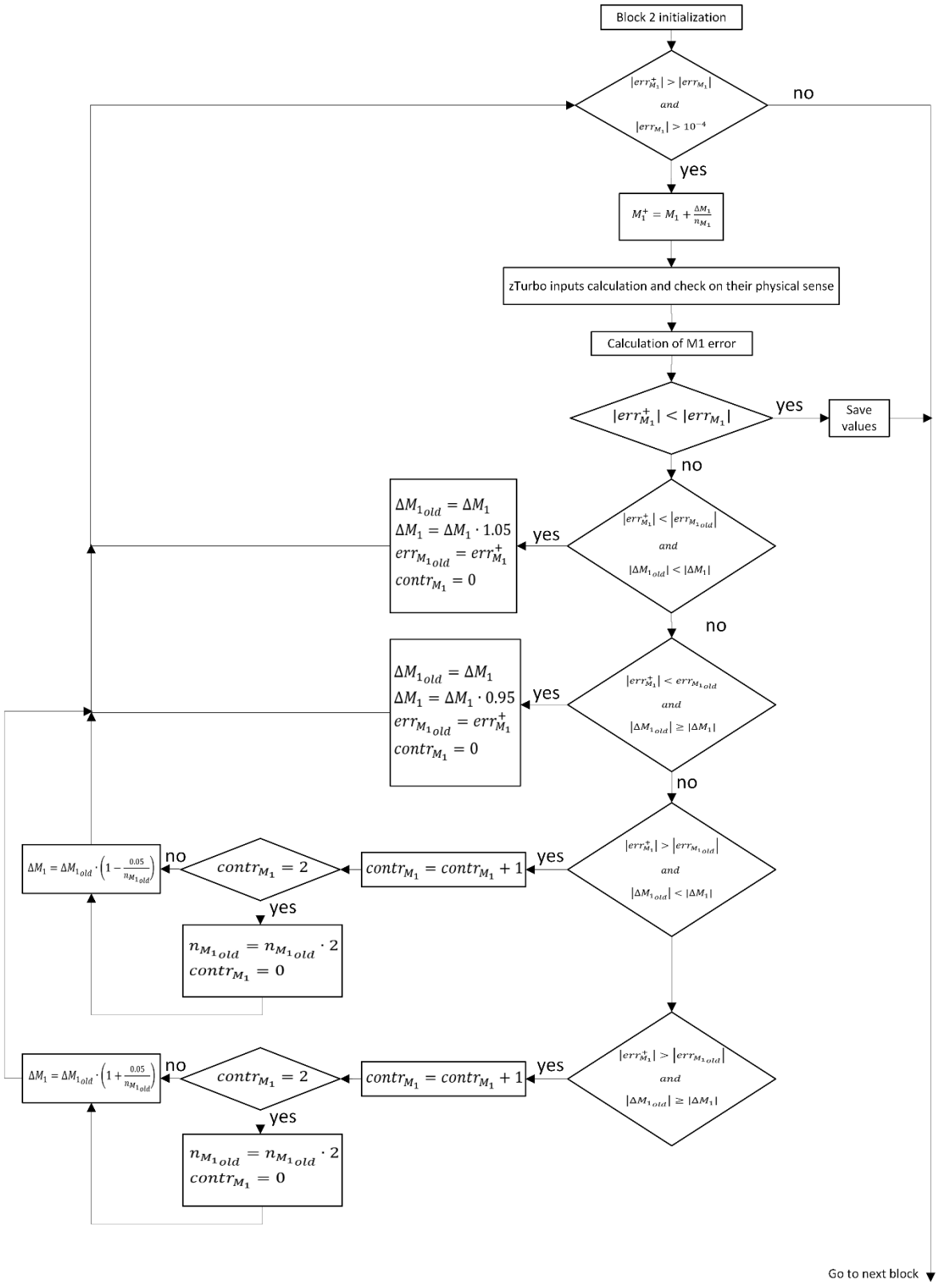

Figure 2.1.8: Block 2 flow chart

2.1.3.3 Block 3

In block 3 there is the inner loop used to reduce the error on stator flaring (it is only on stator because on rotor we decided to constrain α_2, so rotor flaring must be free to not over constraint the system). Its flow chart is reported in Figure 2.1.9.

From row 60 to 65 there is the initialization of values for the loop. $err_{fl_{cycle}}$ has the same function of $err_{M_1}^{+}$ of block 2: it contains the last smallest value of the error calculated from the modified flaring (fl^{+} or fl^{-}). Instead err_{fl} has the same function of err_{M_1}, so it contains the error of flaring before the beginning of the loop. The logic of this loop is to modify fl until $err_{fl_{cycle}}$ is smaller than err_{fl}, meaning that fl_z is closer to fl_{ref} than before entering the loop. The maximum number of iterations the loop can do is 20, because I found that, if it uses more iterations, than it does not converge. In this case the algorithm proceeds with the old value of flaring because it is the one that gives the best results.

The loop works in the following way: firstly, flaring is increased finding fl^{+} (row 67). Then the new inputs for zTurbo are found and their physical sense is checked in the same way of block 2 (rows from 68 to 72). Successively zTurbo is run and the new error is calculated (rows from 73 to 75). Compared to the last best result of previous iterations, which is stored in fl and $err_{fl_{cycle}}$', if improvements are reached, so $err_{fl}^{+} < err_{fl_{cycle}}$', the value of fl is updated with fl^{+} and $err_{fl_{cycle}}$ is updated with err_{fl}^{+} (rows from 94 to 98). For the first iterations there is no best result of previous iterations, so the comparison of the error of the first iteration does not lead to a real improving of $err_{fl_{cycle}}$', but it is needed as starting point from which $err_{fl_{cycle}}$ is then improved. If increasing the value of fl does not lead to any improvements (row 76), then it is reduced (row 77) and fl^{-} is found. So, the new inputs for zTurbo are calculated, checked, zTurbo is run and the new error, i.e. err_{fl}^{-}, is calculated (rows from 78 to 85). If reducing fl gives improvements, so $err_{fl}^{-} < err_{fl_{cycle}}$', then the values of fl and $err_{fl_{cycle}}$ are updated with fl^{-} and err_{fl}^{-} (rows from 86 to 89). Otherwise, it means that both increasing and decreasing of fl does not produce any improvement, so the amplitude of flaring variation is reduced through n_{fl} (row 90). I found that using 0.05 as value for flaring variation gives good results in terms of convergence of the loop.

As already said, this inner loop does not go to convergence for every iteration of the outer loop, so it means that, at the end of the inner loop, $err_{fl_{cycle}}$ is bigger than err_{fl}. When this happens, it means that the flaring value fl that gives the best results is the one before entering the loop, but fl in modified by the loop. This is why there is fl_{old} (row 62): it stores the value of fl before it is modified by the loop and is used

between row 101 and 103 to assign to fl its old value in case no improvements are reached by the loop, i.e. $err_{fl_{cycle}} > err_{fl}$.

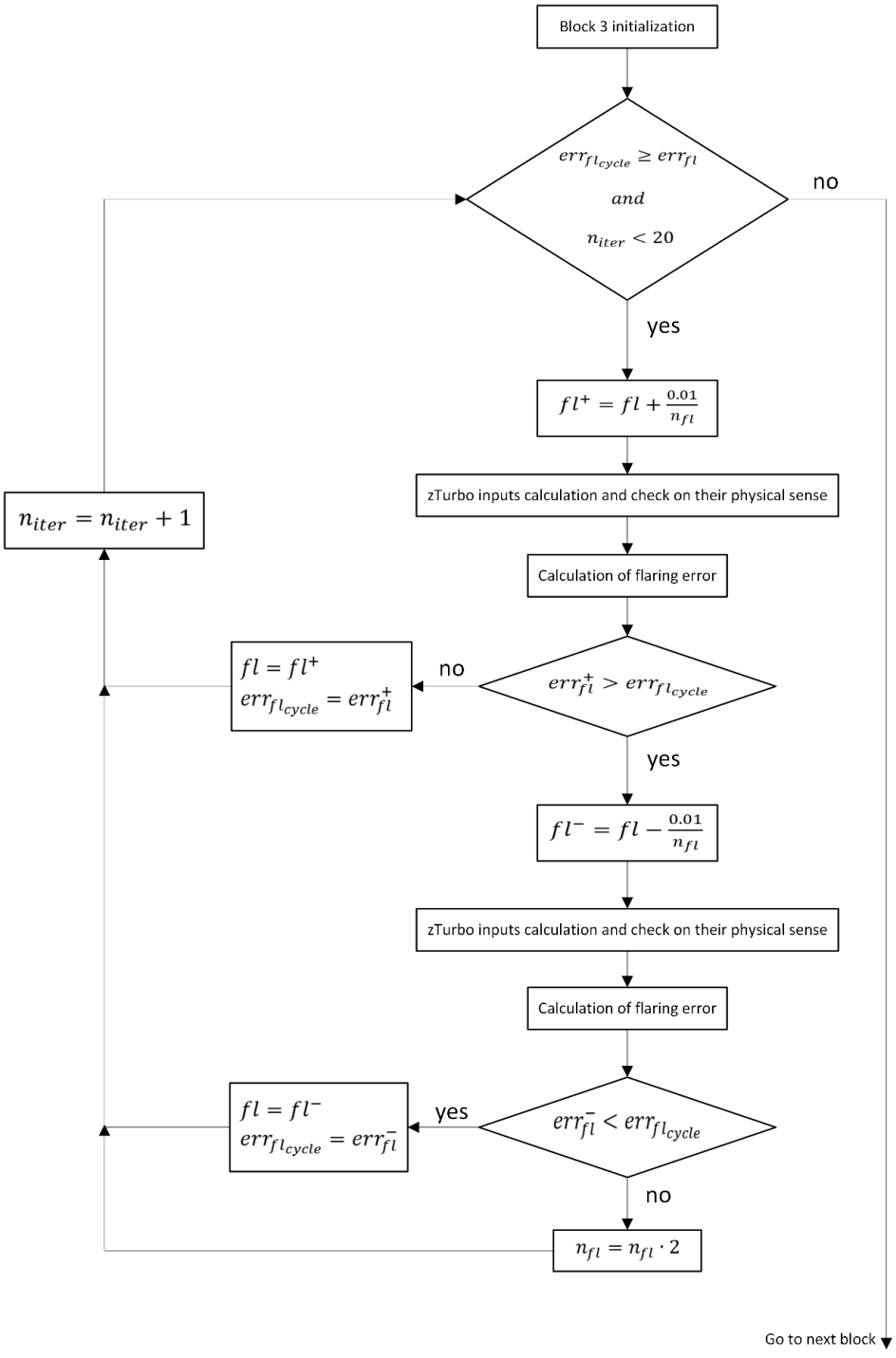

Figure 2.1.9: Block 3 flow chart

2.1.3.4 Block 4

Block 4 is used to reduce the error on the relative Mach number at the stator outlet (M_{2w}). Its functioning is exactly equal to Block 2, the only difference is that here M_{2w} is considered, and not M_1.

2.1.3.5 Block 5

In block 5 there is the reduction of the error for α_2. I found that there was no need of using an inner loop. The working logic is similar to previous blocks: α_2 is varied and then there is a check to see if the error is reduced or not. Here the error does not only consider the difference between α_{2_z} and $\alpha_{2_{ref}}$, but it also considers the effects that α_2 variation has on the Mach numbers (row 3). The flow chart of this block is reported in Figure 2.1.10.

First of all, the algorithm tries to increase α_2 (row 156), than looks if this variation gives a lower error than the one before the increasing (row 160 and 171). If the error is reduced then the new value of α_2 is stored (rows 172 and 173) and the algorithm can go to the next outer loop iteration, otherwise it tries to reduce α_2 (row 161). If the reduction works, it reduces the error, then the new value of α_2 is stored (rows 166 and 167), otherwise it means that the modulus of the variation is too high, so it is reduced through n_{α_2} (row 169) for the next outer loop iteration.

A good α_2 variation value for the convergence of the iterative algorithm is 3°.

At the end of this procedure, the errors on M_{1_z} and M_{2w_z} are calculated again because the modification of flaring will also modify the value of M_{1_z}, then, the modification of α_2 will modify M_{2w_z}. So there is the need to update the two errors for the next outer loop iteration.

This is how this algorithm works.

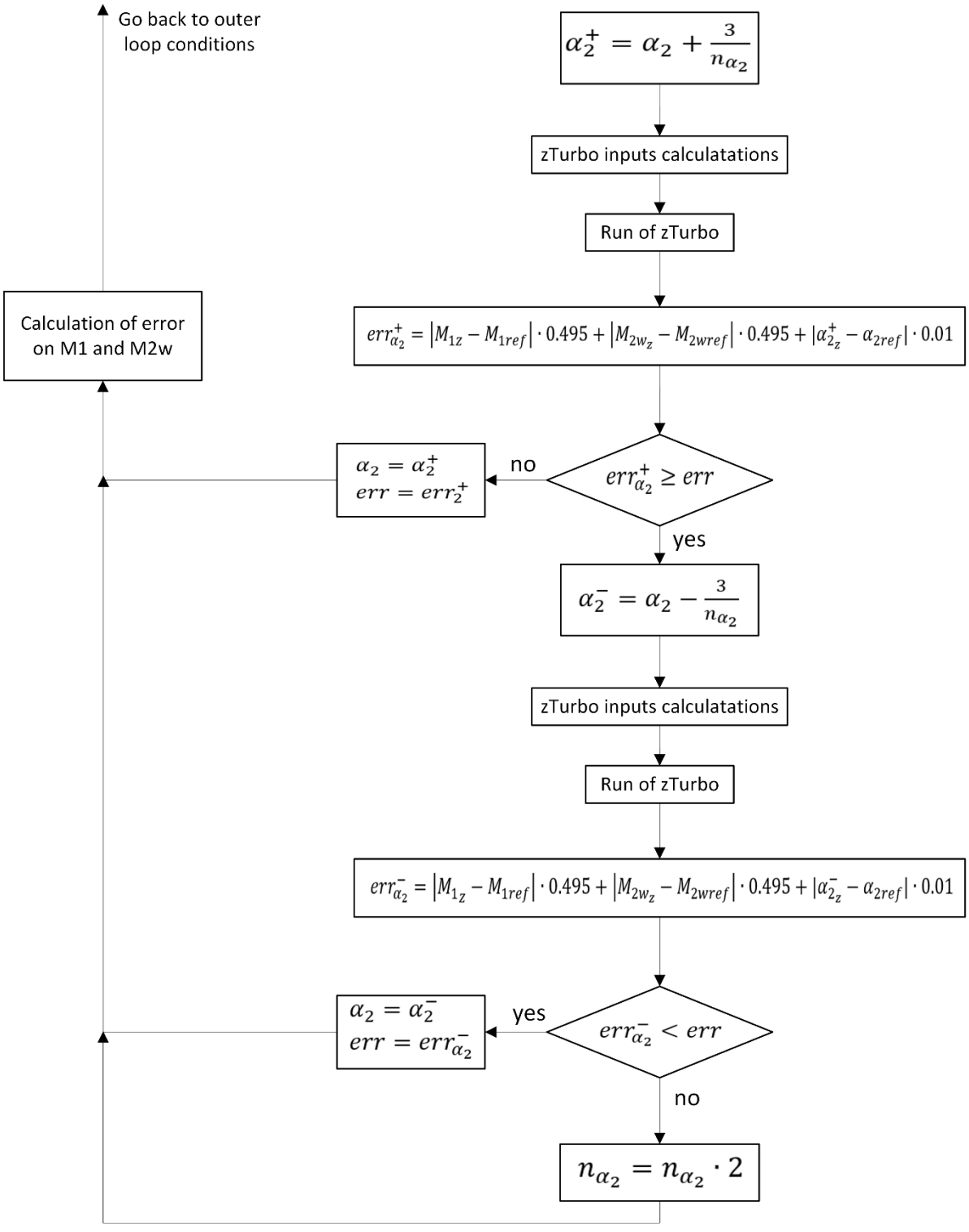

Figure 2.1.10: Block 5 flow chart

Algorithm 1 zTurbo output iterative algorithm

Calculation of zTurbo input
Run zTurbo code
$err = \left|M_{1z} - M_{1ref}\right| \cdot 0.495 + \left|M_{2w_z} - M_{2wref}\right| \cdot 0.495 + \left|\alpha_{2_z} - \alpha_{2ref}\right| \cdot 0.01$
$err_{M_1} = M_{1ref} - M_{1z}$
$err_{M_{2w}} = M_{2w_{ref}} - M_{2w_z}$
$err_{fl} = \left|fl_z - fl_{ref}\right|$
while $err > 10^{-4}$ *and* $err_{M_1} > 10^{-4}$ *and* $err_{M_{2w}} > 10^{-4}$ *and* $err_{fl} > 10^{-4}$ ***do***
    $err_{M_1}^{+} = |err_{M_1}| + 1$
    $err_{M_1 old} = err_{M_1}^{+}$
    $\Delta M_1 = 0.3 \cdot err_{M_1}$
    $\Delta M_{1_{old}} = \Delta M_1$
    $n_{M_1} = 1$
    $n_{M_{1_{old}}} = 1$
    while $|err_{M_1}^{+}| > |err_{M_1}|$ *and* $|err_{M_1}| > 10^{-4}$ ***do***
        $M_1^{+} = M_1 + \frac{\Delta M_1}{n_{M_1}}$
        Calculation of zTurbo input using M_1^{+}
        if *new input values are* <u>*not*</u> *physical* ***then***
            $n_{M_1} = n_{M_1} \cdot 2$
            $\Delta_{M_{1_{old}}} = \frac{\Delta M_1}{n_{M_1}}$
        else
            Run zTurbo code
            $err_{M_1}^{+} = M_{1ref} - M_{1z}$
            $\Delta M_1 = \frac{\Delta M_1}{n_{M_1}}$
            $n_{M_1} = 1$
            if $|err_{M_1}^{+}| < |err_{M_1}|$ ***then***
                $M_1 = M_1^{+}$
                $err_{M_1} = err_{M_1}^{+}$
            else
                if $|err_{M_1}^{+}| < |err_{M_{1_{old}}}|$ *and* $|\Delta M_{1_{old}}| < |\Delta M_1|$ ***then***
                    $\Delta M_{1_{old}} = \Delta M_1$

$\Delta M_1 = \Delta M_1 \cdot 1.05$
$err_{M_{1\,old}} = err^{+}_{M_1}$
$contr_{M_1} = 0$
end if
if $|err^{+}_{M_1}| < err_{M_{1\,old}}$ *and* $|\Delta M_{1\,old}| \geq |\Delta M_1|$ ***then***
$\Delta M_{1\,old} = \Delta M_1$
$\Delta M_1 = \Delta M_1 \cdot 0.95$
$err_{M_{1\,old}} = err^{+}_{M_1}$
$contr_{M_1} = 0$
end if
if $|err^{+}_{M_1}| > |err_{M_{1\,old}}|$ *and* $|\Delta M_{1\,old}| < |\Delta M_1|$ ***then***
$contr_{M_1} = contr_{M_1} + 1$
if $contr_{M_1} = 2$ ***then***
$n_{M_{1\,old}} = n_{M_{1\,old}} \cdot 2$
$contr_{M_1} = 0$
end if
$\Delta M_1 = \Delta M_{1\,old} \cdot \left(1 - \frac{0.05}{n_{M_{1\,old}}}\right)$
end if
if $|err^{+}_{M_1}| > |err_{M_{1\,old}}|$ *and* $|\Delta M_{1\,old}| \geq |\Delta M_1|$ ***then***
$contr_{M_1} = contr_{M_1} + 1$
if $contr_{M_1} = 2$ ***then***
$n_{M_{1\,old}} = n_{M_{1\,old}} \cdot 2$
$contr_{M_1} = 0$
end if
$\Delta M_1 = \Delta M_{1\,old} \cdot \left(1 + \frac{0.05}{n_{M_{1\,old}}}\right)$
end if
end if
end if
end while

$fl_z = \frac{b_1}{b_0}$
$n_{fl} = 1$
$fl_{old} = fl$
$err_{fl} = |fl_z - fl_{ref}|$
$err_{fl_{cycle}} = err_{fl} + 1$
$n_{iter} = 0$

66: ***while*** $err_{fl_{cycle}} \geq err_{fl}$ *and* $n_{iter} < 20$ ***then***
67: $fl^{+} = fl + \frac{0.01}{n_{fl}}$
68: *Calculation of zTurbo input using* fl^{+}
69: ***if*** *new input values are* <u>*not*</u> *physical* ***then***
70: $n_{fl} = n_{fl} \cdot 2$
71: $n_{iter} = n_{iter} + 1$
72: ***else***
73: *Run zTurbo code*
74: $fl_z = \frac{b_1}{b_0}$
75: $err_{fl}^{+} = |fl_z - fl_{ref}|$
76: ***if*** $err_{fl}^{+} > err_{fl_{cycle}}$ ***then***
77: $fl^{-} = fl - \frac{0.01}{n_{fl}}$
78: *Calculation of zTurbo input using* fl^{-}
79: ***if*** *new input values are* <u>*not*</u> *physical* ***then***
80: $n_{fl} = n_{fl} \cdot 2$
81: $n_{iter} = n_{iter} + 1$
82: ***else***
83: *Run zTurbo code*
84: $fl_z = \frac{b_1}{b_0}$
85: $err_{fl}^{-} = |fl_z - fl_{ref}|$
86: ***if*** $err_{fl}^{-} < err_{fl_{cycle}}$ ***then***
87: $fl = fl^{-}$
88: $err_{fl_{cycle}} = err_{fl}^{-}$
89: ***else***
90: $n_{fl} = n_{fl} \cdot 2$
91: ***end if***
92: $n_{iter} = n_{iter} + 1$
93: ***end if***
94: ***else***
95: $fl = fl^{+}$
96: $err_{fl_{cycle}} = err_{fl}^{+}$
97: $n_{iter} = n_{iter} + 1$
98: ***end if***
99: ***end if***
100: ***end while***
101: ***if*** $err_{fl_{cycle}} > err_{fl}$ ***then***

$fl = fl_{old}$

end if

$err^{+}_{M_{2w}} = |err_{M_{2w}}| + 1$

$err_{M_{2w}old} = err^{+}_{M_{2w}}$

$\Delta M_{2w} = 0.3 \cdot err_{M_{2w}}$

$\Delta M_{2w_{old}} = \Delta M_{2w}$

$n_{M_{2w}} = 1$

$n_{M_{2w}old} = 1$

while $|err^{+}_{M_{2w}}| > |err_{M_{2w}}|$ *and* $|err_{M_{2w}}| > 10^{-4}$ ***do***

$M^{+}_{2w} = M_{2w} + \frac{\Delta M_{2w}}{n_{M_{2w}}}$

Calculation of zTurbo input using M^{+}_{2w}

if *new input values are <u>not</u> physical* ***then***

$n_{M_{2w}} = n_{M_{2w}} \cdot 2$

$\Delta M_{2w_{old}} = \frac{\Delta M_{2w}}{n_{M_{2w}}}$

else

Run zTurbo code

$err^{+}_{M_{2w}} = M_{2w_{ref}} - M_{2w_z}$

$\Delta M_{2w} = \frac{\Delta M_{2w}}{n_{M_{2w}}}$

$n_{M_{2w}} = 1$

if $|err^{+}_{M_{2w}}| < |err_{M_{2w}}|$ ***then***

$M_{2w} = M^{+}_{2w}$

$err_{M_{2w}} = err^{+}_{M_{2w}}$

else

if $|err^{+}_{M_{2w}}| < \left|err_{M_{2w}old}\right|$ *and* $|\Delta M_{2w_{old}}| < |\Delta M_{2w}|$ ***then***

$\Delta M_{2w_{old}} = \Delta M_{2w}$

$\Delta M_{2w} = \Delta M_{2w} \cdot 1.05$

$err_{M_{2w}old} = err^{+}_{M_{2w}}$

$contr_{M_{2w}} = 0$

end if

if $|err^{+}_{M_{2w}}| < |err_{M_{2w}}|$ *and* $\left|\Delta M_{2w_{old}}\right| \geq |\Delta M_{2w}|$ ***then***

$\Delta M_{2w_{old}} = \Delta M_{2w}$

$\Delta M_{2w} = \Delta M_{2w} \cdot 0.95$

$err_{M_{2w}old} = err^{+}_{M_{2w}}$

$contr_{M_{2w}} = 0$

end if

137: *if* $|err^{+}_{M_{2w}}| > |err_{M_{2w}old}|$ *and* $|\Delta M_{2w_{old}}| < |\Delta M_{2w}|$ ***then***
138: $contr_{M_{2w}} = contr_{M_{2w}} + 1$
139: *if* $contr_{M_{2w}} = 2$ ***then***
140: $n_{M_{2w}old} = n_{M_{2w}old} \cdot 2$
141: $contr_{M_{2w}} = 1$
142: ***end if***
143: $\Delta M_{2w} = \Delta M_{2w_{old}} \cdot \left(1 - \frac{0.05}{n_{M_{2w}old}}\right)$
144: ***end if***
145: *if* $|err^{+}_{M_{2w}}| > |err_{M_{2w}old}|$ *and* $|\Delta M_{2w_{old}}| \geq |\Delta M_{2w}|$ ***then***
146: $contr_{M_{2w}} = contr_{M_{2w}} + 1$
147: *if* $contr_{M_{2w}} = 2$ ***then***
148: $n_{M_{2w}old} = n_{M_{2w}old} \cdot 2$
149: $contr_{M_{2w}} = 1$
150: ***end if***
151: $\Delta M_{2w} = \Delta M_{2w_{old}} \cdot \left(1 + \frac{0.05}{n_{M_{2w}old}}\right)$
152: ***end if***
153: ***end if***
154: ***end if***
155: ***end while***

156: $\alpha_2^+ = \alpha_2 + \frac{3}{n_{\alpha_2}}$
157: *Calculation of zTurbo input using* α_2^+
158: *Run zTurbo code*
159: $err^{+}_{\alpha_2} = |M_{1z} - M_{1ref}| \cdot 0.495 + |M_{2w_z} - M_{2wref}| \cdot 0.495 + |\alpha^{+}_{2_z} - \alpha_{2ref}| \cdot 0.01$
160: *if* $err^{+}_{\alpha_2} \geq err$ ***then***
161: $\alpha_2^- = \alpha_2 - \frac{3}{n_{\alpha_2}}$
162: *Calculation co zTurbo input using* α_2^-
163: *Run zTurbo code*
164: $err^{-}_{\alpha_2} = |M_{1_z} - M_{1ref}| \cdot 0.495 + |M_{2w_z} - M_{2wref}| \cdot 0.495 + |\alpha^{-}_{2_z} - \alpha_{2ref}| \cdot 0.01$
165: *if* $err^{-}_{\alpha_2} < err$ ***then***
166: $\alpha_2 = \alpha_2^-$
167: $err = err^{-}_{\alpha_2}$
168: ***else***
169: $n_{\alpha_2} = n_{\alpha_2} \cdot 2$
170: ***end if***

171: ***else***
172: $\alpha_2 = \alpha_2^+$
173: $err = err_2^+$
174: ***end if***
175: $err_{M_1} = M_{1_z} - M_{1ref}$
176: $err_{M_{2w}} = M_{2w_z} - M_{2w_{ref}}$
177: ***end while***

2.1.3.6 Algorithm variant

For all the loops I set a condition to limit the number of iterations, namely 20 iterations for each loop. This because not always the algorithm converged. This algorithm converges if both profile and secondary losses are considered, but if only profile losses are considered this algorithm does not work. So, I changed the instructions in blocks 2 and 3. I changed only them because M_{1_z} and fl_z were the only parameters that gave problems.

In practice I put block 3 into block 2. This modification is reported in Algorithm 2 at row 9, and in Figure 2.1.11. In this way, after M_1 modification, the inner loop of flaring is run with also the new value of Mach M_1^+ (Figure 2.1.12). This allows to have fl_z closed to fl_{ref} coherently with M_1^+, so that, at the end of the loop on M_1, both fl and M_1 gives the right fl_z and M_{1_z}. In this way, flaring value is not modified after the loop on M_1 (i.e. block 2) causing a modification on M_{1_z} that can be recovered only in the following outer loop iteration. With this modification fl and M_1 are contemporarily modified, so that there is no need to recover some changings in M_{1_z} caused by flaring modification out of M_1 loop.

This logic works only with profile losses.

The reason for which I used these two algorithms and not only the one that works with both profile and secondary losses is to be able to compare the effects of profile losses with 2D CFD calculations and then compare the effects of profile and secondary losses with 3D CFD calculations. This because we have modified Traupel correlations, so we want to see how good these modifications are for both profile and secondary losses.

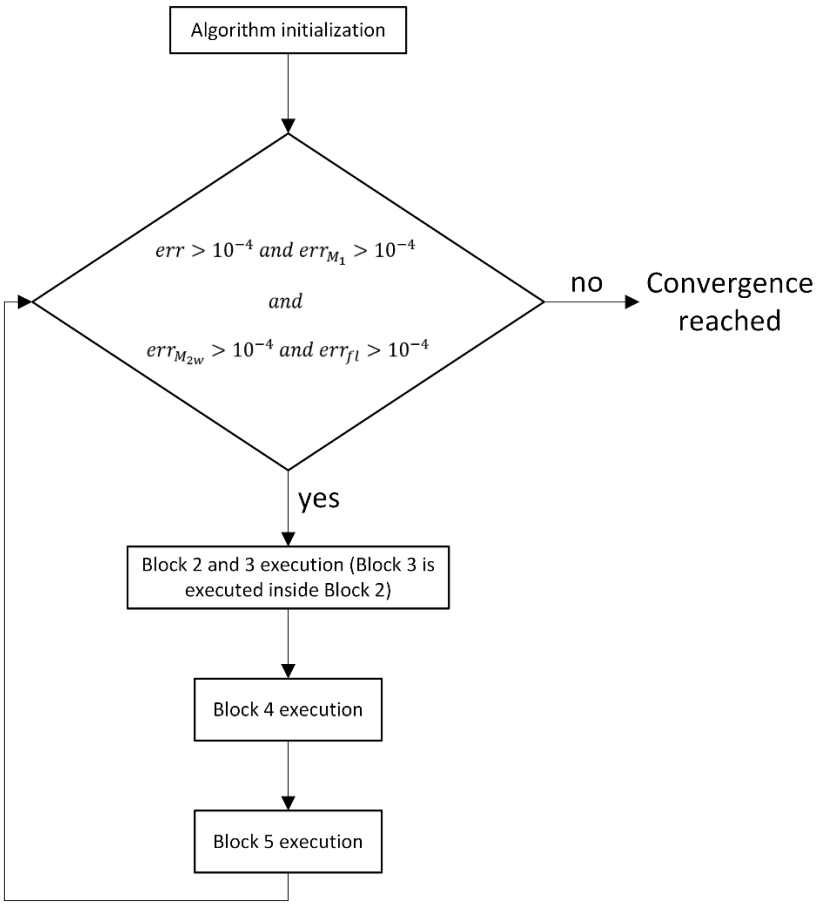

Figure 2.1.11: Iterative algorithm variant flow chart

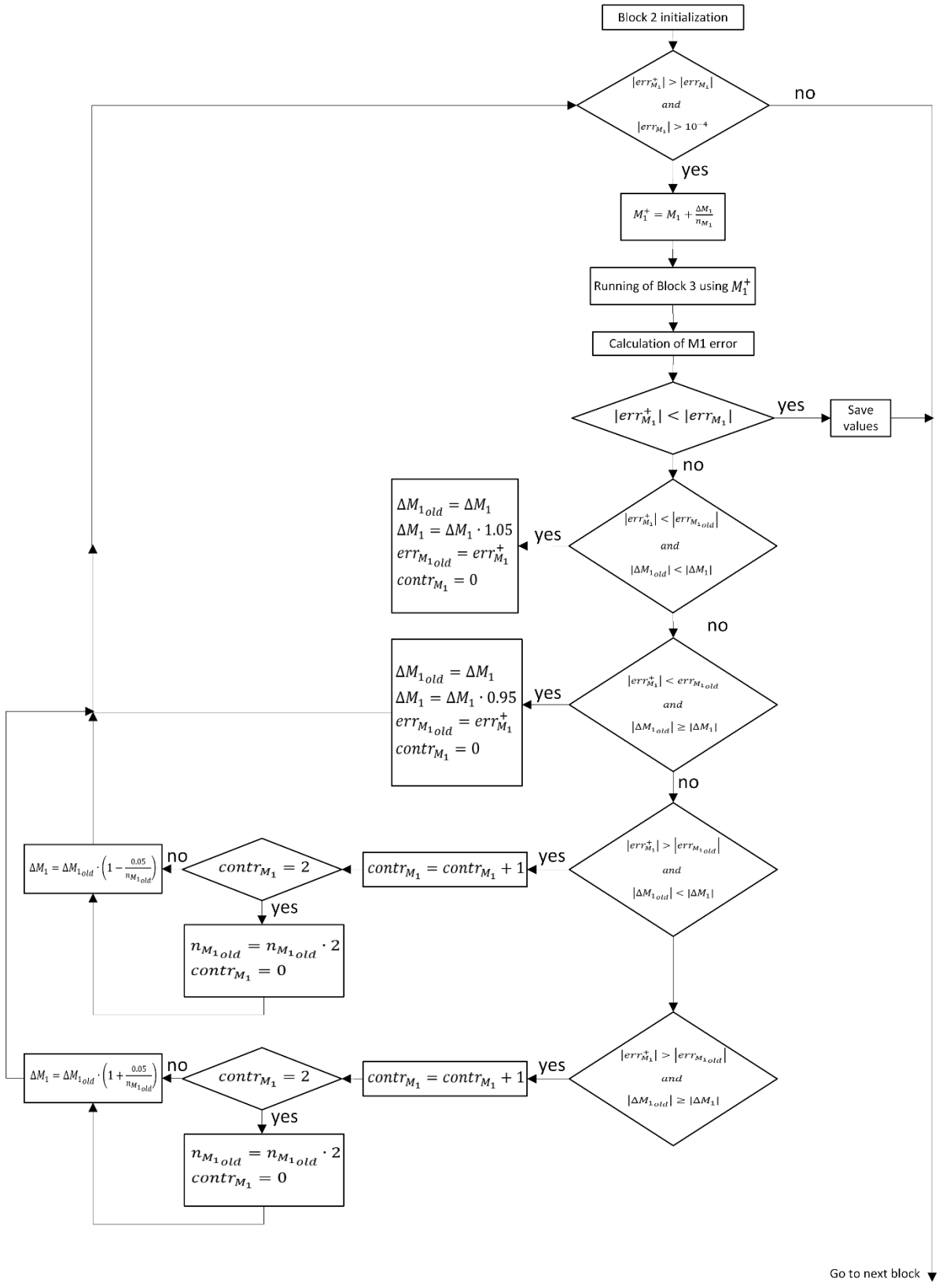

Figure 2.1.12: Block 2 variant flow chart

Algorithm 2 zTurbo output iterative algorithm variant of blocks 2 and 3

$err_{M_1}^{+} = |err_{M_1}| + 1$

$err_{M_1 old} = err_{M_1}^{+}$

$\Delta M_1 = 0.3 \cdot err_{M_1}$

$\Delta M_{1_{old}} = \Delta M_1$

$n_{M_1} = 1$

$n_{M_{1_{old}}} = 1$

while $|err_{M_1}^{+}| > |err_{M_1}|$ *and* $|err_{M_1}| > 10^{-4}$ ***do***

  $M_1^{+} = M_1 + \frac{\Delta M_1}{n_{M_1}}$

  Running of block 3 to find the right flaring with the Mach value M_1^{+}

  $err_{M_1}^{+} = M_{1ref} - M_{1z}$

  $\Delta M_1 = \frac{\Delta M_1}{n_{M_1}}$

  $n_{M_1} = 1$

  if $|err_{M_1}^{+}| < |err_{M_1}|$ ***then***

    $M_1 = M_1^{+}$

    $err_{M_1} = err_{M_1}^{+}$

  else

    if $|err_{M_1}^{+}| < |err_{M_{1_{old}}}|$ *and* $|\Delta M_{1_{old}}| < |\Delta M_1|$ ***then***

      $\Delta M_{1_{old}} = \Delta M_1$

      $\Delta M_1 = \Delta M_1 \cdot 1.05$

      $err_{M_{1_{old}}} = err_{M_1}^{+}$

      $contr_{M_1} = 0$

    end if

    if $|err_{M_1}^{+}| < err_{M_{1_{old}}}$ *and* $|\Delta M_{1_{old}}| \geq |\Delta M_1|$ ***then***

      $\Delta M_{1_{old}} = \Delta M_1$

      $\Delta M_1 = \Delta M_1 \cdot 0.95$

      $err_{M_{1_{old}}} = err_{M_1}^{+}$

      $contr_{M_1} = 0$

    end if

    if $|err_{M_1}^{+}| > |err_{M_{1_{old}}}|$ *and* $|\Delta M_{1_{old}}| < |\Delta M_1|$ ***then***

      $contr_{M_1} = contr_{M_1} + 1$

      if $contr_{M_1} = 2$ ***then***

        $n_{M_{1_{old}}} = n_{M_{1_{old}}} \cdot 2$

33: $contr_{M_1} = 1$

34: ***end if***

35: $\Delta M_1 = \Delta M_{1_{old}} \cdot \left(1 - \frac{0.05}{n_{M_{1_{old}}}}\right)$

36: ***end if***

37: ***if*** $|err_{M_1}^{+}| > |err_{M_{1_{old}}}|$ *and* $\left|\Delta M_{1_{old}}\right| \geq |\Delta M_1|$ ***then***

38: $contr_{M_1} = contr_{M_1} + 1$

39: ***if*** $contr_{M_1} = 2$ ***then***

40: $n_{M_{1_{old}}} = n_{M_{1_{old}}} \cdot 2$

41: $contr_{M_1} = 1$

42: ***end if***

43: $\Delta M_1 = \Delta M_{1_{old}} \cdot \left(1 + \frac{0.05}{n_{M_{1_{old}}}}\right)$

44: ***end if***

45: ***end if***

46: ***end while***

2.2 Computational Fluid Dynamics Analysis

Modern calculators allow to deal successfully with a lot of problems related to turbomachinery thanks to the implementation of numerical procedures to solve the equations that govern the problem physics. The case studied in this thesis is a thermo-fluid dynamic problem, so the equations that describe the physics are the Navier-Stokes equations and the set of numerical procedures to solve them is called Computational Fluid Dynamics, i.e. CFD. Calculators allow to simulate the flow-field evolution in time scale of industrial interest in an acceptable amount of time, although with frequency still too low with respect to the turbulence one. Despite the relevant progress in CFD, it is always necessary to reduce the model complexity acting on geometrical features and on thermo-fluid dynamic assumptions. This is particularly true since recursive calculations have to be implemented for design optimization of the machine. Some considerations need to be exposed before reporting the governing equations solved by means CFD techniques:

- Navier-Stokes equations for compressible fluids include mass conservation (Equation 3.1b), momentum conservation (Equation 3.1c) and energy conservation (Equation 3.1a) equations along with two equations of state, inherent the fluid nature itself. So, they are three non-linear partial differential equations and two algebraic equations (sometimes the equation of state is substituted with tabular relation to deal with real gas models).
- Differential equations include diffusive terms, linked to disturbances propagation without mass transportation (second derivatives in the equations), and convective term, associated to system transport properties (first derivatives in equations).
- Governing equations include stress terms, that are expressed in function of the strain rate.
- The equations are generically time-variant, but the turbulent effects, essentially statistical and characterized by frequencies much larger than those of industrial interest, are often introduced through turbulent viscosity and appropriate models.

Depending on the hypotheses and simplifications, it is possible to face different form of these equations. The mathematical model is based on the formulation of conservation laws, i.e. the variation of the total amount of a quantity inside a given domain is equal to the balance between the amount of that quantity entering and leaving the considered domain, plus the contribution from eventual sources generating that quantity. It is possible to adopt different modelling strategies for the fluid flow. Below, for example, are reported the tout-court Navier-Stokes partial differential system of equations (Equation 3.1) for Calorically Perfect (Equation 3.1e)

Ideal Gas (Equation 3.1f), in differential and conservative form. Moreover, the gas is modelled as a Newtonian fluid, which means that the stress tensor (not explicitly visible here) is isotropic, linear in strain rates and it is divergence zero for fluid at rest.

$$\frac{\partial}{\partial t}(\rho e_{tot}) + \nabla \cdot \left(\rho \boldsymbol{u} h_{tot} + \boldsymbol{q} + \frac{2}{3}\mu(\nabla \cdot \boldsymbol{u})\boldsymbol{u} - \mu(\nabla \boldsymbol{u} + \nabla \boldsymbol{u}^T) \cdot \boldsymbol{u}\right) = \rho \boldsymbol{g} \cdot \boldsymbol{u} \quad \text{Equation 3.1a}$$

$$\frac{\partial \rho}{\partial t} + \nabla \cdot (\rho \boldsymbol{u}) = 0 \quad \text{Equation 3.1b}$$

$$\frac{\partial}{\partial t}(\rho \boldsymbol{u}) + \nabla \cdot (\rho \boldsymbol{u} \times \boldsymbol{u}) = -\nabla p + \nabla \cdot \left\{\mu \left(\nabla \boldsymbol{u} + \nabla \boldsymbol{u}^T - \frac{2}{3}(\nabla \cdot \boldsymbol{u})\boldsymbol{I}\right)\right\} + \rho \boldsymbol{g} \quad \text{Equation 3.1c}$$

$$\boldsymbol{q} = -\lambda \nabla T \quad \text{Equation 3.1d}$$

$$h_{tot} = c_p T + \frac{\|\boldsymbol{u}\|^2}{2} = e_{tot} + \frac{p}{\rho} \quad \text{Equation 3.1e}$$

$$p = \rho R_{uni} T / n \quad \text{Equation 3.1f}$$

With p [Pa] static pressure; $\rho[\frac{kg}{m^3}]$ density; $\boldsymbol{u}$ $[\frac{m}{s}]$ velocity vector; $\boldsymbol{g}$ $[\frac{m}{s^2}]$ gravitational acceleration vector; T [K] static temperature; h_{tot} $[\frac{J}{gk}]$ total enthalpy; e_{tot} $[\frac{J}{kg}]$ total internal energy; $\boldsymbol{q}$ $[\frac{J}{s \cdot m^2}]$ heat flux density, c_p $[\frac{J}{kg \cdot K}]$ constant pressure specific heat capacity; n $[\frac{kg}{mol}]$ molar mass of gas mixture; R_{uni} $[\frac{J}{K \cdot mol}]$ universal gas constant; μ $[Pa \cdot s]$ dynamic viscosity; λ $[\frac{J}{s \cdot m \cdot K}]$ fluid thermal conductivity.

Due to the strong non-linearity and the compressibility of the flow, an analytical solution of these equations can be found in a small number of simple cases. This is why numerical models are needed: to solve them in all the other cases.

The direct numerical solution of Navier-Stokes equations requires a very high computational cost. Turbulence is the principal cause that increase computational time, so different ways to model it were found. Some modelling strategies are more accurate but will require higher computational time to be solved. For turbomachinery, the development of Boundary Layer (B.L.) is of main importance, so the turbulence model used for this thesis is the $k\omega - sst$, because it describes very well the boundary layer behaviour on blade and endwalls.

For the sake of completeness, it must be noted that μ, λ and c_p are function of temperature and pressure (or other two thermodynamic intensive properties). To model them it was decided to use the NASA format for c_p and Sutherland model for μ and λ. These models are more accurate than considering these quantities as constant but depends only on temperature and not on pressure. This fact allows to

have a good approximation of gas behaviour with simple polynomial relations. In Appendix E gas model is reported.

2.2.1 Model setup

The software used to numerically solve the Navier-Stokes equations is Ansys CFX. Two kinds of simulations were performed: the simulation of stator alone and the simulation of stator and rotor together. This to firstly study the stator characteristics and then perform the study on the rotor looking also at the interaction with stator, which are not negligible since the relative flow at rotor inlet is subsonic.

2.2.1.1 Domain

The domain in which calculations are performed is one blade channel both for stator and rotor. This choice was done to reduce the physical volume to be modelled compared to the whole turbine stage, allowing to reduce computational time for running different simulations.

Both 2D and 3D simulations were performed. About 2D simulations, Ansys CFX is not able to run them directly because it is able to manage only 3D domains. To bypass this problem and perform 2D simulations with a 3D domain, it is possible to take a very thin slice of the blade channel along span, like extracting a streamtube (Figure 2.2.1 a) and use only two layers of cells along blade height (Figure 2.2.1 b). In this way the 3D effects cannot be seen.

The streamtube extracted is taken considering its mean radius as constant in order to reduce the possible numerical problems that can arise during the simulation of stator and rotor together, but, as can be seen from Figure 2.2.1, it considers the divergence of the channel, indeed the area ratio between the outlet and inlet section of the streamtube is equal to the area ratio of the real channel. So the inlet height of the streamtube chosen is of 4 mm, and its development depends on the area ratio between inlet and outlet.

For stator alone simulations, the domain continues for an axial length which is the double of stator axial chord downstream of the trailing edge, in order to look at the development of the flow (Figure 2.2.2).

For stator-rotor simulations, the mixing plane is placed at a distance of $\frac{1}{5}$ of stator axial chord from both stator and rotor. The outlet is placed downstream of rotor trailing edge, at a distance of one rotor axial chord (Figure 2.2.3). In this case it cannot

be the double of axial chord because the maximum number of cells or nodes allowed in the student version of the software (512000 cells/nodes) was not enough to represent well the domain. In both cases (stator alone and stator-rotor) the domain inlet is placed at one axial chord upstream from stator leading edge to consider uniform inlet conditions. It is an assumption to start this design phase and look at how the stage behaves with the high inlet Mach number, because we already saw that the flow coming from a rotating detonation combustor is highly non uniform, but we prefer to focus the work on the high Mach number problem.

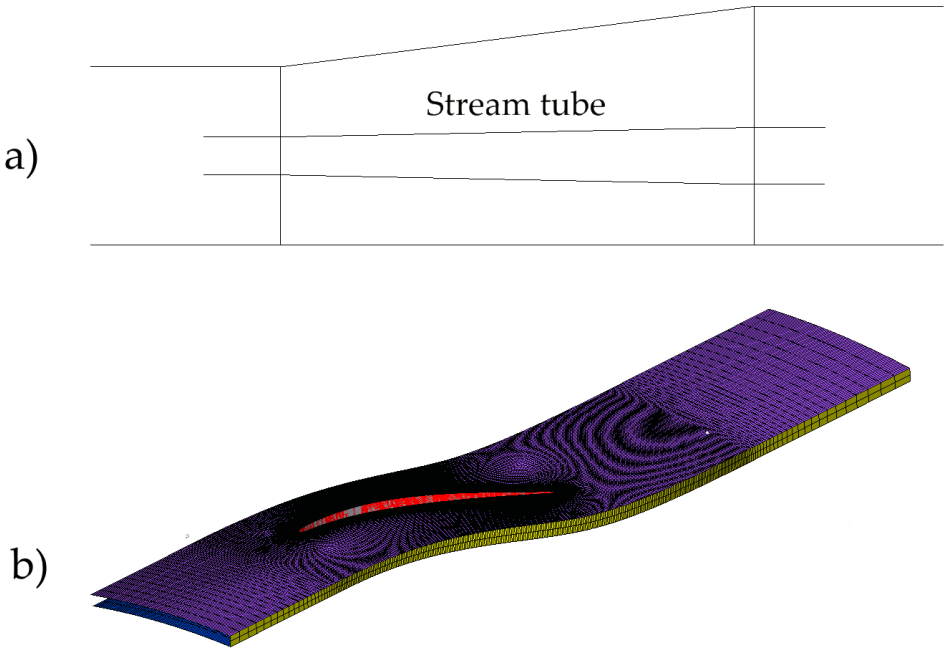

Figure 2.2.1: a) representation of the streamtube extracted for 2D simulations b) example of mesh for 2D simulations

2.2.1.2 Boundary Conditions

Boundary conditions for the 2D simulations are:

- Inlet: total pressure of 15 bar, total temperature of 1500° C and axial velocity
- Hub: free slip wall
- Shroud: free slip wall
- Blade: no slip wall
- Channel sides: periodic boundary conditions
- Outlet: static pressure
- Stator-rotor interface: stage mixing plane

For the simulations of stator alone and stator-rotor the Inlet, Hub, Shroud, Blade and Channel sides boundary conditions are the same. For the 2D stator simulations the Outlet was set with a static pressure of 8.1 bar, which is the result coming out from zTurbo considering only profile losses since the simulations are 2D, so does not consider secondary losses. Also with the 3D stator simulation the pressure will be 8.1 bar because it will be shown that the secondary losses of zTurbo are overestimated.

For stator-rotor simulations, the interface between the two domain is the stage mixing plane and the *Downstream Velocity Constraint* must be set to *Stage Average Velocty* for chocked cases unless simulations will not work correctly using Ansys CFX. The static pressure at rotor outlet was set to 6.2 bar for both 2D and 3D simulations, for the same reasons of stator simulations. Rotor domain is placed in the rotating frame of reference.

As outlet condition, there is also the possibility to set the mass flow rate, but in this case this setting cannot be used because the stage is chocked. This means that the mass flow rate depends on losses and on the geometry, so it cannot be imposed unless convergence of the numerical procedure cannot be reached. So, the only boundary condition that can be placed at outlet is the static pressure. Of course, total pressure cannot be used at outlet either, imposing it means to impose stage losses, but they are an output we want to find.

In figure Figure 2.2.2 and Figure 2.2.3 it is shown the places of the different boundary conditions for the 2D simulations.

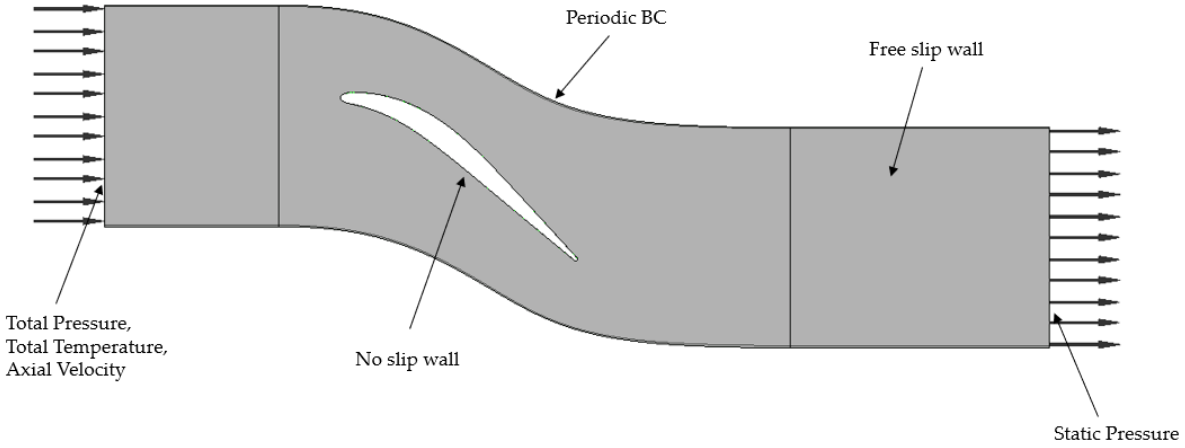

Figure 2.2.2: Stator domain and boundary conditions

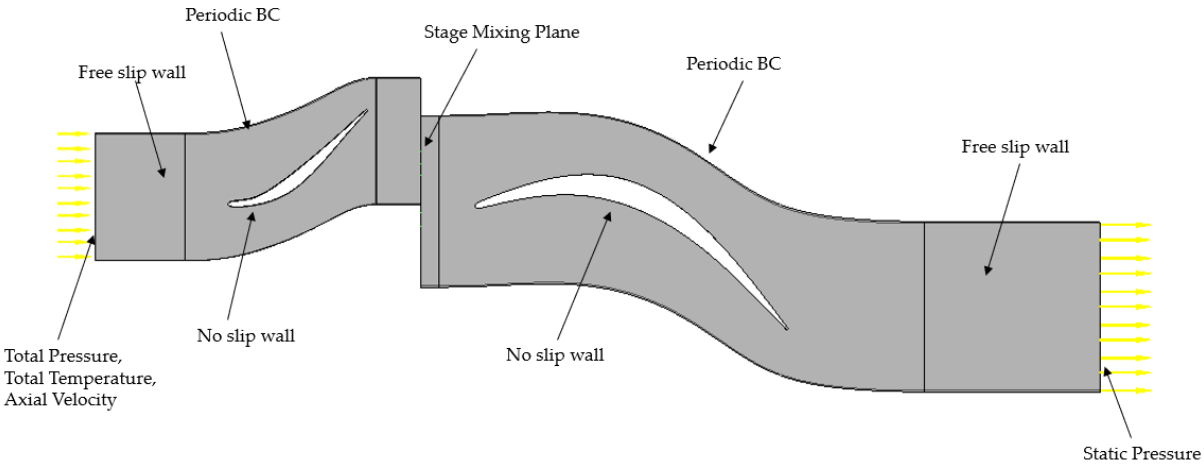

Figure 2.2.3: Stator-Rotor domain and boundary conditions

For the 3D simulations, the Hub and Shroud walls will be *no slip wall* because in this case their effect must be considered. Moreover the presence of the tip gap is neglected to focus more on the profile and secondary losses than on the interaction between rotor and casing

2.2.1.3 Simulation Convergence

There are different quantities to check if the simulation has reached the convergence:

- Equations residuals
- Efficiency behaviour during the solution process
- Mass flow imbalance
- y^+ at walls with *no slip wall* boundary conditions

Equations residuals are the residuals of the numerical solution of the Navier-Stokes equations. For this case I set their maximum values at $5 \cdot 10^{-7}$, which means that residuals must be lower than this value to satisfy convergence.

About efficiency, to satisfy convergence its behavior in function of the number of iteration of the numerical procedure must be flat during the final iterations, like shown in Figure 2.2.4.

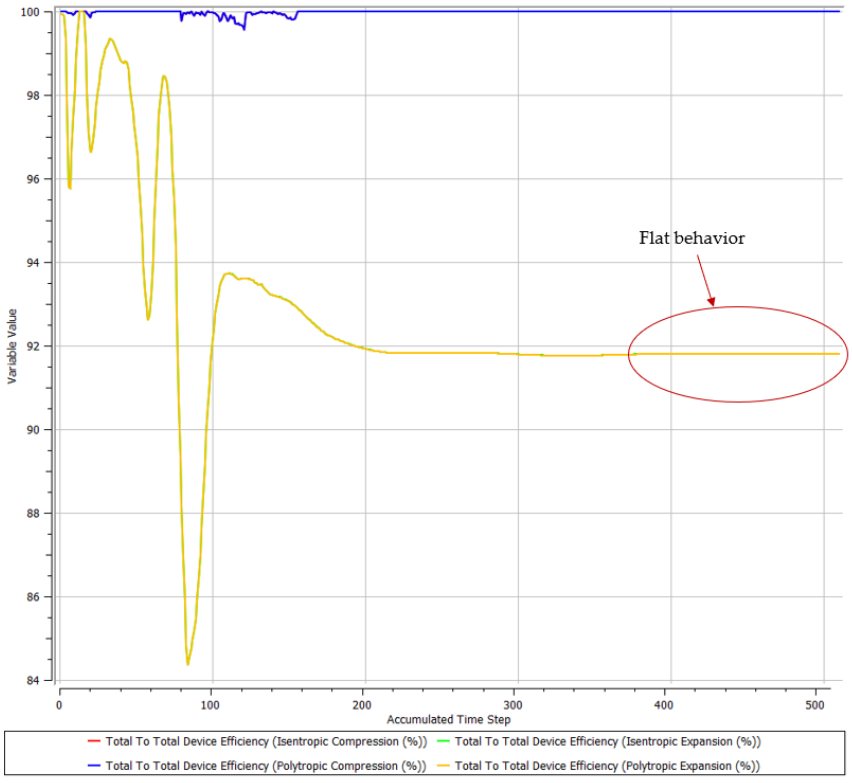

Figure 2.2.4: Efficiency behavior to reach convergence

Instead, the mass flow imbalance between inlet and outlet of the domain must be lower than 10^{-5} to satisfy the convergence, unless the variation of mass between inlet and outlet will be too high to consider the results as good.

About y^+, its value depends on the turbulence model adopted. In this case we are using the $k\omega - sst$, so it models the turbulence also in the boundary layer. This means that the y^+ must be lower that 1 where boundary layer exists, i.e. in correspondence of *no slip walls*. This because it means that the first layer of the mesh attached to the wall is thinner than the boundary layer, meaning that the mesh is able to capture boundary layer behaviour. In Figure 2.2.5 the plot of y^+ value along blade walls is reported. Having some points that are slightly higher than 1 in correspondence of leading edge and trailing edge is normal. They are due to stagnation points and do not create problems.

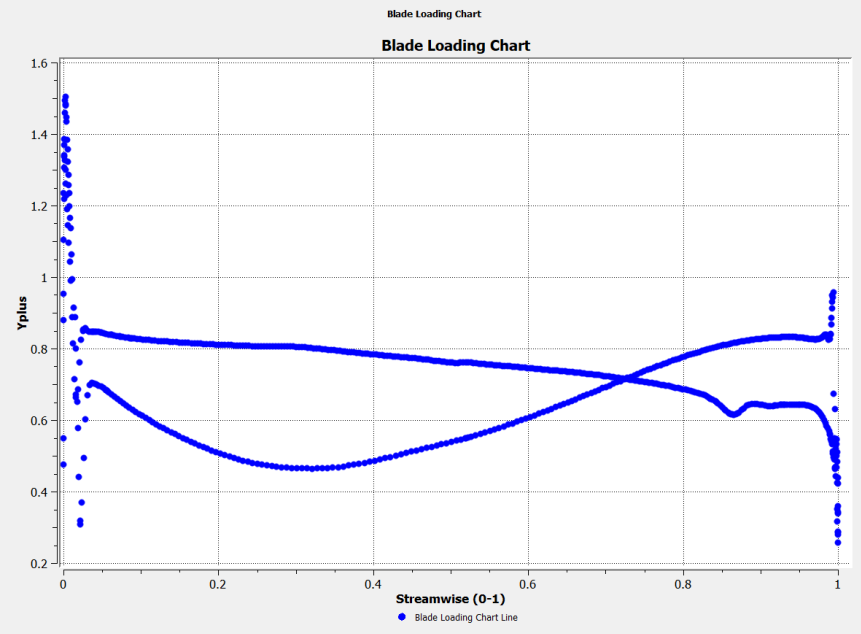

Figure 2.2.5: Example of y^+ along blade walls

2.2.1.4 Mesh Independence Analysis

In a CFD analysis there is always the need to perform the mesh independence analysis. It consists in generating 3 different meshes for the same domain and compare the results obtained using them. When the difference between the results is

very low, it means that results do not depend on mesh anymore, so the mesh cannot change the results.

The procedure that I followed to determine the level of independence can be found in [25] and is briefly explained.

First of all, there is the need to define a representative mesh size:

$$h = \left[\frac{1}{N} \cdot \sum_{i=1}^{N} \Delta V_i\right]^{\frac{1}{3}} \qquad \text{Equation 2.2.1}$$

Where ΔV_i is the volume of the i^{th} cell and N the total number of cells used for the mesh. It is important that the ratio between two different mesh sizes is greater than 1.3, namely $\frac{h_{coarse}}{h_{fine}} \geq 1.3$, in order to get significant values for mesh analysis.

Then, let consider the three different meshes with size $h_1 < h_2 < h_3$ and define the ratios $r_{21} = \frac{h_2}{h_1}$ and $r_{32} = \frac{h_3}{h_2}$. Now it is possible to calculate the apparent order p of the independence analysis method through Equation 2.2.2:

$$p = \frac{1}{\ln(r_{21})} \cdot \left|\ln\left(\left|\frac{\varepsilon_{32}}{\varepsilon_{21}}\right|\right) + q(p)\right| \qquad \text{Equation 2.2.2a}$$

$$q(p) = ln\left(\frac{r_{21}^{p} - s}{r_{32}^{p} - s}\right) \qquad \text{Equation 2.2.2b}$$

$$s = 1 \cdot sing\left(\frac{\varepsilon_{32}}{\varepsilon_{21}}\right) \qquad \text{Equation 2.2.2c}$$

Where $\varepsilon_{32} = \varphi_3 - \varphi_2$, $\varepsilon_{21} = \varphi_2 - \varphi_1$ and φ_k denotes the solution on the k^{th} grid. Equation 2.2.2 can be solved using an iterative method.

Next step is to define the relative error $e_a^{21} = \left|\frac{\varphi_1 - \varphi_2}{\varphi_1}\right| \cdot 100$ and finally find the convergence index (GCI) which indicates the percentual error between the medium and fine mesh (Equation 2.2.3).

$$GCI = \frac{1.25 \cdot e_a^{21}}{r_{21}^{p} - 1} \qquad \text{Equation 2.2.3}$$

The results of 2D stator mesh independence analysis are summarised in Table 2.2.1 and the results for the 2D stator-rotor mesh independence analysis are summarised

in Table 2.2.2. For both the analysis, the GCI values are acceptable to consider to have reached the independence of the mesh. Stator mesh can be finer, but the GCI is still acceptable and using 150000 cells allows to have a good computational time.

The physical quantity used for the analysis (φ) is the entropy change between outlet and inlet of the domain. It was used entropy variation because, for the design of the stage, the optimization of stator and rotor will be performed and the criterion to look for improvements will be the entropy variation, in order to find the geometry that has the minimum entropy increase across the stage.

When simulations that includes both stator and rotor will be performed, the stator region will be meshed with 100000 cells due to the limitations in the maximum number of cells/nodes that can be used in the Ansys CFX student version. This reduction of cells from 150000 to 100000 is still acceptable for two main reasons: first of all, for the optimisation process there is no need to use the independent mesh, there is only the need to get comparable results to find which profile generates the smallest amount of entropy, then the real amount of entropy generated can be found through the independent mesh. Secondly, the stator domain in the stator-rotor simulations is almost a half respect to stator domain for only stator simulations, so the refinement of the stator domain does not vary significantly. This because for only stator simulation the domain after the trailing edge continues for the length of two stator axial chords, while for stator-rotor simulations it continues for $\frac{1}{5}$ of stator axial chord after the trailing edge. Always for these reasons the number of cells related to the rotor independence analysis is referred to only the rotor region, while stator region is kept at 100000 cells.

Rotor independence analysis was performed including the stator in order to be able to see also its effects.

Table 2.2.1: 2D Stator mesh independence values

Cells number	**ΔEntropy** $\left[\frac{J}{kg \cdot K}\right]$	**Volume** $[m^3]$	**Mesh size h [m]**
75k (mesh 3)	4.94	8.27E-05	3.67532E-10
150k (mesh 2)	4.84	8.27E-05	1.83766E-10
300k (mesh 1)	4.77	8.27E-05	9.1883E-11
r_21	2		
r_32	2		
eps_32	0.07		
eps_21	0.1		
s	1		
p	0.51457		
ea_21	0.014675052		
GCI	4.28%		

Table 2.2.2: 2D Stator-Rotor mesh independence values

Cells number	**ΔEntropy** $\left[\frac{J}{kg \cdot K}\right]$	**Volume** $[m^3]$	**mesh size h [m]**
50k (mesh 3)	6.38	1.85396E-4	1.23597E-09
100k (mesh 2)	6.22	1.85396E-4	6.17987E-10
200k (mesh 1)	6.16	1.85396E-4	3.08993E-10
r_21	2		
r_32	2		
eps_21	0.06		
eps_32	0.16		
s	1		
p	1.415		
ea_21	0.00974026		
GCI	0.73%		

For the stator, the mesh with 150k cells was used and for rotor the mesh with 100k cells was used.

One last consideration on meshes must be done. Due to the limited number of cells and nodes of Ansys student version, the 3D analyses were performed with the cluster of Politecnico di Milano, since it does not have this limitation and its computational power is much higher than a laptop, allowing to perform simulations with millions of cells in an acceptable amount of time. The mesh independence analysis of the 3D domain is reported in Table 2.2.3 for stator and in Table 2.2.4 for rotor.

Table 2.2.3: 3D Stator mesh independence values

Cells number	**ΔEntropy** $\left[\frac{J}{kg \cdot K}\right]$	**Volume** $[m^3]$	**Mesh size h [m]**
2M (mesh 3)	5.31	4.63E-04	7.71163E-11
4M (mesh 2)	5.1	4.63E-04	3.85582E-11
7M (mesh 1)	5.16	4.63E-04	2.20332E-11
r_21	1.75		
r_32	2		
eps_32	0.21		
eps_21	-0.06		
s	-1		
p	1.8927884		
ea_21	0.011627907		
GCI	0.77%		

Table 2.2.4: 3D Rotor mesh independence values

Cells number	**ΔEntropy** $\left[\frac{J}{kg \cdot K}\right]$	**Volume** $[m^3]$	**Mesh size h [m]**
2M (mesh 3)	13.05	1.75E-03	2.91087E-10
4M (mesh 2)	12.8	1.75E-03	1.45543E-10
7M (mesh 1)	12.22	1.75E-03	8.31676E-11
r_21	1.75		
r_32	2		
eps_32	0.25		
eps_21	0.58		
s	1		
p	2.2086		
ea_21	0.047463175		
GCI	2.43%		

2.2.2 Optimization

To increase as much as possible the performances of the geometries we have generated, an optimization procedure was performed for both stator and rotor which aim is to minimize entropy production across cascades. The software used for this process is FORMA (Fluid-dynamic OptimizeR for turbo-Machinery Airfoils). It is an evolutionary shape-optimization code developed by the laboratory of fluid machines at Politecnico di Milano, based on a geometrical parametrization technique built on B-Splines, a high-fidelity and experimentally validated CFD solver and a surrogate-based evolutionary algorithm [22].

A detailed but brief description about FORMA can be found in [22]. Here the explanation of what is needed to run FORMA is given.

The very basic idea behind FORMA is to modify the blade and endwalls geometry to find the one that is closest to the objective of the analysis, which is the minimization of entropy production for our case. So, the first thing FORMA needs is the parametrization of blade and endwalls geometries.

The parametrization is performed through B-splines because they give some advantages:

- smoothness: the curves are piecewise polynomials, which means that they are infinitely differentiable in all the points except the breakpoints;
- local controllability: changing the position of a single control point will result in a local variation of the curve without affecting the points that are far from the moved control point. This property is vital to properly interpolate both the regions with small and high curvature (for example in a blade profile the centre of the blade can have a much smaller curvature compared to the leading edge).

Once parametrization is completed, there is the need to specify which control points of the B-splines we want to move to change the shape of the blade or endwalls, of how much we want to move them and in which direction.

Finally, we can pass to FORMA the objective we want to reach and the constraints it must respect. Then FORMA can be run.

To check the convergence of the optimization procedure there is the need to look at the objective and constraints: the improvements of the objective must be negligible in the last iterations and the constraints must be respected. For example, in Figure 2.2.6, if we look at the green line, which represents the true entropy variation across the stator cascade, we see that the minimum values obtained during the last 100 iterations do not reduces. It means that there is no more margin for improving the cascade performances, so that we have reached the minimum level of entropy production for the given geometry. The blue line instead represents the forecast of the algorithm of what it thinks to find as entropy production, so it is not extracted from a CFD simulation, it is a forecast. This is why we should look at green line to see the convergence.

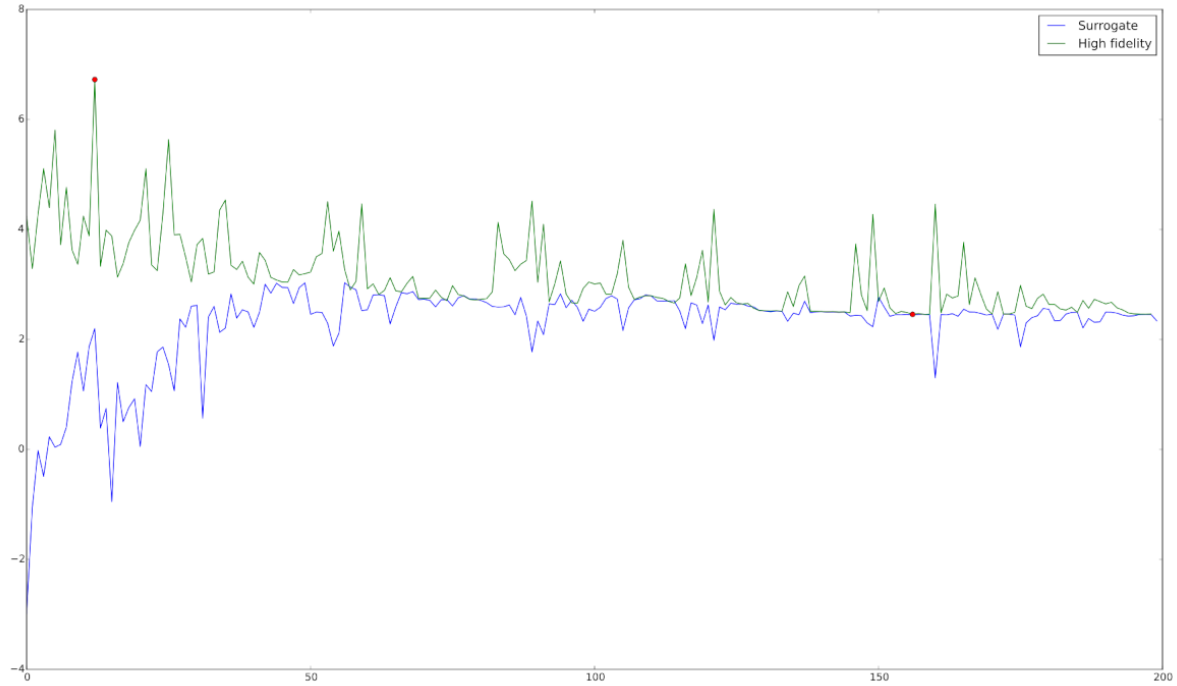

Figure 2.2.6: Stator entropy variation vs iteration

The optimization was performed on 2D profiles but considering also to change the shape of the endwalls (endwalls contouring). This because optimisation requires the running of a lot of CFD simulations, so doing it to a 3D profile would have required too much computational time. Always for this reason, the optimization was run with the cluster of Politecnico di Milano, because a laptop has not the computational power to perform the optimization in an acceptable amount of time, even with 2D simulations. The 3D analysis was performed after the optimization process to assess the performances of the optimized profile.

2.2.2.1 Stator Parametrization

In order to be able to perform significant variations to the geometry but in an acceptable computational time, the points to be changed were set to 14 and are distributed as shown in Figure 2.2.7 and Figure 2.2.8. The green points are the B-splines control points that can be moved (adjustable control points), while the light green area represent the region in which the curve can move due to the motion of control points. Each control point can move only perpendicularly to the curve and can move towards or forward respect to the curve.

About enwalls parametrization, the adjustable control points (green ones) are placed in correspondence of the blade, while the closest fixed points (red points) to them are placed at $\frac{1}{5}$ of axial chord from leading and trailing edge. For both hub and shroud the control points maximum displacement is of 0.75 mm, which is about the 20% of the inlet blade height (4 mm). The values are small because here we are performing a 2D optimization, so, as already explained, CFX need a 3D profile also for 2D simulations, so the 2D profile will be a profile with a small height. It was decided to use 4 mm as inlet height to be enough small but allow hub and shroud variations.

For all the adjustable control points the displacements were chosen in order to generate geometries for which the CFD solver (i.e. Ansys CFX) goes to convergence. This because the simulations that do not converge introduces bad results in the optimization process and, when these results will be compared with the results of the other simulations, they will make appear the results from converged simulations better then they effectively are, making more difficult to achieve improvements with the optimization. This is why it is important to get convergence in the simulations and so why the control points are moved in order to avoid bad geometries.

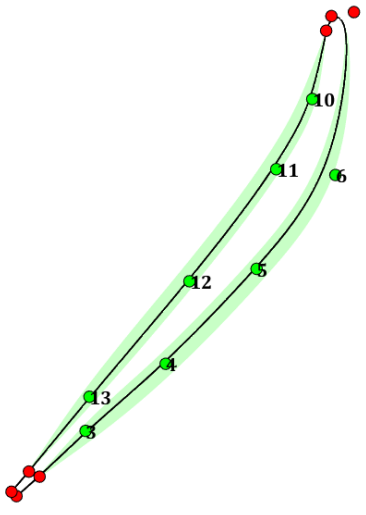

Figure 2.2.7: Stator blade parametrization

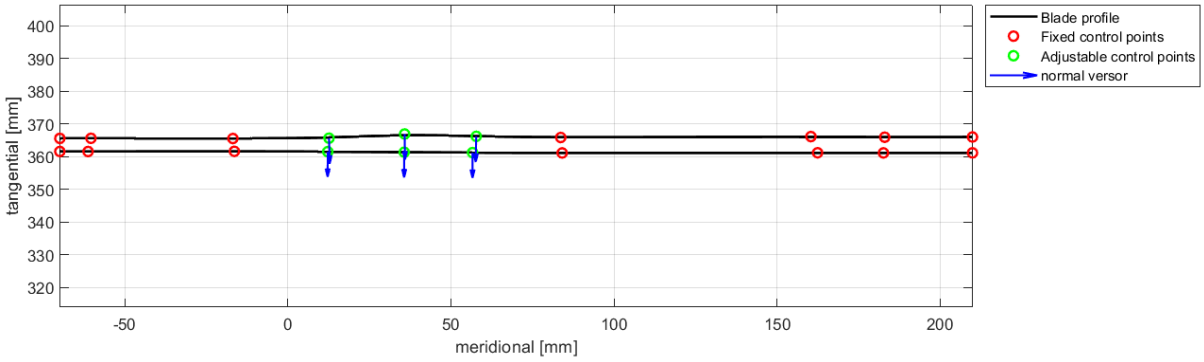

Figure 2.2.8: Stator endwalls parametrization

The constraint imposed to stator optimization was only one: the velocity flow angle can be varied from +1° to -1°. This because since the outlet section and pressure does not vary and the stator total temperature is constant since it is a nozzle, then, if we set the velocity flow angle, we also set the mass flow rate, so the stator outlet Mach number. There is the need to introduce this constraint because FORMA, in order to reduce entropy production, can reduce stator deflection to have a lower acceleration of the flow and so remove the shock losses due to chocking, but this means that the work that can be extracted by the rotor will be lower due to the lower deflection of the flow, and we do not want work reduction.

2.2.2.2 Rotor Parametrization

The same reasonings of stator parametrisation are valid also here. So, in Figure 2.2.9 and Figure 2.2.10 are presented the adjustable control points for stator geometries. In this case, due to the small portion of domain upstream of rotor leading edge, caused by stator presence, the second fixed control point of hub and shroud is placed in correspondence of leading edge and not at $\frac{1}{5}$ of axial chord upstream of leading edge. Instead, the first fixed control point after the adjustable ones is placed at $\frac{1}{5}$ of rotor axial chord downstream of trailing edge.

In this case the adjustable control points displacement of hub and shroud was set to 0.5 mm, about 10% of rotor inlet blade height for the 2D domain. It is a smaller value than stator because it was found that rotor was more sensible on endwalls contouring than stator, and that it was easy to have boundary layer detachment from blade suction side for a too strong endwalls variation.

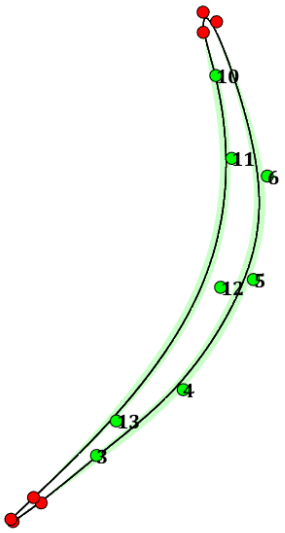

Figure 2.2.9: Rotor Parametrization

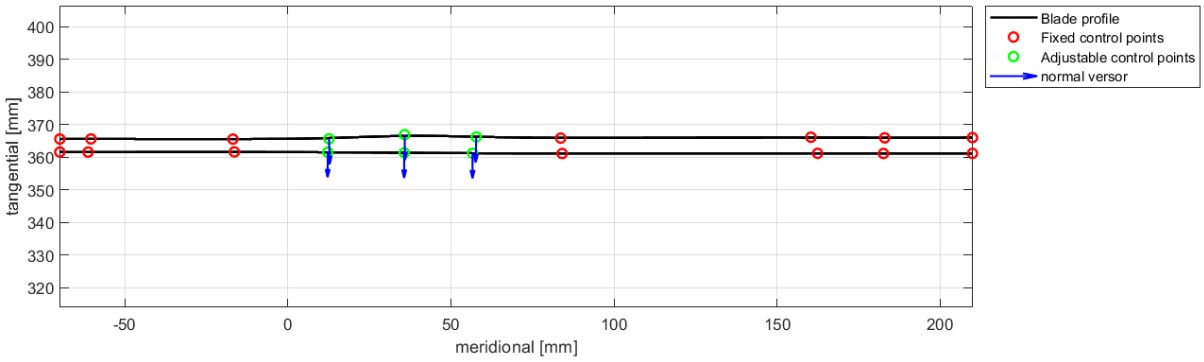

Figure 2.2.10: Rotor enwalls parametrization

For the rotor, the constraints are two: stator outlet Mach number maximum variation of ± 0.15 and rotor outlet velocity flow angle maximum variation of $\pm 1.5°$. About flow angle the reasons are the same of stator, instead about Mach number there is the need to constraint it to avoid that FORMA, to reduce entropy production, reduces the Mach number at stator outlet reducing so the losses related to the high speed of the flow. M_1 can be reduced by the rotor because since the relative flow at rotor inlet is not supersonic, rotor can influence stator flow, so if rotor blockage increases then

flow speed decreases. In this way FORMA can reduce M_1 simply increasing rotor blockage. We want to avoid this because it means that the mass flow rate is no more the wanted one and that rotor extracted power is lower than the one with higher flow speed.

2.2.2.3 3D profile generation

FORMA is allowed to change the shape of the meridional passage of the stage (Figure 2.2.8 and Figure 2.2.10), so the result of the optimization will not have a linear blade height variation from inlet to outlet, like shown in Figure 2.2.11.

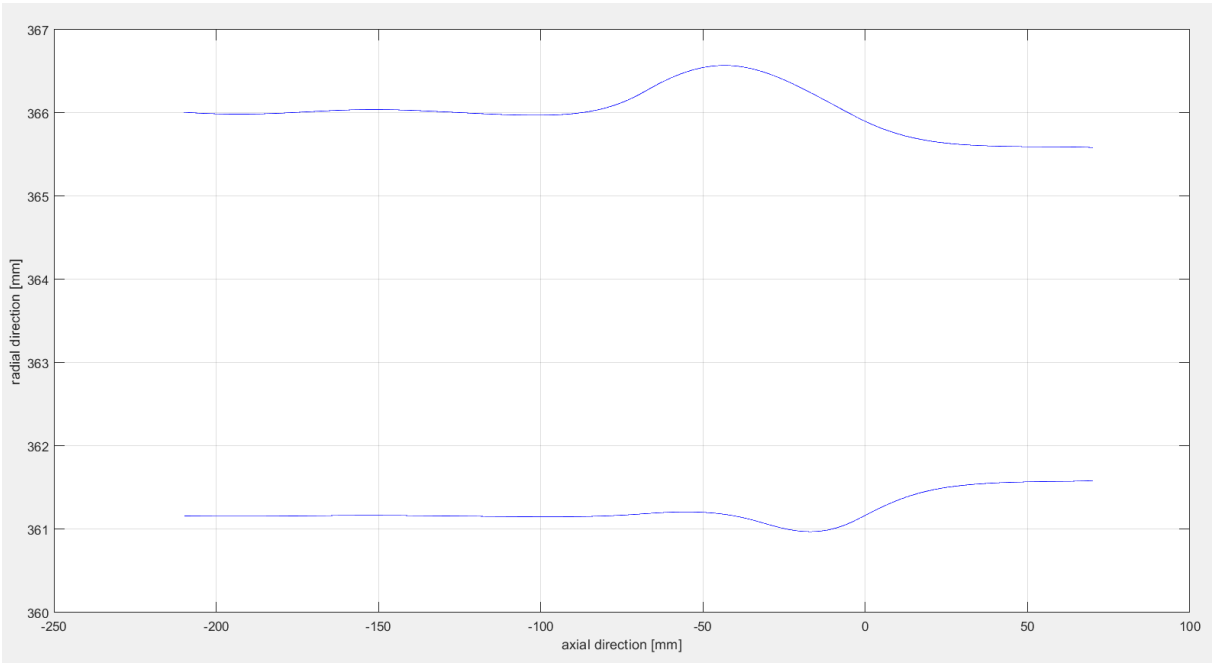

Figure 2.2.11: Meridional view of optimized 2D stator channel

So, there is the need of a strategy to give the right blade height to the 3D channel. To do so, blade height ratio was considered. Lets' look at Figure 2.2.12 , it represents the meridional view of the baseline channel showing the 3D profile blade height (b) and the 2D profile blade height (b_{2D}). From here I took their ratio: $r = \frac{b}{b_{2D}}$ and to generate the 3D profile from the optimized meridional section I considered the same ratio: $b_{3D_{opt}} = b_{2D_{opt}} \cdot r$.

Obviously, applying endwalls contouring, hub radius will not be constant anymore, as we first guessed during the mean line analysis (Figure 2.1.1).

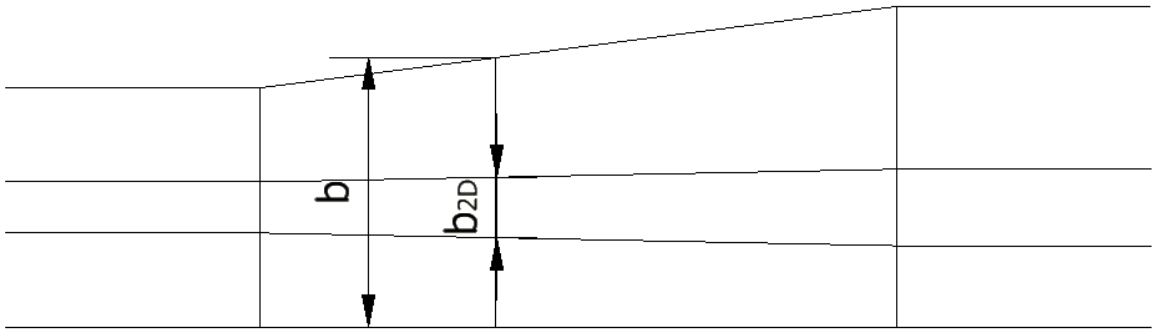

Figure 2.2.12: Stator baseline meridional view for 2D and 3D channel

2.3 Mechanical stress analysis setup

Before performing the optimization procedure, since it takes some days of computational time, a mechanical stress analysis was performed on the profiles to be optimized to be sure that they can withstand pressure loadings and centrifugal loading (for rotor only). To perform the analysis, Ansys Structural was used as software.

The geometric model is pretty simple. It consists of the blade in which are present two cooling channels (Figure 2.3.1).

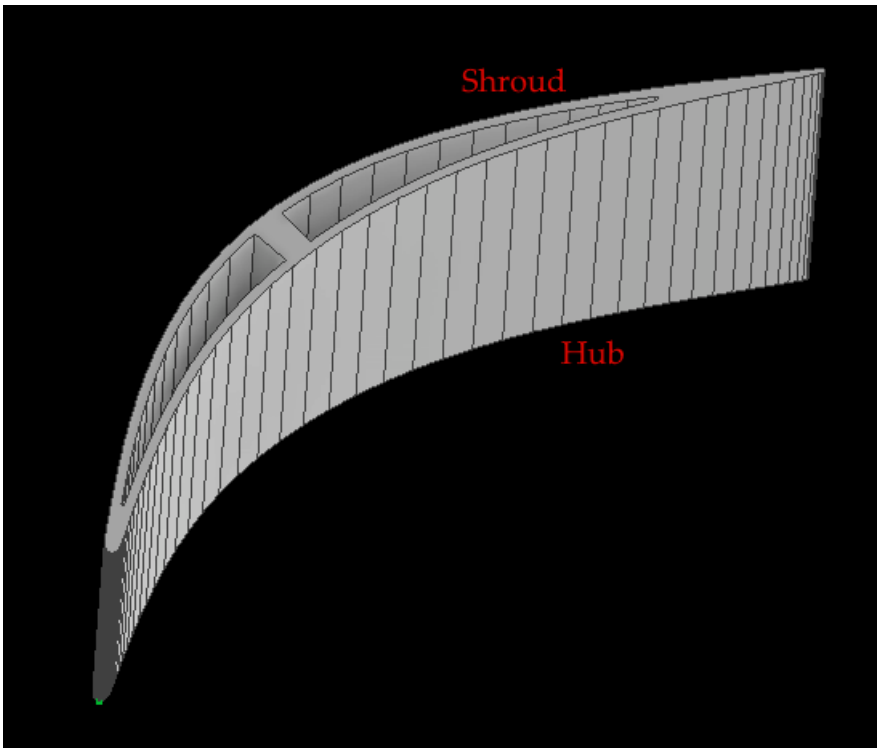

Figure 2.3.1: Blade model for mechanical stress analysis

At the hub it is placed the fixed constraint, while the pressure loading extracted from the corresponding CFD simulation (Figure 2.3.2) is applied on the blade, constant along the span. This because the CFD simulation is 2D (the 3D analysis was performed after the optimization process), while mechanical analysis must be performed on the 3D model of the blade to consider the right stresses, so the 2D

pressure loading is extrapolated along the span considering it as uniform along blade height.

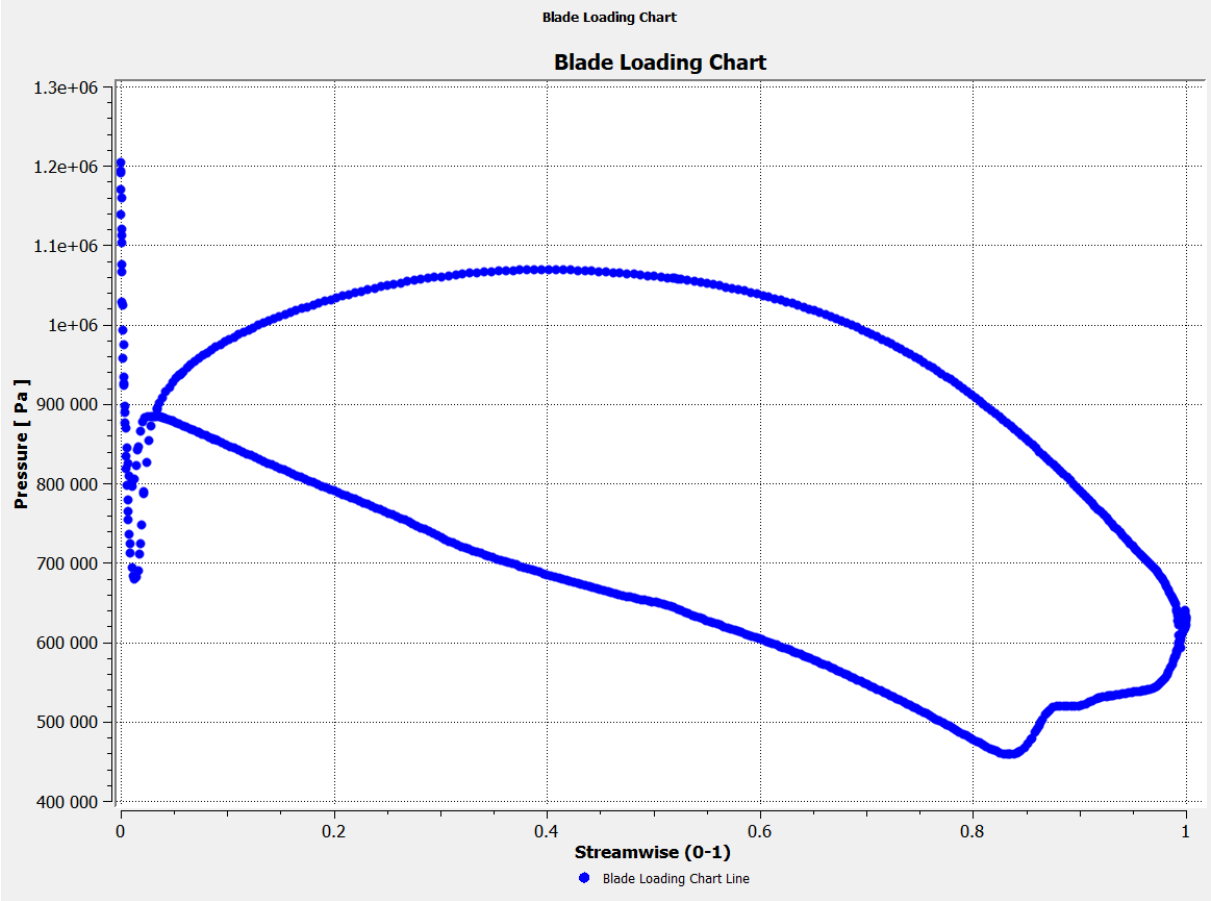

Figure 2.3.2: Blade pressure loading

The material used for the blade is the Inconel 718. Its characteristics are reported in Appendix F. The tabulated data of material properties in function of temperature are for temperatures up to 760°C, but the blade will be at higher temperature, about 900°. But thanks to modern techniques to increase blade resistance like film cooling, ceramic coating and generating the blade with a single metal crystal, the material characteristics can be considered almost constant up to 900° (Figure 2.3.3). Figure 2.3.3 shows also that with these technologies, the flow temperature can be up to 1600°, while our flow max temperature is 1500°. So, the yielding strength considered for the calculation of the safety coefficient will be of 758 MPa.

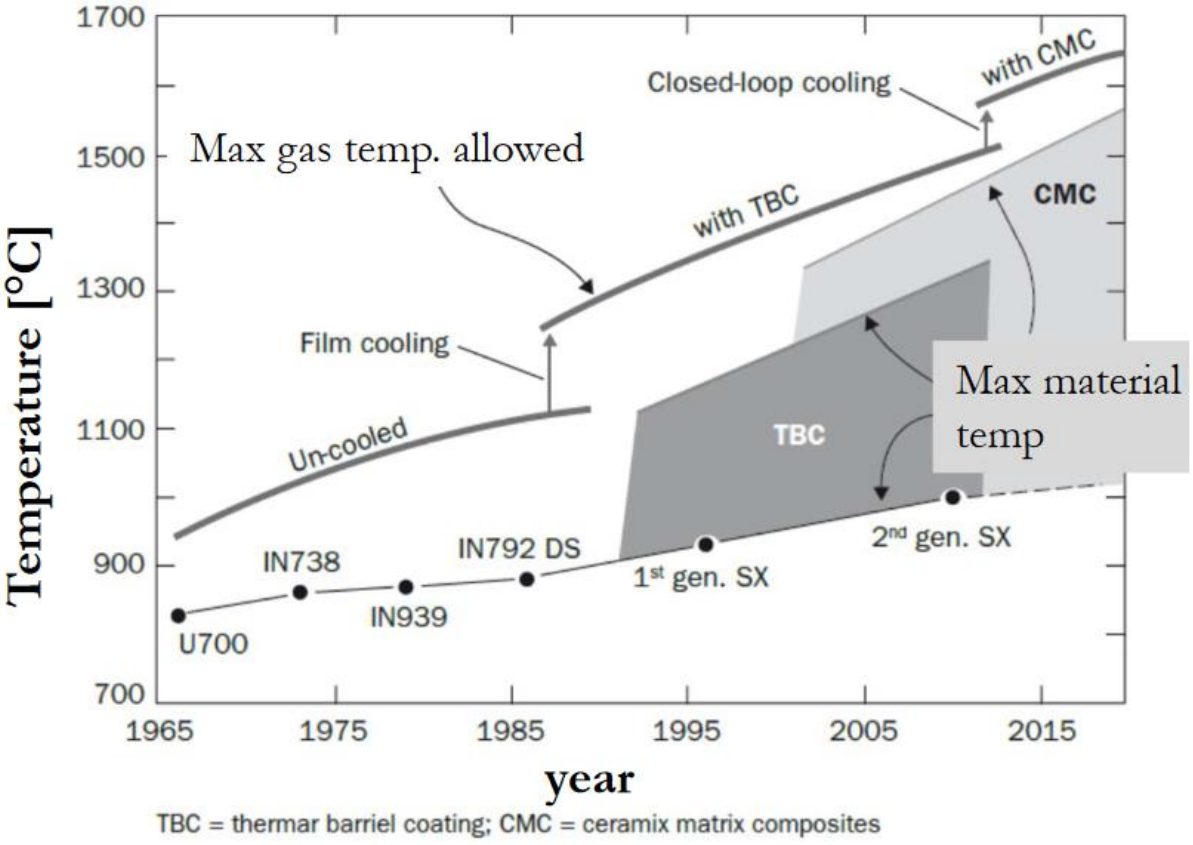

Figure 2.3.3: Max temperature allowed based on material and technology

3. Results

3.1 Parametric Analysis Results

Now that we have seen how zTurbo works and how to get the desired values of parameters (2.1 Mean Line Analysis), it is possible to look at the results of the parametric analysis.

The first set of results is taken considering the variation of the inlet Mach number M_0, stator flaring fl and hub radius R_i. In particular, the variation intervals are:

- $M_0 = 0.6 \div 0.8$
- $fl = 1 \div 1.2$
- $R_i = 0.23 \div 0.345\ [m]$

In Figure 3.1.1 are reported the effects of these parameters on efficiency. Each surface represents the results for the different flaring values. These results were taken considering $\alpha_2 = 0°$ and rotational speed $\omega = 6000\ rpm$.

It is possible to see that efficiency increases for higher values of fl and R_i and for lower values of M_0. This is because, when fl increases, to reach $M_1 = 1$ the flow needs to turn more than at low fl. This allows to have a higher tangential component of absolute speed V_{1tan} increasing so the extracted work from rotor. Efficiency increases also for larger R_i because, for bigger radius at constant ω, the peripheral velocity U of the rotor is higher, so also this fact increases the extracted work. Instead, about M_0, efficiency increases for lower inlet Mach number because losses will be smaller and because higher M_0 reduces the stator deflection to reach $M_1 = 1$, so reduces rotor work.

So, the trend in Figure 3.1.1 suggests that, in order to maximise efficiency, there is the need to reduce as much as possible the flow speed from rotating detonation combustor and increase as much as possible flaring and hub radius to increase work exchanged.

In Figure 3.1.2 it is shown in a clearer way the effects of flaring and hub radius on efficiency considering the results taken at constant Mach ($M_0 = 0.6$).

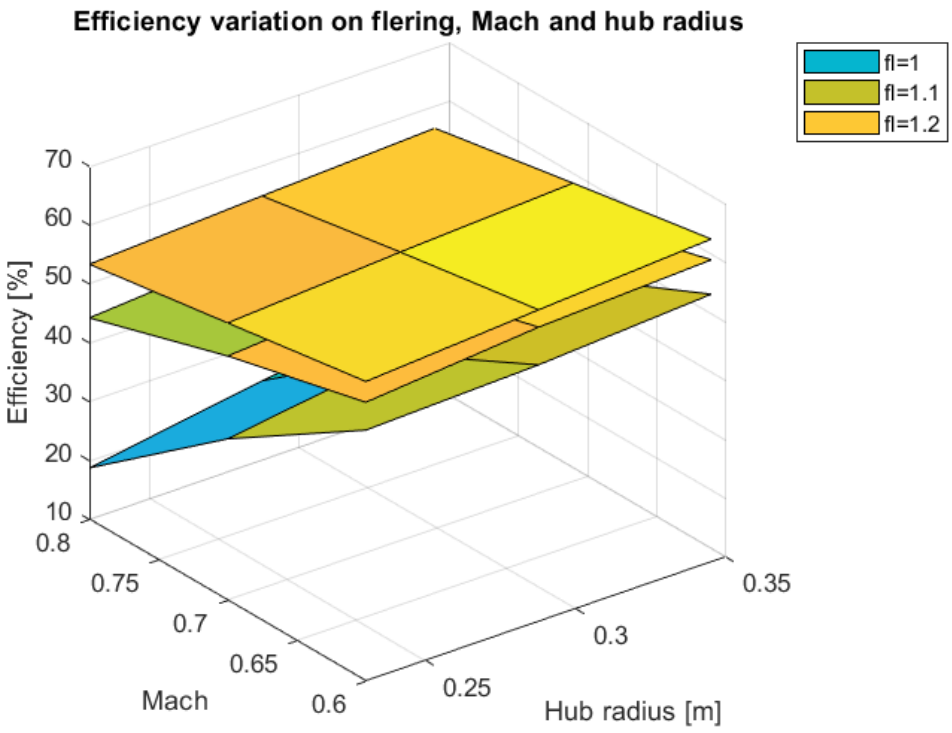

Figure 3.1.1: M_0, fl and R_i effects on efficiency

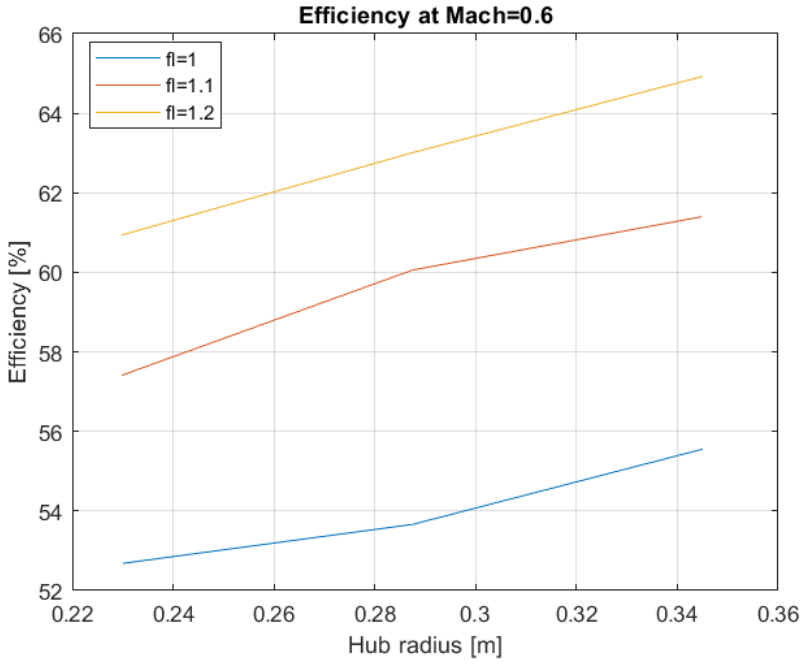

Figure 3.1.2: fl and R_i effects on efficiency at $M_0 = 0.6$

The problem is that it is not possible to increase hub radius as much as we want because when it increases, the inlet blade height will decrease, as shown in Figure 3.1.3. If blade height is too small then the endwalls losses will be so high that the advantages coming from the higher peripheral velocity will vanish. Fortunately, at M_0 reduction the blade height increases, giving a one more reason to reduce M_0 as much as possible.

It is not possible to bring M_0 to conventional values of 0.2 or 0.3 because, due to the highly non uniform flow coming from the RDC, a so strong deceleration will cause a lot of losses and will increase a lot the non-uniformities. So, we considered as limit the value of $M_0 = 0.6$.

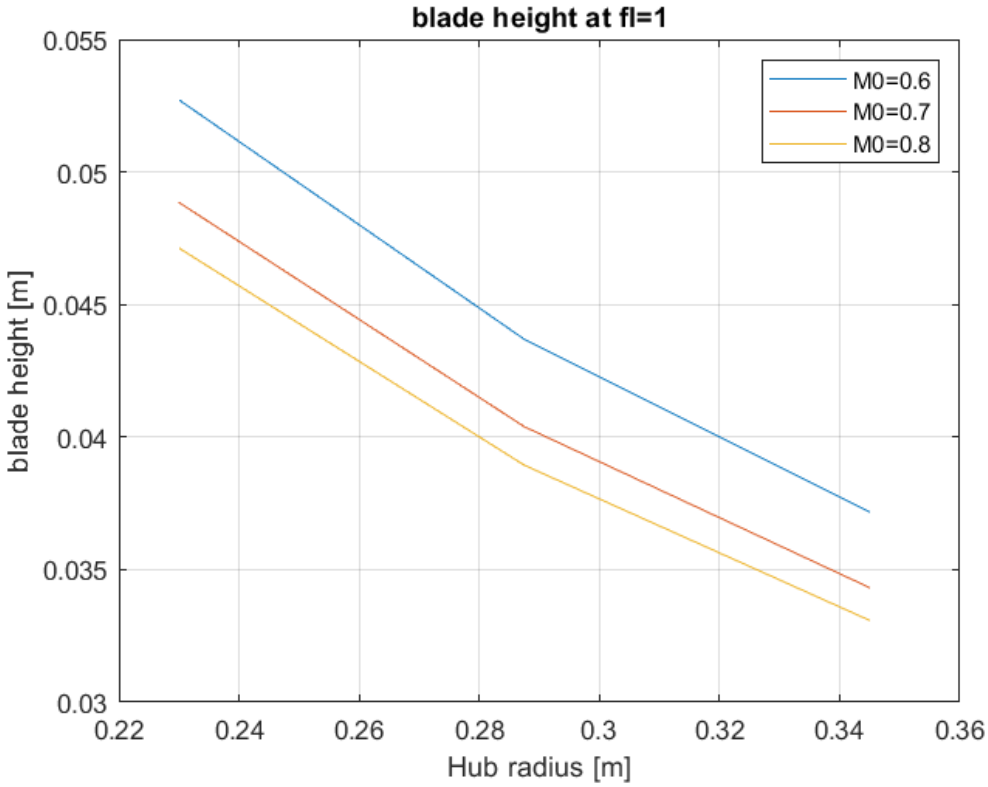

Figure 3.1.3: R_i and M_0 effects on blade height at constant flaring

The following step is to look at the effects of rotational speed ω and absolute rotor outlet angle α_2. They were varied in the following intervals:

- $\omega = 6000 \div 8000\ [rpm]$
- $\alpha_2 = -30° \div 0°$

α_2 is taken from axial direction and the sign is taken from peripheral velocity direction, so a negative angle means that the tangential component of the flow is in the opposite direction of peripheral velocity.

These calculations were performed considering $M_0 = 0.6$, $fl = 1.2$ and $R_i = 0.345\ m$, so the point of maximum efficiency from the previous analysis. It was decided to not overcome flaring value of 1.2 to avoid flow separation at endwalls. Also $R_i = 0.345\ m$ was used in [22] and we decided to not overcome these values of flaring and hub radius in order to make the stage designed in [22] comparable with the stage designed in this thesis since they treat the same topic, but considering two different solutions (i.e. in [22] the flow is brought to fully supersonic from RDC outlet to turbine inlet, in this thesis the flow is decelerated to be fully subsonic at turbine inlet).

The effects of ω and α_2 on efficiency are reported in Figure 3.1.4 . It is possible to see that efficiency increases for increasing of ω and decreasing of α_2. This is because increasing ω at constant radius increases peripheral velocity, allowing a higher extraction of work. While, if α_2 decreases, it means that the tangential component of absolute speed is increasing in modulus, but in the opposite direction of peripheral velocity. So, if we look at Euler's equation for work exchange in a machine (Equation 3.1) we see that the term $V_{2t} \cdot U_2$ is negative, so, combined with the minus of the equation, it gives a positive contribution to rotor extracted work, so to efficiency.

$$\dot{W} = V_{1t} \cdot U_1 - V_{2t} \cdot U_2 \qquad \text{Equation 3.1}$$

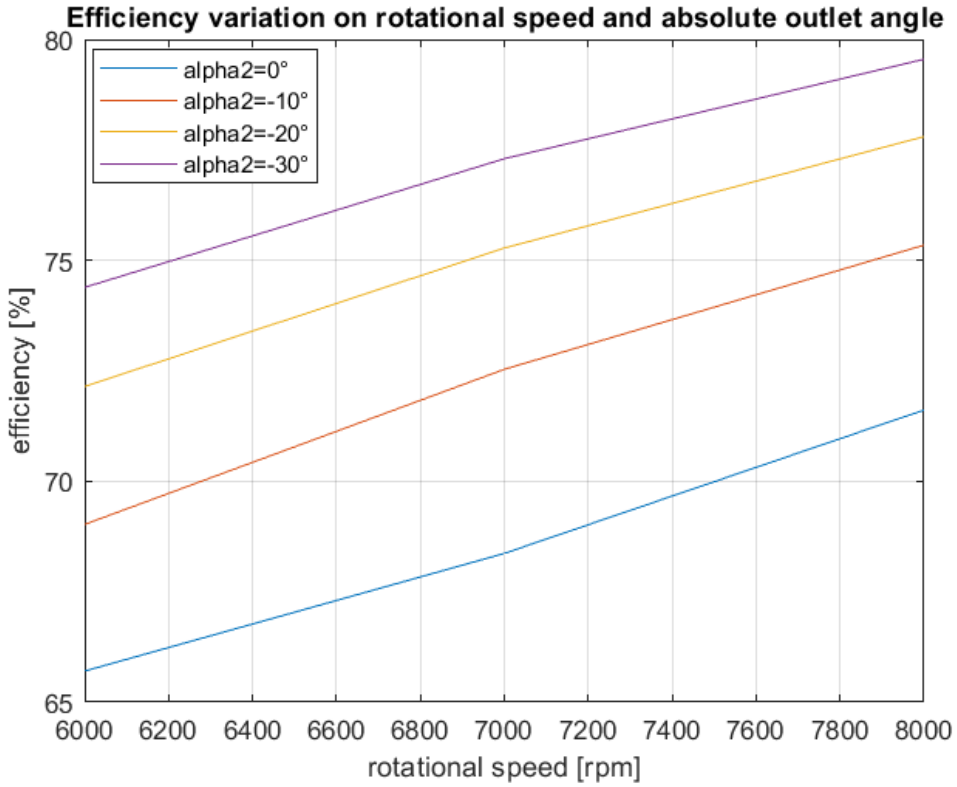

Figure 3.1.4: α_2 and ω effects on efficiency

It must be noticed that rotor flaring is an output, as already mentioned, but also it cannot go above the value of 1.2, for the same reason seen for stator. So, there is the need to look at the effects of ω and α_2 variation on rotor flaring. The results are reported in Figure 3.1.5. It is possible to see that for ω increasing and α_2 decreasing rotor flaring increases.

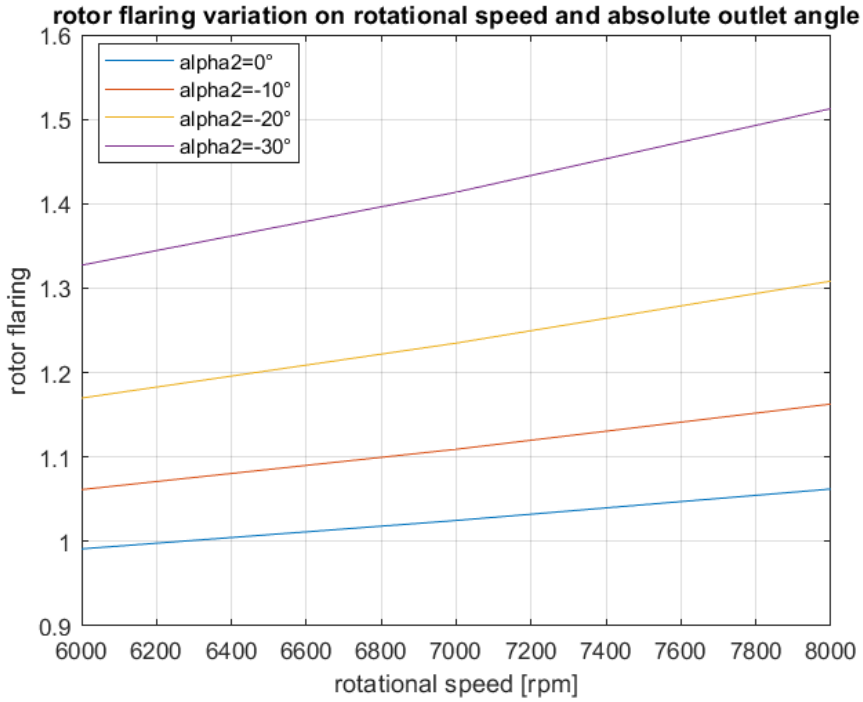

Figure 3.1.5: α_2 and ω effects on rotor flaring

So, to maximize efficiency, ω must be increased as much as possible. The limit is given by mechanical strength of the material, because, at rotational speed increasing, also centrifugal loading increases. For this reason, a mechanical study of the rotor will be performed in 3.3.3 Mechanical analysis results. About α_2, at its reduction the efficiency increases, but also rotor flaring does. So α_2 is limited by flaring.

It was decided to set $\omega = 8000\, rpm$ because it seams reasonable as first guess before a stress analysis can be done on the blade considering also pressure loading effects, that are not negligible. So, starting from this ω, it was found the minimum α_2 that allows to have the value of 1.2 for rotor flaring. In this way the constraint on flaring is respected while efficiency is maximised as much as possible with these constraints. This minimum α_2 depends on which losses are considered: if only profile losses are considered then $\alpha_{2_{min}} = -21°$, while if both profile and secondary losses are considered then $\alpha_{2_{min}} = -13°$.

Also stator outlet angle α_1 depends on losses once flaring is fixed: considering only profile losses, to get $fl = 1.2$ we get $\alpha_1 = 42°$, while considering both profile and secondary losses we get $\alpha_1 = 38°$.

3.2 Stator Results

3.2.1 2D Results

Since the first CFD analysis are 2D, then the values chosen from zTurbo will be the ones that maximizes efficiency, but that come from the calculations with only profile losses. So the characteristics of the stator from zTurbo are:

- $M_0 = 0.6$
- $R_i = 0.345\ m$
- $fl_s = 1.2$
- $N_{blades} = 110$
- $h_{in} = 3.717 \cdot 10^{-2}\ m$
- $h_{out} = 4.46 \cdot 10^{-2}\ m$
- $\alpha_1 = 42°$
- $chord_s = 3.717 \cdot 10^{-2}\ m$
- $TE = 1\ mm$
- $P_1 = 8.1\ bar$
- $\sigma_s = 1.89$

Where N_{blades} is the number of blades, h_{in} is stator inlet blade height, h_{out} is stator outlet blade height, α_1 is the geometric outlet angel, $chord_s$ is the stator axial chord, TE is trailing edge thickness, P_1 is stator outlet static pressure and σ is the solidity of the cascade.

Now the problem is that the geometric values refers to the 3D blade, so to generate the 2D profile for Ansys CFX, as already explained in 2.2.1 Model setup, it was chosen to take the stream-tube with 4 mm inlet height and with mean radius equal to the stage inlet mean radius ($R_m = 0.363585\ m$) (Figure 2.2.1 a).

zTurbo does not give the leading edge thickness and profile shape since it is a mean line code. We decided to use a leading edge thickness (LE) of 2.5 mm to allow an efficient blade cooling and to use different shapes to find the one that gives the best performances. It was also decided to perform a study on the solidity to find if it exists a solidity different from the one given by Zweifel that gives better performances. It was also done to understand if it was possible to reduce the number of blades to make the stage lighter and reduce its production costs.

The Mach field of the first stator generated is represented in Figure 3.2.1. The shape of the camber line and the thickness distribution around it were generated in order to have a straight trailing edge to reduce the possible boundary layer detachment. The maximum thickness of the blade is of 4 mm (10% of the axial chord) at 50% of the chord.

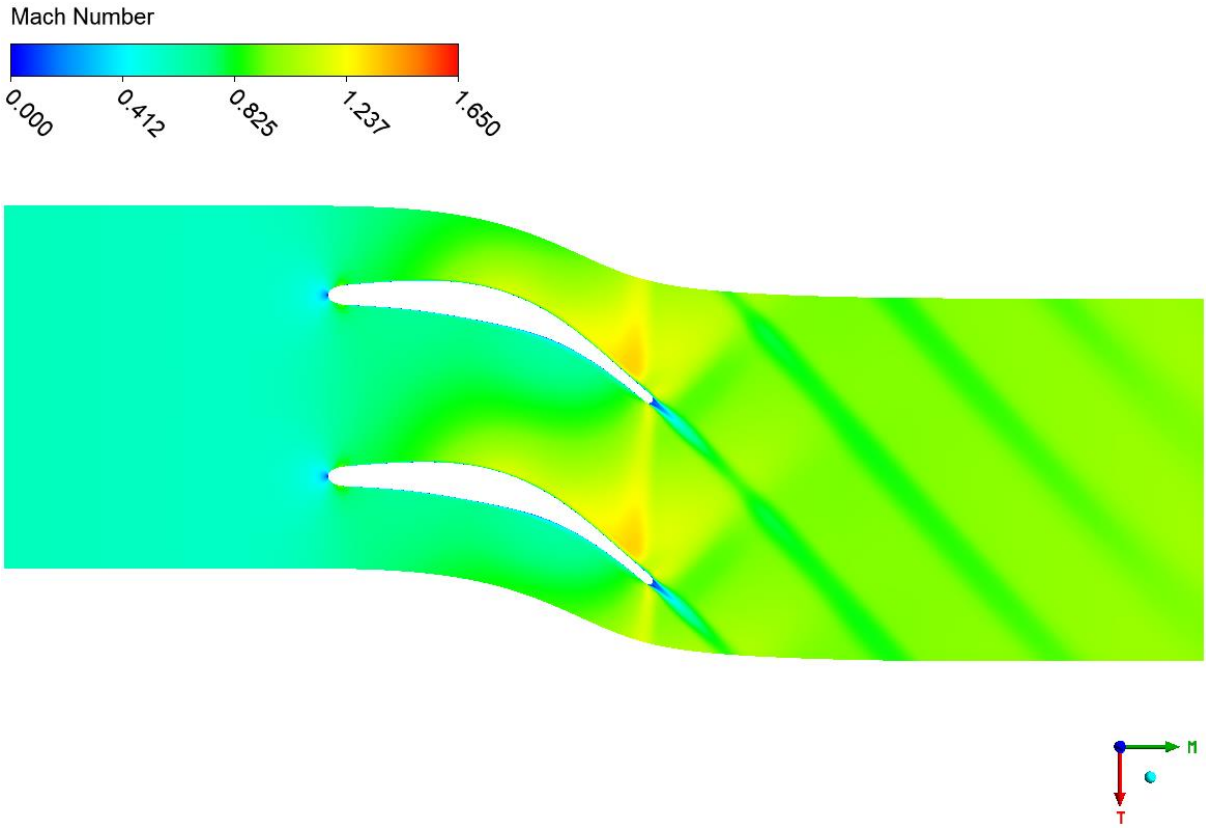

Figure 3.2.1: Mach field of the first stator generated

The inlet Mach number is $M_0 = 0.594$, while the pressure losses are $y_s = 6.9\%$. There is the presence of fish tails at the trailing edge that interact with the suction side boundary layer of the adjacent blade causing a small separation just before the trailing edge. At a little distance downstream the trailing edge there is a normal shock that brings the flow to $M_1 = 1$.

Starting from this profile a study on the effects of the number of blades is performed and the main results are reported in Figure 3.2.2.

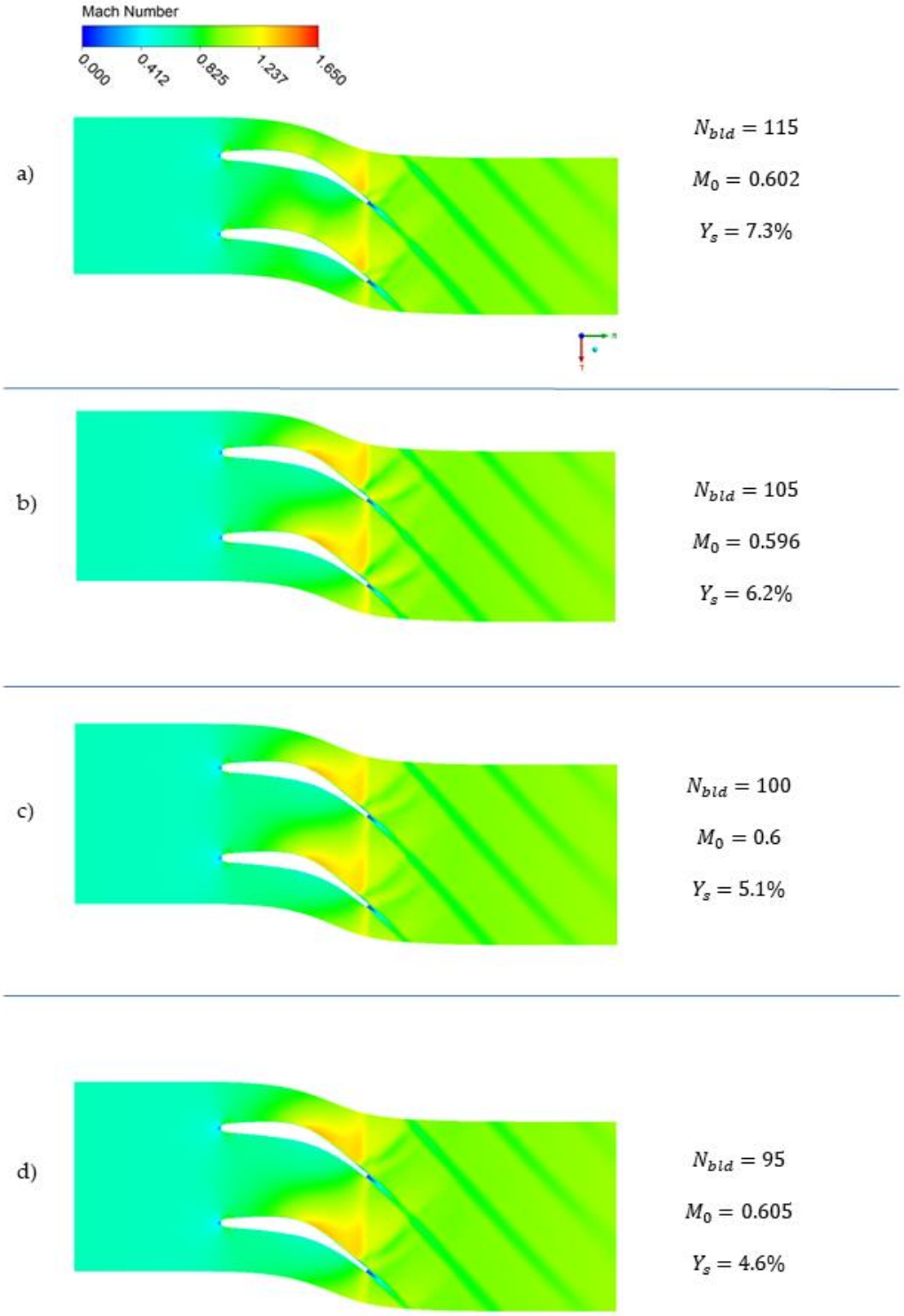

Figure 3.2.2: Effects of stator blades number

With a lower number of blades, the losses decrease thanks to the lower wetted surface of blades. It is interesting to notice that the flow stays attached to the blade, showing that there is margin for solidity reduction. In all the cases the outlet Mach number M_1 is equal to 1, while the inlet Mach number M_0 is very close to the reference value of 0.6, showing that the variation of mass flow rate is very small from one case to the other, making them comparable. It can be also noticed that the maximum Mach number reached on the suction side of blades increases at blades reduction. This because blade loading increases.

At a lower number of blades, fish tails are still present, the pattern of the shocks changes, but there is still the interaction between shocks and blades. So, to try to remove this feature, it was tried to generate a blade with axial chord of 70 mm. It was chosen to use the same solidity of the first blade generated ($\sigma_s = 1.89$), which is the one given by Zweifel, so the number of blades will be 62 with this new geometry. About blade thickness we kept the same distribution of the first blade generated: maximum blade thickness of 4 mm at 50% of the chord.. The main results of this new blade are reported in Figure 3.2.3.

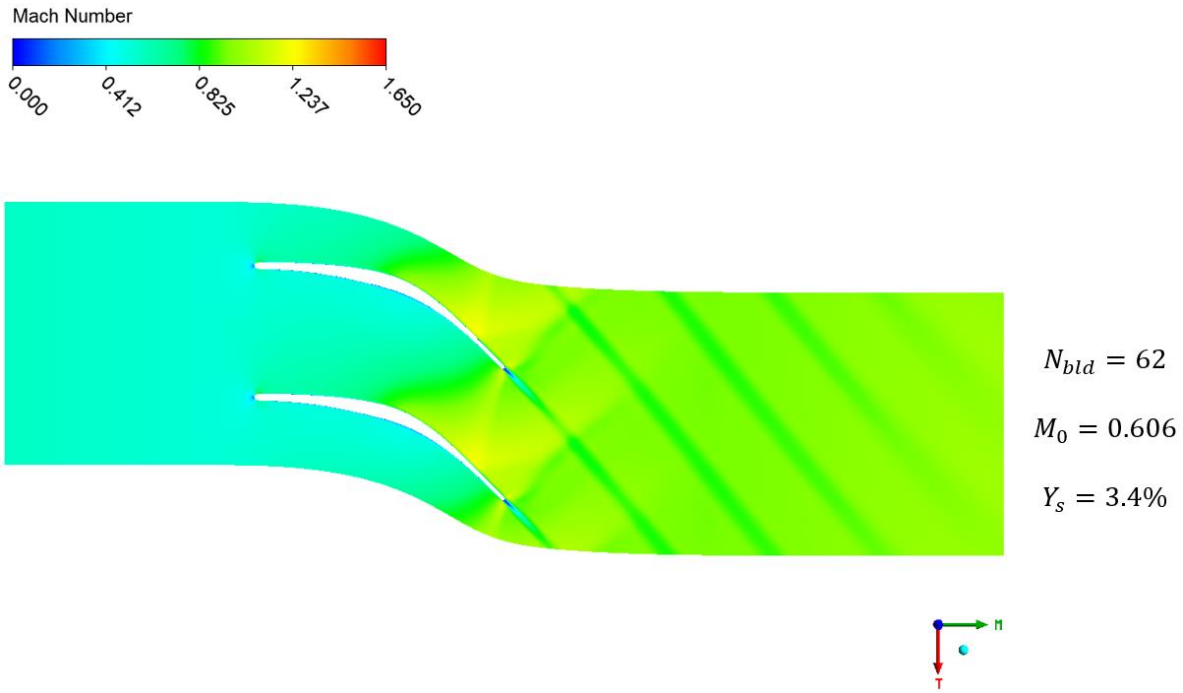

Figure 3.2.3: Stator with axial chord of 70 mm and 62 blades

The first observation that can be done is that the profile is very thin. But it shows that, keeping the same solidity of the first blade, the losses are reduced simply by increasing the axial chord. This is mainly due to the reduction of the overspeed on the suction side: the highest Mach goes from 1.336 (Figure 3.2.1) to 1.245 (Figure 3.2.3). Fish tails are still present, but this simulation showed that the increment of axial chord had a positive effect on the losses.

So, putting together the reduction of blades number and increment of axial chord, it was decided to generate a profile with 70 mm axial chord, 35 blades and a NACA thickness profile with maximum thickness of 10% of the axial chord placed at $\frac{1}{3}$ of axial chord. Then it was decided to look at the effects of axial chord on this profile. Main results of this analysis are reported in Figure 3.2.4.

The profile for which losses are the lowest is the one with 70 mm axial chord, even if it shows an important boundary layer detachment (Figure 3.2.4 a). The other two profiles losses are still lower than the profiles with 37 mm axial chord, but presents higher losses than the 70 mm axial chord because they present more wet surface. It is important to notice that increasing axial chord keeping the same number of blades also increases the solidity, reducing a lot the flow separation. The problem of fish tails is reduced, but they are still present.

Reducing the number of blades to 35 but using a chord of 90 or 80 millimetres does not reduce sensibly the weight of the stage, so, combining this consideration with the fact that the profile with 70 mm axial chord has the lowest losses, we decided to improve the features of that profile by changing the shape of the camber line, the profile thickness and the shape of endwalls to change the cross-sectional area.

To reduce the flow separation and remove the fish tails it was decided to generate a profile that is front loaded, in which the deviation happens in the first part of the profile (Figure 3.2.5). The thickness was chosen to be small at the leading edge to reduce blade blockage and then it was increased to allow sufficient space for internal cooling of the blade and improve mechanical resistance. Then different endwalls shapes were tried to reduce the overspeed on the suction side and to reduce losses. Endwalls contouring changes the flow cross-sectional area, and this area changing is the element that influence the flow speed. For this reason, in Figure 3.2.6 are reported the Mach field of the different trials with the corresponding cross-sectional areas trends along blade channel meridional length. The curve of the area we should look are the ‘quasi orthogonal with blades with flow angle correction’ because it is the area seen by the flow.

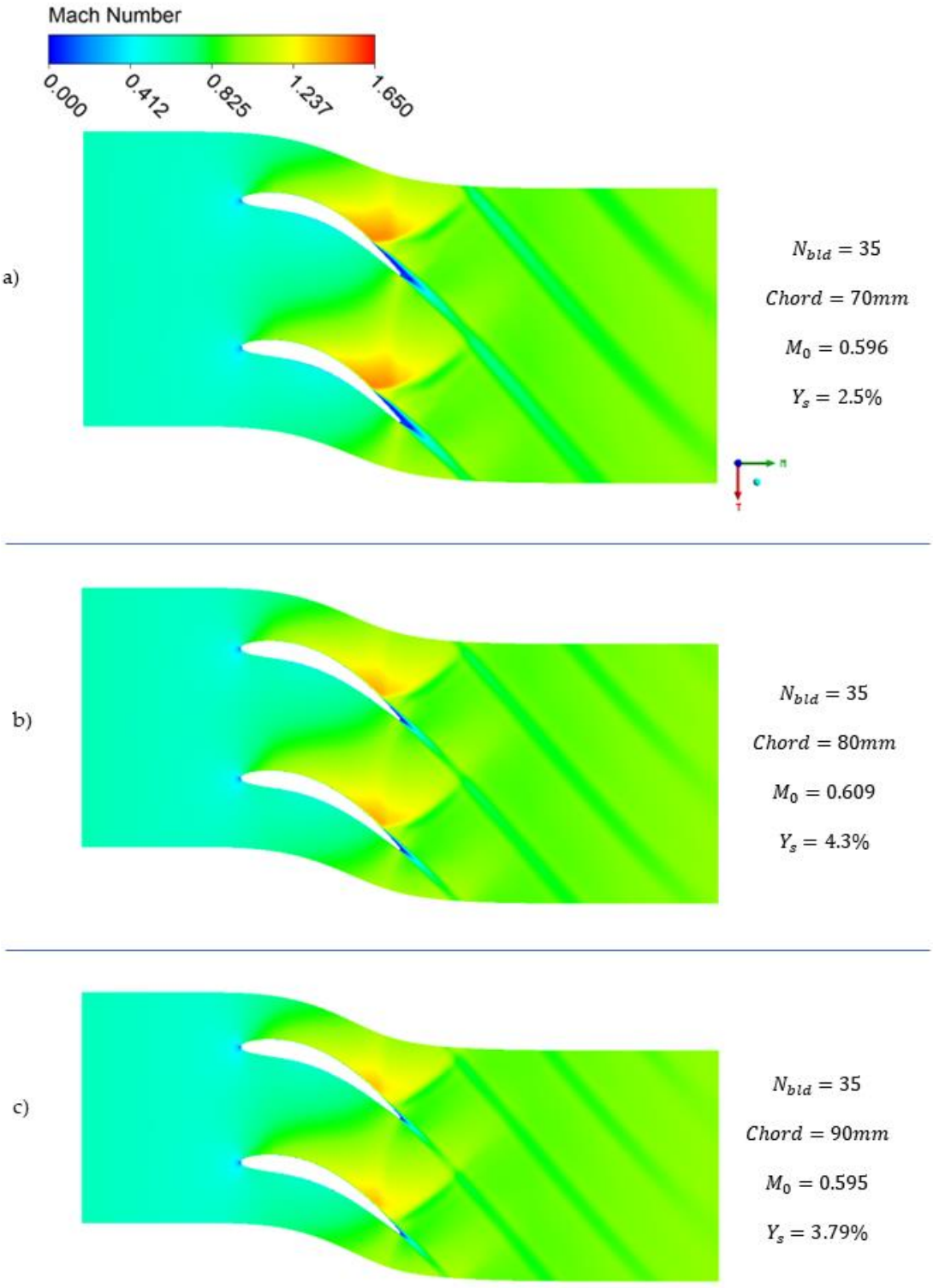

Figure 3.2.4: Comparison of stator NACA profiles

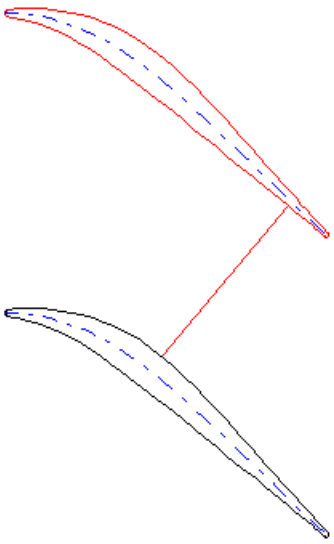

Figure 3.2.5: Front loaded stator

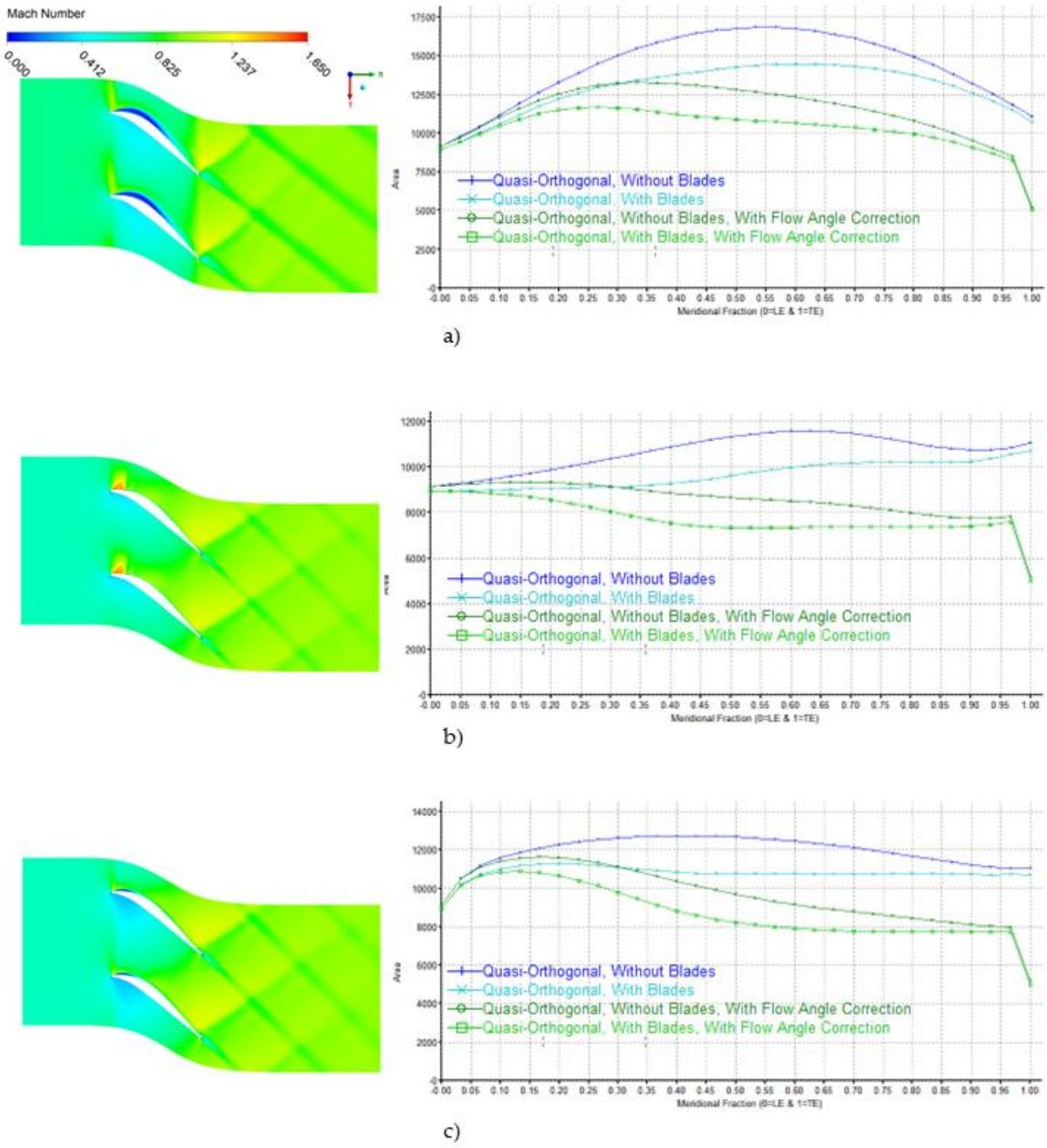

Figure 3.2.6: Stator endwalls comparison. Area in in mm^2

It is clear that for Figure 3.2.6 a) the boundary layer detachment is due to the high adverse pressure gradient caused by the too high area expansion. For the same reason in Figure 3.2.6 c) there is flow separation, but of a lower intensity due to the smaller area increase. The best enwall shape is for Figure 3.2.6 b), where the area is not increased, but it is kept constant for a while and then decreased. This allows to

have the flow attached to the blade and reduces the intensity of shocks, bringing them downstream of the trailing edge. The fish tails interaction with suction side of adjacent blades is much weaker than all the other case considered.

So, it was decided to try to reduce a little bit the thickness of the profile while keeping the endwalls contouring of Figure 3.2.6 b). This was done to reduce blade blockage and weight and rely on results of mechanical analysis (3.2.4 Mechanical analysis results). This is the final stator profile before optimization process and is reported in Figure 3.2.7. The associated pressure losses are 3.2%. They are not as small as Figure 3.2.4 a), but the flow field is much better, so we decided to optimize the shape of this last profile.

As it can be seen from Figure 3.2.7, for this last profile the fish tails are significantly weaker. It has only a small detachment of the boundary layer just after the overspeed region, but then it is reabsorbed. This feature will be removed by the optimization.

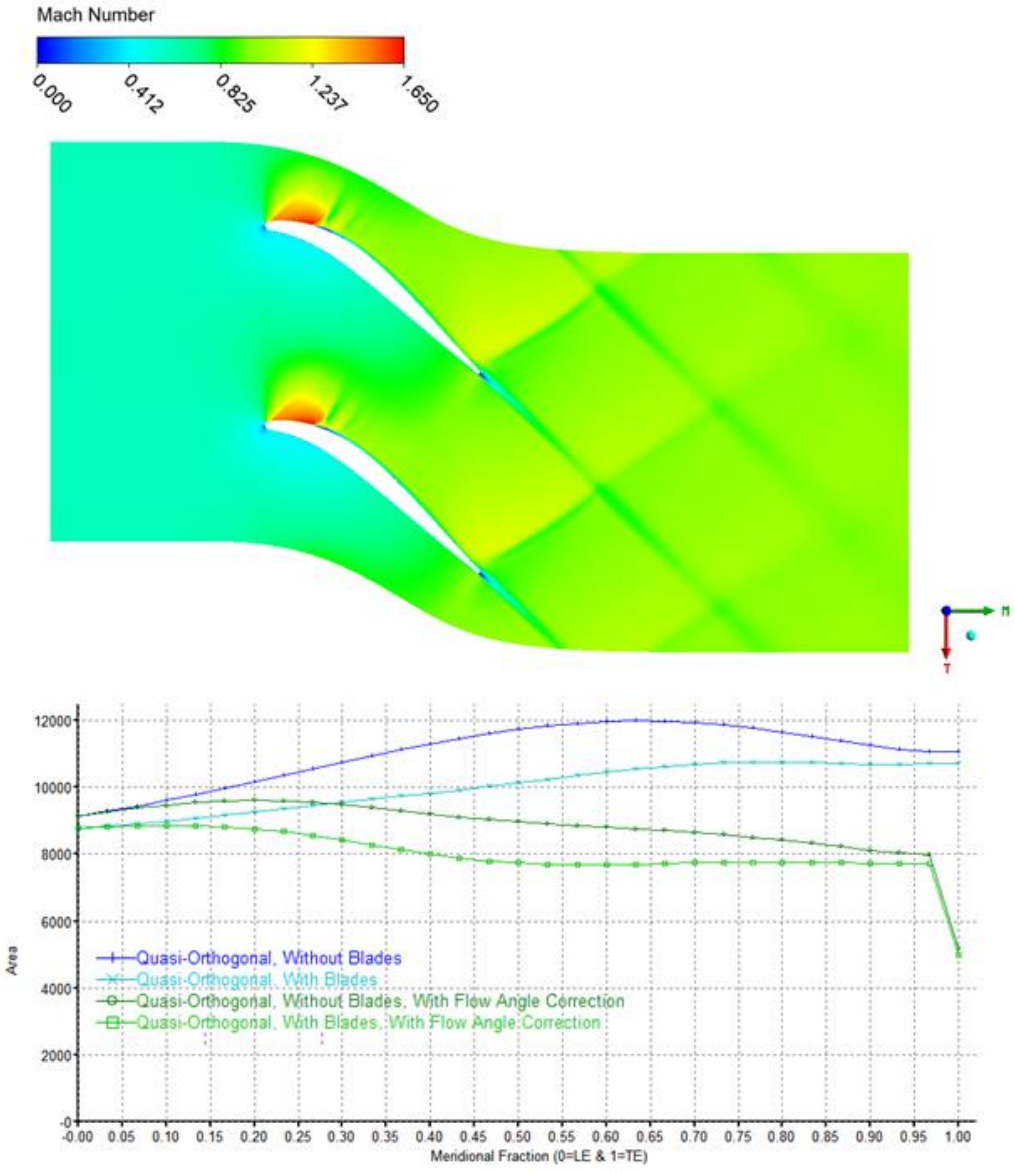

Figure 3.2.7: Stator profile for optimization. Area is in mm^2

3.2.2 Stator Optimization

As reported in 2.2.2 Optimization, the optimization process of the profile aims at finding a geometry which produces the lowest amount of entropy possible. The optimization process, starting from the last 2D profile presented, that will be called 'base profile' (Figure 3.2.7), will modify blade, hub and shroud geometries (2.2.2.1 Stator Parametrization) to reach its aim.

The geometric results are reported in Figure 3.2.8 and Figure 3.2.9, while the Mach number field is reported in Figure 3.2.10.

In the optimized blade, the profile thickness after le leading edge is smaller than base profile thickness and the optimized blade deflects a little bit more downstream than the base profile. In the meridional view of the optimized profile, both hub and shroud open up increasing the flow passage area. The combination of these two evident modifications allows an increasing of flow cross-sectional area reducing a lot the overspeed region on the suction side, near the leading edge (Figure 3.2.10).

Thanks to overspeed reduction, also the intensity of the shock downstream of trailing edge is reduced. For these reasons, the entropy produced across the optimized stator is $2.455 \frac{J}{kg \cdot K}$, which, compared to base profile entropy production of $4.289 \frac{J}{kg \cdot K}$, is 42.76% lower than base profile.

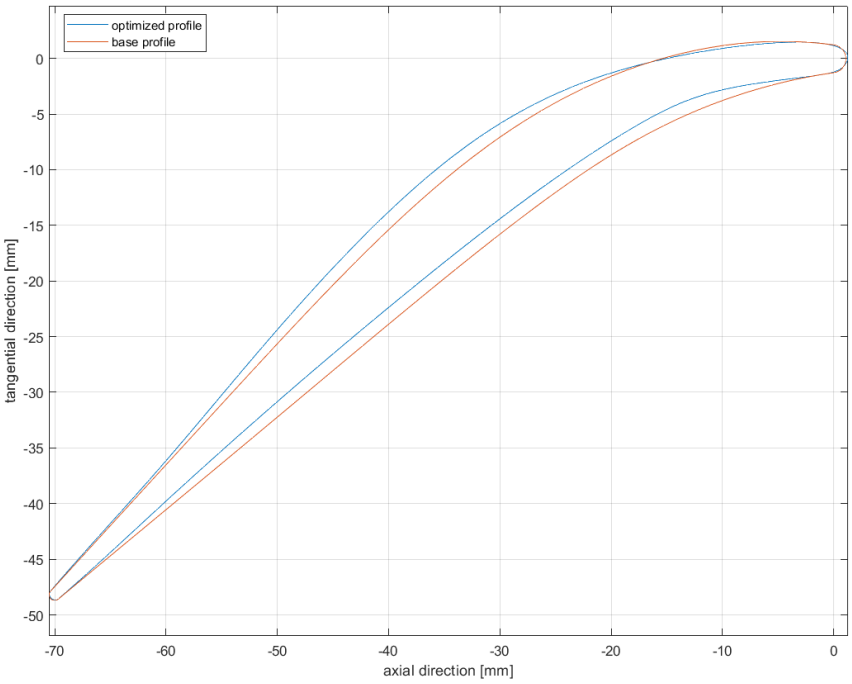

Figure 3.2.8: Comparison between optimized and base profile

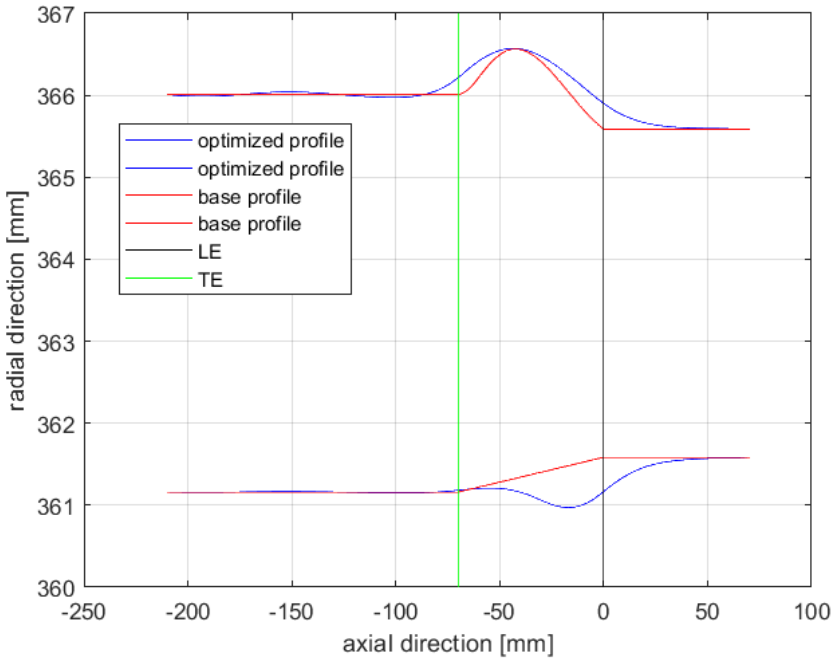

Figure 3.2.9: Comparison between meridional view of optimized and base profile

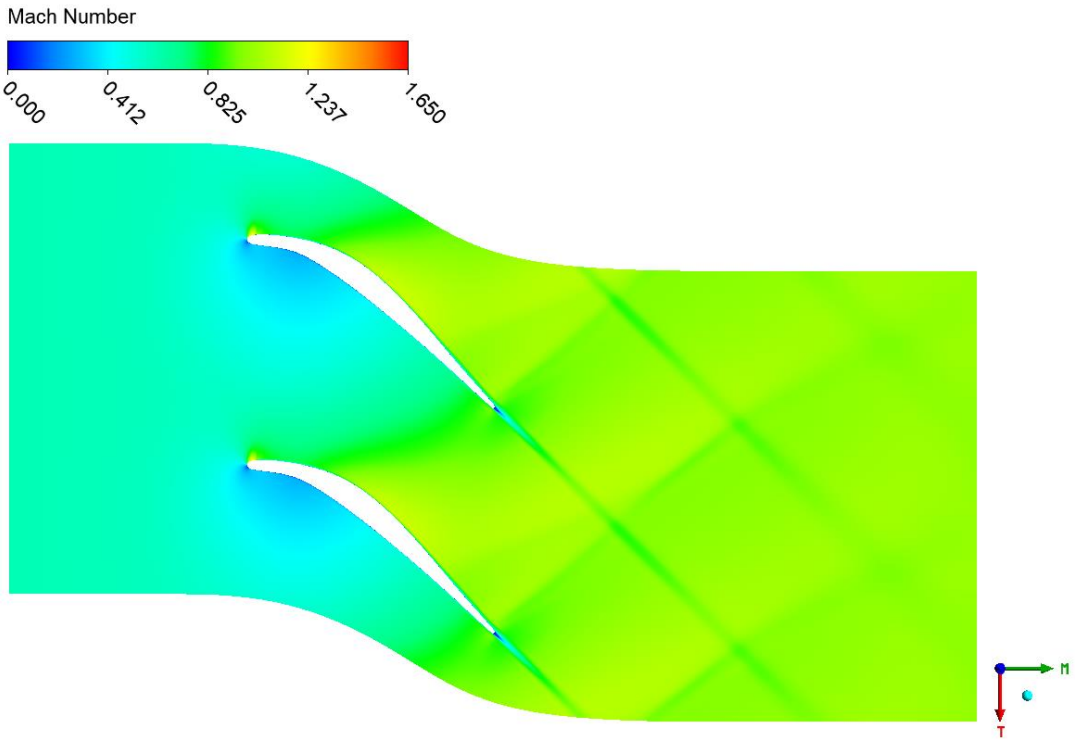

Figure 3.2.10: Optimized stator Mach field

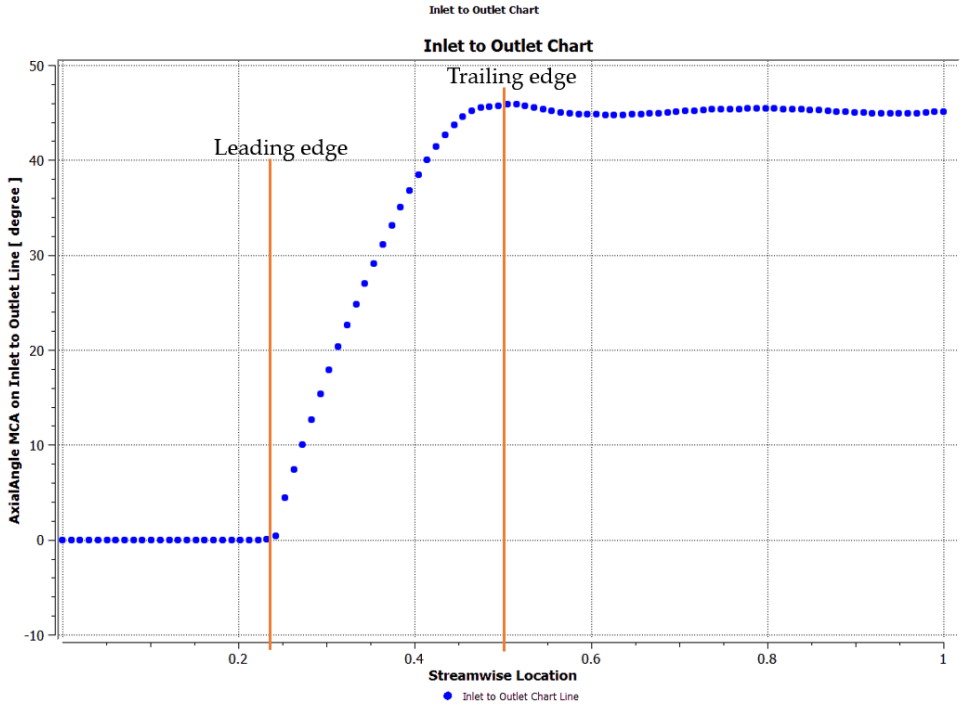

Figure 3.2.11: Optimized profile flow angle from inlet to outlet

In Figure 3.2.11, it is reported also the variation of the flow angle along blade channel to show that the flow follows very well the blades since discontinuities and kinks are not present and the outlet angle is equal to 44°, exactly the blade one. The angle is no more of 42° because changing the number of blades also changed the outlet angle, but this variation was calculated with zTurbo for the base profile and then this angle was constrained during optimization, as specified in 2.2.2 Optimization.

The pressure losses of the optimized profile are 1.85%, which results in a reduction of the 42.19% compared to base profile losses. This also produce an increase of the inlet Mach number: $M_0 = 0.612$. This leads to a mass flow rate of $101\frac{kg}{s}$, which is a little bit higher than the design one of $100\frac{kg}{s}$, but considering that rotor is not present, yet, and that it has influence on the upstream flow since the absolute axial velocity is lower than sound speed, we accepted this difference.

The losses calculated by zTurbo for this case are 2.1%. Considering that it is a mean line code, it is not able to see the difference between the optimized profile and the base one because their inlet and outlet blade heights are equal, their blades number is equal and also the geometric angles are equal. Since pressure losses of the base and optimized profile are respectively of 3.2% and 1.85%, then zTurbo losses of 2.1% are between them. This shows that the extrapolation method for Traupel profile losses can give a good estimation of the losses, staying very closed to the optimized ones.

3.2.3 Stator 3D analysis

The 3D channel is reported in Figure 3.2.12.

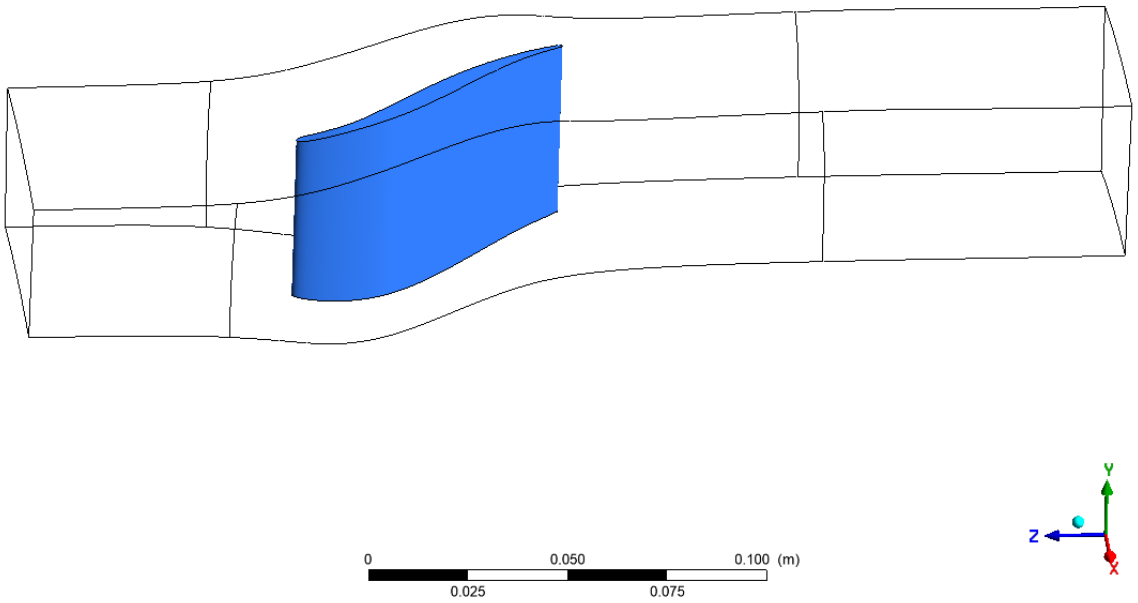

Figure 3.2.12: 3D stator blade channel

The main 3D features that can be reported are a small flow detachment on hub and shroud in correspondence of leading edge (Figure 3.2.13) and two small separations on suction side of the trailing edge (Figure 3.2.14).

As shown in Figure 3.2.13, the hub and shroud separations are recovered at about $\frac{1}{4}$ of the axial chord (Figure 3.2.13 d), so where the blade deflects and so where there is the area restriction. This acceleration allows the boundary layer to get reattached. So this shows that the endwalls contouring does not create problems on hub and shroud.

Separations on trailing edge suction side (Figure 3.2.14 a) are due to the presence of secondary flows, as shown by the vorticity in Figure 3.2.14 b). This kind of structure could not be seen in 2D simulations since they develop in the surface perpendicular to the blade to blade plane.

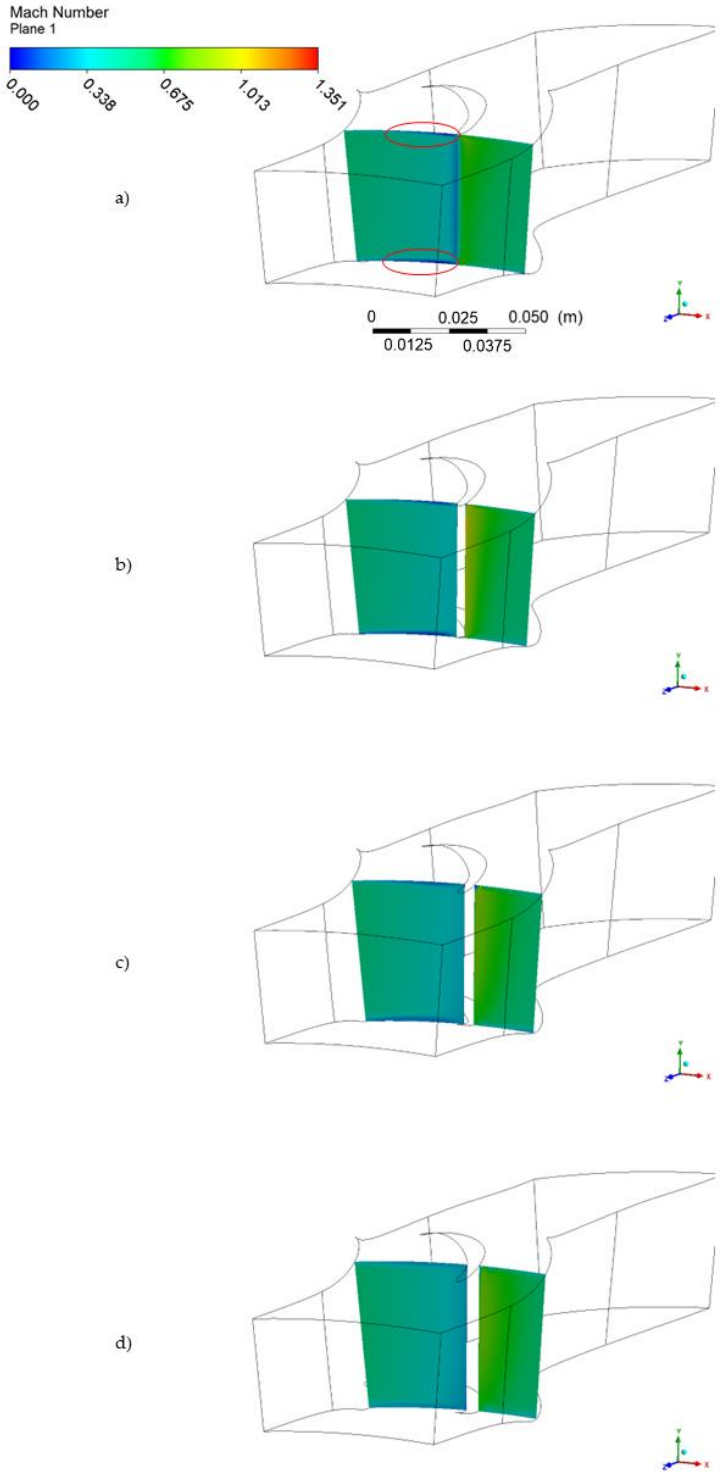

Figure 3.2.13: Hub and shroud separation. In a) the separations are evidenced with two red ellipses. From a) to d) the plane moves downstream to show the separation behavior.

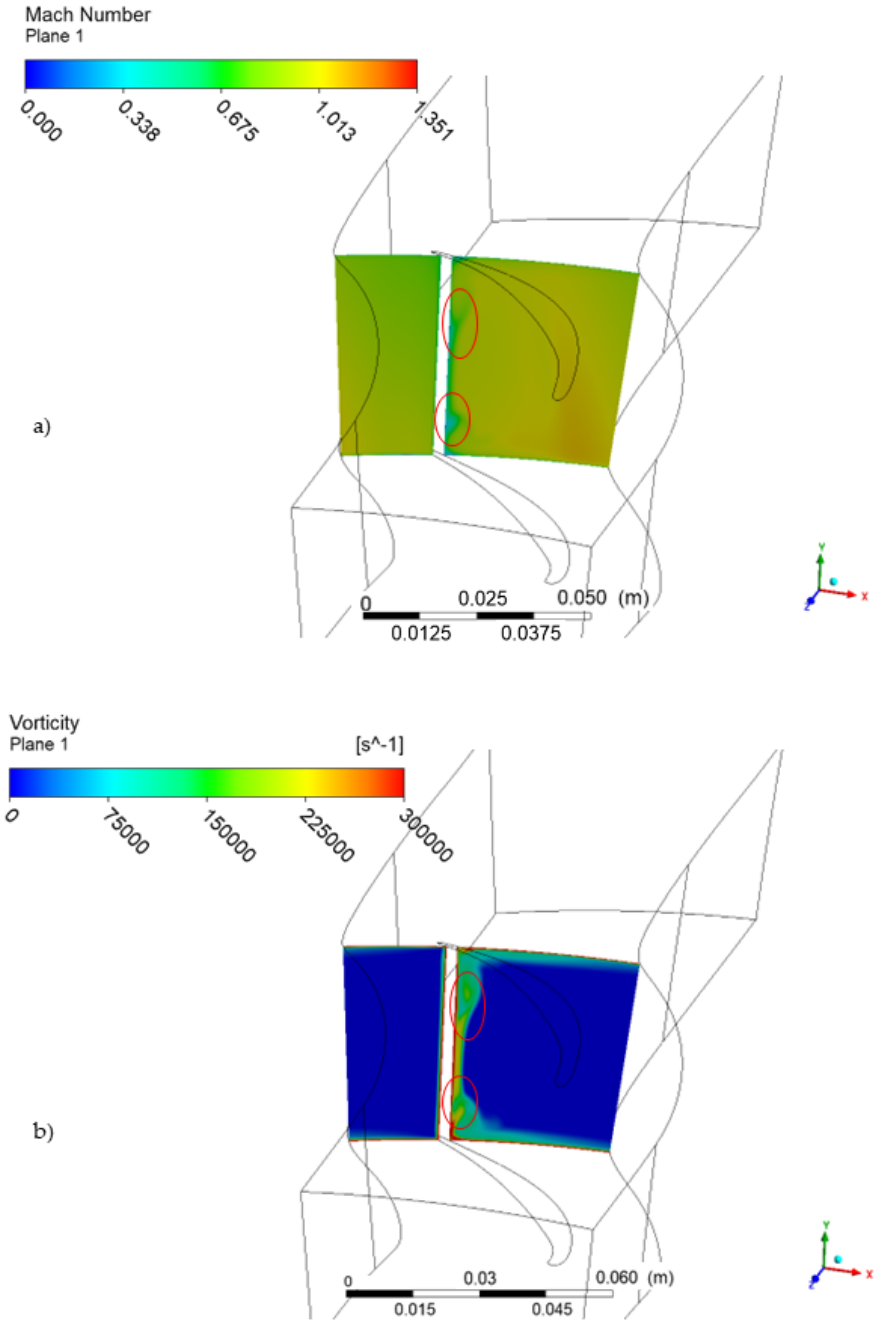

Figure 3.2.14: Separations evidenced with red ellipses on suction side of trailing edge. a) represents the Mach field, b) represents the vorticity.

This 3D simulation gives as pressure losses 7.07% and a mass flow rate of 98.34 $\frac{kg}{s}$, so a little bit smaller than the design one. The increment of losses from the 2D analysis is due to the presence of the secondary flows and to the friction with endwalls, that cannot be taken into account in 2D simulations.

zTurbo for this case estimates pressure losses of 16.97%. This shows that the secondary losses are totally overestimated and that the extrapolation of Traupel correlations does not work for secondary losses, but only for profile ones.

3.2.4 Mechanical analysis results

Mechanical resistance of turbine blades is not a negligible aspect. Even if it is not the focus of this work, it is important also to consider it, because a blade that is fluid-dynamically perfect but that breaks during its operation is useless.

For this reason, a mechanical assessment was performed on the base profile in order to be sure to have a good optimization starting point also from this point of view. Then, also the optimized profile was assessed to check if it can withstand the applied loadings. These two assessments gave both positive results, summarized in Figure 3.2.15 and Figure 3.2.16.

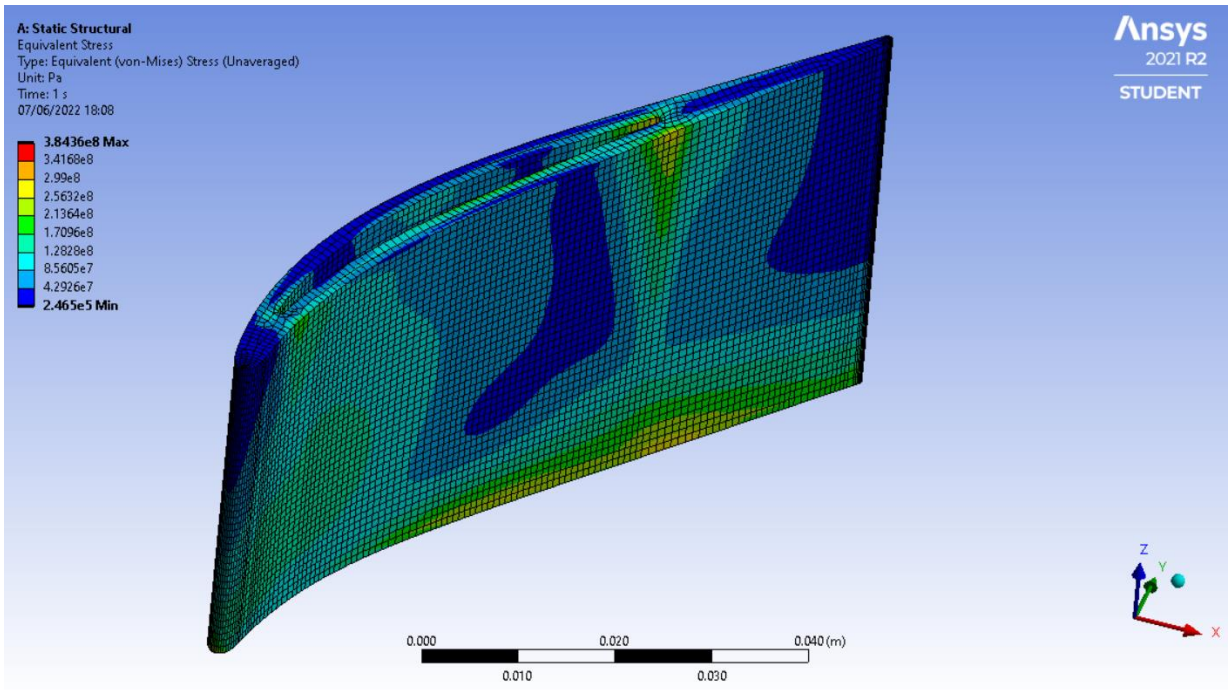

Figure 3.2.15: Base profile stress.

a)

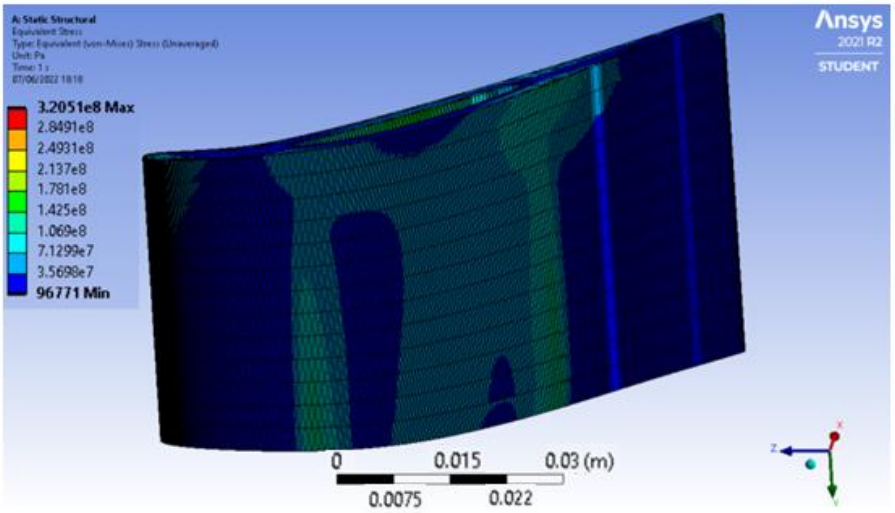

b)

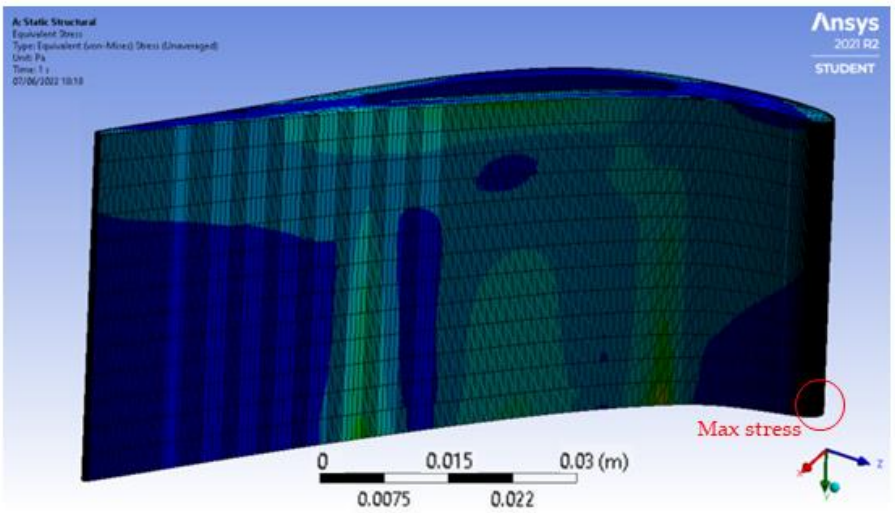

Figure 3.2.16: Optimized profile stress. a) represents suction side region, b) pressure side region.

For the base profile maximum stress is 384 MPa, so, considering the yield strength of the material at 760° C of 758 MPa, the safety coefficient is of 1.97.

For the optimized profile the maximum stress is of 320 MPa, so the safety coefficient is 2.37.

For both profiles the maximum stress is placed at the base of leading edge (Figure 3.2.16 b). Considering that in the real application there is a fillet between blade and base, the real maximum stress should be lower than the one calculated from these simulations.

3.2.5 Off-Design analysis

Due to the highly non uniformities present in the flow coming from rotating detonation combustor, a brief analysis of how the stator behaves in off-design condition was done. There were simulated high inlet total pressure ($P_{t_0} = 20\ bar$) and incidence variation ($\pm 10°$) (Figure 3.2.18 and Figure 3.2.19).

The effects of high pressure are the increasing of the mass flow rate, the arise of the fish tails at stator trailing edge and the increase of the intensity of the shocks since they are at higher Mach number than in design conditions (comparison between Figure 3.2.10 and Figure 3.2.18).

The inlet Mach number for the higher pressure is $M_0 = 0.616$, which is similar to the 0.612 of design conditions. Referring to Equation 3.2, we can see the elements that influence the mass flow rate in a duct.

$$\dot{m} = \left(1 + \frac{\gamma-1}{2} \cdot M\right)^{\frac{\gamma}{\gamma-1}} \cdot M \cdot \sqrt{\gamma} \cdot \frac{P_t \cdot S}{\sqrt{R \cdot T_t}} \qquad \text{Equation 3.2}$$

Since Mach did not vary in a sensible way and the inlet total temperature is constant, then also the static temperature will not be varied in a sensible way. This means that also the variation of γ is small since we used NASA polynomials to model it and they depend only on temperature. The section of the duct is constant, so at the end what is significantly changed is the inlet total pressure. This is why mass flow rate increases up to $\dot{m} = 135\ \frac{kg}{s}$ for higher pressure. The pressure losses for this case are of 3.32%, so the stator is able to manage an increase in the mass flow rate still keeping good performances.

The arise of the fish tails cause a very small boundary layer separation on the suction side of the adjacent blade, a little bit upstream of the trailing edge. This is caused by the interaction between the fish tail shock and the boundary layer.

About incidence variation, there is a good resistance for negative incidences (Figure 3.2.19 b), but for positive ones the flow easily detaches from the blade pressure side (Figure 3.2.19 a). Convention for incidence sign is reported in Figure 3.2.17.

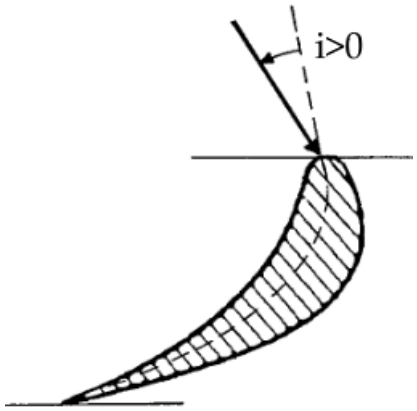

Figure 3.2.17: Incidence sign convention

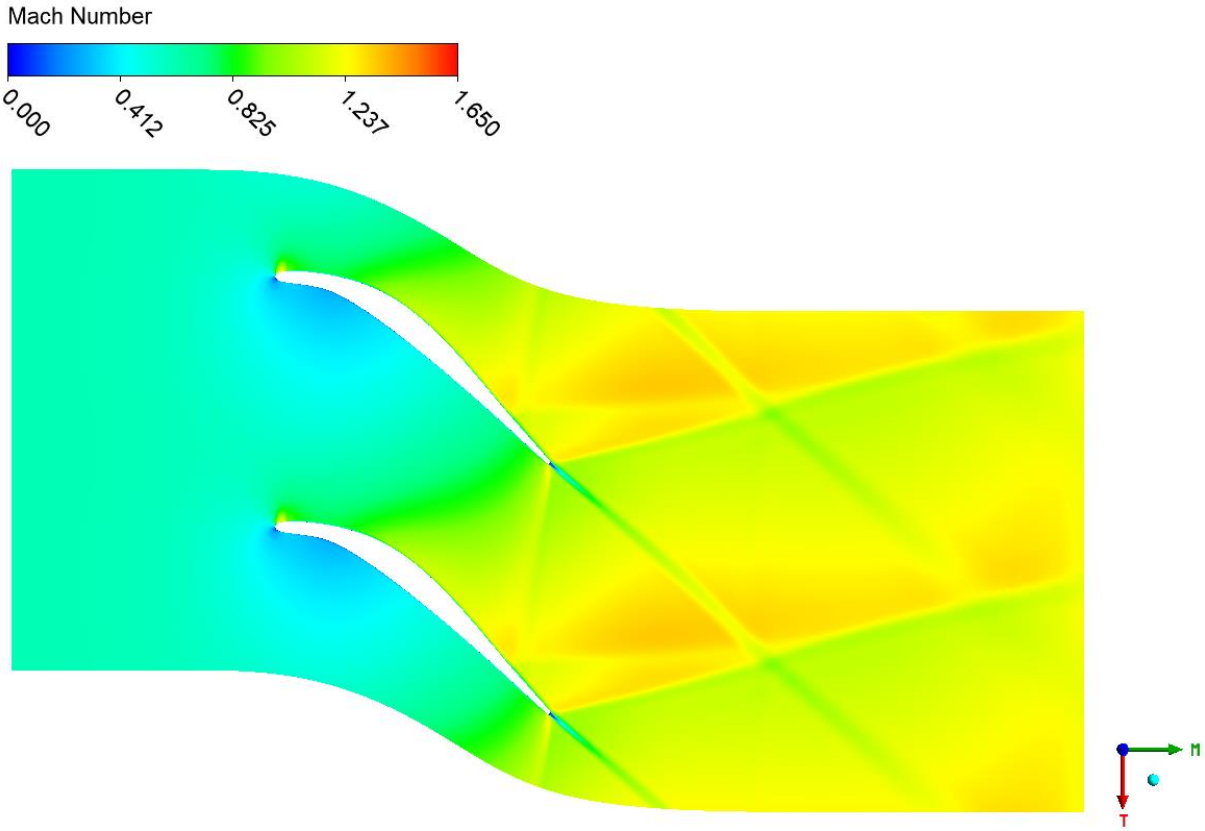

Figure 3.2.18: Off design condition: inlet total pressure of 20 bar.

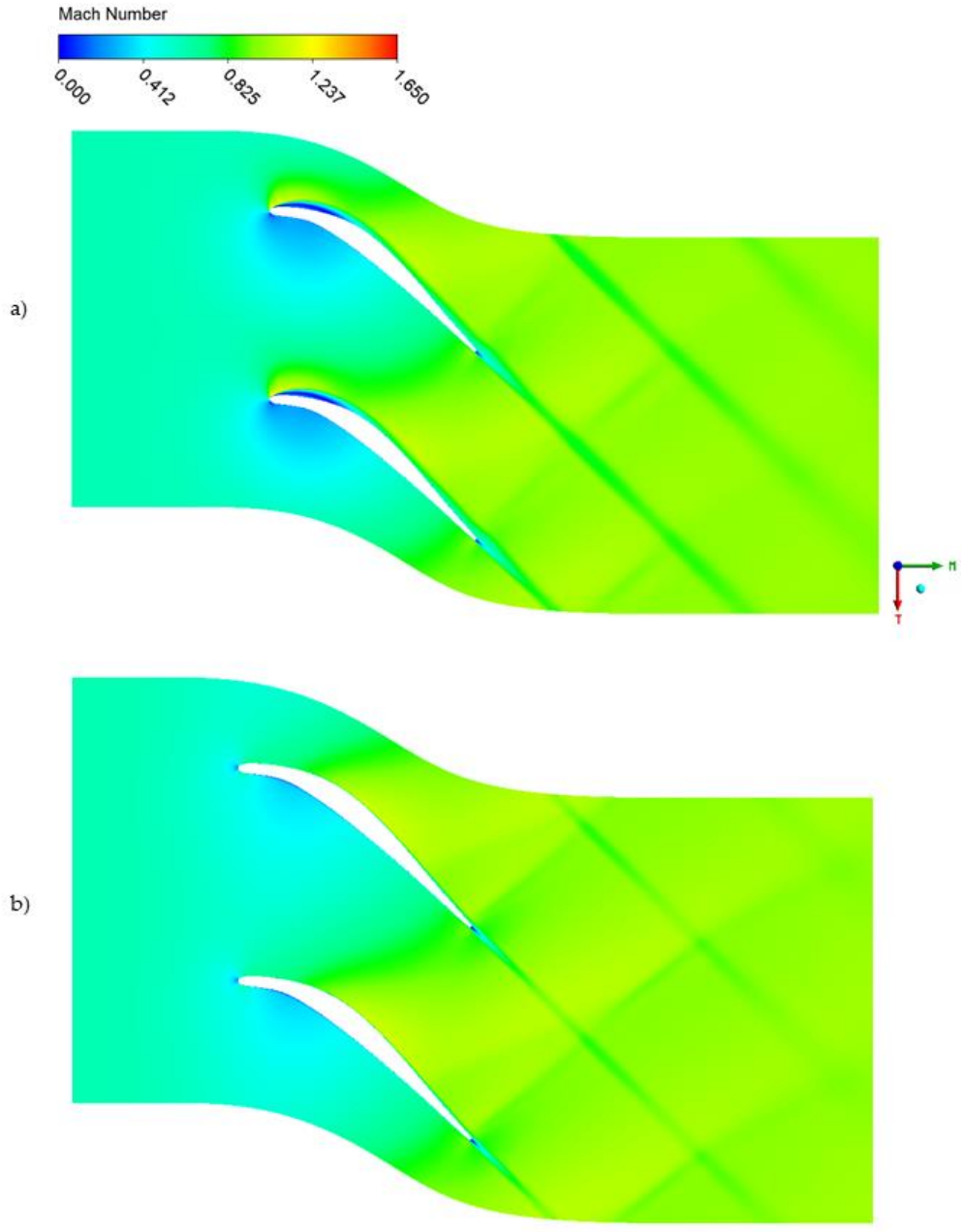

Figure 3.2.19: Off design conditions: a) positive incidence of 10°, b) negative incidence of -10°.

3.3 Rotor Results

3.3.1 2D results

About rotor profile generation, we firstly considered to take the rotational speed $\omega = 8000\,rpm$ from the mean line analysis. Then we used it to calculate the rotor inlet peripheral speed $U_1 = 304.6\frac{m}{s}$. From optimized stator 2D CFD simulation we found the absolute speed entering the rotor, which components are $V_{1_{ax}} = 536.09\frac{m}{s}$ and $V_{1_{tan}} = 538.36\frac{m}{s}$. So, from these values we found the relative inlet velocity with its components: $W_1 = (W_{1_{ax}}, W_{1_{tan}}) = (V_{1_{ax}}, V_{1_{tan}} - U_1) = (536.09, 233.76)$. Considering that the static temperature is $T_1 = 1541\,K$, it results that the inlet relative Mach number is $M_{1w} = 0.8$.

Then we chose to use a leading edge thickness $LE_r = 3$ mm, a little bit higher than stator because rotor is more loaded due to centrifugal force. Due to blade presence, the cross sectional area reduces when the flow encounters blades leading edge (Figure 3.3.1).

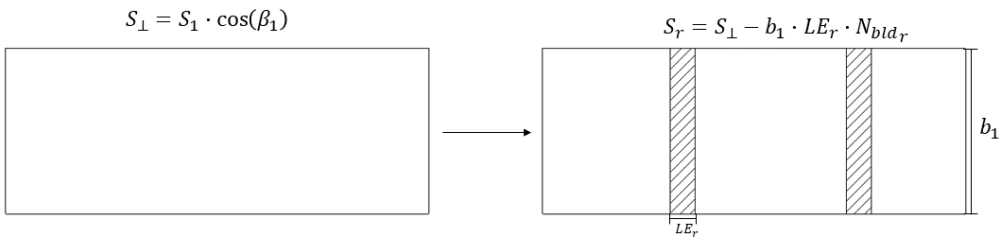

Figure 3.3.1: Cross sectional area perpendicular to the flow

Where $S_\perp$ is the area perpendicular to the flow direction, S_r is the area perpendicular to the flow considering also blades thickness.

The problem is that we are at high Mach number, so for a small area reduction we get strong accelerations, as demonstrated by the star quantities of Figure 3.3.2. It means that, to reach the sonic condition at the leading edge of rotor blades, the ratio between S_r and $S_\perp$ should be grater or equal to 0.9632.

Having the sonic condition at rotor inlet means that the rotor should be transonic, but we want to avoid the design of a transonic cascade, so, applying this decision to

the previous considerations, it is possible to find the maximum number of blades that does not produce sonic flow at rotor leading edge (Equation 3.3).

$$\frac{S_r}{S_\perp} \geq 0.9632$$
$$\rightarrow \frac{S_1 \cos(\beta_1) - b_1 LE_r N_{bld_r}}{S_1 \cos(\beta_1)} \geq 0.9632$$
$$\rightarrow 1 - \frac{b_1 LE_r N_{bld_r}}{S_1 \cos(\beta_1)} \geq 0.9632$$
$$\rightarrow b_1 LE_r N_{bld_r} \leq (1 - 0.9632) \cdot S_1 \cos(\beta_1)$$
$$\rightarrow N_{bld_r} \leq \frac{(1-0.9632) \cdot S_1 \cos(\beta_1)}{b_1 LE_r}$$ Equation 3.3

From the relative velocity components we get $\beta_1 = \arctan\left(\frac{W_{1tan}}{W_{1ax}}\right) = 23.6°$. The other values are known from mean line analysis and are: $S_1 = 0.1029\ m^2$, $b_1 = 44.6\ mm$, $LE_r = 3\ mm$. So, it results that $N_{bld_r} \leq 25.93\ blades \rightarrow N_{bld_r} = 25\ blades$.

The outlet blade height is $b_2 = 53.5\ mm$, considering the flaring of 1.2 also for rotor. The endwalls variation is linear from inlet to outlet. To generate the profile for the 2D simulations we followed the same procedure of the stator: we considered both 3D and 2D profiles to have the same outlet to inlet area ratio. The rotor inlet blade height for the 2D profile is equal to the 2D stator outlet blade height. Then the 2D rotor outlet blade height was found through the area ratio.

M	p/p_0	ρ/ρ_0	T/T_0	a/a_0	A^*/A
.70	.7209	.7916	.9107	.9543	.9138
.71	.7145	.7865	.9084	.9531	.9197
.72	.7080	.7814	.9061	.9519	.9254
.73	.7016	.7763	.9037	.9506	.9309
.74	.6951	.7712	.9013	.9494	.9362
.75	.6886	.7660	.8989	.9481	.9412
.76	.6821	.7609	.8964	.9468	.9461
.77	.6756	.7557	.8940	.9455	.9507
.78	.6690	.7505	.8915	.9442	.9551
.79	.6625	.7452	.8890	.9429	.9592
.80	.6560	.7400	.8865	.9416	.9632
.81	.6495	.7347	.8840	.9402	.9669
.82	.6430	.7295	.8815	.9389	.9704
.83	.6365	.7242	.8789	.9375	.9737
.84	.6300	.7189	.8763	.9361	.9769
.85	.6235	.7136	.8737	.9347	.9797
.86	.6170	.7083	.8711	.9333	.9824
.87	.6106	.7030	.8685	.9319	.9849
.88	.6041	.6977	.8659	.9305	.9872
.89	.5977	.6924	.8632	.9291	.9893
.90	.5913	.6870	.8606	.9277	.9912
.91	.5849	.6817	.8579	.9262	.9929
.92	.5785	.6764	.8552	.9248	.9944
.93	.5721	.6711	.8525	.9233	.9958
.94	.5658	.6658	.8498	.9218	.9969
.95	.5595	.6604	.8471	.9204	.9979
.96	.5532	.6551	.8444	.9189	.9986
.97	.5469	.6498	.8416	.9174	.9992
.98	.5407	.6445	.8389	.9159	.9997
.99	.5345	.6392	.8361	.9144	.9999
1.00	.5283	.6339	.8333	.9129	1.0000

Figure 3.3.2: Star quantities table. Red ellipses show the point in which we are.

So, now we have the leading edge thickness, the inlet blade angle and the number of blades. For the trailing edge we decided to keep it 1 mm thick as the stator one. For the outlet blade angle, the absolute outlet angle should be $\alpha_2 = -21°$ to have a flaring of 1.2. This leads to have a relative outlet angle of $\beta_2 = -37°$, which is also the blade geometrical angle. These values are taken from zTurbo, considering only profile losses since we are performing 2D simulations.

Now there is the need to find the axial chord. We started from considering the solidity given by Zweifel (Equation 3.4b), then, knowing the pitch from trailing edge thickness, outlet blade angle and the number of blades (Equation 3.4a), it is possible to find the axial chord through Equation 3.4b.

$$pitch_r = \frac{2\pi R_m}{N_{bld_r}} - \frac{TE_r}{\cos(\beta_2)} = 0.09\ m \qquad \text{Equation 3.4a}$$

$$\frac{pitch_r}{chord_r} = 0.559 \quad \rightarrow \quad chord_r = 0.161\ m \qquad \text{Equation 3.4b}$$

Finally, for the thickness distribution, it was decided to apply a maximum thickness of 14 mm at 50% of axial chord because it seemed good both from mechanical and fluid dynamic points of views. Mechanical stress analysis will show that it is a good value.

For the generation of the first profile, we used a camber line with the deflection applied at the centre of the blade, so we created a blade that will be called "central loaded".

Now there is the need to decide the distance between stator and rotor. Usually two main aspects influence this decision: the interaction between stator wakes and rotor and the mixing losses. Reducing the distance, the importance of wakes-rotor interaction increases, while the one of mixing losses decreases. Increasing the distance, the importance of wakes-rotor interaction decreases, while the one of mixing losses increases. So, there is an optimum distance where the combination of the two kinds of losses is the smallest. But in this work there are also other aspects to consider: from stator optimization, the modification of the endwalls was allowed up to $\frac{1}{5}$ of stator chord downstream of stator trailing edge, so we could not place the rotor at a lower distance since it will modify the stator channel optimized shape; from a numerical point of view it is better to have the mixing plane at equal distance from stator and rotor and, finally, the computational time to perform the optimum stator-rotor distance analysis was too high for the scope of this thesis. So, considering all these aspects, it was decided to place the rotor at a distance of $\frac{2}{5}$ of stator chord from stator. In this way the mixing plane could be placed at $\frac{1}{5}$ of stator axial chord from both the cascades without changing stator optimized geometry. So, the total distance between stator and rotor is of 56 mm.

The Mach field of the first profile is reported in Figure 3.3.3, with also the stage main performances. For the stator, the represented field is the absolute Mach number, instead, for the rotor, the represented Mach is in the rotating frame of reference. This consideration will be valid for all the fields presented unless explicitly specified.

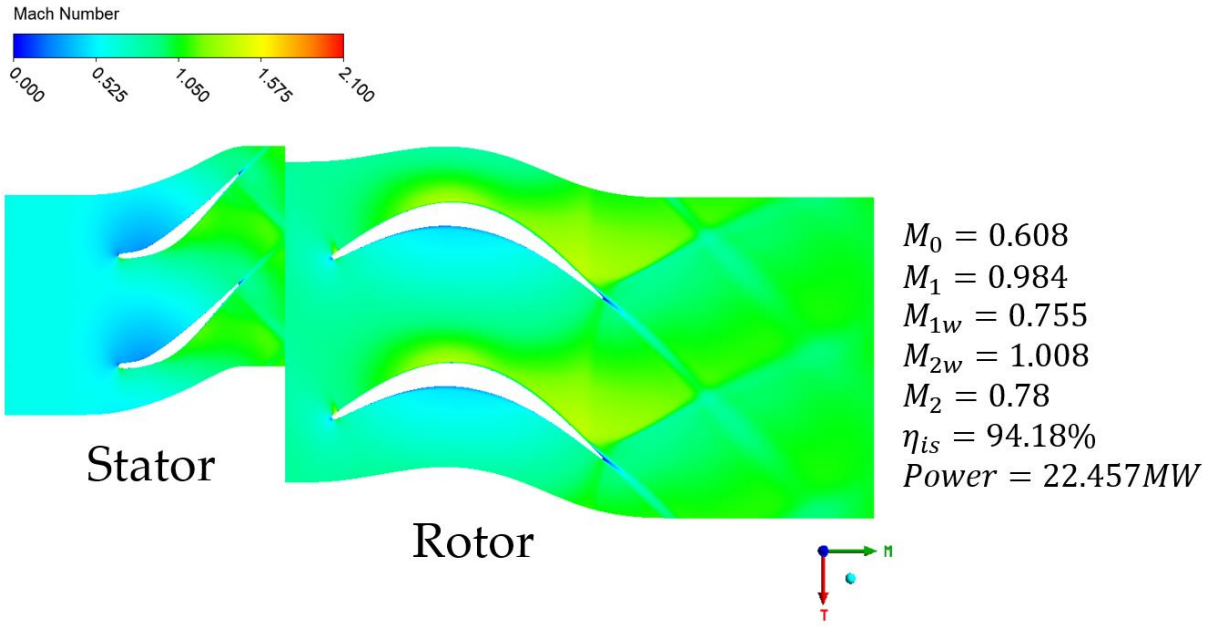

Figure 3.3.3: First rotor profile

The performances are pretty good, the efficiency is of 94.18%, similar to the 95.36% predicted by zTurbo, showing again that for profile losses the extrapolation is good.

The presence of the rotor causes a blockage to the flow that is cause of the small reduction of M_1 compared to the simulation of the stator. This is why the rotor relative inlet Mach number M_{1w} is smaller than the previously calculated 0.8.

For the flow behaviour there is a small overspeed region on the suction side of rotor leading edge, but it does not create problems to the boundary layer. There is also a weak fish tail that interacts with the suction side of the adjacent blade causing a small separation just before the trailing edge.

Since the rotor axial chord is very long and the blade number is already small, here we tried to reduce axial chord to reduce the weight of the stage. We tried to bring the chord to 0.12 m and 0.14 m (Figure 3.3.4).

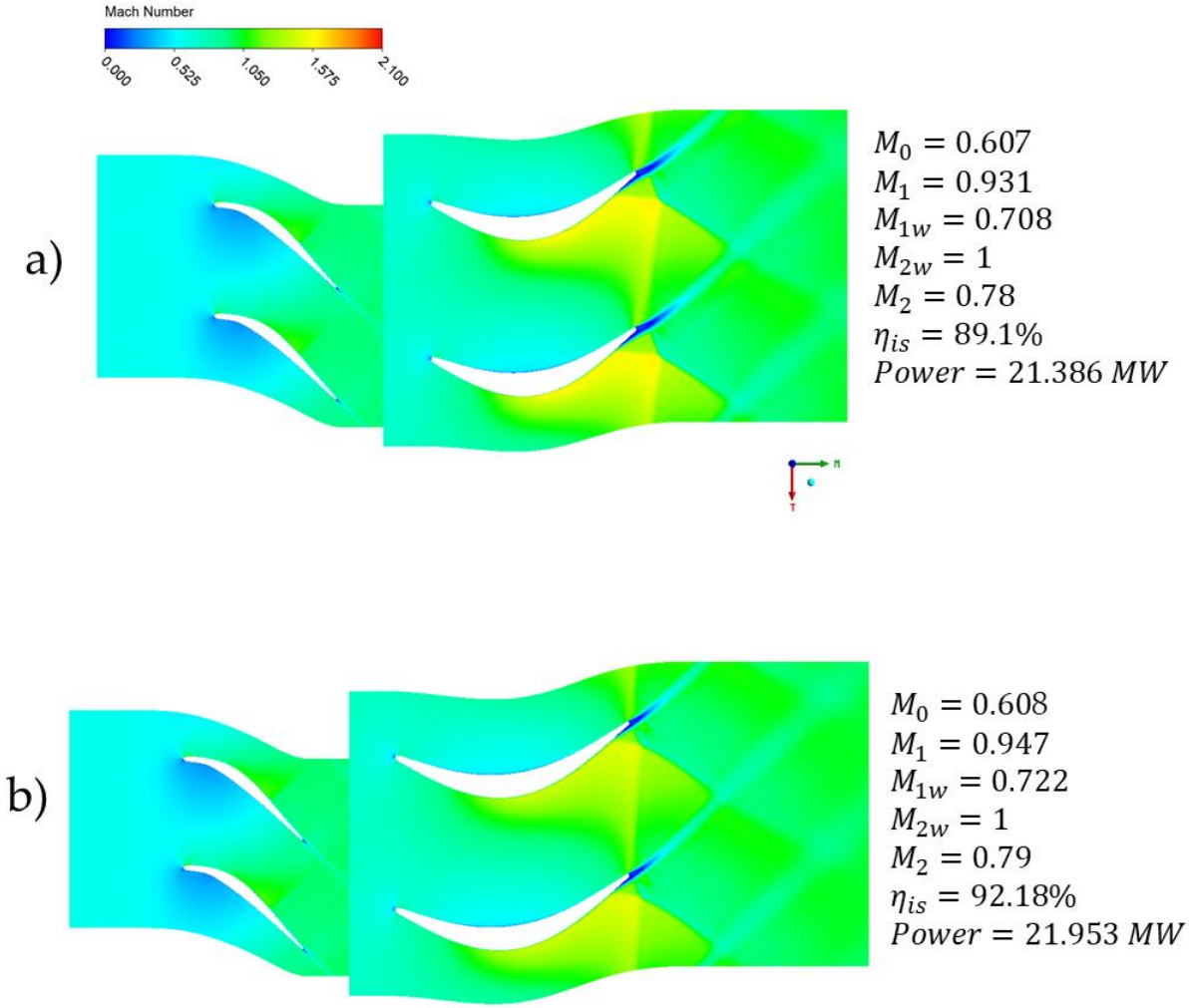

Figure 3.3.4: Rotor axial chord comparison. a) is the 0.12 m chord, b) is the 0.14 m chord

It can be seen that in both cases we get a worsening of performances due to the important flow separation and shocks interaction at rotor trailing edge. Different trials with endwalls contouring were made to try to increase performances, like it was done for stator, but in this case it did not worked: the most of the simulation did not reached the convergence either, due to strong flow detachment. In Figure 3.3.5 are reported different trials for the profile with 0.12 m axial chord, to show their negative results. So, it was decided to keep the axial chord of 0.161 m.

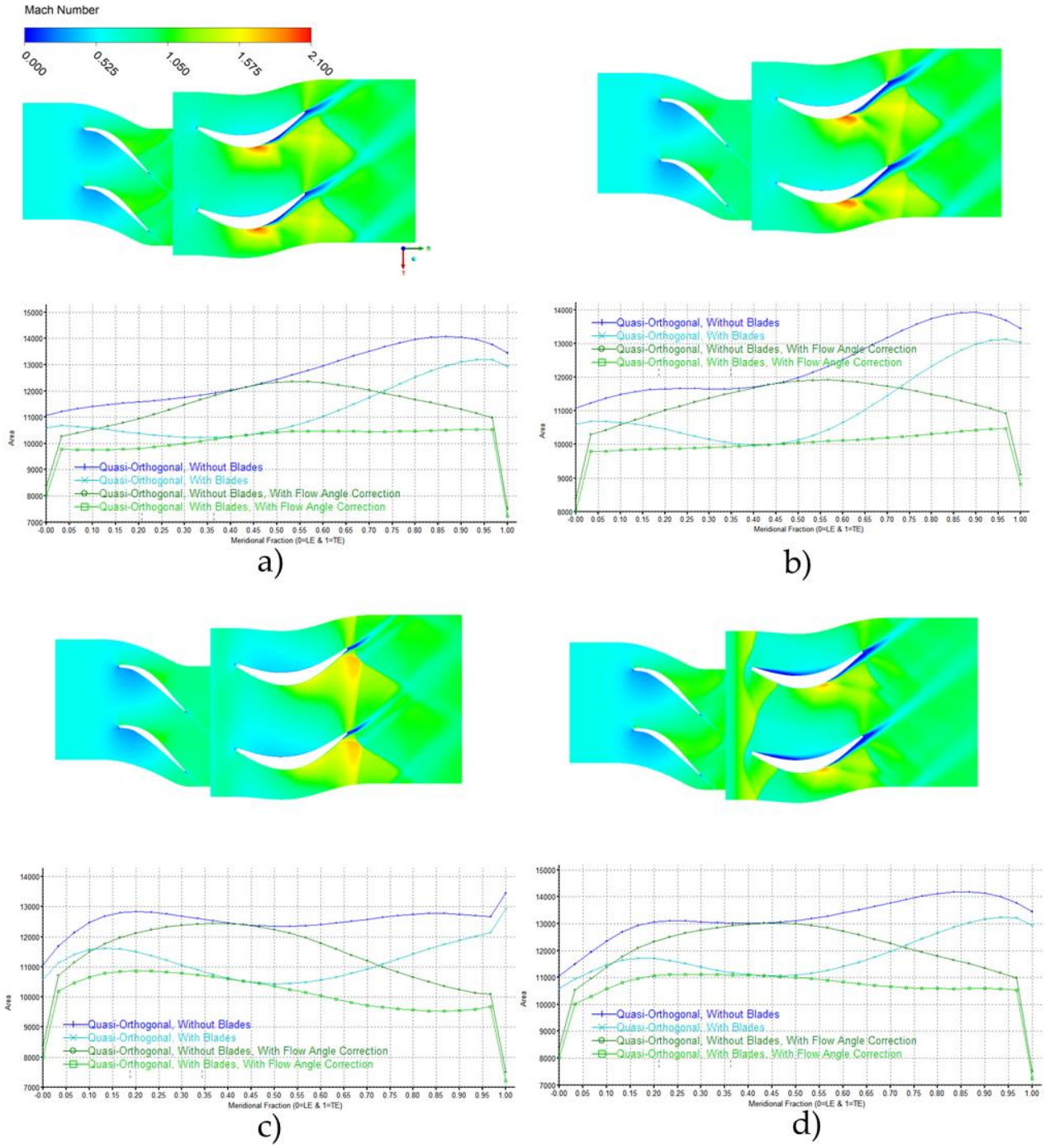

Figure 3.3.5: Axial chord 0.12 m different endwalls trials. Area is in mm^2

At this point we tried two different camber line shapes: one that is more front loaded (Figure 3.3.6 a) and one that is more back loaded (Figure 3.3.6 b). The back loaded did not reached the convergence, so we did not use it for further improvements.

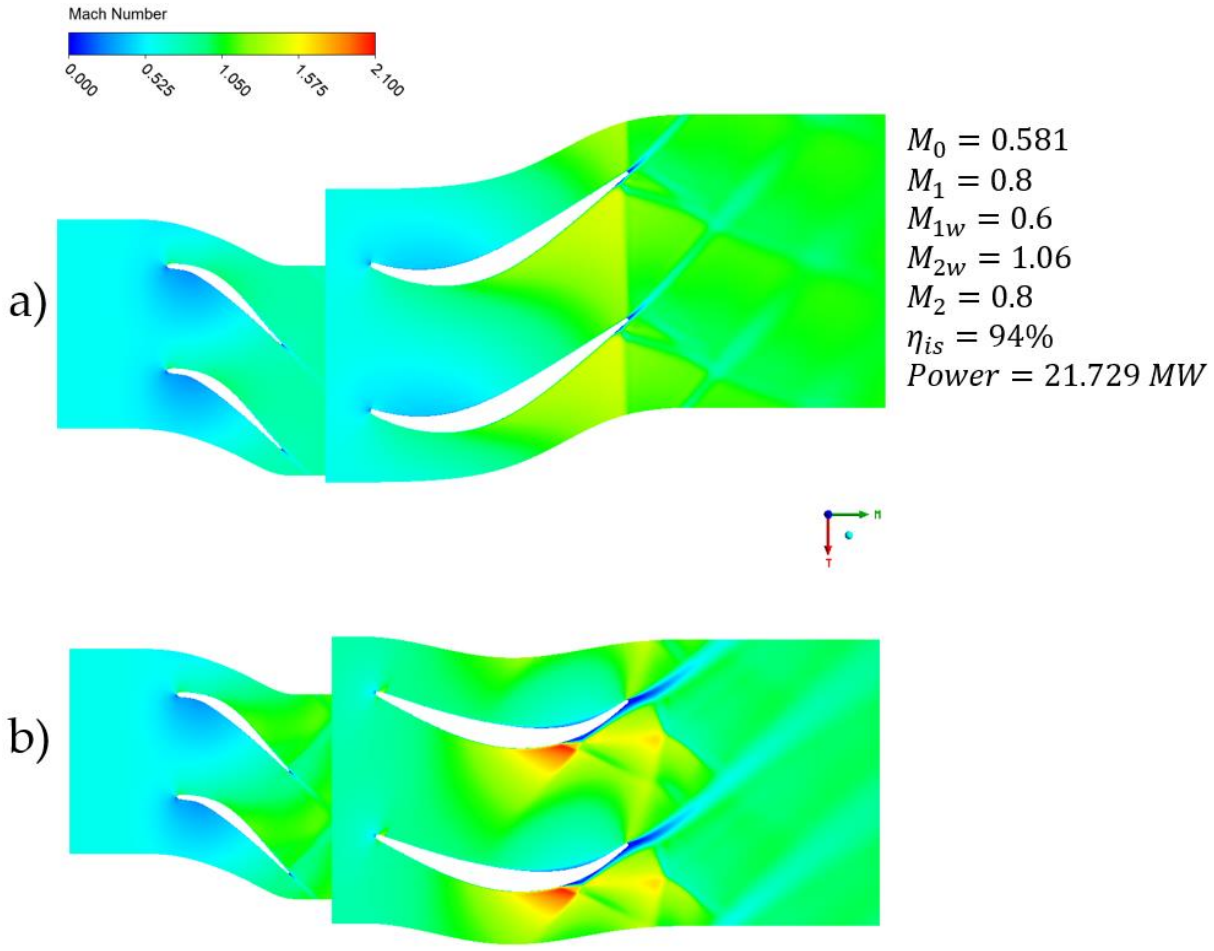

Figure 3.3.6: a) blade front loaded; b) blade back loaded

About front loaded, the shocks and their interaction at trailing edge are stronger than for the central loaded blade. This results in a higher flow blockage, so lower Mach numbers in section 1, and in a small flow separation on the suction side of the blade, just before the trailing edge. The efficiency is slightly smaller than central loaded blade.

For this front loaded blade different changes in the endwalls contouring were tried to reduce the shocks intensity and interactions, but with no success.

So, at this point, it was decided to proceed with the optimization process. We had two profiles that seems good to be improved: the central loaded and the front loaded. A mechanical stress analysis was performed for both the profiles in order to assess that the optimization is performed on blades able to withstand the loading. It shows that both the profiles do not have any problems and that there is margin to increase the loading, since both safety coefficients are greater than 1.5.

Different path could be followed from this point to continue the stage analysis. We decided to firstly optimize the front loaded profile, since it was the one with higher margin of improvements, and look at how much improvement we could get. Since the results were not satisfactory, we decided to improve central loaded blade.

Before starting the optimization of the central loaded blade, we decided to increase its flaring because, given the axial chord length, we considered that bringing rotor flaring to 1.4 was acceptable to avoid flow separations from endwalls in the 3D simulations. With this flaring, the outlet angle is $\beta_2 = -50°$. Then we decided to increase the rotational speed to reach the mechanical safety coefficient of 1.5. To do so we tried different speeds and for each speed the inlet angle and the number of blades were adjusted following the same procedure explained at the beginning of this paragraph (3.3.1 2D results), while the outlet blade angle was adjusted to reach the flaring of 1.4. So, for each speed different CFD simulations were performed to find the pressure loading to import in the mechanical stress analysis and look at the blade maximum stress.

These modifications were done because we saw that there was margin to increase mechanical stress, allowing the increase in flow deflection ad rotor speed. So we took that margin to increase the work exchanged and so the stage efficiency. Mach flow field and main performance of this blade are reported in Figure 3.3.7. The rotational speed is $\omega = 9500\ rpm$, the inlet angle is $\beta_1 = 18°$, the outlet blade angle is $\beta_2 = -50°$ and the blades number is 26.

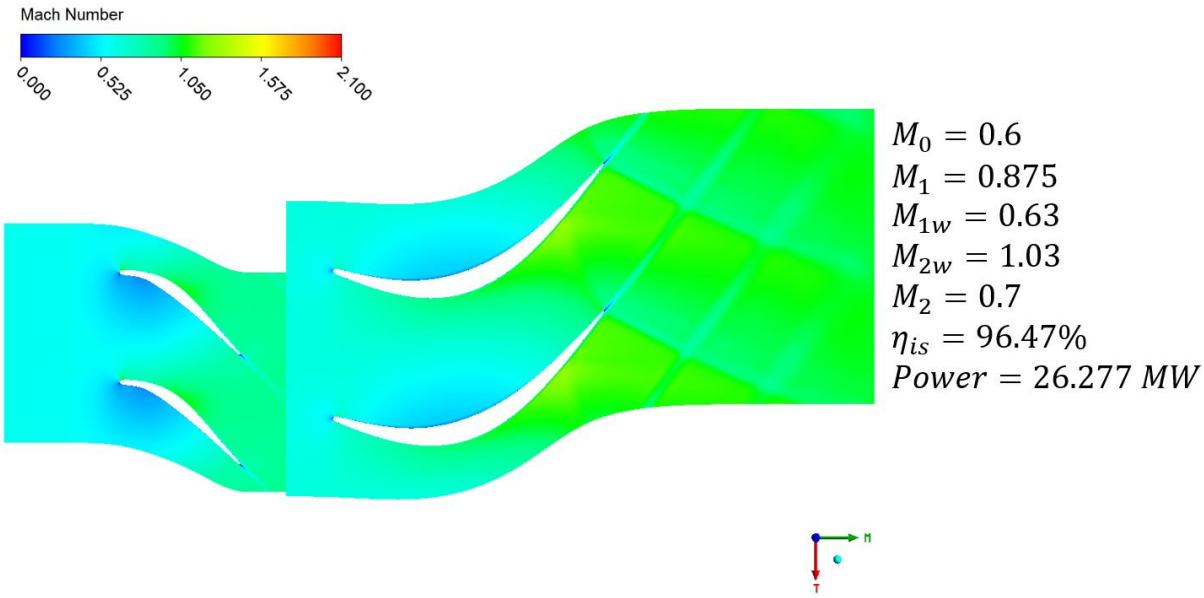

Figure 3.3.7: Profile for higher rotational speed and flaring

The maximum Mach number reached is lower than for the others profile analysed, so also the shocks intensity is lower. There is no flow separation and the gain in the exchanged work allows an increase of efficiency of 2% compared to the first central loaded profile generated. So, we decided to optimize this blade even if the Mach numbers in section 1 are lower than the desired ones.

The detailed results of the different optimizations ad mechanical analysis are reported in the following paragraphs (3.3.2 Rotor Optimization, 3.3.3 Mechanical analysis results).

3.3.2 Rotor Optimization

3.3.2.1 Front loaded blade optimization

The Mach field of the optimized profile is reported in Figure 3.3.8. From here it is also possible to look at the profile geometry which is not so good: it starts thin, then it deflects with a small curvature radius, then it increases its thickness and finally it returns thin to link with trailing edge. The meridional view of the profile is reported in Figure 3.3.9. The flow field generated by the geometry results in the generation of a fish tail that interacts with the suction side boundary layer of the adjacent blade causing its separation near the trailing edge. Moreover, the blockage given by the rotor is important since M_1 is pretty far from the value of 1. The positive aspect is the

increase of the efficiency of 1.27% compared to the front loaded base profile (Figure 3.3.6 a).

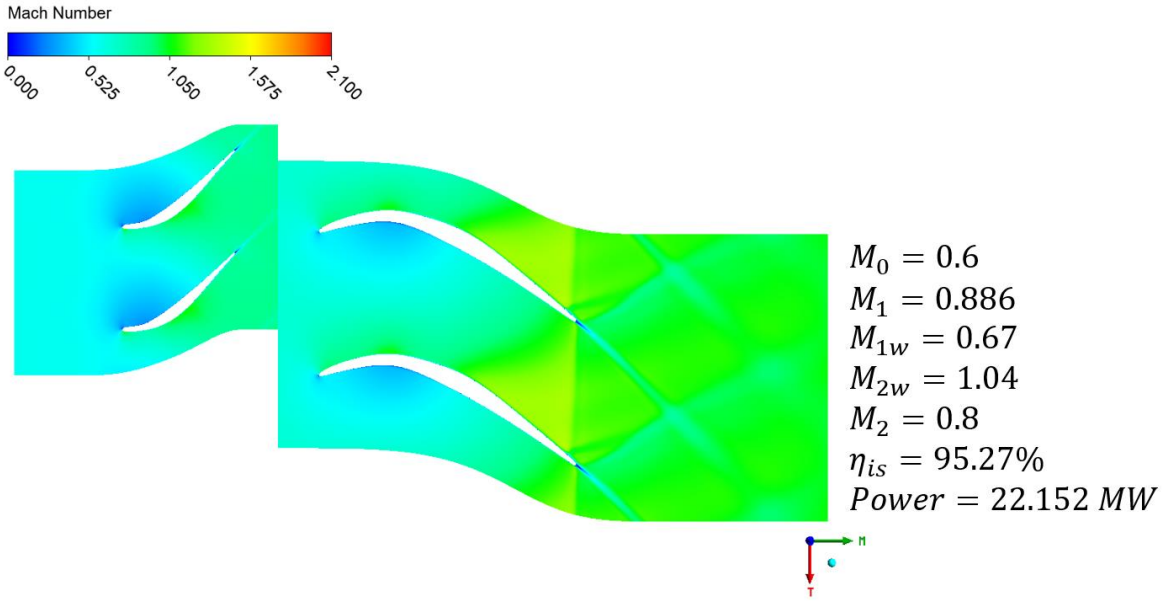

Figure 3.3.8: Front loaded optimized blade Mach field

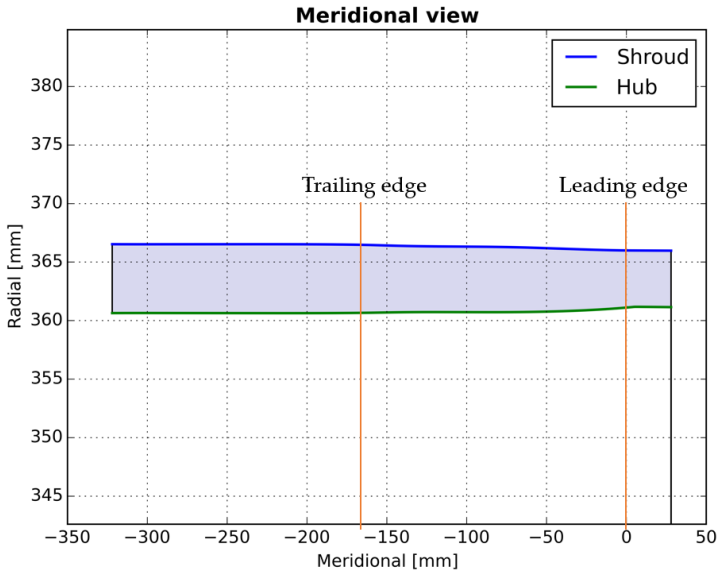

Figure 3.3.9: Front loaded optimized blade meridional view

If we look at blade pressure loading (Figure 3.3.10) and the flow angle along meridional direction (Figure 3.3.11) we can see that results are bad: in the first half chord, pressure distribution on suction side has two strong oscillations that can cause severe problems to boundary layer; there is an important overturning of the flow of about 10° downstream of trailing edge, so the blade channel is not good for this flow.

For these reasons we decided to improve the central loaded profile and not the front loaded one.

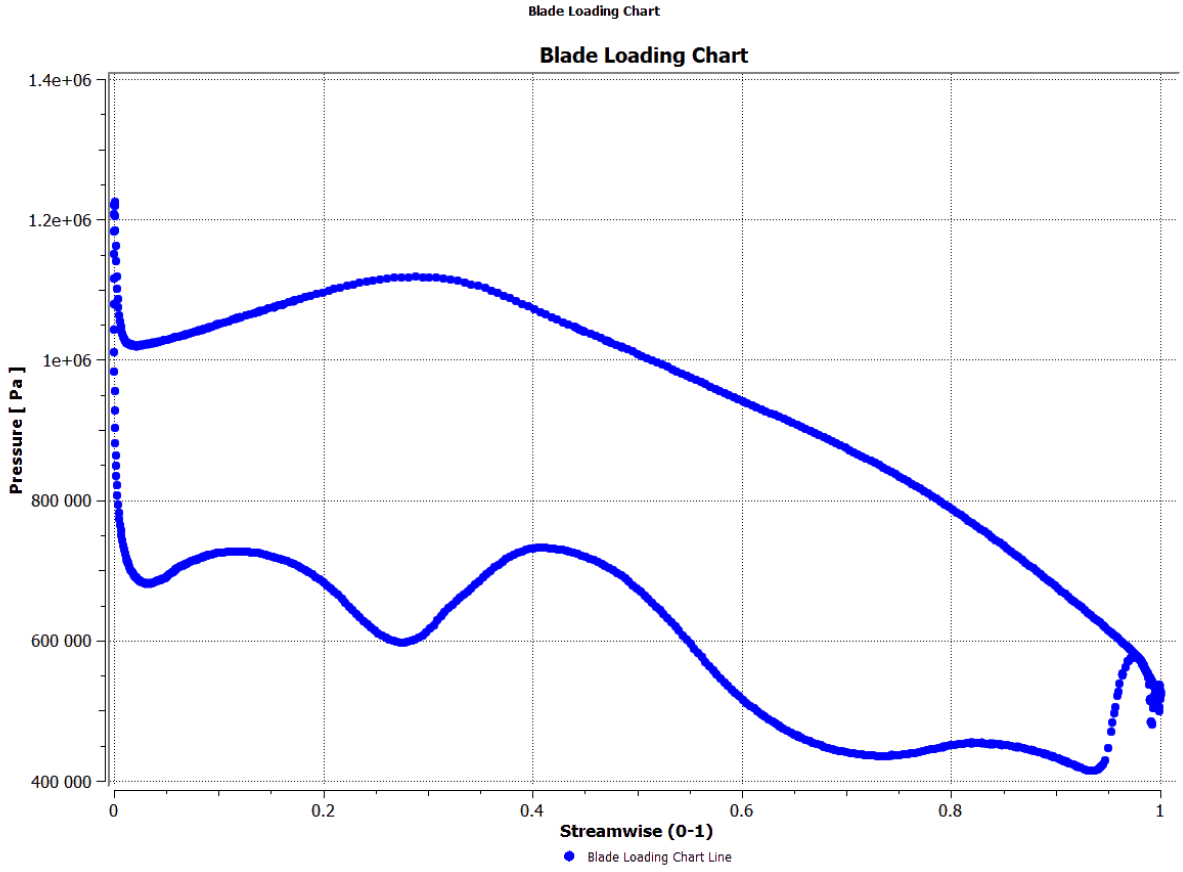

Figure 3.3.10: Front loaded optimized profile pressure loading

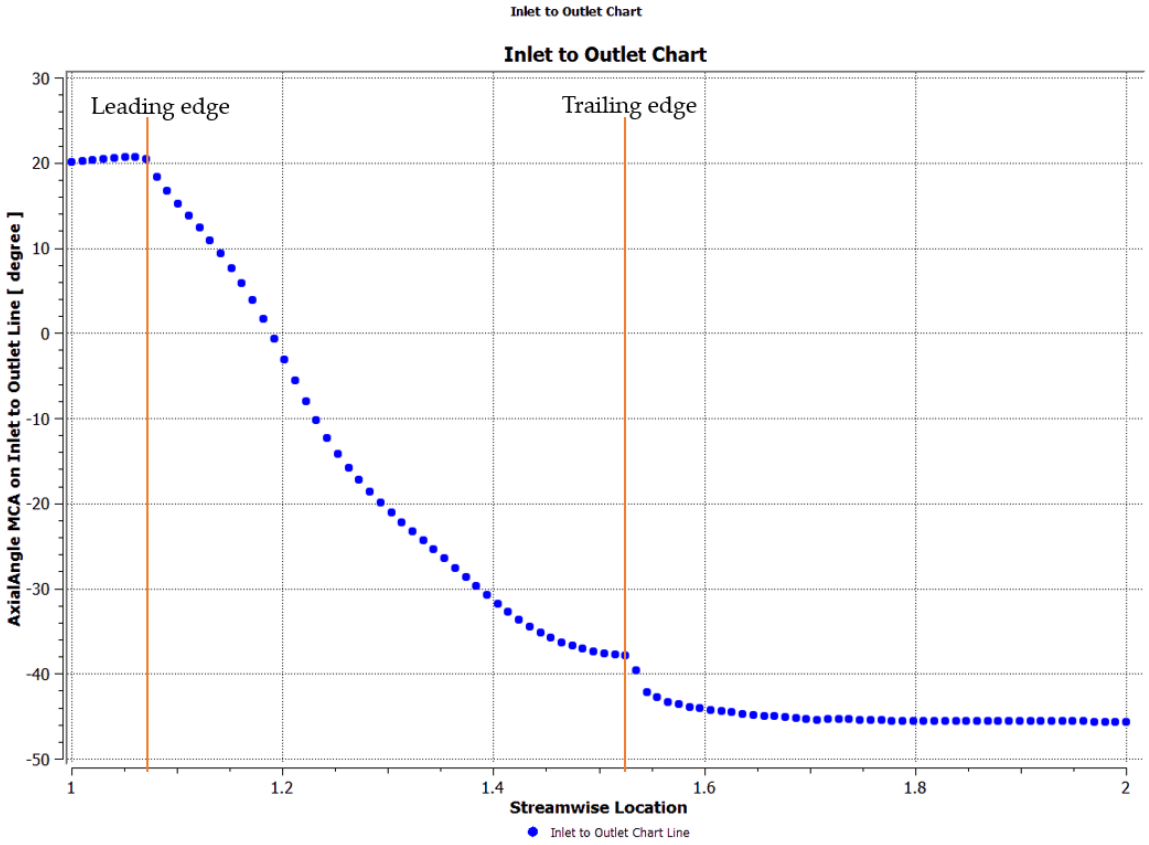

Figure 3.3.11: Front loaded optimized profile flow angle

3.3.2.2 *Central loaded blade optimization*

The optimized profile is reported in Figure 3.3.12. The optimized profile near the leading edge is lightly thinner than the base profile and then the deflection is a little bit delayed.

The meridional view is reported in Figure 3.3.13. The hub and shroud shapes coming from the optimization process presents a kink a little bit upstream of the leading edge (blue lines in Figure 3.3.13). This kind of geometry is very bad since it causes flow separation very easily. For this reason, we decided to remove manually the kink through an elliptic fillet (black lines in Figure 3.3.13). The 2D performances do not vary from the endwalls with kink to endwalls with elliptic fillet, so we kept the fillet to avoid strong flow separation in the 3D channel.

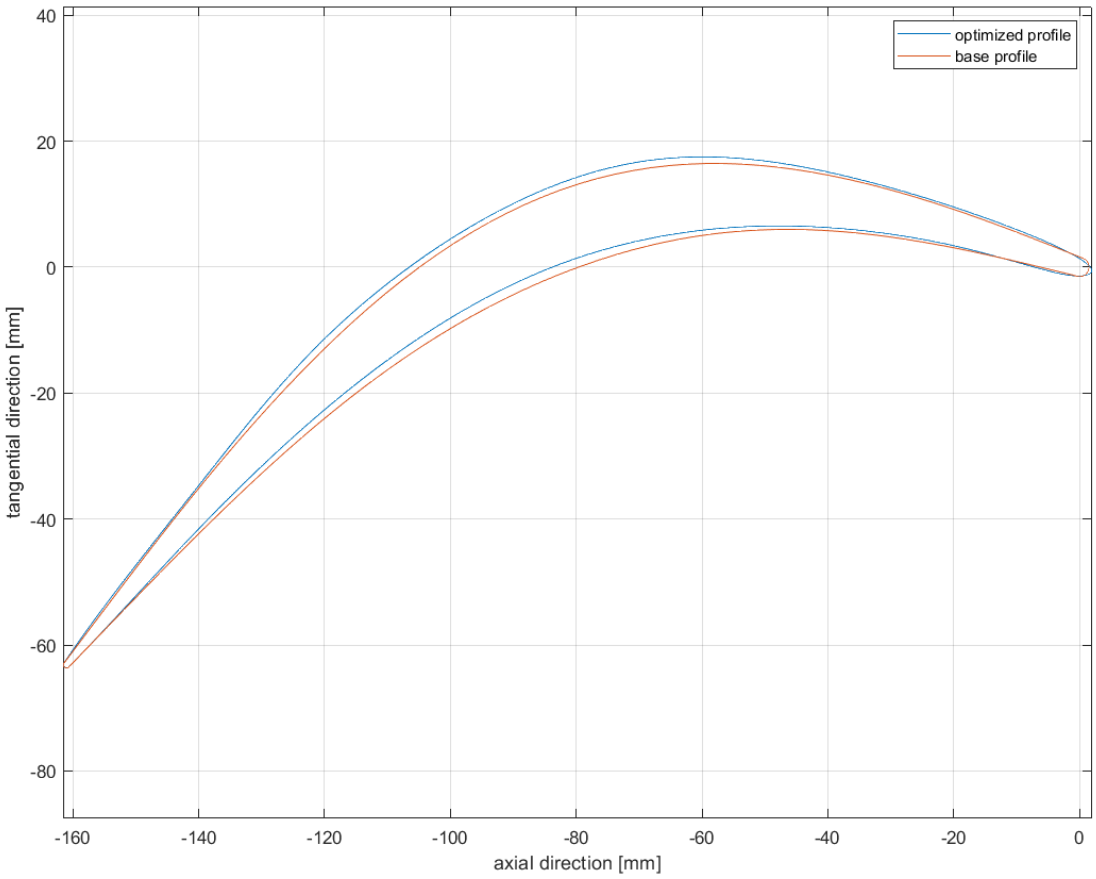

Figure 3.3.12: Central loaded optimized profile

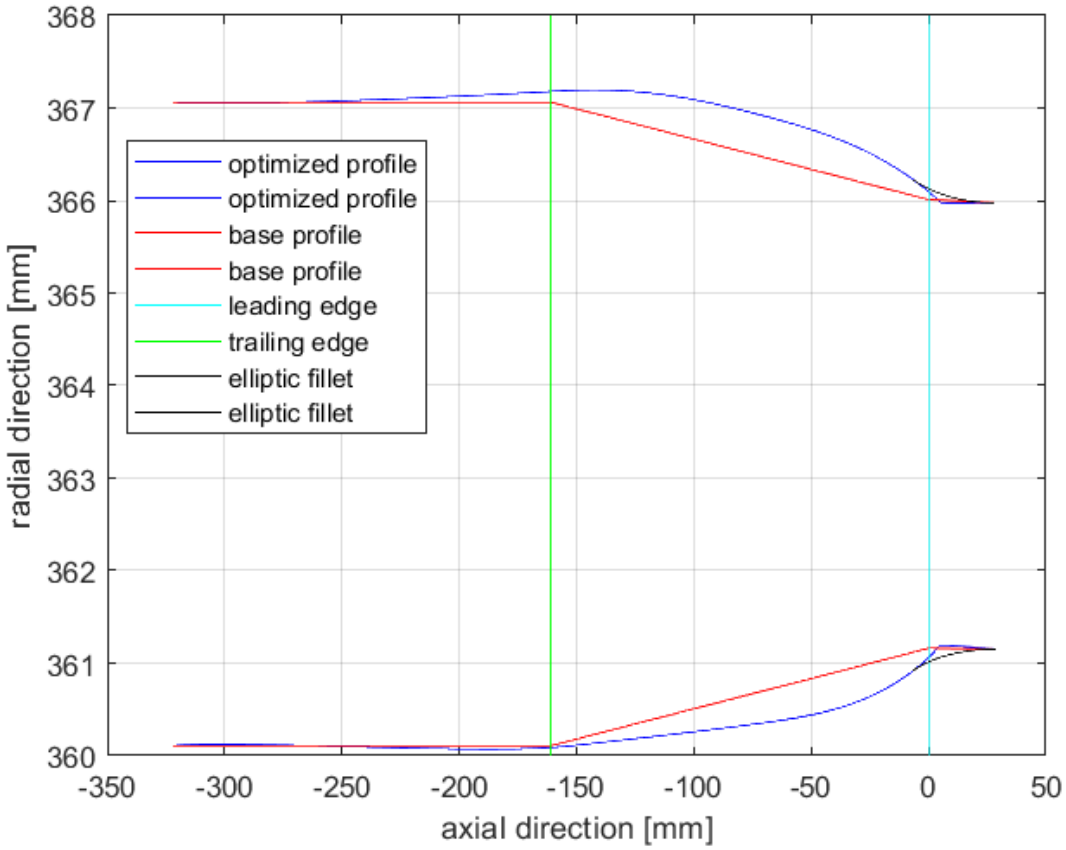

Figure 3.3.13: Central loaded optimized profile meridional view comparison

The Mach field is reported in Figure 3.3.14. As it can be seen the fish tail on the trailing edge is almost disappeared and there is only a normal shock in correspondence of trailing edge that brings the flow to have $M_{2w} = 1$. The efficiency gain from the base profile is of 0.41%. It is a small increase, but we expected it because the starting point was already with high efficiency, so the improvement margin was small. The mass flow rate associated to these flow conditions is of 100.82 $\frac{kg}{s}$, so very closed to the design value of 100 $\frac{kg}{s}$.

So, the 2D performances of this stage are satisfactory. Moreover, as shown in Figure 3.3.15, the pressure oscillations on the suction side are not present and from Figure 3.3.16 we can see that the flow follows very well the blade channel. There is only a small incidence angle, but it does not cause any problem. So, this profile was developed for 3D simulation.

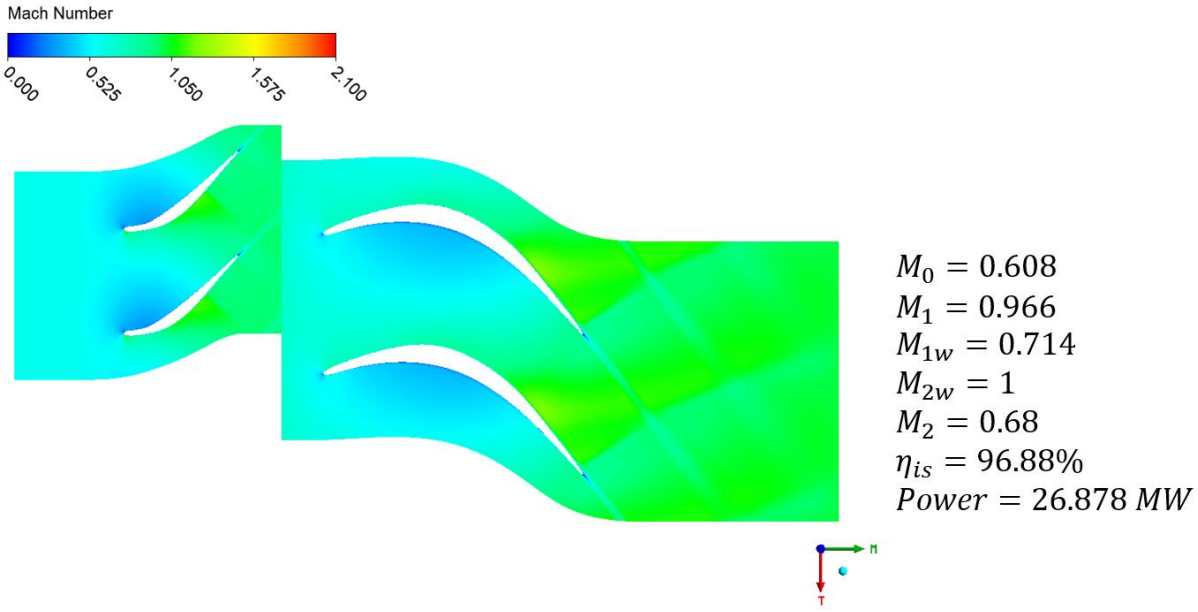

Figure 3.3.14: Central loaded optimized profile Mach field

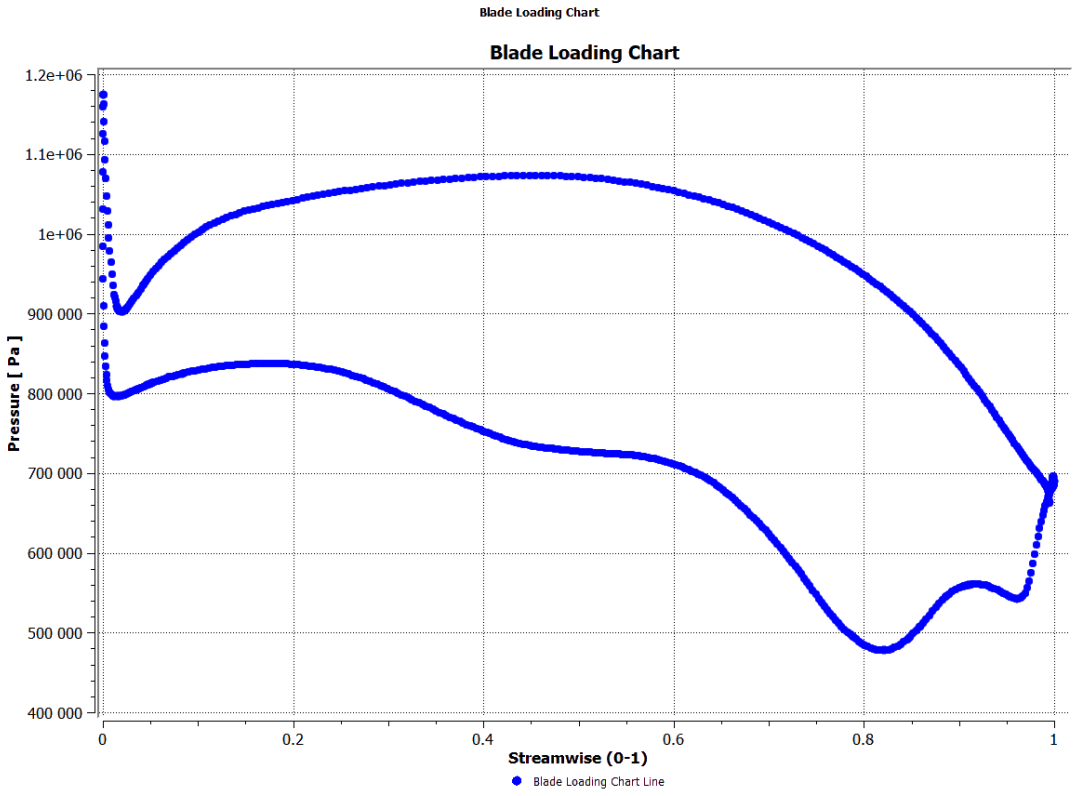

Figure 3.3.15: Central loaded optimized profile pressure loading

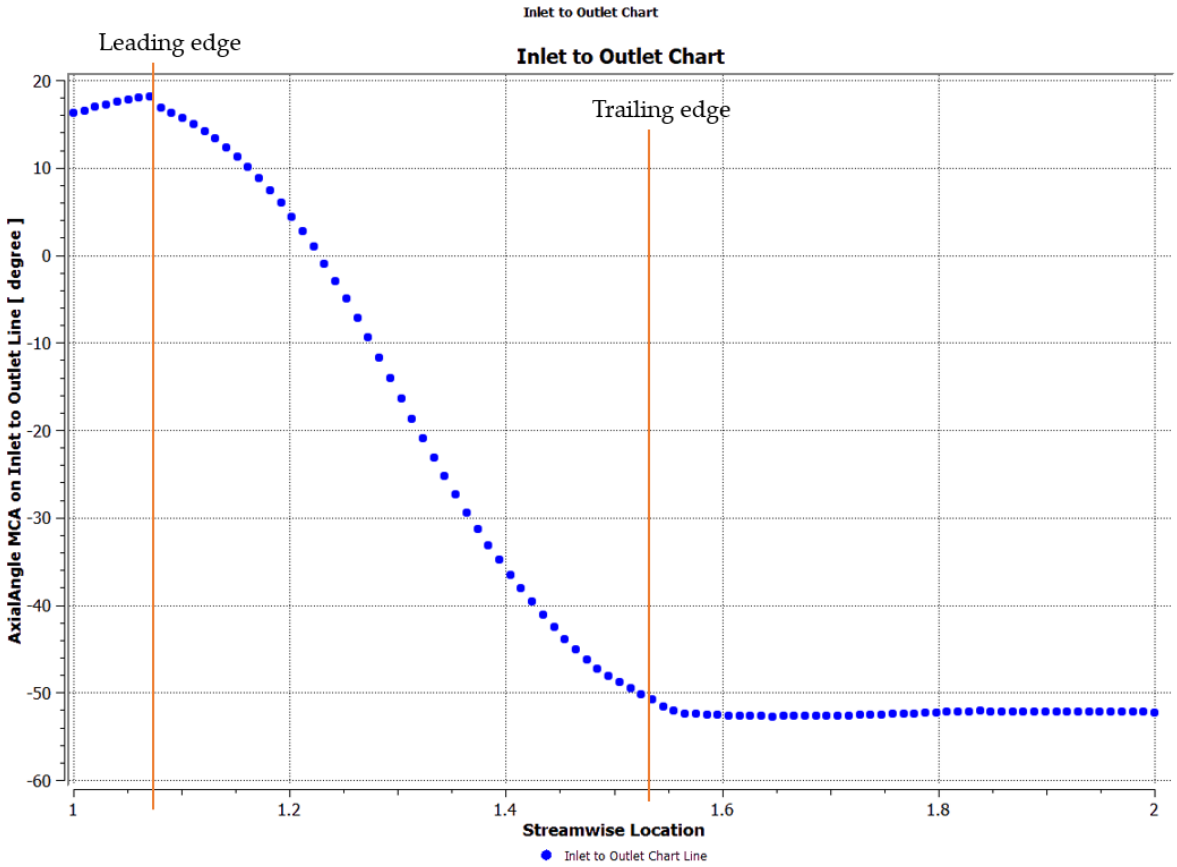

Figure 3.3.16: Central loaded optimized profile flow angle along meridional direction

3.3.3 Mechanical analysis results

3.3.3.1 Front loaded blade analysis

The mechanical stress analysis of the front loaded profile is reported in Figure 3.3.17. The maximum stress is placed at leading edge hub and in correspondence of the rib and it is equal to 409.62 MPa, so the safety coefficient is 1.85.

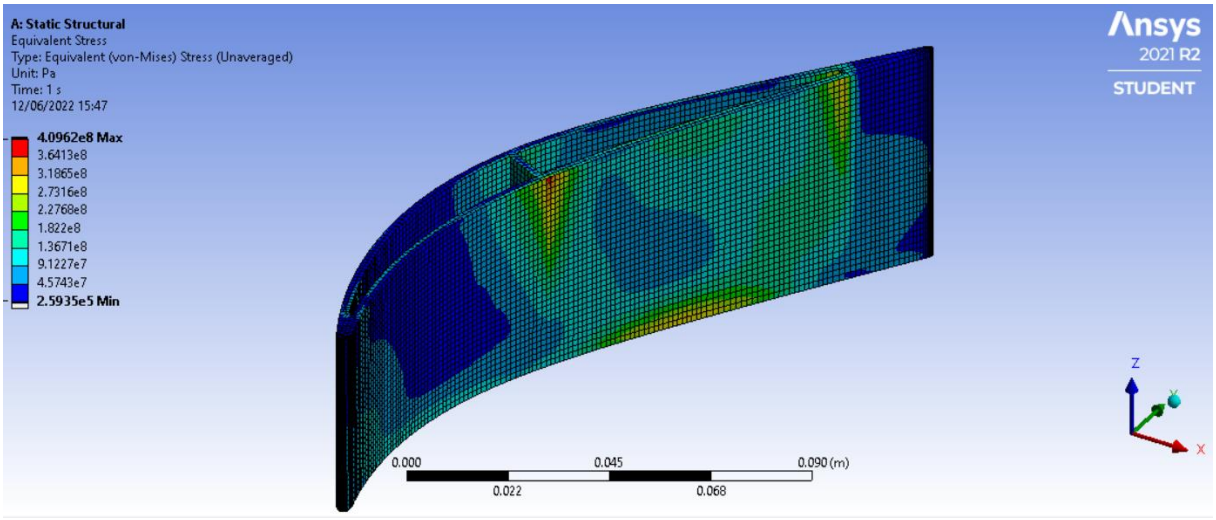

Figure 3.3.17: Front loaded blade mechanical stress

3.3.3.2 *Central loaded blade analysis*

The mechanical analysis of the central loaded blade that rotates at 8000 rpm (the first profile generated) is reported in Figure 3.3.18. The maximum stress is in correspondence of leading edge hub and it is equal to 442.62 MPa, so the safety coefficient is of 1.71. So, there is margin before reaching a safety coefficient of 1.5.

At this point, as explained in 3.3.1 2D results, we decided to improve the first central loaded profile generated by increasing its flaring to 1.4 and finding out the rotational speed that allows to have a safety coefficient of 1.5. So, a study on the effects of ω on mechanical stress was performed. In Figure 3.3.19 are reported the different blades generated for the different rotational speeds, their rotational speed (ω) and the corresponding maximum mechanical stress (σ_{max}) and safety coefficient (η_{safe}). The profile of the blade changes from one ω to the other because ω influences the flow angles, as explained in 3.3.1 2D results. So, for each blade also the pressure loading changes and it is possible to see that the increase of speed brought the maximum stress not only on the leading edge hub, but also on the hub of suction side, in the last half chord. Anyway, it was found that with a rotational velocity of 9500 rpm the safety coefficient is of 1.49, a value that we considered acceptable. So, the optimization process was performed on that profile, which is the optimization base profile.

The mechanical stress assessment of the optimized profile is reported in Figure 3.3.20. The maximum stress is of 495.99 MPa, so a little bit lower than the base profile and it leads to a safety coefficient of 1.53, which is a good value.

a)

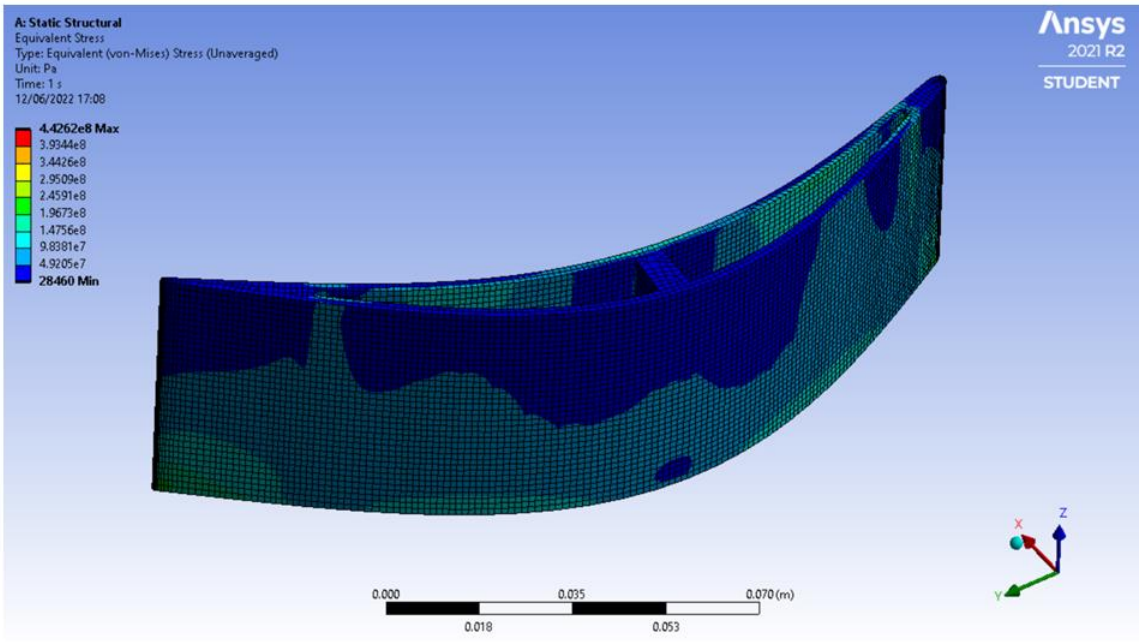

b)

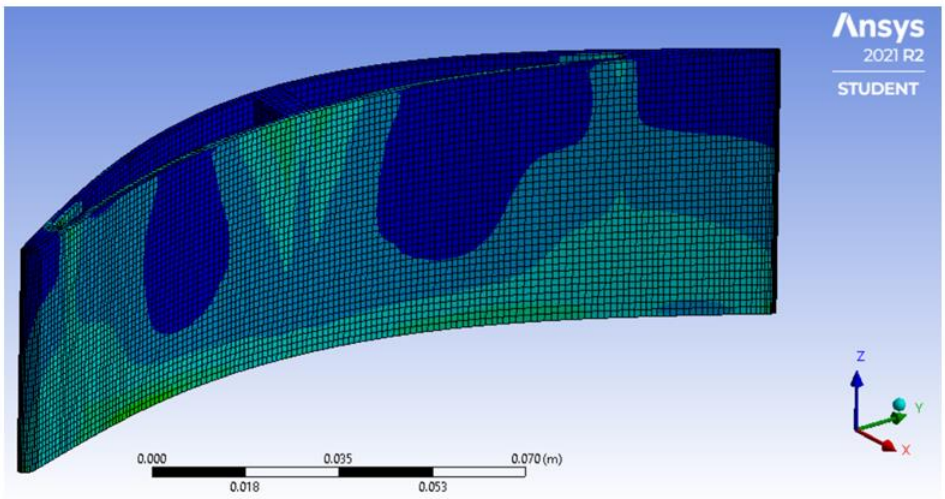

Figure 3.3.18: Central loaded blade mechanical stress. $\omega = 8000\ rpm$. a) blade suction side, b) blade pressure side

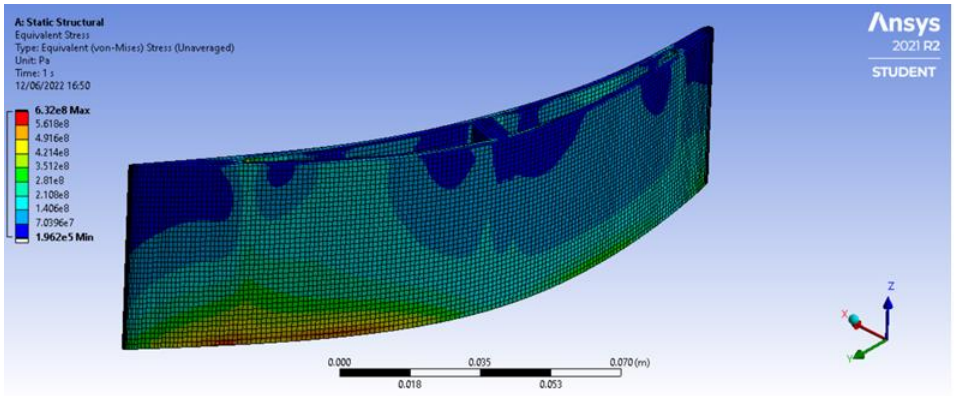

$\omega = 12000\ rpm$
$\sigma_{max} = 632\ MPa$
$\eta_{safe} = 1.2$

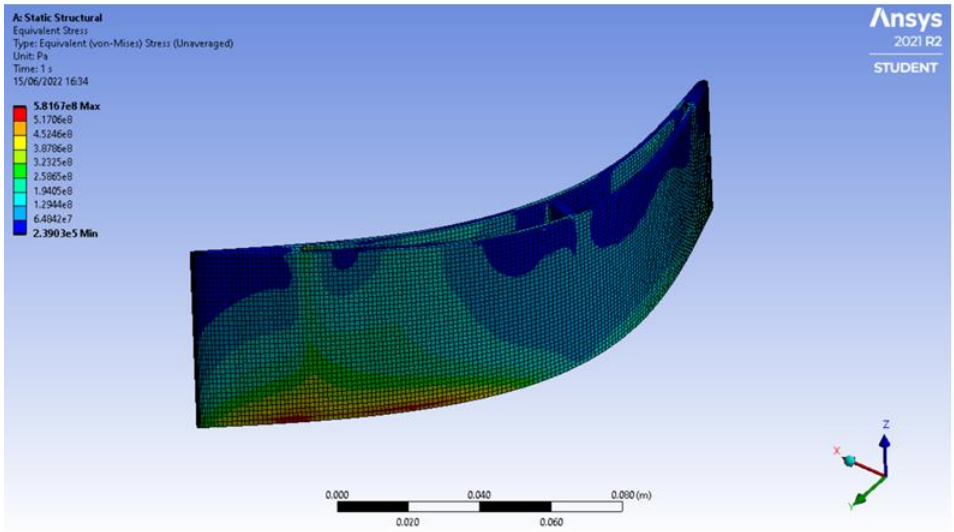

$\omega = 10500\ rpm$
$\sigma_{max} = 581\ MPa$
$\eta_{safe} = 1.32$

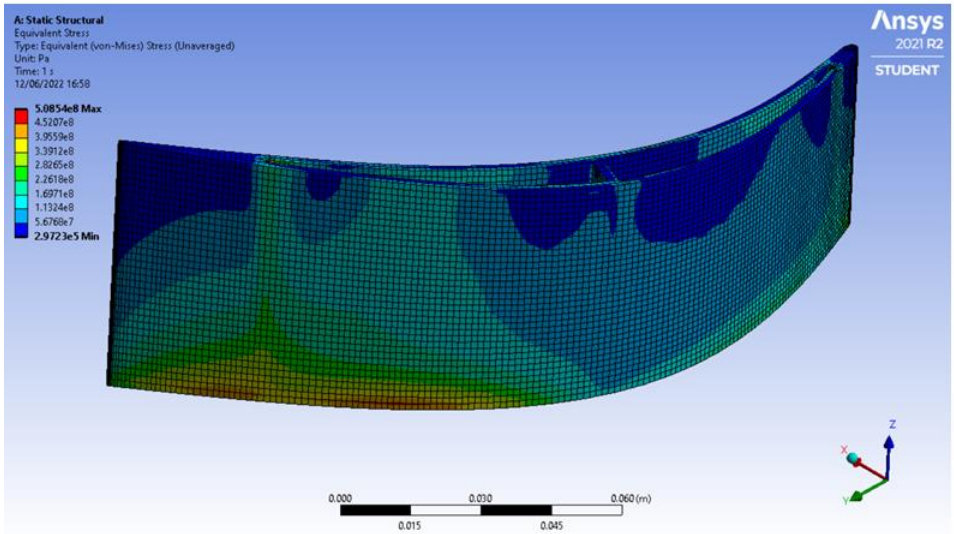

$\omega = 9500\ rpm$
$\sigma_{max} = 508\ MPa$
$\eta_{safe} = 1.49$

Figure 3.3.19: Analysis of rotational velocity effects on mechanical stress

a)

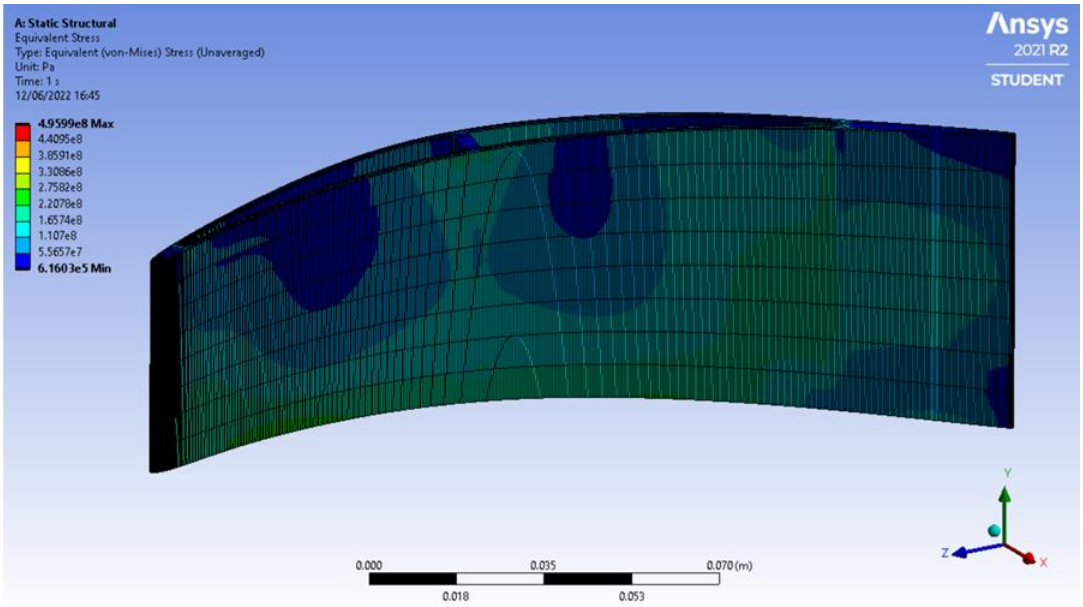

b)

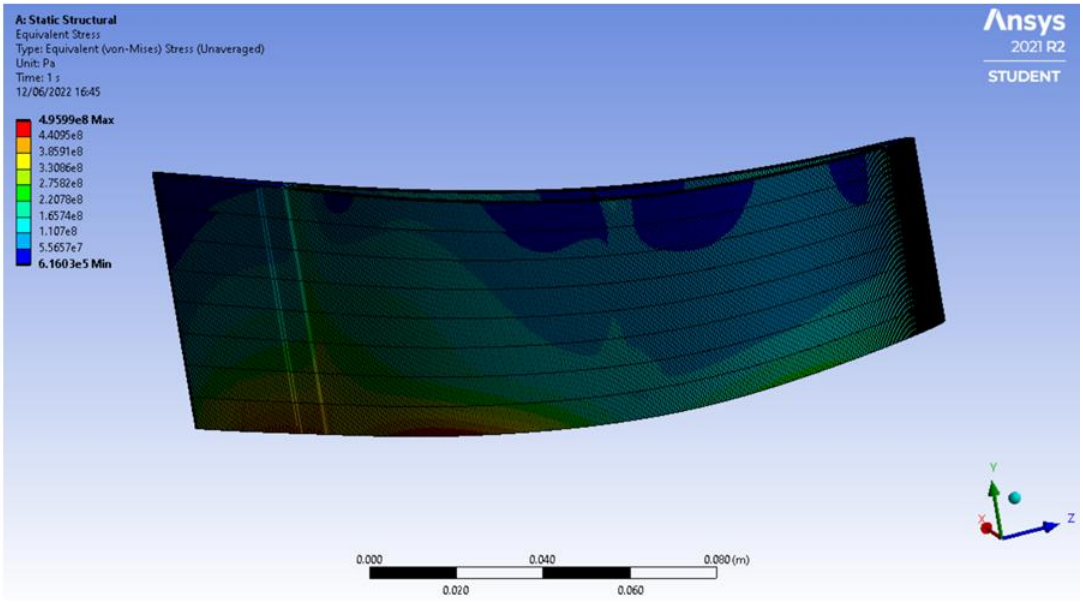

Figure 3.3.20: Optimized blade mechanical stress. a) pressure side, b) suction side

3.3.4 Rotor 3D analysis

The 3D channel is reported in Figure 3.3.21. The presence of the rotor does not change the stator flow filed, as demonstrated in Figure 3.3.22: the separation on hub and shroud in correspondence of blade leading edge (Figure 3.3.22 a) and the separation on blade suction side (Figure 3.3.22 b) are still present.

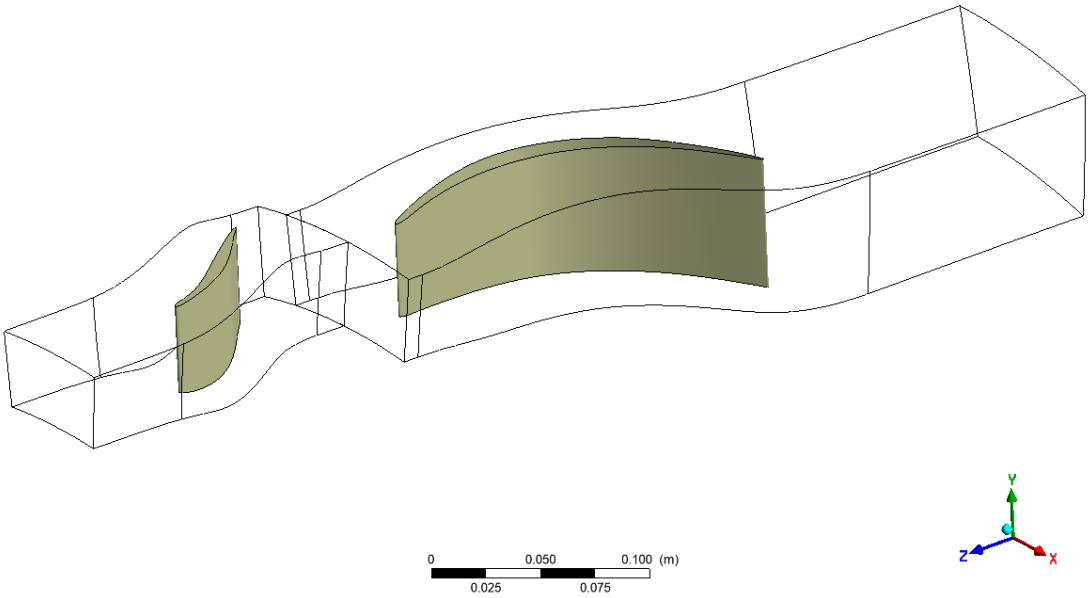

Figure 3.3.21: Stator-Rotor 3D channel

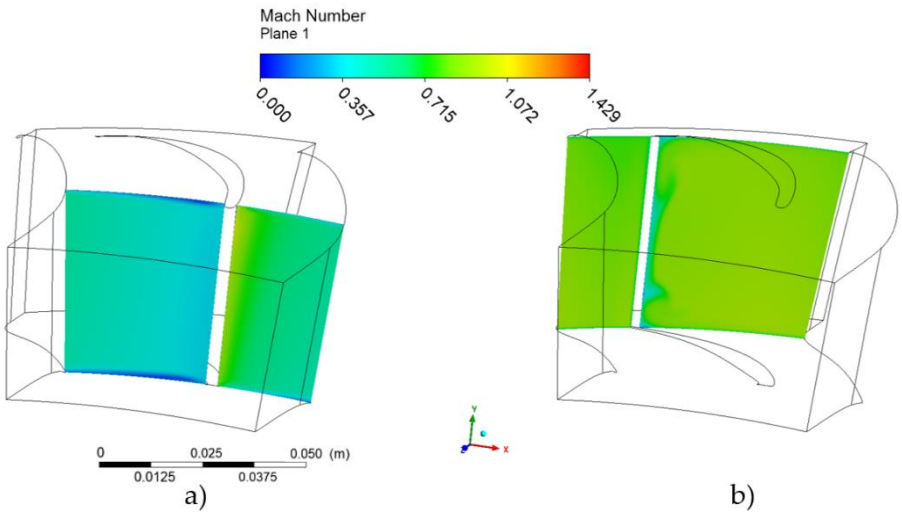

Figure 3.3.22: Stator flow field. a) hub and shroud separation, b) suction side separation

About rotor flow field, two main flow separations are present: one separation in correspondence of hub and shroud (Figure 3.3.23), that starts from the leading edge (Figure 3.3.23 a) and that vanishes at $\frac{1}{2}$ of rotor chord (Figure 3.3.23 d), with the most important width in correspondence of shroud pressure side (Figure 3.3.23 b); the other separation starts form $\frac{3}{4}$ of chord on blade suction side (Figure 3.3.24 a) and generates two big vortexes that continue downstream (Figure 3.3.24 and Figure 3.3.25).

Despite the presence of these separations, the isentropic stage efficiency is good since it is 90.33%. The one predicted by zTurbo for this case was 76%, so the secondary losses were significantly overestimated like as it happened also for the stator.

The extracted power is of 24.682 MW, so we lost about 2 MW of power from the 2D simulation.

The mass flow rate is of 97.68 $\frac{kg}{s}$, so a little bit smaller than the one calculated from 3D stator simulation, which was of 98.34 $\frac{kg}{s}$. It means that the rotor introduces an additional blockage to the flow, and it could be mainly due to the flow separations that reduces the available cross-sectional area. Even if the mass flow rate is a little bit lower than the wanted value of 100 $\frac{kg}{s}$, the stage performances are good and it is able to manage the high inlet Mach number.

The stage outlet absolute Mach number is $M_2 = 0.69$, which is quite high as inlet Mach number for the following stage, so there is the need to reduce it. To do so it is possible to apply a diffuser downstream of the stage, which is a practice that is already applied in Airbus A380 GP7000 engines (Figure 3.3.26), where the intermediate duct between high pressure and low pressure turbines is a diffuser. This deceleration can bring the Mach number to more conventional values of 0.3÷0.4 for the next stage. This kind of deceleration could not be done for our stage inlet because, as already explained in 2.1 Mean Line Analysis, the outlet flow from a rotating detonation combustor is supersonic or in supersonic-subsonic mixed conditions, so, a so strong deceleration will introduce too much losses, while a declaration from Mach 0.7 to 0.3÷0.4 is more affordable in terms of losses.

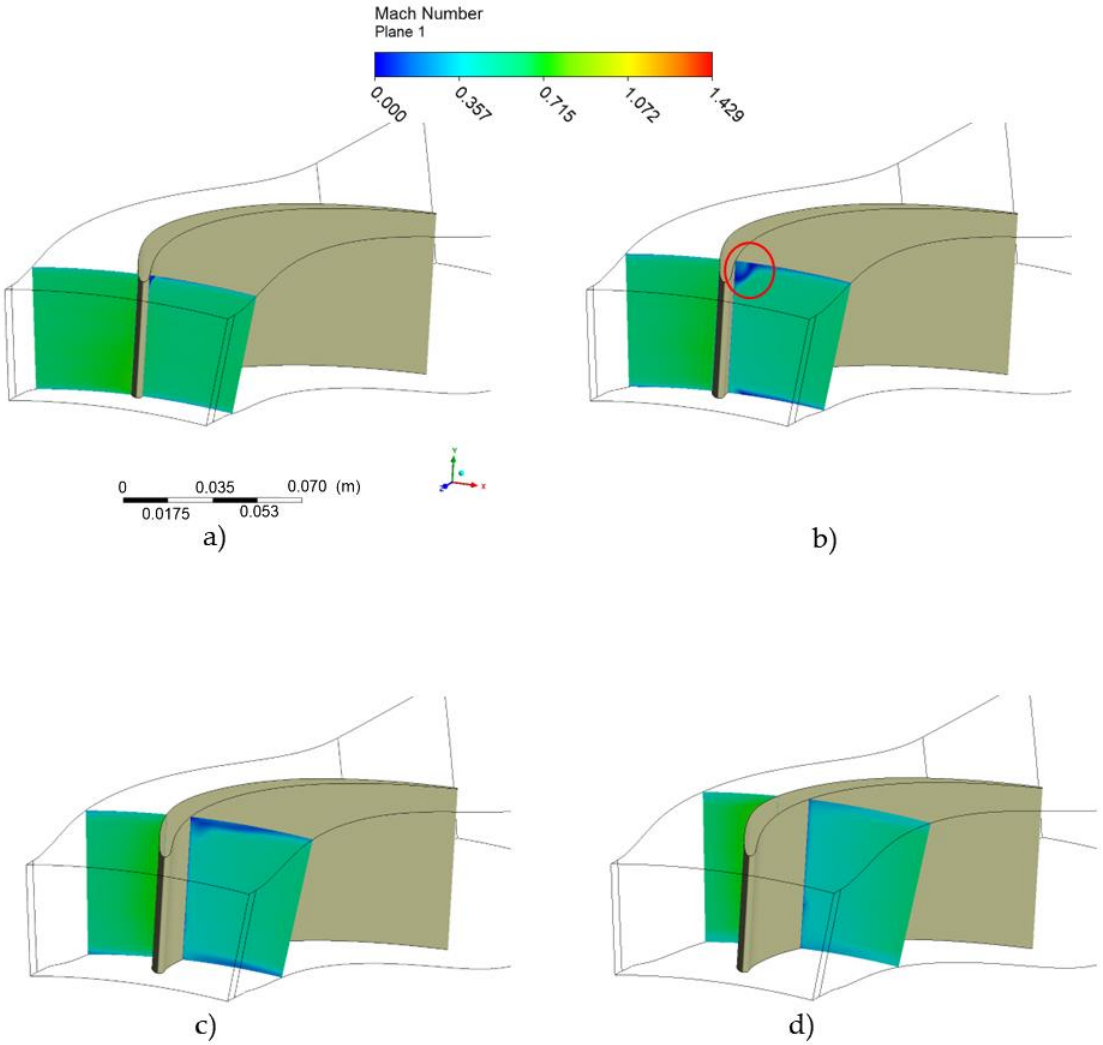

Figure 3.3.23: Rotor leading edge flow separation. In b) the strong pressure side separation is evidenced by a red ellipse. From a) to d) the plane moves downstream to show the separation behavior.

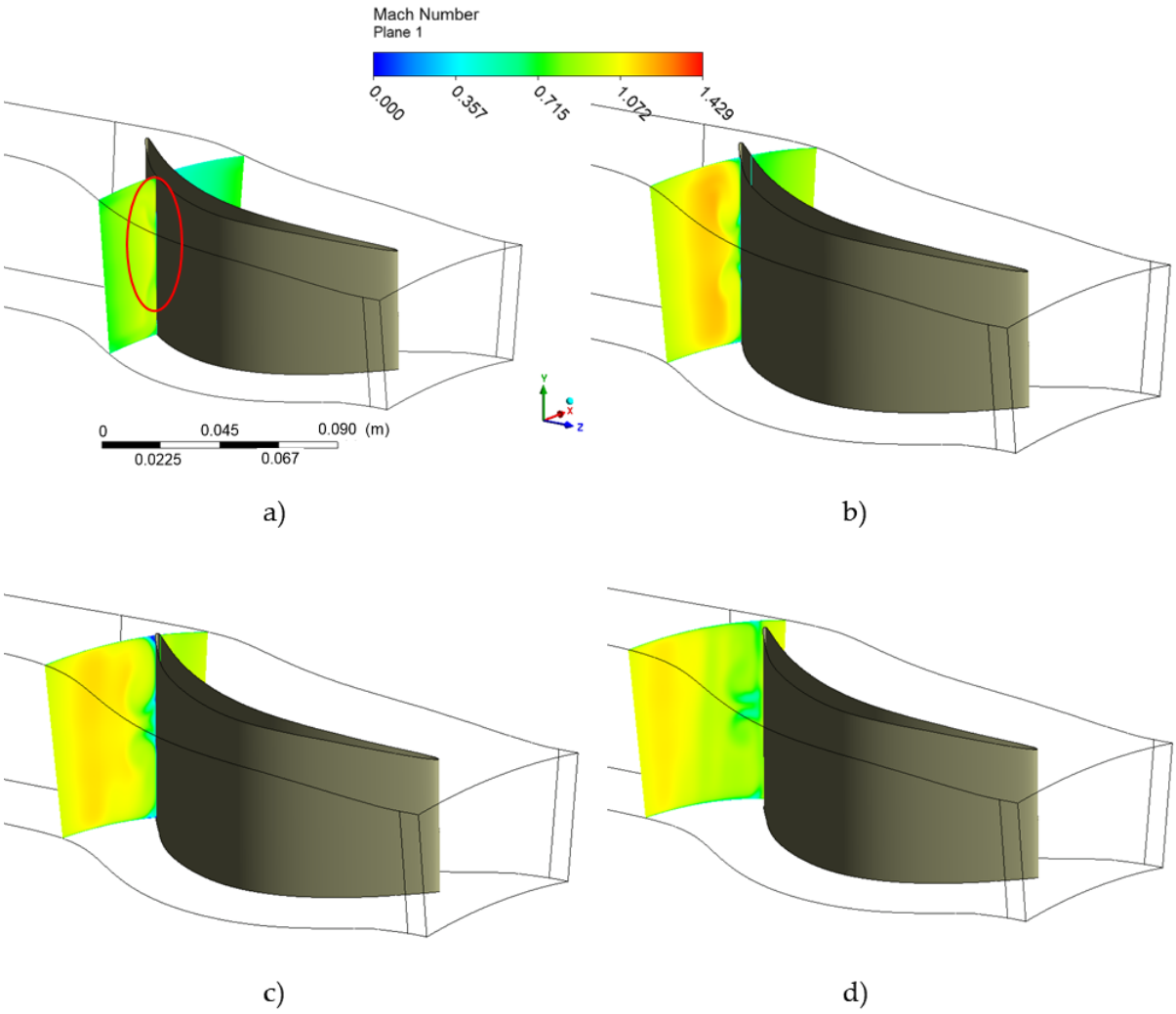

Figure 3.3.24: Rotor suction side flow separation. In a) the separation is evidenced with a red ellipses. From a) to d) the plane moves downstream to show the separation behavior.

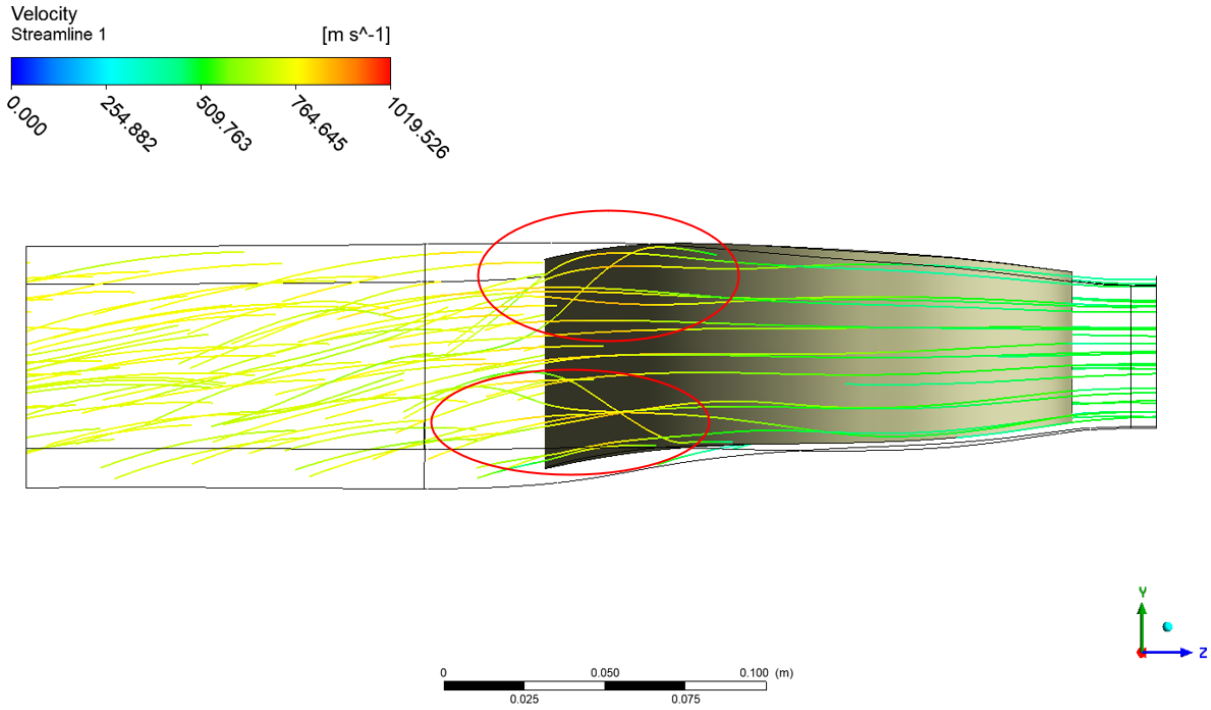

Figure 3.3.25: Rotor suction side separation streamlines. With two red ellipses are evidenced the two vortexes.

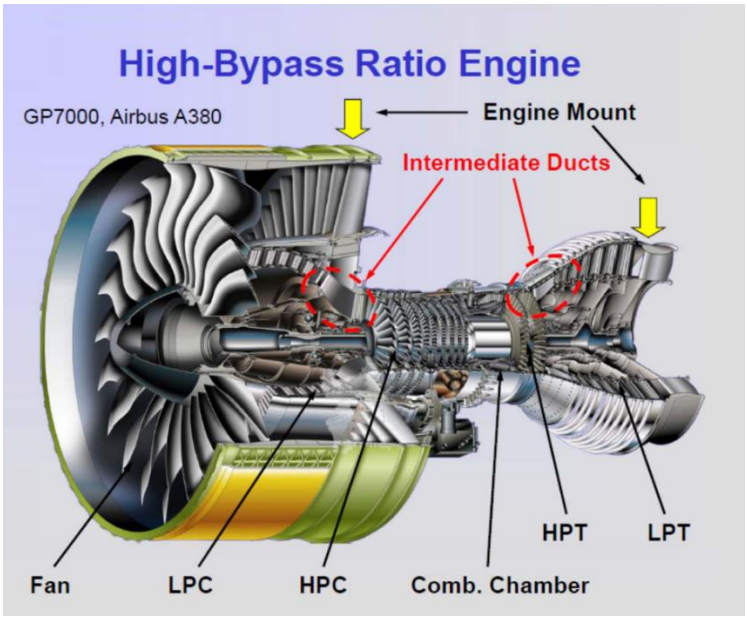

Figure 3.3.26: Airbus A380 GP 7000 engine

3.3.5 Off Design analysis

A brief analysis of performances in off-design conditions was performed also for the rotor. A high total inlet pressure of $P_{tin} = 20\ bar$ and incidence variation between -10° to +10° were simulated on the 2D profile, like what was done for the stator.

The Mach flow field for the high pressure is reported in Figure 3.3.27. There is the formation of fish tails on rotor leading edge that interacts with adjacent blades, while for stator the changes in the flow field are very small. The maximum Mach number reached is higher than in design conditions (look at Figure 3.3.14 for comparison). These elements cause losses that reduce the efficiency of 1.81% from the design conditions. The increase of pressure allows to extract more work, this is why there is only a small reduction in stage isentropic efficiency. Referring to Equation 3.2, also here the only element that changes significantly is the total pressure, in fact it causes an increase in the mass flow rate bringing it to $\dot{m} = 134.41 \frac{kg}{s}$. A non-negligible problem of this off-design condition is the very high outlet absolute Mach number M_2, that can easily bring the flow to be supersonic causing important losses in the downstream stage.

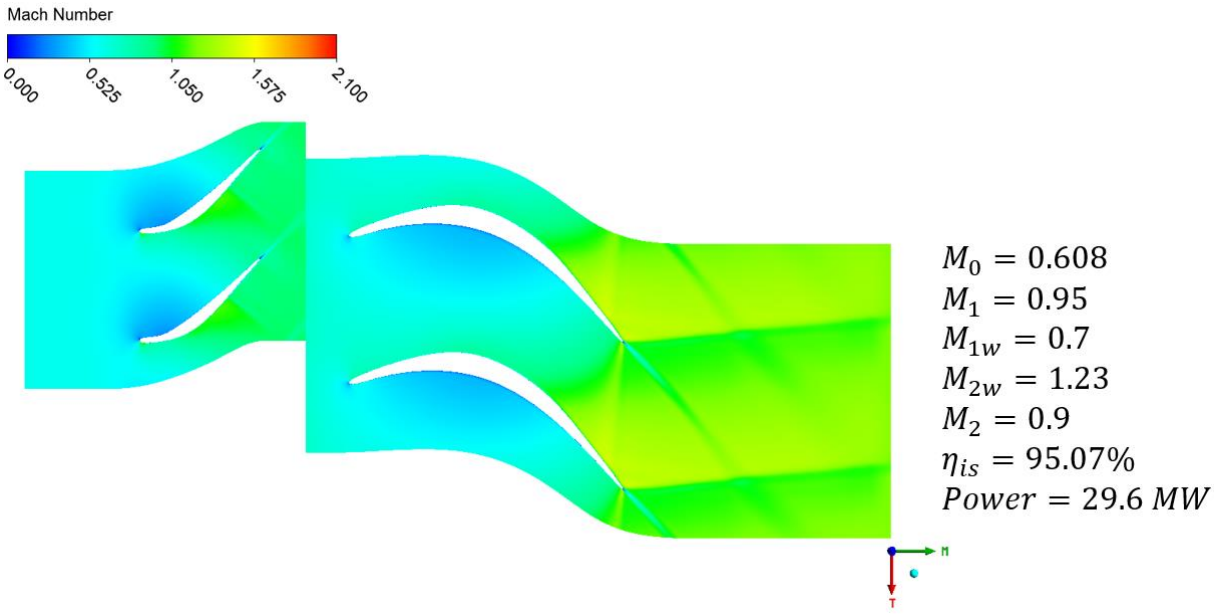

Figure 3.3.27: Rotor off design inlet pressure: Mach field and performances

About incidence variation, its effects are reported in Figure 3.3.28. Globally the performances do not worsen a lot, the highest worsening is obtained for positive incidence where there is a flow separation in correspondence of stator leading edge (Figure 3.3.28 a).

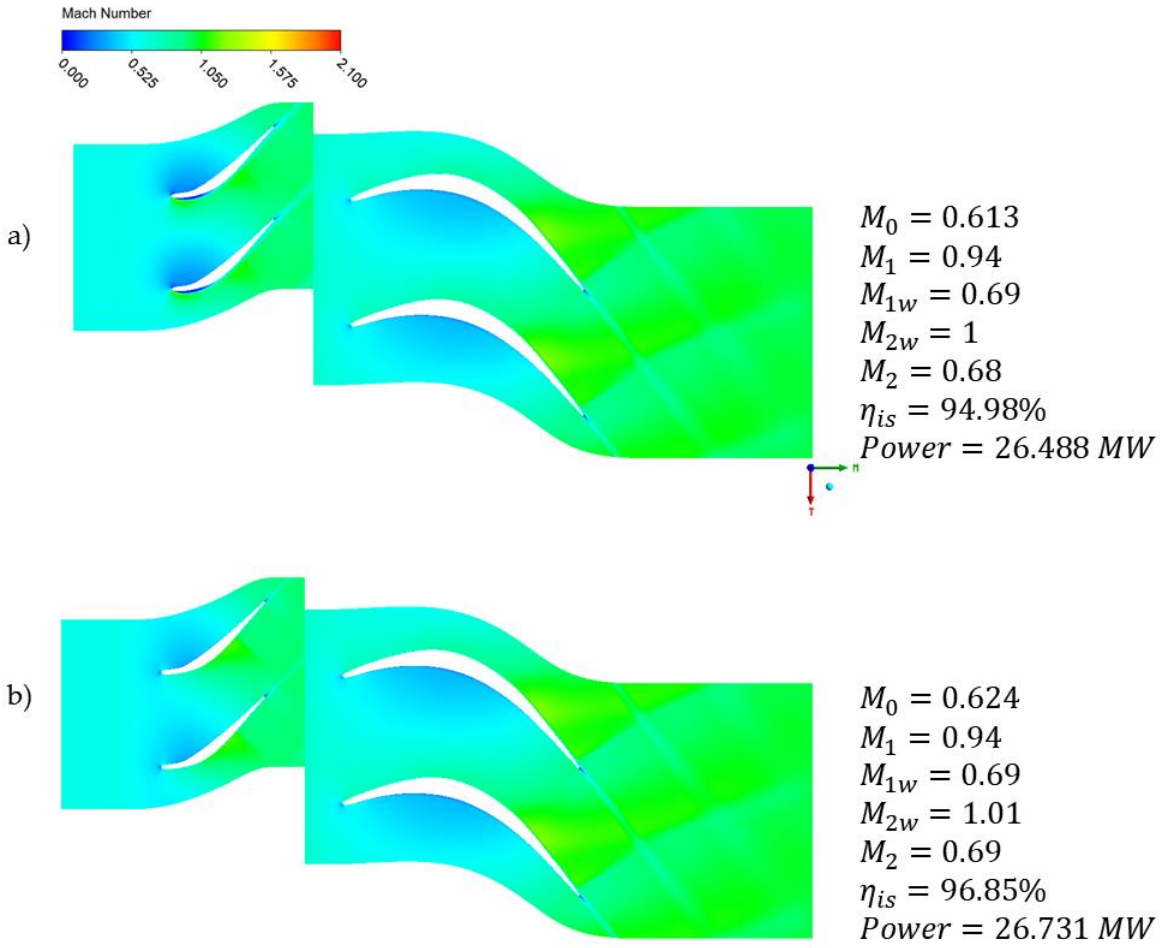

Figure 3.3.28: Rotor off design inlet angle. a) incidence = +10°, b) incidence = -10°

This brief discussion on off design conditions shows that the stage can work well also in conditions different from the design ones. Obviously a deeper analysis is required to better understand the stage behaviour at the variation of working conditions.

4. Conclusion and future development

In this thesis work, a subsonic turbine stage was designed to deal with non-conventional inlet conditions. The research field of interest is the development of Rotating Detonation Engines, a novel technology able to increase the gas turbine performance adopting detonation combustion mode.

This work aims at exploring a way to couple gas turbine with a rotating detonation combustor. The flow coming out from this kind of combustors presents complex features: high speed flow, that can be supersonic or mixed supersonic-subsonic, and strong non-uniformities. The coupling can be done by a transition duct that accelerate the flow bringing it to be fully supersonic, or by a transition duct that behaves like a diffuser and that decelerates the flow to be fully subsonic, but still with high Mach number.

The design of the supersonic stage was already performed by my colleague Noraiz Mushtaq, so the aim of this thesis was to find out a way to couple the RDC with the gas turbine using a subsonic flow to reduce the losses generated by shock waves. So, the main focus of this work is to find a turbine design that is able to manage high inlet Mach numbers, rather than focusing on the non-uniformities.

The first step of this thesis was to study the effects of different parameters on the stage performances through the use of a mean line software: zTurbo. In particular, the parameters of interest were inlet Mach number, turbine hub radius, blades flaring, rotational speed and rotor outlet absolute angle. For our purposes, there was the need to generate an algorithm to get from zTurbo desired outputs, because some of our design constraints were zTurbo outputs, such as stator and rotor outlet Mach numbers. Then, before performing the parametric analysis, some adjustments to Traupel losses correlations were performed. This because it was decided to use Traupel as losses correlations, but the values of parameters used for this work were out of Traupel validity, so it was implemented a strategy to extrapolate losses. The validation through CFD calculations of this strategy showed that for profile losses it works well, but it is inadequate for the prediction of secondary losses. The results of the parametric analysis showed that the efficiency of the stage increases at lower inlet Mach number and rotor outlet absolute angle, and at higher turbine hub radius, blades flaring and rotational speed. So, as starting points for the next step, which is the CFD analysis of the stage, we decided to use the values that maximizes efficiency, considering physical limitations such as mechanical stress for rotational velocity or

boundary layer detachment for too high flaring values. These limitations were assessed in the CFD analysis to check we had taken the correct limits.

The CFD analysis started from the 2D analysis of the stator. A study on the effects of solidity was performed by changing the cascade number of blades and blade axial chord, to find out the one that give best performances in terms of losses. Then different camber line shapes and thickness distributions were analyzed to look at their impact on losses and flow field and, finally, also the effects of endwalls contouring were studied to find a cascade geometry that minimizes losses production with a good flow field. At this point, the best profile found was subjected to an optimization process through the software FORMA, developed by Politecnico di Milano. This was done to maximize the stator performances and the results obtained are good. The optimized profile was then subjected to a mechanical stress assessment that showed it is able to withstand the pressure loading; 3D CFD analysis was also performed to assess the effect of the three-dimensional flow behavior. Due to the presence of contained flow separations, the 3D losses were higher than the 2D ones, but the results from 3D analysis remained satisfactory.

The final step was the coupled stator-rotor CFD analysis. To choose the rotor number of blades an assessment on the rotor inlet sonic conditions was performed to avoid the presence of shocks on rotor leading edge. Then a study of the effects on performances of rotor axial chord and camber line shapes was performed. Then the two most promising blades were mechanically assessed and then optimized. The best result obtained was for the central loaded blade and it is promising. So, this rotor blade was developed in 3D and the flow presented some separations, but overall, the performances were good. Finally, an off-design analysis was done, showing that performances reduction was low.

Many future developments regarding the design of subsonic turbines to be coupled with RDE are possible. All of them are required to make the detonation engines available for improving the gas turbine performances. Starting from this thesis work, a list of hypotheticals following steps in this research field is presented below:

- Improving the validity range of mean line losses correlation in order to have more reliable results for the mean line design.
- Extract the flow field from RDC numerical simulations and use it to perform a deep analysis on the turbine stage to get a better estimation on its efficiency.
- Perform a robust multi point geometry optimization considering the real inlet flow, so with spatial and time non-uniformities.
- An internal cooling system must be designed. This is an important problem for this novel turbine, if coupled with RDC. Indeed, the bleed air coming from last compressor stage is at a lower pressure than the burned gas in the turbine,

which means that an external cooling is unfeasible. Alternatively, an external compressor will be required.

- A 3D optimization of both stator and rotor profile shapes and endwalls geometry can be done, in order to reduce the flow separation from endwalls and blades suction side.
- A study on the optimal distance between stator and rotor can be performed.
- The optimization of the transition duct from RDC to the turbine can be done, in order to minimize the losses produced by the deceleration.

In summary, it is clear that a lot of work has to be done before a gas turbine equipped with an RDE can be made available for the free market. Nevertheless, the interest for this technology is increasing across the globe and optimistic results from experiments and from numerical simulations are already available for supersonic turbines. This thesis work adds positive results also for the subsonic turbine stage, showing that multiple solutions are available for the coupling of turbomachinery with rotating detonation combustors.

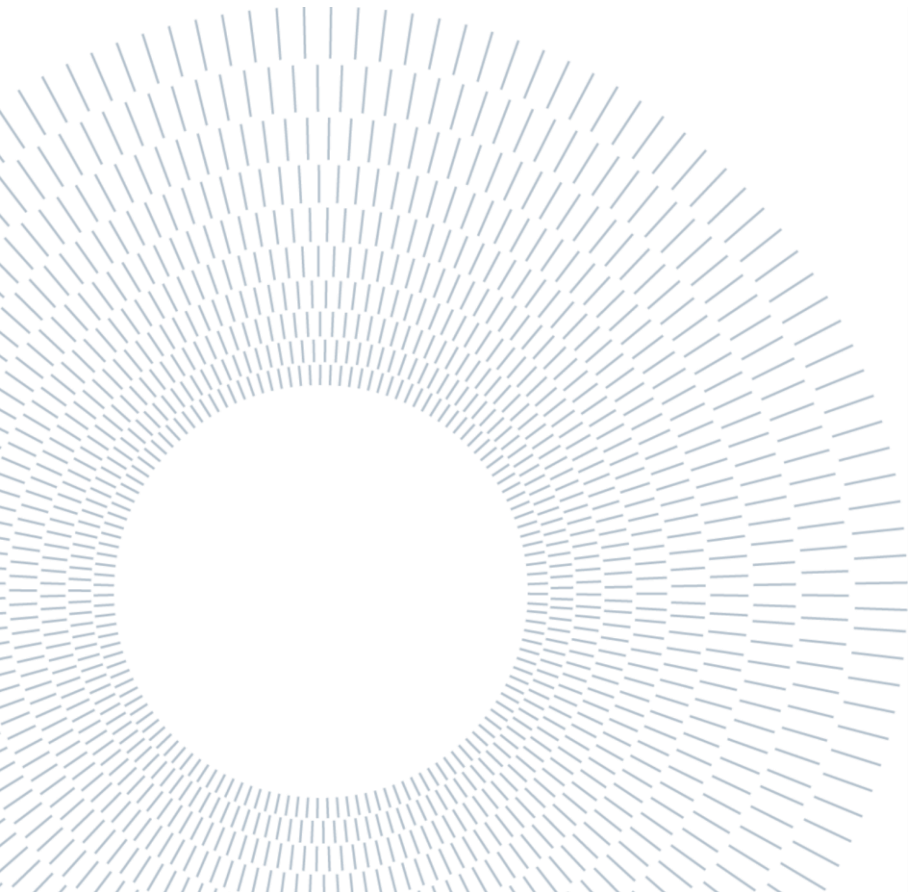

Bibliography

[1] P. Wolański, "Detonation Engines ", *Journal of KONES Powertrain and Transport*, vol. 18, no. 3, pp. 515-521, 2011.

[2] P. Wolański, "Detonative Propulsion", Proceedings of The Combustion Institute, vol. 34, pp. 125-158, 2013.

[3] J. M. Seitzman, Pressure Gain Combustion, Georgia Tech, 2018.

[4] A.J. Dean, A. Rasheed, V.E. Tangirala, P.F.Pinard, GT-2005-69141, Proceedings of International Gas Turbine Institute, ASME Turbine Expo 2005, June 2005, 1275–1284.

[5] S. M. Jones, D. E. Paxson, "Benefits to Commercial Propulsion Systems from Pressure Gain Combustion", American Institute of Aeronautics and Astronautics, 2013.

[6] Dmitry M. Davidenko, Iskender Gökalp, Alexey N. Kudryavtsev, "Numerical simulation of the continuous rotating hydrogen-oxygen detonation with a detailed chemical mechanism", West-East high speed flow field conference, Moscow, Russia, 2007.

[7] D. A. Schwer, K. Kailasanath, "Numerical Investigation of Rotating Detonation Engines", 46th AIAA/ASME/SAE/ASEE Joint Propulsion Conference, 2010.

[8] Mitsuru Kurosaka, Carl Knowlen, Jacob A. Boening, "Theoretical and Experimental Consideration of the Continuous Rotating Detonation Engine", 52nd AIAA/SAE/ASEE Joint Propulsion Conference, 2016.

[9] Hannah Ritchie, Max Roser, "Energy", Published online at OurWorldInData.org, 2020.

[10] M. Kurosaka, N. Tsuboi, "Spinning detonation, cross-currents, and Chapman-Jouguet velocity", Journal of Fluid Mechanics, vol. 756, pp. 728-757, 2014.

[11] F. K. Lu, E. M. Braun, "Rotating Detonation Wave Propulsion: Experimental Challenges, Modeling, and Engine Concepts", Journal of Propulsion and Power, Vol. 30, No. 5, 2014.

[12] D. A. Schwer, K. Kailasanath, “On Reducing Feedback Pressure in Rotating Detonation Engines”, Aerospace Sciences Meeting including the New Horizons Forum and Aerospace Exposition, 2013.

[13] F. A. Bykovskii, S. A. Zhdan, E. F. Vedernikov, ‘‘Continuous spin detonations'', Journal of Propulsion and Power, Vol. 22, pp. 1204, 2006.

[14] S. Zhou, H. Ma, Y. Ma, C. Zhou, D. Liu, S. Li, “Experimental study on a rotating detonation combustor with an axial-flow turbine”, Acta Astronautica, Vol. 151, pp. 7-14, 2018.

[15] D. A. Schwer, K. Kailasanath, “Numerical Study of the Effects of Engine Size on Rotating Detonation Engines”, Aerospace Sciences Meeting including the New Horizons Forum and Aerospace Exposition, 2011.

[16] D. E. Paxson, “Numerical and Analytical Assessment of a Coupled Rotating Detonation Engine and Turbine Experiment”, 55th AIAA Aerospace Sciences Meeting, 2017.

[17] Tae-Hyeong Yi, J. Lou, C. Turangan, “Effect of Nozzle Shapes on the Performance of Continuously Rotating Detonation Engine”, 48th AIAA Aerospace Sciences Meeting Including the New Horizons Forum and Aerospace Exposition, 2010.

[18] D. M. Davidenko, Y. Eude, I. Gökalp, “Theoretical and Numerical Studies on Continuous Detonation Wave Engines”, 17th AIAA International Space Planes and Hypersonic Systems and Technologies Conference, 2011.

[19] Tae-Hyeong Yi, J. Lou, C. Turangan, “Propulsive Performance of a Continuously Rotating Detonation Engine”, Journal of Propulsion and Power, Vol. 27, No. 1, 2011.

[20] Z. Ji, H. Zhang, B. Wang, “Performance analysis of dual-duct rotating detonation aero-turbine engine”, Aerospace Science and Technology, Vol. 92, pp. 806-819, 2019.

[21] D. A. Schwer, K. Kailasanath, “Characterizing NOx Emissions for Air-Breathing Rotating Detonation Engines”, Propultion and Energy forum, 52nd AIAA/SAE/ASEE Joint Propulsion Conference, 2016.

[22] N. Mushtaq, “Design and preliminary optimization of a supersonic turbine for Rotating Detonation Engine”, Politecnico di Milano, 2019-2020.

[23] N. Wei, “Significance of Loss Models in Aerothermodynamic Simulation for Axial Turbines”, Department of Energy Technology Division of Heat and Power Technology Royal Institute of Technology, Doctoral Thesis, 2000.

[24] H. R. M. Craig, H. J. A. Cox, "Performance estimation of axial flow turbines", Proc Instn Mech Engrs, Vol 185 32/71, 1970-71.

[25] I. B. Celik, U. Ghia, P. J. Roache, C. J. Freitas, H. Coleman, P. E. Raad, "Procedure for Estimation and Reporting of Uncertainty Due to Discretization in CFD Applications", Journal of Fluids Engineering, Vol. 130, 2008.

A. Appendix A

A portion of the look up table used by zTurbo is reported in Figure A.1 .

```
VARIABLES = "s(kJ/kgK)","P(bar)", "rho(kg/m^3)", "h(kJ/kg)", "c (m/s)", "cp(kJ/kgK)", "cv(kJ/kgK)", "T(°C)",  "mu(Pa.s)", "q(kgv/kg)
 ZONE i=          30 ,j=          30  DATAPACKING=POINT
    7.71207      2.00000      0.85148    841.83367    563.78419      1.10312      0.81577    544.33986      0.00004    999.00000
    7.72571      2.00000      0.84103    853.05243    567.06327      1.10543      0.81808    554.49926      0.00004    999.00000
    7.73935      2.00000      0.83073    864.41046    570.35468      1.10774      0.82040    564.76329      0.00004    999.00000
    7.75299      2.00000      0.82058    875.90920    573.65853      1.11006      0.82273    575.13279      0.00004    999.00000
    7.76663      2.00000      0.81058    887.55009    576.97493      1.11238      0.82505    585.60857      0.00004    999.00000
    7.78027      2.00000      0.80071    899.33458    580.30401      1.11470      0.82738    596.19148      0.00004    999.00000
    7.79391      2.00000      0.79099    911.26422    583.64590      1.11702      0.82971    606.88245      0.00004    999.00000
    7.80754      2.00000      0.78140    923.34036    587.00070      1.11934      0.83204    617.68223      0.00004    999.00000
    7.82118      2.00000      0.77195    935.56453    590.36854      1.12166      0.83436    628.59177      0.00004    999.00000
    7.83482      2.00000      0.76264    947.93826    593.74955      1.12398      0.83669    639.61196      0.00004    999.00000
    7.84846      2.00000      0.75345    960.46305    597.14385      1.12629      0.83901    650.74375      0.00004    999.00000
    7.86210      2.00000      0.74439    973.14043    600.55158      1.12860      0.84132    661.98805      0.00004    999.00000
    7.87574      2.00000      0.73546    985.97194    603.97284      1.13090      0.84363    673.34583      0.00004    999.00000
    7.88938      2.00000      0.72666    998.95913    607.40778      1.13320      0.84593    684.81805      0.00004    999.00000
    7.90302      2.00000      0.71798   1012.10358    610.85652      1.13549      0.84823    696.40572      0.00004    999.00000
    7.91665      2.00000      0.70942   1025.40687    614.31919      1.13777      0.85051    708.10982      0.00004    999.00000
    7.93029      2.00000      0.70098   1038.87058    617.79590      1.14004      0.85279    719.93139      0.00004    999.00000
    7.94393      2.00000      0.69265   1052.49634    621.28680      1.14231      0.85506    731.87145      0.00004    999.00000
    7.95757      2.00000      0.68444   1066.28575    624.79201      1.14456      0.85731    743.93107      0.00004    999.00000
    7.97121      2.00000      0.67635   1080.24046    628.31164      1.14680      0.85956    756.11132      0.00004    999.00000
    7.98485      2.00000      0.66836   1094.36213    631.84584      1.14903      0.86179    768.41328      0.00004    999.00000
    7.99849      2.00000      0.66049   1108.65241    635.39472      1.15125      0.86401    780.83806      0.00004    999.00000
    8.01213      2.00000      0.65272   1123.11300    638.95842      1.15345      0.86622    793.38679      0.00005    999.00000
    8.02577      2.00000      0.64506   1137.74558    642.53704      1.15565      0.86842    806.06060      0.00005    999.00000
    8.03940      2.00000      0.63750   1152.55187    646.13073      1.15782      0.87060    818.86066      0.00005    999.00000
    8.05304      2.00000      0.63004   1167.53370    649.73961      1.15999      0.87277    831.78822      0.00005    999.00000
    8.06668      2.00000      0.62269   1182.69265    653.36379      1.16213      0.87492    844.84432      0.00005    999.00000
    8.08032      2.00000      0.61543   1198.03056    657.00339      1.16427      0.87705    858.03025      0.00005    999.00000
    8.09396      2.00000      0.60828   1213.54919    660.65854      1.16638      0.87917    871.34722      0.00005    999.00000
    8.10760      2.00000      0.60121   1229.25036    664.32935      1.16848      0.88128    884.79649      0.00005    999.00000
    7.71207      2.48276      0.99926    894.07717    578.92641      1.11373      0.82636    591.45388      0.00004    999.00000
    7.72571      2.48276      0.98712    905.94185    582.26200      1.11605      0.82869    602.09591      0.00004    999.00000
    7.73935      2.48276      0.97514    917.95237    585.61044      1.11837      0.83101    612.84638      0.00004    999.00000
    7.75299      2.48276      0.96334    930.11025    588.97187      1.12069      0.83334    623.70621      0.00004    999.00000
    7.76663      2.48276      0.95171    942.41700    592.34641      1.12300      0.83566    634.67630      0.00004    999.00000
    7.78027      2.48276      0.94024    954.87413    595.73419      1.12532      0.83798    645.75757      0.00004    999.00000
    7.79391      2.48276      0.92893    967.48316    599.13532      1.12762      0.84030    656.95094      0.00004    999.00000
    7.80754      2.48276      0.91777    980.24562    602.54995      1.12993      0.84261    668.25737      0.00004    999.00000
    7.82118      2.48276      0.90678    993.16306    605.97819      1.13223      0.84492    679.67781      0.00004    999.00000
    7.83482      2.48276      0.89594   1006.23705    609.42017      1.13452      0.84721    691.21326      0.00004    999.00000
```

Figure A.1: Portion of look up table

For example, if I know the entropy and the pressure in a section, all the other quantities are interpolated from the values in the table. This allows to reduce calculation time.

B. Appendix B

The total losses by Traupel consist of profile losses, secondary losses, tip leakage losses and fan losses [23].

Profile losses are due to the friction on the profile surfaces and the separation of the boundary layers on the blade. Secondary losses are caused by vortexes formation due to the interaction between boundary layer and profile and the presence of pressure gradients in blade channel. Tip leakage losses are due to the fact that rotor blades cannot be attached to the turbine casing, so there will be a small gap between blade and casing where fluid can pass through. Fan losses are due to the fact that the blade spacing is not constant over the radius. Traupel losses can be calculated through Equation B.1 [23].

$$\zeta = \zeta_{prof} + \zeta_{sec} + \zeta_{tip} + \zeta_{fan} \qquad \text{Equation B.1}$$

These losses are based on enthalpy as shown by Equation B.2 [23].

$$\begin{cases} \zeta_{stator} = \frac{h_1 - h_{1is}}{h_{t0} - h_1} \\ \zeta_{rotor} = \frac{h_2 - h_{2is}}{h_{t1w} - h_2} \end{cases} \qquad \text{Equation B.2}$$

Since this is a preliminary design, we look at profile and secondary losses, neglecting tip and fan losses for sake of simplicity.

Profile losses can be calculated through Equation B.3 [23].

$$\zeta_{prof} = \chi_R \chi_M \zeta_{p0} + \zeta_{Te} + \zeta_c \qquad \text{Equation B.3}$$

- ζ_{p0}: basic profile loss, decided by the inlet and outlet flow angles.
- χ_R: Reynolds number correction factor based on the influence of Reynolds number and surface roughness.
- χ_M: Mach number correction factor, where the free stream velocity is taken into account.

- ζ_{Te}: trailing edge loss, caused by the wake after the trailing edge.
- ζ_c: Carnot shock loss which appears in a fluid that is undergoing a sudden expansion, for example after the trailing edge.

All these losses can be found from empirical correlations as shown by Figure B.1 and Figure B.2 [23].

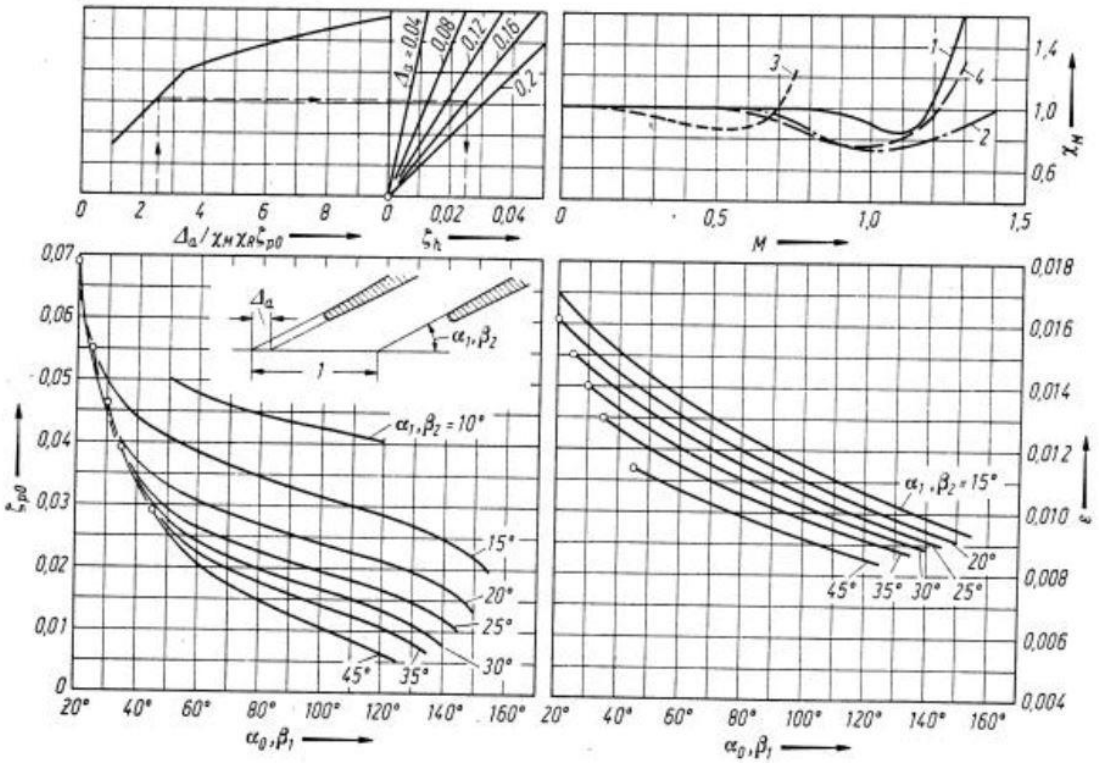

Figure B.1: Traupel Profile Losses

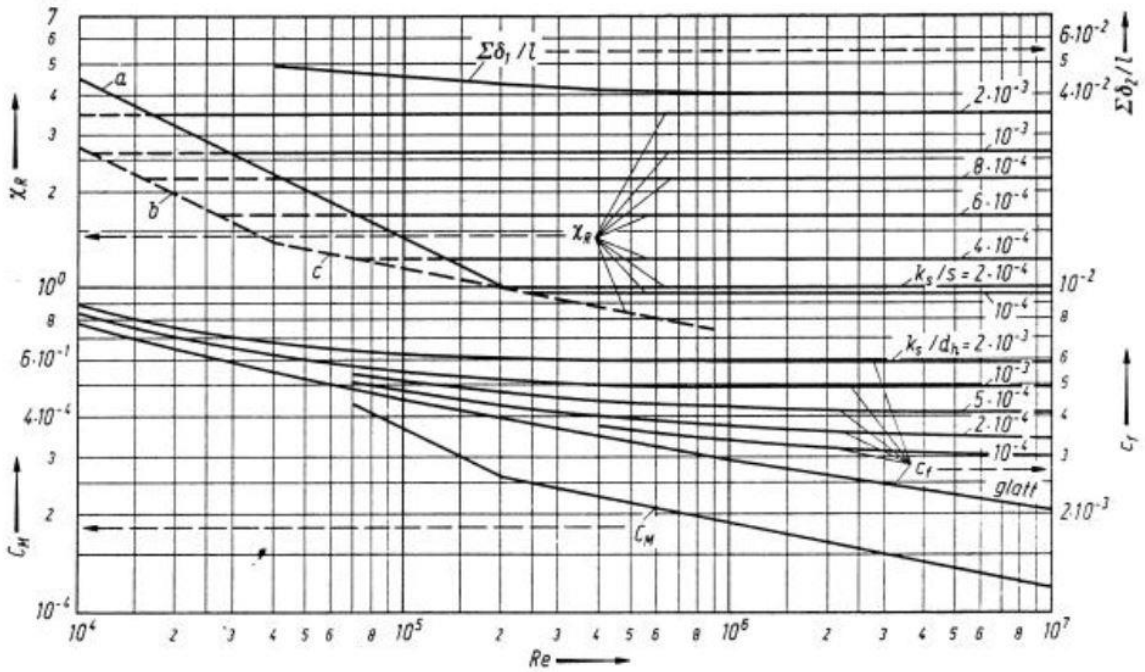

Figure B.2: Reynolds correction for Traupel correlations

It should be noted that the definition of the flow angles is made from the tangential direction. In Figure B.1, ζ_h in the top left diagram refers to ζ_{Te} and Δa is the trailing edge thickness.

From the bottom left diagram of Figure B.1 it is possible to see that Traupel correlation is valid for cascade outlet angle up to 45° respect to tangential direction. The problem is that, in this case, we reach outlet angle of 70° due to the high speed at inlet. This is why we are out of the validity range of Traupel. So, we added the conditions that for a straight profile (outlet angle of 90° from tangential direction) the basic profile losses are of 1%. This means we added the red line in Figure B.3.

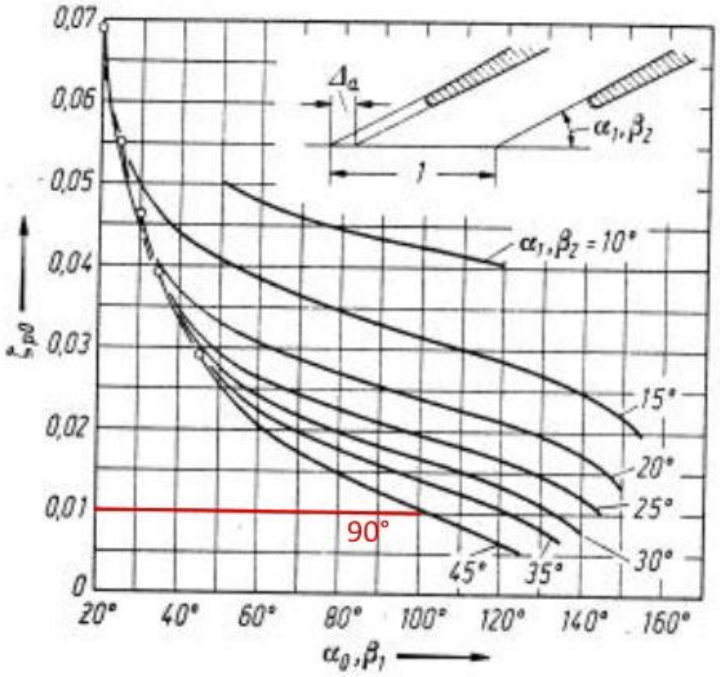

Figure B.3: Traupel basic profile losses modified

This modification allows a better extrapolation of profile losses values.

Carnot losses are calculated through Equation B.4 and Equation B.5 for stator and rotor respectively [23].

$$Stator: \zeta_{cs} = \left(\frac{\Delta a_s}{1-\Delta a_s}\right)^2 \cdot \sin(\alpha_1^2) \qquad \text{Equation B.4}$$

$$Rotor: \zeta_{cr} = \left(\frac{\Delta a_r}{1-\Delta a_r}\right)^2 \cdot \sin(\beta_2^2) \qquad \text{Equation B.5}$$

Then, about secondary losses, correlations were kept as they are, so as reported in equation B.6 [23].

$$\begin{cases} If\ \frac{b}{pitch} \geq \left(\frac{b}{pitch}\right)_k \rightarrow \zeta_{sec} = \frac{\zeta_{prof}}{\zeta_{p0}} \cdot F \cdot \frac{pitch}{b} + \zeta_a \\ If\ \frac{b}{pitch} < \left(\frac{b}{pitch}\right)_k \rightarrow \zeta_{sec} = \frac{\zeta_{prof}}{\zeta_{p0}} \cdot F \cdot \frac{pitch}{b} + \zeta_a + A \cdot \left(\frac{l}{b} - \frac{\frac{l}{pitch}}{\left(\frac{b}{pitch}\right)_k}\right) \end{cases} \qquad \text{Equation B.6}$$

The first term is the loss from the secondary flow in the blade channel, ζ_a is representing the losses from the endwalls between the stator and the rotor disk, and the unsteady effects due to the rotor-stator interaction. For sake of simplicity ζ_a is neglected in this case. The third term, in Equation B.6 is a correction factor due to the fact that there is no undisturbed flow core in the blade channel. The factor of $\frac{\zeta_{prof}}{\zeta_{p0}}$ in Equation B.6 (ratio of losses at given Reynolds number Mach number and trailing edge thickness to losses at reference conditions) indicates that the secondary losses are affected by the same parameters, such as blade angles, trailing edge, Mach and Reynolds numbers, as the profile losses. The span/pitch ratio $\left(\frac{b}{pitch}\right)$ is considered in this model. It is obvious that a small value of the ratio will make the secondary flow strong, and the losses will be large. When this ratio is more than the critical value $\left(\frac{b}{pitch}\right)_k$, there will be the risk of the interaction between the secondary vortexes on at two endwalls, therefore the third term of loss is added in Equation B.6. The critical $\left(\frac{b}{pitch}\right)_k$ ratio is reported in Equation B.7 [23]:

$$\left(\frac{b}{pitch}\right)_k = B \cdot \sqrt{\zeta_{prof}} \quad \text{B=7 for stator, B=10 for rotor} \quad \text{Equation B.7}$$

Coefficient A of Equation B.6 can be deduced from experimental records, and he has the value of 0.02 for strongly accelerating blades and 0.035 for equal pressure blades.

The parameter F in Equation B.6 represents how the secondary flow in the blade channel is affected by the flow turning, i.e. the difference between the inlet and the outlet flow angle, and the velocity ratio, i.e. how the flow is accelerated through the blade channel. The more turning and less acceleration, the higher F and thus higher secondary losses. The variation of F with the blade turning was given in Figure B.4 [23]. C_0 and C_1 are absolute velocities, so they must be used for stator calculations, while W_1 and W_2 are relative velocities, so they must be used for rotor calculations.

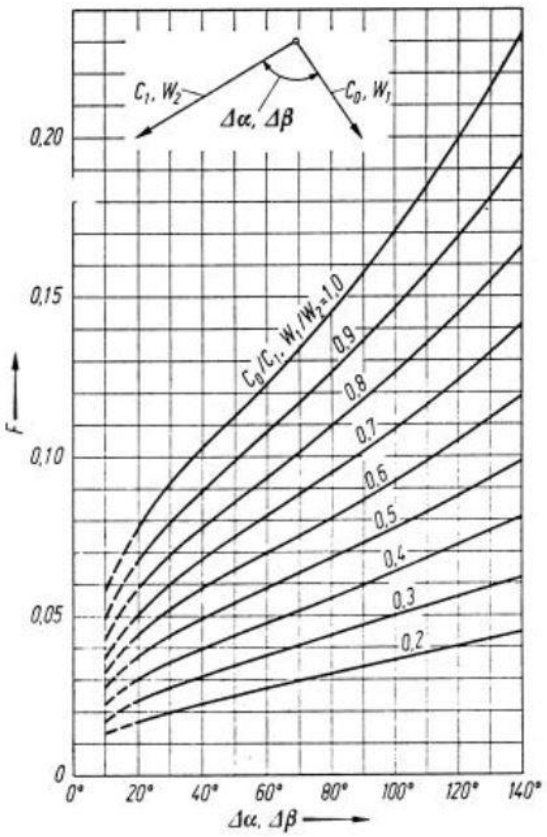

Figure B.4: Factor F for secondary losses given by Traupel

C. Appendix C

Equations to be solved are the following ones:

$$T_{t1} = T_{t0} \quad \text{Equation C.1}$$

$$T_1 = T_{t1} - \frac{V_1^2}{2C_p} \quad \text{Equation C.2}$$

$$V_1 = a_1 \cdot M_1 \quad \text{Equation C.3}$$

$$a_1 = \sqrt{\gamma \cdot R \cdot T_1} \quad \text{Equation C.4}$$

$$\frac{P_{t1}}{P_1} = \left(\frac{T_{t1}}{T_1}\right)^{\frac{\gamma}{\gamma-1}} \quad \text{Equation C.5}$$

$$Y_s = \frac{P_{t0} - P_{t1}}{P_{t1} - P_1} \quad \text{Equation C.6}$$

Unknowns are $T_{t1}, V_1, a_1, T_1, P_{t1}, P_1$. It is known that $M_1 = 1$ and $Y_s = 0$. Moreover, I used the specific heat ratio of air at 1500°C, so $\gamma = 1.305$.

T_{t1} is found from Equation C.1. From Equation C.4 and Equation C.3 I found Equation C.7 and Equation C.8:

$$T_1 = \frac{a_1^2}{\gamma R} \quad \text{Equation C.7}$$

$$V_1 = a_1 \cdot M_1 \quad \text{Equation C.8}$$

Substituting Equation C.7 and Equation C.8 in Equation C.2 leads to:

$$\frac{a_1^2}{\gamma R} = T_{t1} - \frac{(a_1 \cdot M_1)^2}{2c_p} \quad \rightarrow \quad a_1 = \sqrt{\frac{T_{t1}}{\frac{1}{\gamma R} + \frac{M_1^2}{2c_p}}} \quad \text{Equation C.9}$$

So a_1 is found from Equation C.9, then, substituting it into Equation C.7 and Equation C.8, also T_1 and V_1 are found.

Successively, from Equation C.5 I found Equation C.10:

$$P_{t1} = \left(\frac{T_{t1}}{T_1}\right)^{\frac{\gamma}{\gamma-1}} \cdot P_1 \qquad \text{Equation C.10}$$

Substituting Equation C.10 into Equation C.6 and applying some mathematical passages, I came to Equation C.11.

$$Y_s = \frac{P_{t0} - \left(\frac{T_{t1}}{T_1}\right)^{\frac{\gamma}{\gamma-1}} \cdot P_1}{\left(\frac{T_{t1}}{T_1}\right)^{\frac{\gamma}{\gamma-1}} \cdot P_1 - P_1} \quad \rightarrow$$

$$\rightarrow \quad Y_s \cdot P_1 \cdot \left[\left(\frac{T_{t1}}{T_1}\right)^{\frac{\gamma}{\gamma-1}} - 1\right] = P_{t0} - \left(\frac{T_{t1}}{T_1}\right)^{\frac{\gamma}{\gamma-1}} \cdot P_1 \quad \rightarrow \qquad \text{Equation C.11}$$

$$\rightarrow P_1 = \frac{P_{t0}}{Y_s \cdot \left[\left(\frac{T_{t1}}{T_1}\right)^{\frac{\gamma}{\gamma-1}} - 1\right] + \left(\frac{T_{t1}}{T_1}\right)^{\frac{\gamma}{\gamma-1}}}$$

So P_1 is found from Equation C.11 and subsequently P_{t1} is found from Equation C.10. In this way all the unknowns are found.

D. Appendix D

The equations to be solved are the following ones:

$$Rot_1 = c_p T_1 + \frac{W_1^2}{2} - \frac{U_1^2}{2} = c_p T_2 + \frac{W_2^2}{2} - \frac{U_2^2}{2} \quad \text{Equation D.1}$$

$$M_{2w} = \frac{W_2}{a_2} \quad \text{Equation D.2}$$

$$a_2 = \sqrt{\gamma R T_2} \quad \text{Equation D.3}$$

$$\frac{P_1}{P_2} = \left(\frac{T_1}{T_2}\right)^{\frac{\gamma}{\gamma-1}} \quad \text{Equation D.4}$$

$$\dot{m} = \frac{P_2}{R \cdot T_2} \cdot V_2 \cdot \cos(\alpha_2) \cdot S_2 \quad \text{Equation D.5}$$

$$T_{t2w} = T_2 + \frac{W_2^2}{2c_p} \quad \text{Equation D.6}$$

$$V_{2tan} = V_2 \cdot \sin(\alpha_2) \quad \text{Equation D.7}$$

$$V_{2ax} = V_2 \cdot \cos(\alpha_2) \quad \text{Equation D.8}$$

$$W_{2tan} = V_{2tan} - U_2 \quad \text{Equation D.9}$$

$$W_{2ax} = V_{2ax} \quad \text{Equation D.10}$$

$$W_2^2 = W_{2ax}^2 + W_{2tan}^2 \quad \text{Equation D.11}$$

$$U_2 = \omega \cdot \frac{R_{e2} + R_i}{2} \quad \text{Equation D.12}$$

$$S_2 = \pi \cdot (R_{e2}^2 - R_i^2) \quad \text{Equation D.13}$$

The unknowns are T_2, a_2, W_2, U_2, V_2, P_2, S_2, T_{t2w}, V_{2tan}, V_{2ax}, W_{2tan}, W_{2ax}, R_{e2}. From paragraph 2.1.2.3 Section 2, it is known that $M_{2w} = 1$ and $\alpha_2 = 0°$.

From Equation D.4 I found Equation D.14.

$$P_2 = P_1 \cdot \left(\frac{T_2}{T_1}\right)^{\frac{\gamma}{\gamma-1}} \quad \text{Equation D.14}$$

Substituting Equation D.13 and Equation D.14 into Equation D.5 results into Equation D.15.

$$\dot{m} = \frac{P_1 \cdot \left(\frac{T_2}{T_1}\right)^{\frac{\gamma}{\gamma-1}}}{R \cdot T_2} \cdot V_2 \cdot \cos(\alpha_2) \cdot \pi \cdot (R_{e2}^2 - R_i^2) \quad \rightarrow$$

$$\rightarrow V_2 = \frac{\dot{m} \cdot R \cdot T_2}{P_1 \cdot \left(\frac{T_2}{T_1}\right)^{\frac{\gamma}{\gamma-1}} \cdot \cos(\alpha_2) \cdot \pi \cdot \left(R_{e2}^2 - R_i^2\right)} \qquad \text{Equation D.15}$$

Then, substituting Equation D.3 into Equation D.2 and performing some calculations, I found Equation D.16.

$$M_{2w} = \frac{W_2}{\sqrt{\gamma R T_2}} \quad \rightarrow \quad W_2 = M_{2w} \cdot \sqrt{\gamma R T_2} \qquad \text{Equation D.16}$$

Substituting Equation D.16 and Equation D.12 into Equation D.1 the result is Equation D.17.

$$c_p T_2 + \frac{M_{2w}^2 \cdot \gamma R}{2} \cdot T_2 - \frac{\omega^2}{4} \cdot (R_{e2} + R_i)^2 = Rot_1 \quad \rightarrow$$

$$\rightarrow T_2 = \frac{Rot_1 + \frac{\omega^2}{4} \cdot (R_{e2} + R_i)^2}{c_p + \frac{M_{2w}^2 \cdot \gamma R}{2}} \qquad \text{Equation D.17}$$

Substituting Equation D.17 into Equation D.15 ends up with Equation D.18.

$$V_2 = \frac{\dot{m} \cdot R \cdot \left(\frac{Rot_1 + \frac{\omega^2}{4} (R_{e2} + R_i)^2}{c_p + \frac{M_{2w}^2 \cdot \gamma R}{2}} \right)}{P_1 \cdot \left(\frac{Rot_1 + \frac{\omega^2}{4} (R_{e2} + R_i)^2}{T_1 \cdot \left(c_p + \frac{M_{2w}^2 \cdot \gamma R}{2} \right)} \right)^{\frac{\gamma}{\gamma-1}} \cdot \cos(\alpha_2) \cdot \pi \cdot \left(R_{e2}^2 - R_i^2\right)} \qquad \text{Equation D.18}$$

Successively, I substituted Equations D.7, D.8, D.9, D.10, and D.12 into Equation D.11, finding Equation D.19.

$$W_2^2 = V_2^2 \cdot \cos^2(\alpha_2) + \left(V_2 \cdot \sin(\alpha_2) - \frac{\omega}{2} \cdot (R_{e2} + R_i)\right)^2 \qquad \text{Equation D.19}$$

Substituting Equation D.16 into equation D.19 I found Equation D.20.

$$M_{2w}^2 \cdot \gamma R T_2 = V_2^2 \cdot \cos^2(\alpha_2) + \left(V_2 \cdot \sin(\alpha_2) - \frac{\omega}{2} \cdot (R_{e2} + R_i)\right)^2 \qquad \text{Equation D.20}$$

So, substituting Equation D.17 and Equation D.18 into Equation D.20, I found Equation D.21.

$$M_{2w}^2 \cdot \gamma R \cdot \frac{Rot_1 + \frac{\omega^2}{4}\cdot(R_{e2}+R_i)^2}{c_p + \frac{M_{2w}^2 \cdot \gamma R}{2}} = \left(\frac{\dot{m} \cdot R \cdot \left(\frac{Rot_1 + \frac{\omega^2}{4}(R_{e2}+R_i)^2}{c_p + \frac{M_{2w}^2 \cdot \gamma R}{2}} \right)}{P_1 \cdot \left(\frac{Rot_1 + \frac{\omega^2}{4}(R_{e2}+R_i)^2}{T_1 \cdot \left(c_p + \frac{M_{2w}^2 \cdot \gamma R}{2}\right)} \right)^{\frac{\gamma}{\gamma-1}} \cdot \cos(\alpha_2) \cdot \pi \cdot \left(R_{e2}^2 - R_i^2\right)} \right)^2 \cdot \cos^2(\alpha_2) +$$

$$\left(\frac{\dot{m} \cdot R \cdot \left(\frac{Rot_1 + \frac{\omega^2}{4}(R_{e2}+R_i)^2}{c_p + \frac{M_{2w}^2 \cdot \gamma R}{2}} \right)}{P_1 \cdot \left(\frac{Rot_1 + \frac{\omega^2}{4}(R_{e2}+R_i)^2}{T_1 \cdot \left(c_p + \frac{M_{2w}^2 \cdot \gamma R}{2}\right)} \right)^{\frac{\gamma}{\gamma-1}} \cdot \cos(\alpha_2) \cdot \pi \cdot \left(R_{e2}^2 - R_i^2\right)} \cdot \sin(\alpha_2) - \frac{\omega}{2} \cdot (R_{e2} + R_i) \right)^2 \qquad \text{Equation D.21}$$

The only unknown of this equation is R_{e2}, so I solved it numerically. Now that R_{e2} is known, it can be substituted into Equation D.17 finding T_2. Now, from Equation D.15 I found also V_2. Successively I found P_2 from Equation D.14, so finally also the other equations of the system can be easily solved substituting these values.

E. Appendix E

The gas model used is based on the NASA polynomials and air was considered an ideal mixture of gases. The molar fraction of the different gases is presented in Table E.1.

Table E.1: Gases molar fraction and molar mass

Gas	Molar fraction [%]	Molar Mass kg/kmol
N_2	78.084	28.02
O_2	20.9476	32
Ar	0.934	39.95
CO_2	0.041177	44.01

Air molar mass is the weighted average of gases molar mass on molar fraction, and it results 28.9717 $\frac{kg}{kmol}$.

The NASA polynomial coefficients for the lower temperature interval are reported in Table E.2, while for the upper temperature interval are reported in Table E.3. The temperature interval depends on the gas, so, for the mixture, the most restrictive case was considered: lower interval goes from 200 K to 1000 K, while the upper interval goes from 1000 K to 3500 k.

Table E.2: NASA polynomial coefficient for lower interval

Coefficient	N_2	O_2	Ar	CO_2
a_1	3.298677	3.78245636	2.5	2.35677352
a_2	$1.4082404 \cdot 10^{-3}$	$-2.99673416 \cdot 10^{-3}$	0	$8.98459677 \cdot 10^{-3}$
a_3	$-3.963222 \cdot 10^{-6}$	$9.84730201 \cdot 10^{-6}$	0	$-7.12356269 \cdot 10^{-6}$
a_4	$5.641515 \cdot 10^{-9}$	$-9.68129509 \cdot 10^{-9}$	0	$2.45919022 \cdot 10^{-9}$
a_5	$-2.444854 \cdot 10^{-12}$	$3.24372837 \cdot 10^{-12}$	0	$-1.43699548 \cdot 10^{-13}$
a_6	$-1.0208999 \cdot 10^{3}$	$1.06394356 \cdot 10^{3}$	$-7.45375 \cdot 10^{2}$	$-4.83719697 \cdot 10^{4}$
a_7	3.950372	3.65767573	4.366	9.90105222

Table E.3: NASA polynomial coefficients for upper interval

Coefficient	N_2	O_2	Ar	CO_2
a_1	2.92664	3.28253784	2.5	3.85746029
a_2	$1.4879768 \cdot 10^{-3}$	$1.48308754 \cdot 10^{-3}$	0	$4.41437026 \cdot 10^{-3}$
a_3	$-5.68476 \cdot 10^{-7}$	$-7.57966669 \cdot 10^{-7}$	0	$-2.21481404 \cdot 10^{-6}$
a_4	$1.0097038 \cdot 10^{-10}$	$2.09470555 \cdot 10^{-10}$	0	$5.23490188 \cdot 10^{-10}$
a_5	$-6.753351 \cdot 10^{-15}$	$-2.16717794 \cdot 10^{-14}$	0	$-4.72084164 \cdot 10^{-14}$
a_6	$-9.227977 \cdot 10^{2}$	$-1.08845772 \cdot 10^{+3}$	$-7.45375 \cdot 10^{2}$	$-4.8759166 \cdot 10^{4}$
a_7	5.980528	5.45323129	4.366	2.27163806

Then the coefficients of the mixture are found with Equation E.1.

$$a_i = \sum_{j=1}^{n} a_{i_j} \cdot \frac{(\chi_j \cdot MM_j)}{\sum_{k=1}^{n} \chi_k \cdot MM_k} \qquad \text{Equation E.1}$$

Where a_i is the i^{th} coefficient, j and k represent the gas considered, n is the total number of gases, MM is the molar mass of the j^{th} gas, a_{i_j} is the i^{th} coefficient of the j^{th} gas and χ is the molar fraction. So, the ratio $\frac{(\chi_j \cdot MM_j)}{\sum_{k=1}^{n} \chi_k \cdot MM_k}$ represents the mass fraction of the element j in the mixture mass.

NASA coefficients are used in the NASA polynomials for the computation of specific heat capacity (Equation E.2a), enthalpy (Equations E.2b) and entropy (Equations E.2c) of the gas in function of temperature.

$$c_p = R \cdot (a_1 + a_2 \cdot T + a_3 \cdot T^2 + a_4 \cdot T^3 + a_5 \cdot T^4) \qquad \text{Equation E.2a}$$

$$H = RT \cdot \left(a_1 + \frac{a_2 \cdot T}{2} + \frac{a_3 \cdot T^2}{3} + \frac{a_4 \cdot T^3}{4} + \frac{a_5 \cdot T^4}{5} + \frac{a_6}{T}\right) \qquad \text{Equation E.2b}$$

$$S = R \cdot \left(a_1 \cdot \ln(T) + a_2 \cdot T + \frac{a_3 \cdot T^2}{2} + \frac{a_4 \cdot T^3}{3} + \frac{a_5 \cdot T^4}{4} + a_7\right) \qquad \text{Equation E.2c}$$

Sutherland model was used to describe viscosity and thermal conductivity behaviour in function of temperature. Sutherland formula for viscosity is Equation E.3, while the formula for thermal conductivity is Equation E.4.

$$\mu = \mu_0 \cdot \left(\frac{T}{T_0}\right)^{\frac{3}{2}} \cdot \frac{T_0 + S_\mu}{T + S_\mu} \qquad \text{Equation E.3}$$

$$k = k_0 \cdot \left(\frac{T}{T_0}\right)^{\frac{3}{2}} \cdot \frac{T_0 + S_k}{T + S_k} \qquad \text{Equation E.4}$$

Where $\mu_0 = 1.716 \cdot 10^{-5} \frac{N \cdot s}{m^2}$, $S_\mu = 111\ K$, $k_0 = 0.0241 \frac{W}{m \cdot K}$, $S_k = 194\ K$ and $T_0 = 273\ K$. These values are valid for the air.

F. Appendix F

Material chosen is Inconel 718. Its density is $8220\frac{kg}{m^3}$, while the melting range temperature is from 1210° C to 1344° C.

Material properties in function of temperature are reported in Table F.1 .

Table F.1: Inconel 718 mechanical properties in function of temperature

Temperature [°C]	Young modulus [GPa]	0.2% Yield strength [MPa]	Tensile strength [MPa]
21	208		
93	205	1172	1407
204	202	1124	1365
316	194	1096	1344
427	186	1076	1317
538	179	1069	1276
649	172	1027	1158
760	162	758	758

List of Figures

List of Tables

List of Symbols

Variable	Description	SI unit
$\boldsymbol{\Omega}$	Detonation wave rotational speed	$\frac{rad}{s}$
$\boldsymbol{h^*}$	Detonation wave critical height	m
$\boldsymbol{L_b}$	Length in which nozzles are blocked	m
$\boldsymbol{L_{ww}}$	Distance between two consecutive detonation waves	m
$\boldsymbol{P}$	Pressure	Pa
$\boldsymbol{A_t}$	Injector nozzles area	m^2
$\boldsymbol{A_w}$	Combustion chamber inlet area	m^2
$\boldsymbol{\delta}$	Combustion chamber thickness	m
$\boldsymbol{\pi_c}$	Compressor pressure ratio	
$\boldsymbol{T_4}$	Turbine inlet temperature	K
$\boldsymbol{\eta}$	Efficiency	%
$\boldsymbol{S_{fc}}$	Specific fuel consumption	$\frac{kg}{N \cdot h}$
$\boldsymbol{F_s}$	Specific thrust	$\frac{N \cdot s}{kg}$
$\boldsymbol{I_{sp}}$	Specific impulse	s
$\boldsymbol{\pi_{opt}}$	Compressor pressure ratio that maximizes η_{th}	
$\boldsymbol{M_{a0}}$	Flight Mach number	

$\boldsymbol{M}$	Mach number	
$\boldsymbol{R_e}$	Turbine tip radius	m
$\boldsymbol{R_i}$	Turbine hub radius	m
$\boldsymbol{fl}$	Flaring	
$\boldsymbol{\omega}$	Rotor rotational speed	$\frac{rad}{s}$
$\boldsymbol{\alpha}$	Absolute flow angle	deg
$\boldsymbol{\beta}$	Relative flow angle	deg
$\boldsymbol{b}$	Blade height	mm
$\boldsymbol{T}$	Temperature	K
$\boldsymbol{c_p}$	Specific heat ratio at constant pressure	$\frac{J}{kg \cdot K}$
$\boldsymbol{c_v}$	Specific heat ratio at constant volume	$\frac{J}{kg \cdot K}$
$\boldsymbol{\gamma}$	Specific heat ratio	
$\boldsymbol{V}$	Flow absolute velocity	$\frac{m}{s}$
$\boldsymbol{R}$	Specific gas constant of air + H_2O_{vapour} mixture	$\frac{J}{kg \cdot K}$
$\boldsymbol{h}$	Enthalpy	$\frac{kJ}{kg}$
$\boldsymbol{\dot{m}}$	Mass flow rate	$\frac{kg}{s}$
$\boldsymbol{S}$	Duct cross sectional area perpendicular to axial direction	m^2
$\boldsymbol{\rho}$	Density	$\frac{kg}{m^3}$
$\boldsymbol{\pi}$	pi	
$\boldsymbol{a}$	Sound speed	$\frac{m}{s}$
$\boldsymbol{Y}$	Pressure losses	%
$\boldsymbol{U}$	Rotor speed	$\frac{m}{s}$

$\boldsymbol{W}$	Velocity relative to rotor frame of reference	$\frac{m}{s}$
$\boldsymbol{chord}$	Blade axial chord	m
$\boldsymbol{pitch}$	Blade channel pitch	m
$\boldsymbol{bld}$	Number of blades	
$\boldsymbol{Rot}$	Rothalpy	$\frac{kJ}{kg}$
$\boldsymbol{\zeta}$	Losses based on enthalpy	%
$\boldsymbol{err}$	zTurbo output error compared to reference values	
$\boldsymbol{\Delta M_1}$	M_1 variation	
$\boldsymbol{n}$	Counter to modify parameters variation	
$\boldsymbol{contr}$	Counter to check the corrective actions done	
$\boldsymbol{Power}$	Power	MW

Pedex	**Description**
$\boldsymbol{o}$	Combustion chamber inlet
$\boldsymbol{b}$	Combustion chamber outlet
$\mathbf{0}$	Stator inlet section
$\mathbf{1}$	Stator outlet – rotor inlet section
$\mathbf{2}$	Rotor outlet section
$\boldsymbol{w}$	Relating to rotor frame of reference
$\boldsymbol{out}$	Relating to outlet section of the considered cascade
$\boldsymbol{in}$	Relating to inlet section of the considered cascade
$\boldsymbol{t}$	Total quantity

$\boldsymbol{s}$	Relating to stator
$\boldsymbol{r}$	Relating to rotor
$\boldsymbol{ax}$	Relating to axial direction
$\boldsymbol{tan}$	Relating to tangential direction
$\boldsymbol{is}$	Isentropic
$\boldsymbol{prof}$	Profile
$\boldsymbol{sec}$	Secondary
$\boldsymbol{z}$	Referred to zTurbo output
$\boldsymbol{ref}$	Reference value
$\boldsymbol{old}$	Referred to previous iteration
$\boldsymbol{M_1}$	Referred to M_1
$\boldsymbol{M_{2w}}$	Referred to M_{2w}
$\boldsymbol{fl}$	Referred to flaring
$\boldsymbol{\alpha_2}$	Referred to α_2
$\boldsymbol{iter}$	Referred to the iteration number
$\boldsymbol{cycle}$	Referred to the calculations only in that specific loop
$\boldsymbol{th}$	Thermal

Apex	**Description**
+	Modified value of parameter
1, 2, …	Number of iteration

Acronyms

Acronym	Description
PDE	Pulsed Detonation Engine
RDE	Rotating Detonation Engine
RDC	Rotating Detonation Combustor
CFD	Computational Fluid Dynamics
BL	Boundary Layer
TE	Trailing Edge
LE	Leading Edge
GC	Gas Cycle

Acknowledgements

I would like to express my deepest gratitude to Prof. Paolo Gaetani and Dott. Noraiz Mushtaq, for giving me the opportunity to work on such an interesting and innovative topic, for listening, advising and helping me overcoming the many difficulties encountered during this thesis. Without you this work would not have been possible.

A special thanks must go to Prof. Giacomo Persico for the precious advices given for the mean line analysis, helping me in the understanding of zTurbo functioning.

I also want to express my deepest gratitude to my mother Tessa, my father Stefano, and my grandparents Giuseppe and Mariella for their support and for giving me the opportunity to move in different cities and study at Politecnico di Milano, following my dreams.

I want to thank a very special person met for an incredible following of events and that improved my life in a way I could never imagine. Thank you Elisabetta.

I am extremely grateful to Sabrina and Guglielmo for welcoming me in their home and lives.

I want also to thank Michele and Angelo for allowing me to play Krav Maga: it gave me the strength and the mentality to overcome all the difficulties I encountered, and it will give me the strength to deal with future challenges.

A lot of thanks go to Federico, Alessio, Nicola, Marcello and all the friends met at Politecnico: together we faced and overcame a lot of tough challenges.

Finally, to all the people that I did not mention above, but have significantly contributed to my life: I would like to thank all of you one by one, but the page is not enough long. Thank you!

15/06/2022

Matteo Bertelli